A high redshift sample of x-ray selected galaxy clusters

Burke, Douglas John

A High Redshift Sample of X-Ray Selected Galaxy Clusters

Douglas John Burke

A thesis submitted to the University of Durham.
in accordance with the regulations for
admittance to the Degree of Doctor of Philosophy.

Department of Physics
University of Durham
September 1997

A High Redshift Sample of X-Ray Selected Galaxy Clusters

Douglas John Burke

Abstract

This thesis describes the creation of a X-ray selected galaxy cluster catalogue — the Southern Serendipitous High-redshift Archival ROSAT Cluster (SHARC) catalogue — and the use of the high-redshift subsample in constraining models of structure formation.

X-ray selection provides the only way of creating an unbiased catalogue of distant galaxy clusters free from the projection effects that plague optical selection. The ROSAT All Sky Survey has a relatively high flux limit ($\simeq 10^{-12}\,\mathrm{erg\,cm^{-2}\,s^{-1}}$), and has been used to create large, local cluster samples. The public availability of data from the pointed phase of PSPC observations means that deep, small-area, X-ray selected cluster surveys can be created. At the flux limits reachable by the PSPC pointings ($\sim 10^{-14}\,\mathrm{erg\,cm^{-2}\,s^{-1}}$), the dominant source population consists of QSOs and AGNs, with clusters forming $\lesssim 10\%$ of the X-ray population: cluster samples are therefore prone to a high level of contamination. Since clusters are the only class of object which are extended at cosmologically significant distances, this contamination can be greatly reduced by selecting sources which are extended. A reduction method is described which uses a maximum-likelihood fitting procedure, based on the Cash statistic, to detect extended sources.

The survey consists of 66 ROSAT PSPC fields, covering an area of 17.7 deg^2. Optical imaging and spectroscopy has been used to provide spectroscopic confirmation of the presence of distant galaxy clusters. The Southern SHARC catalogue is 90% complete, and consists of 36 clusters with redshifts $0.05 < z < 0.7$ and X-ray luminosities between $7 \times 10^{42}\,\mathrm{erg\,s^{-1}}$ and $4 \times 10^{44}\,\mathrm{erg\,s^{-1}}$. The high-redshift subsample contains 16 clusters with $z \geq 0.3$ and luminosities greater than $2 \times 10^{43}\,\mathrm{erg\,s^{-1}}$. The 11 unidentified sources include systems which could be low-redshift groups, and ones which could be high-redshift clusters.

The high-redshift sample has been used to examine the evolution of the cluster population. Both the redshift distribution of the $z \geq 0.2$ clusters and the XLF of the $0.3 \leq z < 0.7$ redshift shell are consistent with the properties of local cluster samples. The Southern SHARC catalogue is therefore consistent with little, or no, evolution of the $\sim 10^{44}\,\mathrm{erg\,s^{-1}}$ cluster population at $z = 0.44$ — the median redshift of the $z \geq 0.3$ sample. This is in direct contrast with the negative evolution seen in the RIXOS cluster sample. It is presently not clear what the difference is due to, although preliminary results from other ROSAT-selected cluster surveys are also consistent with no evolution. Comparison of the high-redshift XLF of this survey, with that of the EMSS, shows that any evolution of the cluster population can only occur at luminosities $\gtrsim 3 \times 10^{44}\,\mathrm{erg\,s^{-1}}$. The $z \geq 0.2$ redshift distributions of both the Southern.SHARC catalogue, and the EMSS, have been fitted by models for the evolution of the XLF. The best fit model has a spectral index of $n = -1.8^{+0.8}_{-0.3}$, and moderate heating of the gas, $\epsilon = -1.7^{+2.5}_{-2.2}$. Recent constraints on the evolution of the cluster LT relation restrict the model to the range $-1.7 \lesssim n \lesssim -1.0$ and $-1.2 \lesssim \epsilon \lesssim 0.7$. Although the models used assume an Einstein-de Sitter universe, the lack of evolution is also similar to that expected in a low-density universe.

Preface

The work described in this thesis was undertaken between 1993 and 1997 whilst the author was a research student in the Department of Physics at the University of Durham, under the supervision of Dr. R. M. Sharples and Dr. C. A. Collins. This work has not been submitted for any other degree, either at the University of Durham or at any other University.

The work presented here was undertaken in collaboration with Dr. R. M. Sharples and Dr. C. A. Collins. Chapter 2 benefitted considerably from discussions with Dr. D. J. Allan, Chapters 3 and 4 from discussions with Dr. A. K. Romer and Dr. R. C. Nichol. Both Dr. J. P. Henry and Dr. L. R. Jones provided information that was useful for the analysis presented in Chapter 4. However, the majority of the material presented here is the author's own work.

A number of the results presented here have appeared in the following papers :

Collins, C. A., Burke, D. J., Romer, A. K., Sharples, R. M., & Nichol, R.C. 1997, ApJ, 479, L117
Burke, D. J., Collins, C. A., Sharples, R. M., Romer, A. K., Holden, B. P., & Nichol, R. C. 1997, ApJ, 488, L83

Acknowledgments

I have benefitted immensely from the guidance I have received from both Chris Collins and Ray Sharples; I have enjoyed the freedom to make my own mistakes knowing that help was not too far away. Many thanks go out to Kath Romer and Bob Nichol for the support they have put into the project, and the encouragement they gave me. I would like to thank, in no particular order, Andrew Ratcliffe, Vincent Eke, Omar Almaini, Gillian Wilson, Brad Holden, and Paul Young for their rapid response to the teasing questions I set them over the last couple of months. The time spent by Bob Mann and Phil James in proof-reading various drafts of text I have given them is much appreciated.

In Durham, thanks to Roger, Scott (both big and small), Katherine, Ale, Dave, Claire and the rest of the yta-ers. My time of Durham would not have been as enjoyable if I had not played football for GradSoc — let's hope there's many more years of B-team 'success' in the future. Particular thanks to Troll, Slotto and Goatie in that regard. Both Alan Lotts and Jane Chapman deserve many thanks, and the odd bar of chocolate, for their help over the last four years.

Since I've moved to Liverpool John Moores University, I've learnt more about gas dynamics around stars than I ever thought I'd want to know — 'thanks' for that John! Apologies to everyone, particularly Tobes, for being a bit of a lightweight these last few months. Hopefully this is the last time you'll have to buy me a diet-coke ...

This thesis would not have been possible without the support, advice, hot meals, and tee-shirts supplied by my family. Cheers.

Contents

List of Figures

List of Tables

Chapter 1

Introduction

This Chapter is intended to provide an introduction to the way the properties of galaxy clusters can be related to cosmological models. Section 1.1 describes the theoretical background assumed throughout this thesis, whilst Section 1.2 discusses the properties of clusters, including an explanation of why cluster selection is better performed in the X-ray, rather than the optical, pass band. Section 1.2.3 includes a discussion of what is known about the evolution of the X-ray properties of clusters from observations made by satellites launched prior to ROSAT. Section 1.3 provides a brief plan of the following Chapters. In this Chapter, the dependence of distances upon the Hubble parameter are explicitly given, assuming $H_0 = 100h$ km s^{-1} Mpc^{-1}. For the remainder of the thesis h is set to 0.5 and the dependence not explicitly shown.

1.1 Theory

Modern cosmology is based on three observations:

- The universe appears to be homogeneous on the largest scales observable. This was initially suggested by the observations of galaxy counts (Hubble 1926), with limits now set by the very small anisotropies present in the Cosmic Mi-

crowave Background (the Sachs-Wolfe effect; Sachs & Wolfe 1967).

- The universe is expanding, with recession velocities of galaxies being proportional to their distance (e.g. Hubble 1927; Hubble & Humason 1931).

- The existence of an isotropic radiation field, the Cosmic Microwave Background (CMB), which was first detected by Penzias & Wilson (1965), and has a temperature of 2.74K (Gush, Halpern & Wishnow 1990).

The interpretation of these facts — the so called Standard Model — is that the universe is expanding from an initially hot, dense, phase, and that the dynamics of the universe is described by Einstein's theory of General Relativity. There are many comprehensive reviews available on the Standard Model and its implications (e.g. Kolb & Turner 1990; Peebles 1993; Padmanabhan 1993); the presentation below outlines the theory of structure formation within this model.

The structures observed in the universe are assumed to have formed by gravitational collapse of fluctuations in the initial density field. The detection of anisotropies in the CMB by COBE, the Cosmic Background Explorer (e.g. Smoot et al. 1992; Bennett et al. 1996) has been interpreted as a signature of these fluctuations. Since structures grow out of the fluctuations, the form of the initial density field should be related to the structures observed in the universe. However, on small scales, non-gravitational forces can play an important part in the evolution of collapsed objects. Observational cosmology requires objects which are both observable over a large range of look-back times and whose properties can be related to the initial density field. As will be argued at the end of this Section, clusters of galaxies are an example of such objects.

The overdensity of the universe at a spatial position $\boldsymbol{x}$ and time t, $\delta(\boldsymbol{x},t)$, is related to the density field, $\rho(\boldsymbol{x},t)$, by:

$$\delta(\boldsymbol{x},t) = \frac{\rho(\boldsymbol{x},t) - \overline{\rho}(t)}{\overline{\rho}(t)}, \tag{1.1}$$

where $\overline{\rho}(t)$ is the mean density of the universe at time t. It is more common to work with the Fourier transform of the density contrast,

$$\delta(k,t) = \delta_k(t) = \frac{1}{V}\int_V \delta(\boldsymbol{x},t)\, e^{-i\boldsymbol{k}.\boldsymbol{x}}\, \mathrm{d}\boldsymbol{x}\,. \tag{1.2}$$

The initial fluctuations are commonly taken to be a Gaussian random field. For such a field, the power spectrum of the fluctuations is given by $|\delta_k|_p \propto k^n$, where the subscript p indicates the fact that this refers to the primordial values, and n is called the spectral index. Measurements of the CMB anisotropies are consistent with a value of $n = 1$ at large scales — the Harrison-Zel'dovich, or scale invariant, spectrum (Harrison 1970; Zel'dovich 1972).

As the universe expands, longer wavelength modes of the spectrum enter the horizon and are affected by damping processes. For a universe dominated by weakly interacting elementary particles, the form of the damping depends on the thermal velocities of the particles (e.g. Frenk 1986). For relativistic particles (hot dark matter, HDM), free streaming of the particles smooths out density fluctuations at small scales. For the case where the HDM is in the form of neutrinos, with a mass of 30 eV, fluctuations with wavelengths smaller than 41 Mpc are damped by this process (e.g. Bond, Efstathiou, & Silk 1980; Bond & Szaly 1983). For slow-moving particles (cold dark matter, CDM), the reduced growth of matter fluctuations during the radiation-dominated era, when the photon-baryon fluid undergoes acoustic oscillations (the Mészáros effect: Guyot & Zel'dovich 1970; Mészáros 1974), produces a bend in the power spectrum, at a scale corresponding to the horizon scale at the transition between matter and radiation dominance. On small scales, the spectral index tends to $n - 4$. The effect of the damping on the power spectrum is parameterised by the transfer function, $T(k,t)$, which relates the power spectrum at a time t, and wavelength k, to the primordial value by

$$|\delta_k(t)|^2 = T(k,t)\ |\delta_k|_p^2\ . \tag{1.3}$$

In a HDM dominated universe, the first objects to form are large super-clusters, with smaller objects forming through fragmentation of these large masses. This is an example of a top-down formation theory. In contrast, CDM dominated universes

have power at all scales; structure formation is a bottom-up, or hierarchical, process. The first generation of objects to form are of sub-galactic size, with larger structures forming by the subsequent merging of smaller scale objects. The HDM model does not appear to be viable, being unable to fit both the galaxy and cluster distributions (Peebles 1982; White, Frenk & Davis 1983). The CDM model is much more successful at explaining the properties of the observed universe (e.g. Frenk 1991). Although the standard model assumes an Einstein-de Sitter universe, with a scale-invariant power spectrum, recent modifications include: the introduction of a non-zero cosmological constant (e.g. Efstathiou, Maddox & Sutherland 1990; Kofman, Gnedin & Bahcall 1993); tilted models, in which $n < 1$ (e.g. Cen et al. 1992; White et al. 1995); and the inclusion of hot dark matter, so called mixed-dark-matter models (e.g. Davis, Summers & Schlegel 1992; Taylor & Rowan-Robinson 1992). The interest in these models is in response to the realisation that the standard CDM model, when normalised to the temperature fluctuations detected by COBE, has too much power on small scales compared to the results from the APM galaxy survey (e.g. Efstathiou 1996).

The interest in clusters is that they are the largest collapsed objects observed in the universe. In a hierarchical universe, the largest structures are the youngest. Their properties should therefore be less affected by non-gravitational forces than smaller-scale objects. They also correspond to high peaks in the density field, and so are sensitive to the form of the power spectrum. For CDM, the slope of the power spectrum on cluster scales is $n \simeq -1$. The evolutionary behaviour of these objects can be used to measure Ω, the mass density of the universe, since the growth of the fluctuations is strongly dependent upon the value of Ω, and is less sensitive to the values of n and the cosmological constant (e.g. Peebles 1980).

1.2 Clusters of galaxies

In the 1930's clusters of galaxies provided the first evidence for dark matter: the virial estimate of the mass, based on the the cluster velocity dispersion, was found

to be much greater than that associated with the cluster galaxies (Zwicky 1933; Smith 1936). Since clusters are rare objects, it was not until the creation of large-area photographic surveys of the sky that it became possible to study clusters in a systematic manner. The production of these catalogues meant that clusters could be used to test cosmological models.

1.2.1 Optically selected cluster catalogues

The most commonly used cluster survey is that of Abell (1958) and Abell et al. (1989). This is based on visual analysis of photographic plates: the 103a-D red-sensitive emulsion plates of the Palomar Observatory Sky Survey (POSS), for the Northern hemisphere; and the IIIa-J Southern Sky Survey plates, taken by the UK Schmidt telescope, for the Southern hemisphere. Clusters were selected, by eye, as enhancements in the projected two-dimensional density of galaxies. The statistical catalogue of Abell (1958) includes clusters which were selected by the following criteria:

Richness

After correcting for contamination by foreground and background galaxies, the enhancement had to contain at least fifty galaxies in the magnitude range m_3 to $m_3 + 2$, where m_3 corresponds to the magnitude of the third brightest galaxy in the enhancement.

Area

The richness criterion had to be satisfied within a fixed aperture, with a radius equal to 1.5 h^{-1}Mpc, commonly referred to as the Abell radius. Distances to clusters were estimated using the $m_{10} - z$ relationship, which allowed the calculation of the angular size corresponding to the Abell radius.

Redshift

The sample was restricted to those clusters with $0.02 \lesssim z \lesssim 0.20$. Clusters closer than this limit covered more than one Schmidt plate, whilst the depth of the Northern survey set the upper limit.

The final compilation, presented in Abell et al. (1989), consists of 4076 clusters, as well as a supplemental list of 1174 Southern clusters considered to be too poor or too distant to be included in the main catalogue.

The properties of a cluster catalogue depend on the definition used to select the clusters. An example of this is the comparison between the Abell and Zwicky (Zwicky et al. 1968) catalogues. The Zwicky systems were also selected by visual inspection of the POSS plates, although the criteria used were less strict than those of Abell. The resulting systems, which are generally poorer than Abell clusters, were defined by:

Richness

There had to be at least fifty galaxies in the magnitude range m_1 to $m_1 + 3$.

Area

Rather than use a fixed metric aperture as in the Abell catalogue, the richness criterion was required to hold for an area within which the surface density of galaxies was twice that of the field.

Whilst the Abell catalogue has been instrumental in shaping our knowledge of the local cluster population (e.g. Bahcall & Soneira 1983; Scaramella et al. 1991), it is not ideal for cosmological studies. The first, and most obvious, problem is that the clusters were selected visually, and so are prone to unquantifiable biases. The availability of digitised galaxy catalogues — the Edinburgh/Durham Southern Galaxy Catalogue (EDSGC; Heydon-Dumbleton, Collins & McGillivray 1989) and the Automatic Plate Measuring (APM) galaxy survey (Maddox et al. 1990) — means that the subjectivity in cluster selection can be removed by using machine-based algorithms. Two such surveys exist, both based on peak-finding algorithms applied to the galaxy density field: the Edinburgh/Durham Cluster Catalogue (EDCC), which contains 737 cluster candidates in an area of 1500 deg^2 (Lumsden et al. 1992); and the APM cluster catalogue, which contains 229 spectroscopically confirmed clusters over an area of 4300 deg^2 (Dalton et al. 1994).

Although such catalogues remove the subjective nature of cluster selection found in previous catalogues, they still define clusters as enhancements in the surface density of clusters. This method is prone to projection effects: superposition of unrelated galaxies, or groups, along the line-of-sight either artificially inflates the richness of the detected cluster, or suggests the presence of a cluster where none is present. Although there is no consensus as to how serious the contamination rate is for optically-selected samples (e.g. Lucey 1983; Frenk et al. 1990; Strubble & Rood 1991), large redshift surveys of optically-selected clusters do show that projection effects occur (e.g. Collins et al. 1995; Katgert et al. 1996). Similarly, anisotropies in the spatial correlation function of Abell clusters, where the line-of-sight signal is elongated, have been interpreted as projection effects (Sutherland 1988).

The samples discussed above have all been limited to relatively low redshifts, because of the depth of the plates from which they were constructed. Therefore high-redshift cluster samples are required to study the evolution of the cluster mass function. The extension of optical selection to high redshift introduces two difficulties: galaxy number counts increase with magnitude (e.g. Tyson 1988), which decreases the contrast of clusters relative to the background; and galaxies evolve, which means that changes in galaxies — such as bursts of star formation — can affect the resulting cluster catalogues. Both effects can be somewhat reduced by selecting clusters in red pass bands, because the slope of the number-count relation flattens as the wavelength increases (e.g. Smail et al. 1995; Hogg et al. 1997), and the spectral energy distributions of galaxies are less affected by recent star formation at longer wavelengths.

There are three recent surveys of the high-redshift cluster population, based on observations with 4m-class telescopes. Two of the surveys use visual classification from photographic plates — Gunn, Hoessel & Oke (1986), GHO, and Couch et al. (1991), CEMM — and the other uses an algorithm which incorporates both spatial and photometric filters, and is applied to a galaxy catalogue selected from CCD images (PDCS, Postman et al. 1996). Only selected samples of these catalogues have been spectroscopically identified, detecting clusters in the range $0.2 \lesssim z \lesssim 0.9$.

A recent development has been the suggestion of selecting high-redshift clusters from surface-brightness fluctuations in the extra-galactic background light (Dalcanton 1996), with preliminary results from such a survey presented by Zaritsky et al. (1997).

The PDCS catalogue is consistent with a constant comoving density of clusters out to $z \lesssim 0.6$ (Postman et al. 1996) and there is little evidence for evolution of the space density of clusters, in the GHO and CEMM catalogues, out to $z \simeq 0.5$ (Castander et al. 1994). However, the difficulties inherent in optical cluster selection mean that these results should not be over-interpreted. From a comparison of X-ray and optical properties of the Couch et al. (1991) sample, Bower et al. (1997) suggest that such catalogues are dominated by clusters lying in filaments which are aligned along the line-of-sight. An additional complication in comparing theoretical predictions to optical observations is that there is no direct relationship between the mass of a cluster and its richness.

1.2.2 X-ray observations of clusters

Early experiments, with balloon- and rocket-borne detectors, had shown that X-ray emission was associated with clusters (e.g. Byram et al. 1966; Fritz et al. 1971; Meekins et al. 1971). Cavaliere et al. (1971) suggested that the clusters were the source of this emission, which was confirmed by observations with the *Uhuru* satellite (e.g. Kellogg et al. 1971; Gursky et al. 1972; Kellogg et al. 1973). Early spectral observations showed that the degree of low energy absorption of clusters was consistent with that from our own galaxy (Davidsen et al. 1975; Kellogg, Baldwin & Koch 1975; Avni 1976), indicating that the emission was from a diffuse, ionized, plasma, rather than from optically-thick sources. The emission mechanism was, however, unknown — it could be either thermal bremsstrahlung from a hot, thermal, plasma or inverse Compton emission resulting from the scattering of CMB photons by relativistic, non thermal, electrons. Although the thermal bremsstrahlung model produced the better fits to the spectral data, it was not until the detection of a strong emission line

at 7 keV, due to a blend of lines from highly ionized Iron — mainly Fe^{+24} and Fe^{+25} — and Nickel ions (Mitchell et al. 1976; Serlemitsos et al. 1977), that the thermal origin of the emission was confirmed.

The discussion below provides a brief introduction to some of the X-ray properties of clusters; a comprehensive review can be found in Sarazin (1988). The plasma producing the X-ray emission — the Intra-Cluster Medium (ICM) — is the dominant baryonic component of rich clusters, exceeding the mass in stars by a factor of $\simeq 5$ (e.g. Forman & Jones 1994). Whilst it forms part of the 'missing mass' of Zwicky (1933) and Smith (1936), it is not the gravitationally dominant component; the gas-mass fraction reaches values of $10 - 30\%$ at the virial radius (e.g. White et al. 1993; David, Jones & Forman 1995; White & Fabian 1995). Assuming that there is no segregation of baryons and dark matter on scales of $\simeq 10\ h^{-1}$Mpc, the gas-mass fraction of clusters provides a lower limit on the baryon fraction of the universe. The value found for clusters, when coupled with the prediction for the baryon density from Big Bang nucleosynthesis calculations (e.g. Walker et al. 1991), implies a low value for Ω_0 (e.g. White et al. 1993).

The typical parameters of the ICM are: bolometric luminosities in the range $\sim 10^{43} - 10^{46}$ erg s^{-1}; densities of $\sim 10^{-3}$ cm^{-3}; and temperatures $\simeq 2 - 10$ keV. The emission is spatially extended, observable out to radii $\simeq 1\ h^{-1}$Mpc. It has only recently become possible, with the launch of ASCA, to systematically study the temperature profiles of clusters. Results suggest that temperatures fall with radius (Markevitch et al. 1996; Markevitch 1996), although the central regions are well approximated as isothermal. Whilst the majority of the ICM consists of Hydrogen and Helium, the presence of line emission, such as the 7 keV line referred to above, indicates that the gas has been enriched. Measurements show that the average metallicity of clusters is approximately 30% of the solar value (e.g. Edge & Stewart 1991; Mushotzky & Scharf 1997). The gas can therefore not be purely primordial — some of it must have been processed by an early generation of stars.

There are four processes which contribute to cluster X-ray emission: free-free emission (thermal bremsstrahlung); free-bound emission (recombination); two pho-

ton decay of meta-stable levels; and line emission due to electron transitions in highly ionized elements. For the typical plasma temperatures in clusters, $\gtrsim 2$ keV ($\gtrsim 2 \times 10^7$ k), the dominant contribution is from free-free emission. The emissivity (the energy emitted per unit time, frequency and volume) at a frequency ν, of an ion of charge Z, in a plasma with temperature T, is

$$\epsilon_\nu \propto Z^2 n_e n_i \frac{g(\nu, T, Z)}{\sqrt{T}} \exp\left(\frac{-h\nu}{kT}\right), \tag{1.4}$$

where n_e and n_i are the electron and ion number densities respectively, $g(\nu, T, Z)$ is the gaunt factor, and k is Boltzmann's constant (e.g. Sarazin 1988). The gaunt factor, which corrects for Quantum Mechanical effects and the effect of distant collisions, is a slowly varying function of T and ν (Karzas & Latter 1961; Kellogg et al. 1975). Integrating the emissivity over frequency and volume gives the following approximation for the bolometric X-ray luminosity, L, of the ICM,

$$L \propto \int_V n_p n_e \sqrt{T}\, \mathrm{d}V, \tag{1.5}$$

where n_p and n_e are the proton and electron number densities (e.g. Longair 1982). The X-ray luminosity of a rich cluster is therefore much more sensitive to changes in the density than the temperature of the ICM; the luminosity is proportional to the square of the density and the square root of the temperature. Detailed models of the emission spectrum are available, the most popular being the Raymond-Smith (Raymond & Smith 1977) and MEKAL (Mewe, Gronenschild & van den Oord 1985) codes.

For an isothermal model, in which both the gas and galaxies are in hydrostatic equilibrium within the dark-matter potential, the use of the King approximation (King 1962) for the galaxy distribution, as suggested by Cavaliere & Fusco-Femiano (1976), gives the following equation for the gas density:

$$\rho_g(r) \propto \left(1 + \left(\frac{r}{r_c}\right)^2\right)^{-3\beta/2}, \tag{1.6}$$

where

$$\beta = \frac{\mu m_p \sigma^2}{3kT_g}, \tag{1.7}$$

μ is the mean molecular weight of the gas, m_p is the mass of a proton, σ is the three-dimensional velocity dispersion of the galaxy population, T_g is the gas temperature, and r_c the core radius of the cluster. The parameter β measures the ratio of the energy, per unit mass, in the galaxies compared to the gas. In the above model, the gas and galaxy density distributions are related by $\rho_{\rm g} \propto \rho_{\rm gal}^{\beta}$. Since the surface-brightness of a cluster is proportional to the emission measure, EM, where

$$EM = \int n_p n_e \, {\rm d}l \tag{1.8}$$

and l is the line-of-sight distance through the cluster, the surface-brightness profile varies with the projected distance, r, from the cluster centre as

$$S(r) = S_0 \left(1 + \left(\frac{r}{r_c}\right)^2\right)^{0.5-3\beta} , \tag{1.9}$$

where S_0 is the cluster central surface-brightness value.

Jones & Forman (1984) and Forman & Jones (1994) show that this equation is a good description of the local cluster population, with core radii in the range $50-250$ h^{-1}kpc and $\beta \simeq 0.6-1.0$: fiducial values are $r_c = 125$ h^{-1}kpc and $\beta = 2/3$. As the surface brightness outside the core is proportional to $r^{1-6\beta}$, the X-ray emission from clusters is dominated by their core regions. Cooling flow clusters (e.g. Fabian 1994) show central peaks of emission, in excess of the prediction of equation (1.9), where the density of the gas in the core is high enough that significant cooling can occur.

Although rich clusters are very luminous, they are rare objects: the X-ray sky is dominated not by clusters, but by QSO's. Deep, small area, surveys of PSPC fields (e.g. Rosati et al. 1995; Georgantopoulos et al. 1996) show that the surface density of X-ray sources at a flux of 10^{-14} erg cm^{-2} s^{-1} — approximately the limit achievable by ROSAT (e.g. Section 2.1) — is close to 100 deg^{-2}, whereas the surface density of clusters at this limit is ~ 5 deg^{-2}. Therefore clusters form only 5-10 % of the X-ray source population at the flux limits ROSAT is sensitive to, the fraction decreasing for deeper surveys because the cluster log N - log S is flatter than that of the general X-ray source population.

1.2.3 Why use X-ray selection ?

The great advantage of X-ray selection of clusters is that it greatly reduces the biases present in optical catalogues. The detection of X-ray emission indicates the presence of a real physical object — the gas trapped in the cluster potential well — and since the X-ray emission is strongly peaked in the core, as indicated by equation (1.9), the chance of line-of-sight projection effects in X-ray selected cluster catalogues is much less than in optical catalogues. Not only does X-ray selection produce a better-defined catalogue than optical selection, it is easier to relate the properties of clusters in such a catalogue to theoretical models. This is because the relationship between the cluster mass and its X-ray luminosity, or temperature, is better defined than the mass-richness relation (e.g. Evrard 1989; Eke, Cole & Frenk 1996). The sensitivity of current X-ray satellites means that clusters can be observed out to redshifts approaching unity, comparable to the deepest optical surveys.

An example of the advantages of X-ray selection is the measurement of the two-point cluster correlation function, which is the Fourier transform of the power-spectrum of density fluctuations (e.g. Peebles 1980). Samples based on the Abell catalogue show that the correlation length of rich clusters is $\simeq 20 - 25\ h^{-1}$Mpc (e.g. Bahcall & Soneira 1983; Postman, Geller & Huchra 1986; Huchra et al. 1990; Postman, Huchra & Geller 1992). This result is in direct conflict with the predictions of the standard CDM model (White et al. 1987). However, studies using machine-selected cluster catalogues show a smaller correlation length of $\sim 15\ h^{-1}$Mpc (Dalton et al. 1992; Nichol et al. 1992; Croft et al. 1997), suggesting that the results from the Abell catalogue are compromised by projection effects. Lahav et al. (1989) presented the first correlation function from an X-ray selected cluster catalogue, finding a correlation length of $\simeq 20\ h^{-1}$Mpc, although the small sample size (53 clusters) means that the uncertainty in the result is large. Using a sample of 128 clusters, selected on the basis of their X-ray properties from the ROSAT All Sky Survey, Romer et al. (1994) show that the correlation length agrees with the low value found from the machine-generated samples, and that there is no evidence for the line-of-sight anisotropy seen in the Abell catalogue (Bahcall, Soneira & Burgett 1986).

1.2.4 Early X-ray selected cluster catalogues

The first studies of the evolution of the X-ray properties of clusters were based on optically-selected samples — in general the Abell catalogue. Henry & Lavery (1984) showed that the X-ray luminosity function (XLF) of Abell clusters at a redshift of 0.25 is the same as at low redshift, whilst Kowalski, Ulmer & Cruddace (1983) showed that the volume emissivity of Abell clusters was the same at redshifts of 0.07 and 0.17. However, since the samples were optically selected, they are subject to the biases discussed above.

The first X-ray selected cluster sample resulted from the HEAO-1 A-2 experiment (Piccinotti et al. 1982). This consisted of 30 clusters, with $z \lesssim 0.1$, detected over an area corresponding to 66% of the sky. Edge et al. (1990) extended this sample with the *Ariel* V all-sky survey, using observations by EXOSAT and *Einstein* to reduce confusion effects. The resulting catalogue consists of 46 clusters with fluxes greater than 1.7×10^{-11} erg cm^{-2} s^{-1} in the $2 - 10$ keV pass band and high galactic latitude ($|b| > 20°$). The log N - log S slope of the luminous clusters, with $L > 8 \times 10^{44}$ erg s^{-1}, differs from that of the low luminosity sample, with too few luminous clusters detected at faint fluxes. This was interpreted as strong negative evolution of bright clusters at $z \sim 0.1$.

The *Einstein* Extended Medium Sensitivity Survey (EMSS; Gioia et al. 1990b) also produced evidence for negative evolution in the cluster population. The EMSS consists of sources detected serendipitously in *Einstein* observations; although the area covered is smaller than the Edge et al. (1990) survey, the flux limit is approximately one-hundred times fainter, and in a softer pass band ($0.3 - 3.5$ keV). The latest version of the catalogue (Gioia & Luppino 1994) consists of 104 clusters with redshifts less than 0.9. Since the survey is constructed from serendipitous observations, the flux limit is a function of sky coverage, with the faintest limit being 1.3×10^{-13} erg cm^{-2} s^{-1} over an area of 40 deg^2. Gioia et al. (1990a) and Henry et al. (1992) compare the XLF of different redshift shells, and find a steeper slope at $z = 0.33$ than at $z = 0.17$. The conclusion is that there are fewer high-luminosity

clusters at high redshift than at present.

Whilst there are differences in the results — Edge et al. (1990) see very recent evolution for the most luminous clusters and Henry et al. (1992) find evolution of less luminous clusters at a higher redshift — the observations, pre-ROSAT, suggest a recently evolving cluster population. This suggests a high value of the density parameter, as recent evolution of clusters is only expected to occur if Ω is high (e.g. Peebles 1980). However, the negative evolution is unexpected in a universe in which cluster evolution can be described by the action of gravity alone, such as the self-similar model of Kaiser (1986). It indicates that the models have to take account of processes such as cooling, and non-gravitationally induced heating (e.g. Kaiser 1991; Evrard & Henry 1991).

The availability of data from the Position Sensitive Proportional Counter on board ROSAT — which is roughly three times more sensitive and has two times better spatial resolution than the *Einstein* IPC used by the EMSS — allows the testing of these results. As discussed in detail in Chapters 2 and 4, there are two complementary routes: the creation of large, local, cluster samples from the ROSAT All Sky Survey; and the creation of distant catalogues from deep, pointed phase, observations. As the there are several projects following-up clusters detected in the ROSAT All Sky Survey (e.g. Romer et al. 1994; Ebeling et al. 1997; De Grandi et al. 1997), this thesis presents a survey of the distant X-ray galaxy cluster population. Since ROSAT has very limited spectral resolution — a detailed description of ROSAT and its instruments is given in Section 2.1 — the analysis is restricted to the cluster X-ray luminosity function.

1.3 Thesis plan

This Chapter has introduced the idea that clusters of galaxies are useful tools for studying cosmology. Whilst early work in this area used optical samples, the current trend is to use X-ray selected cluster samples, because they are better defined, and

less prone to biases, than optical catalogues.

Chapters 2 and 3 describe the steps taken to produce a distant, X-ray selected cluster catalogue. The X-ray data used for this catalogue comes from the ROSAT PSPC data archive, which contains observations for which the proprietary rights have ended. Chapter 4 compares the properties of the distant cluster sample to those of other catalogues and to theoretical predictions. The discussion extends that found above by including the results of other ROSAT-selected cluster catalogues, at both high and low redshifts, as well as initial results from the ASCA satellite. Chapter 5 presents the conclusions drawn from this work, and discusses several future lines of research.

Chapter 2

Defining the X-ray Catalogue

This Chapter describes the creation of the X-ray source catalogue and the simulations performed to estimate the survey selection function. Section 2.1 describes the instruments on the ROSAT satellite and their use in detecting distant clusters. Details of the reduction process are given in Section 2.2, including a discussion of the best way to select cluster candidates for optical follow-up. Section 2.3 describes the simulations and discusses the results. All fluxes and luminosities are quoted in the $0.5 - 2.0$ keV pass-band, ROSAT and cluster rest-frame respectively, unless stated otherwise. Throughout this Chapter, and the remainder of this thesis, it will be assumed that $H_0 = 50$ km s^{-1} Mpc^{-1} and $q_0 = 0.5$.

2.1 ROSAT

ROSAT was launched into a low Earth orbit, at an altitude of 580 km, on June 1st, 1990. It contains two telescopes: the X-ray telescope (XRT) and the Wide-field Camera (WFC). The XRT consists of three instruments, two German built Position Sensitive Proportional Cameras (PSPC) and one US built High Resolution Imager (HRI). The WFC is the UK contribution to the satellite, a camera which operates at UV wavelengths ($\simeq 20 - 210$ eV). Strong Galactic absorption at UV wavelengths restricts cluster observations to the XRT. A detailed description of the satellite and

its instruments can be found in Briel et al. (1994).

The XRT is a grazing incidence telescope with a 1° radius field of view, sensitive to photons with energies $\simeq 0.1 - 2.5$ keV. The PSPC and HRI instruments are mounted on a wheel to allow the instrument at the telescope focus to be changed. As its name suggests, the PSPC uses proportional counters to detect incoming photons, and has moderate spatial and spectral resolution. On axis, the point spread function (PSF), which is energy dependent, has a full-width half-maximum (FWHM) of $\simeq 25''$ at 1 keV. The energy resolution is $\Delta E/E = 0.43\,(E/0.93)^{-0.5}$ across the detector, where E is measured in keV. The PSPC covers the whole field of view of the XRT; however, the support structure of the PSPC face, shown in Figure 2.1, causes severe vignetting around $20'$ from the field centre. To prevent the meshes, which are opaque to X-rays, from causing significant shadowing of on-axis sources, the telescope is wobbled, in a direction diagonal to the mesh structure, during PSPC observations. As both the PSF and the sensitivity of the instrument quickly degrade beyond the central support ring, most work is restricted to the central region. The HRI, which is very similar to the *Einstein* observatory HRI, uses a detector based on micro-channel plates and has sides of $\sim 38'$, an on-axis PSF of FWHM $\simeq 5''$, and no energy resolution. Both detectors have positional accuracies of $10''$ or better and provide timing information for detected photons.

Although the HRI has a much greater spatial resolution than the PSPC, its poorer sensitivity (one-third that of the PSPC) and much higher background rate (about ten times that of the PSPC) make it less useful for faint cluster surveys. The PSPC has been, until recently, the most used instrument in the XRT, so the XRT pointing database, which contains those observations which are in the public domain, is dominated by PSPC pointings. As the PSPC is the better suited for faint cluster observations, and there is little data currently available for the HRI, the current survey is restricted to PSPC pointings.

After the initial verification phase, the PSPC performed an all-sky survey (the RASS) for six months. Such a large area is ideal for cluster surveys, but the high flux limit of $\sim 10^{-12}$ erg cm^{-2} s^{-1} restricts cluster catalogues to $z \lesssim 0.3$ (e.g. Ebeling

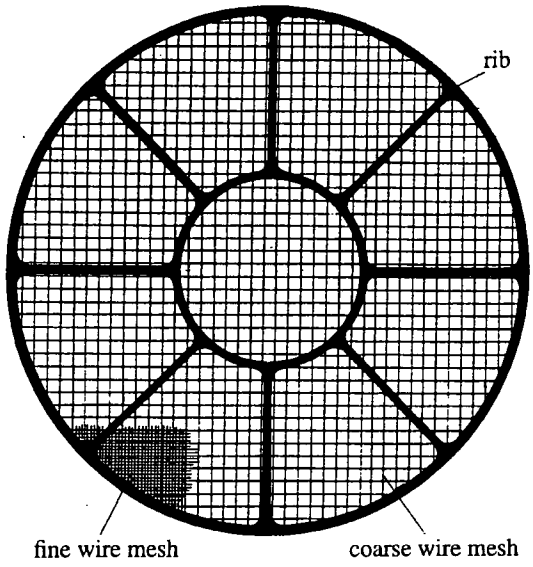

Figure 2.1: The PSPC entrance window is made of thin plastic, a 1μm thick sheet of polypropylene, which needs a support structure to withstand the pressure exerted by the gas within the counter. The Figure shows this support structure, where the ribs and mesh are opaque to X-rays. The central support ring — the central circle from which the ribs radiate — is about 20′ from the detector centre. This Figure is taken from Briel et al. (1994).

et al. 1996; De Grandi et al. 1997). Once the RASS had been completed the pointed phase began, with exposure times ranging from $\sim$ 1 to 100 ks. Twelve months after the completion of the observation, the data entered the public domain; Figure 2.2 illustrates the huge amount of data available in this archive. An exposure time of 10 ks can detect point sources with fluxes $\sim 2 \times 10^{-14}$ erg cm^{-2} s^{-1}, almost one-hundred times fainter than possible with the RASS, at a significance level of 5σ, for a typical background rate of 2×10^{-4} counts s^{-1} arcmin^{-2}. The minimum detectable cluster luminosities for both this flux limit and the faintest flux limit of the EMSS (Henry et al. 1992) are shown in Figure 2.3. Cluster samples selected from the PSPC archive can therefore probe, at redshifts of 0.6, down to $\sim 7 \times 10^{43}$ erg s^{-1} whereas the EMSS only reaches $\sim 2 \times 10^{44}$ erg s^{-1}.

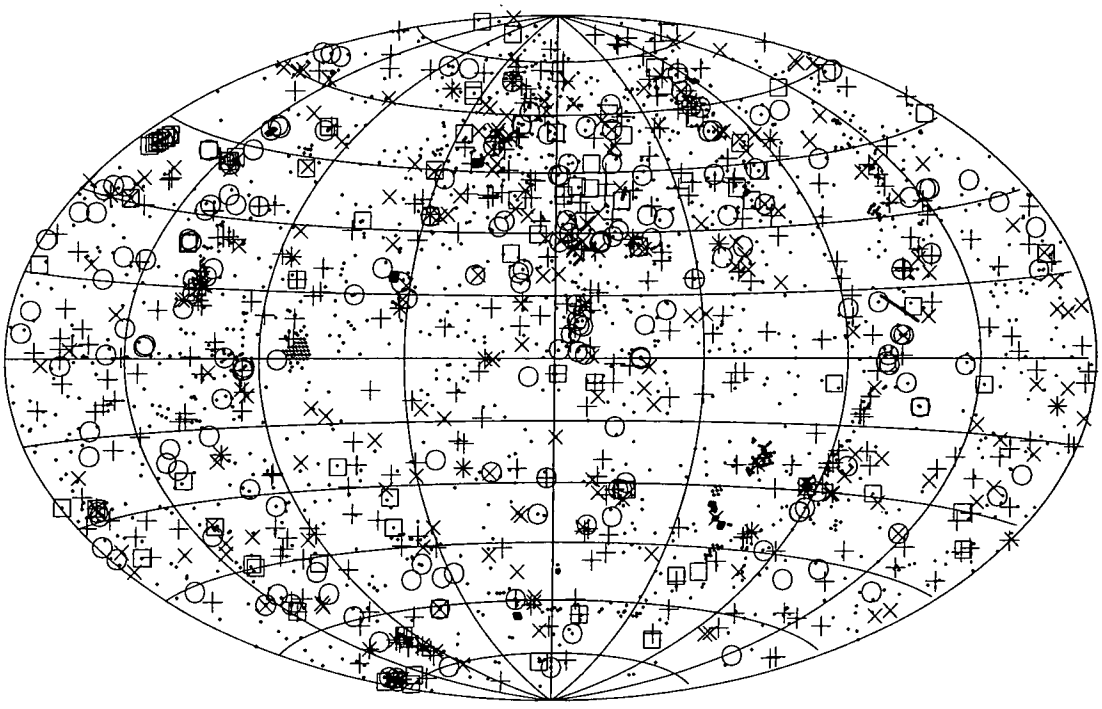

Figure 2.2: Aitoff projection, in equatorial coordinates, of the PSPC pointings in the public domain archive. The exposure time of a pointing is indicated by the symbol type. The center of the plot refers to (12^h, 0°), the lines of longitude are in steps of 3^h, and the lines of latitude are in steps of 15°.

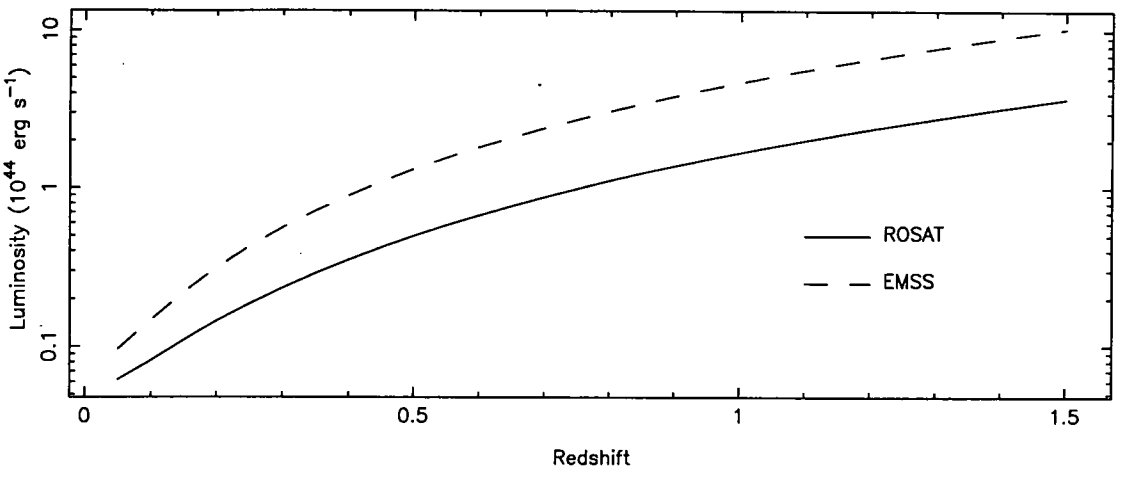

Figure 2.3: The solid line shows the minimum detectable cluster luminosity, as a function of redshift, for a ROSAT flux limit of 2×10^{-14} erg cm^{-2} s^{-1}. The dashed line indicates the minimum detectable cluster luminosity for the faintest flux limit of the EMSS, which corresponds to an area of 40 deg^2 (Henry et al. 1992). Luminosities are quoted in the 0.5 – 2.0 keV pass-band.

2.2 PSPC Data Reduction

This Section describes the creation of the cluster candidate list from ROSAT PSPC observations. In Section 2.2.1 various ways of preferentially selecting clusters from an X-ray catalogue are discussed. The common methods for detection of X-ray sources, together with a discussion of the method used in this work, are described in Section 2.2.2. The Section ends with a description of both the fields used in the survey and the cluster-candidate list created by the reduction process.

2.2.1 Search Criterion

Section 1.2.2 illustrated that clusters are not the dominant source population in the X-ray sky: a 10 ks PSPC pointing has, on average, 7 sources within the central 18′, of which only 0.8 will be clusters (Georgantopoulos et al. 1996; Rosati et al. 1995). Therefore extra criteria must be used to reduce this contamination, in order to produce a catalogue of cluster candidates which can be optically identified in a reasonable amount of telescope time. As the cluster sample is used in Chapter 4 to calculate the X-ray luminosity function, it is important that the selection

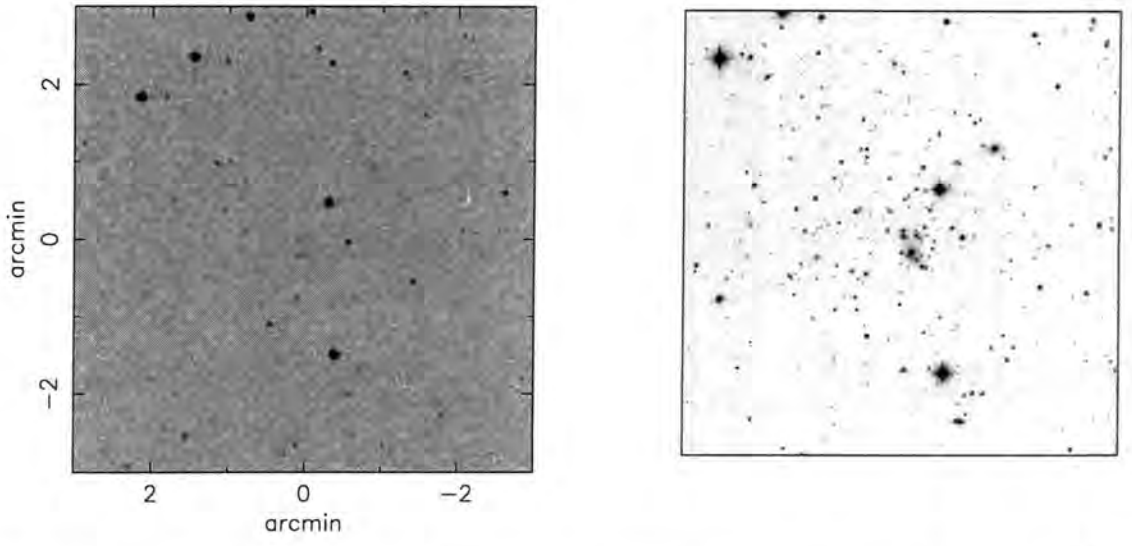

Figure 2.4: The left-hand image shows the photographic sky survey image of the $z = 0.55$ cluster RX J1354.2-0222, detected in the ROSAT survey. The right-hand image shows the same cluster; this time a 10 minute R-band exposure using EFOSC-1 on the ESO 3.6m telescope.

method produces well-defined samples — ones for which a selection function can be estimated.

Optically, clusters are visible as large enhancements in the number of galaxies in a given region of the sky. It would therefore seem reasonable to look at the optical counterparts of the detected X-ray sources to see if a cluster is visible. The only available optical surveys with sufficient sky coverage for this purpose are the photographic Palomar and UK Schmidt Telescope sky surveys. Unfortunately, they are not deep enough to detect clusters much beyond a redshift of 0.2. This is illustrated in Figure 2.4, which shows two optical images of a distant cluster. The cluster is easily visible in the R-band CCD exposure from the ESO 3.6m telescope whilst not appearing on the sky survey image.

Therefore the X-ray data itself has to be used as a discriminant. One possibility is to use the source spectrum, since non-cluster X-ray sources either have power-law spectra (e.g. active galaxies), or thermal spectra at significantly cooler temperatures than clusters (e.g. coronal stellar emission). Unfortunately the PSPC has a very limited spectral resolution which precludes detailed spectral analysis (e.g. Vikhlinin et al. 1995b; Almaini et al. 1996). For the RASS, the PSPC energy range was

divided into 'hard' (0.4 – 2.4 keV) and 'soft' (0.07 – 0.4 keV) bands and used to define the hardness ratio,

$$HR = \frac{\text{Hard} - \text{Soft}}{\text{Hard} + \text{Soft}}, \tag{2.1}$$

with which limited analysis is possible. Hard sources have $HR \rightarrow 1.0$ and soft sources have $HR \rightarrow -1.0$. However, care must be taken in interpreting such hardness ratios, since sources that lie in regions of high Galactic absorption will appear artificially hard, due to absorption of the low energy photons, and strong emission lines can skew the ratio. The hardness ratio does allow some source discrimination, for instance clusters generally have hardness ratios greater than zero (Ebeling et al. 1996), but it does not significantly reduce the contamination rate, as discussed in Section 2.2.4.

As the majority of X-ray sources are compact objects, whereas cluster emission is from a diffuse component, an obvious discriminant is the photon distribution — select those objects which are extended compared to the PSF. This requires that the instrumental PSF is both small enough, and well enough defined, to allow clusters at the redshifts of interest to be detected as extended. Section 2.3 contains detailed simulations to test these concerns, but a simple calculation suggests that the PSPC can detect clusters as extended objects out to $z \sim 0.6$. As shown in Figure 2.5, a core radius of 250 kpc subtends $\sim 30''$ at $z = 0.6$, which is still larger than the on-axis PSF FWHM. At this redshift a 10^{44} erg s^{-1} cluster has a flux of 7×10^{-14} erg cm^{-2} s^{-1}, corresponding to $\sim 5 \times 10^{-3}$ photons per second, or ~ 50 photons in a 10 ks exposure. Although compact clusters will be missed by this technique, it produces a well-defined cluster sample whose selection function can be calculated by simulations.

2.2.2 Overview of the Reduction Procedure

The first choice to make, when analysing ROSAT PSPC data, is which energy band to use. Despite limited spectral resolution, it is possible to define several PSPC pass bands (e.g. Snowden et al. 1994). The choice of band depends upon

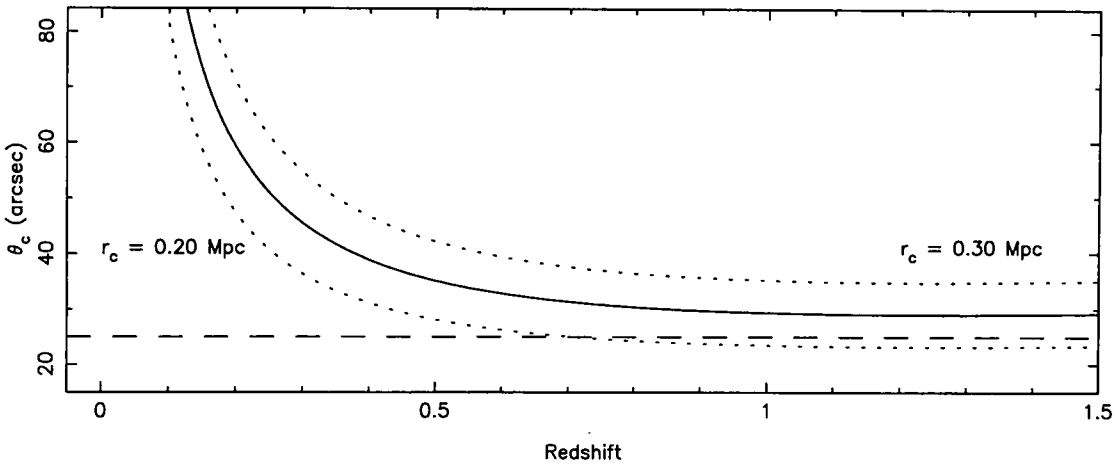

Figure 2.5: The solid line shows the angle subtended by a cluster core radius $r_c = 250$ kpc, as a function of redshift. The dashed horizontal line shows the FWHM of the on-axis PSPC PSF. The two dotted lines are for cluster cores of 200 and 300 kpc.

the source and background spectra — a trade-off between maximising the source counts whilst minimising the background signal. The PSPC has three background components (Snowden et al. 1994): charged particles from the local environment, scattered solar radiation, and the diffuse celestial X-ray background. Whilst the particle background spectrum is roughly independent of energy, the majority of the flux from both the celestial background and scattered solar radiation is at energies below 0.5 keV. The effect of the increased background signal at low energies can be seen in Figure 2.6, where the radial profile of a rich cluster, Abell 3562, is shown as a function of energy. Cool neutral gas in the Galaxy absorbs photons at soft X-ray energies, the amount of absorption parameterised by the column density of neutral Hydrogen, $n_{\rm H}$, along the line-of-sight (e.g. Brown & Gould 1970). Figure 2.7 shows how a typical cluster spectrum is affected by such absorption: the absorption is most severe for photon energies less than 0.5 keV; it is only for column densities greater than 10^{21} cm^{-2} that the absorption significantly affects the spectrum at energies around 1.0 keV. To avoid the effects of absorption by Galactic material, and the increased background level, a lower energy limit of 0.5 keV is used. Above 2.0 keV the telescope effective area rapidly drops to zero and the response function is poorly calibrated. The chosen pass-band for the survey is therefore 0.5 keV to 2.0 keV.

The next decision to be made is which source detection method to use. For an

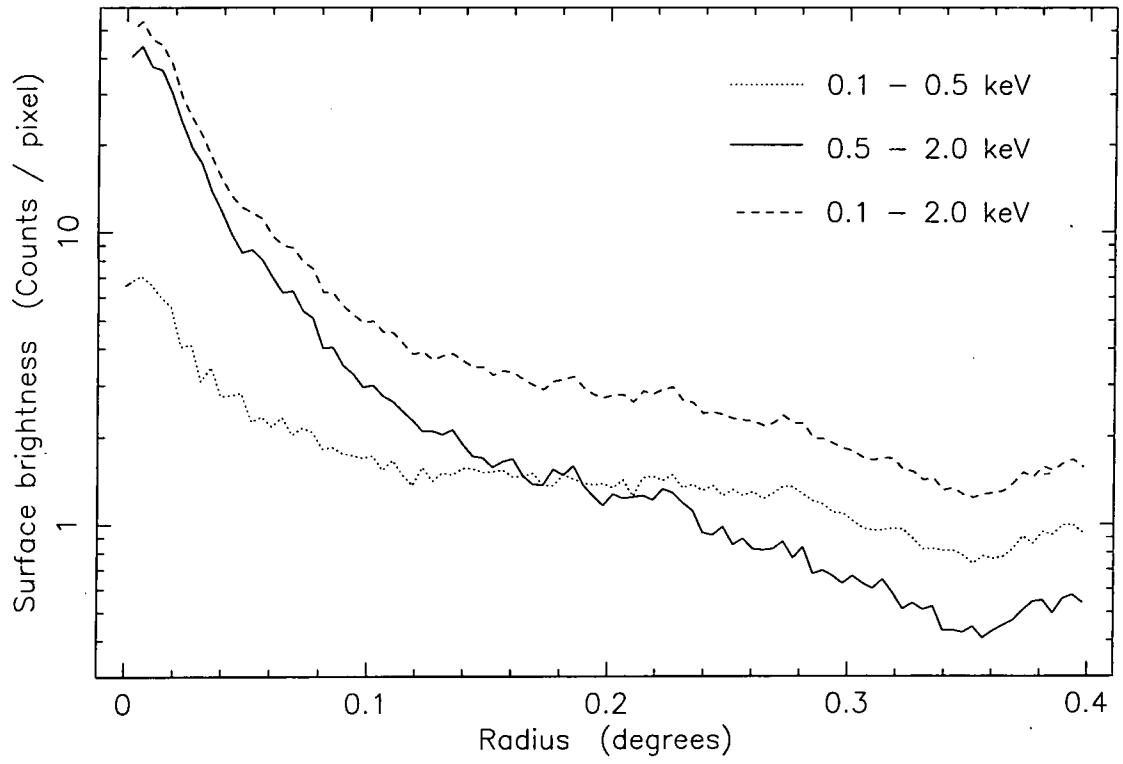

Figure 2.6: This Figure shows radial profiles of a PSPC observation of Abell 3562, a Richness Class 2 cluster at a redshift of 0.050. The line types indicate the different energy bands of the profiles: the solid line is for the $0.5 - 2.0$ keV pass-band, the dotted line is for the $0.1 - 0.5$ keV pass-band, and the dashed line is for the combined pass-band, i.e. $0.1 - 2.0$ keV. The dip in each profile beyond a radius of $0.3°$ is due to shadowing by the support structure.

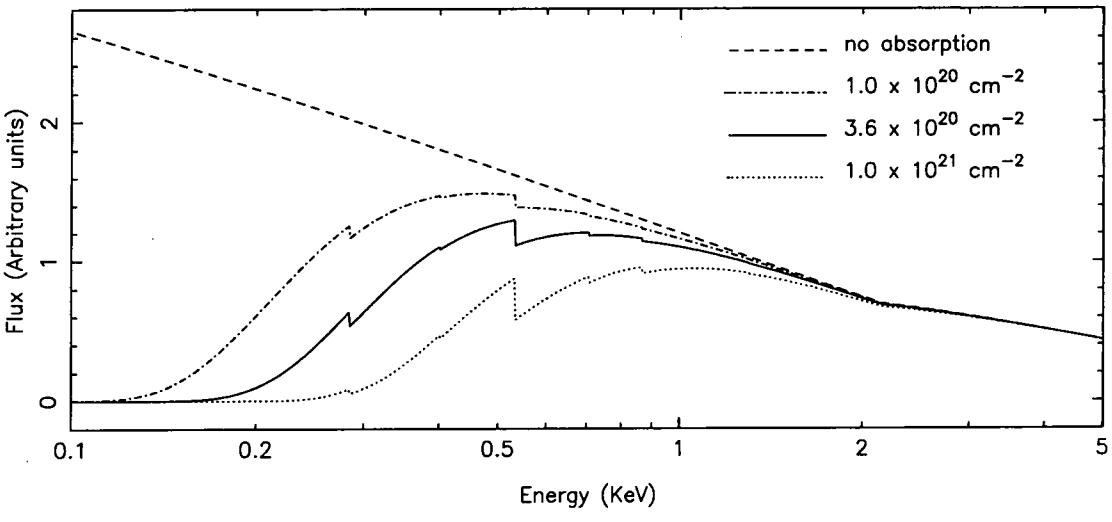

Figure 2.7: The dashed line indicates a thermal bremsstrahlung spectrum at a temperature of 6 keV, with no absorption by cool gas. The other curves show how different column densities of absorbing gas affect the spectrum.

exposure time of 10 ks the typical background is $0.1 - 0.5$ counts per 15″ by 15″ pixel, which means that background fluctuations are described by Poisson, rather than Gaussian, statistics. Several of the most popular search techniques used in X-ray astronomy are listed below.

Sliding Box

An aperture is placed down on the image and the signal-to-noise calculated, where the background is estimated from the edges of the aperture. This aperture is moved across the field, usually in steps of one third the cell size, and the detected sources are then masked out of the field. A background model, usually a two dimensional spline, is fit to the field. The signal-to-noise calculation is then repeated, this time using the model background values. Such an approach was used to produce the *Einstein* EMSS (Gioia et al. 1990b) and by the Standard Analysis Software System (Cruddace et al. 1991) for the RASS.

Smoothing

There are two methods in use in X-ray astronomy which involve smoothing of the data; wavelet analysis, as first used by Slezak, de Lapparent & Bijaoui (1993) with recent examples including Rosati et al. (1995) and Nichol et al. (1997), and the matched filter technique of Vikhlinin et al. (1995a). Both techniques are based upon smoothing the data with a kernel; sources detected in this smoothed image have sizes similar to that of the kernel. A range of object sizes can be detected by using different kernel sizes.

Tessellation and Percolation

Voronoi Tessellation and Percolation (VTP, Ebeling & Wiedenmann 1993; Ebeling 1993) is a departure from the previous techniques, in that it does not assume a source profile during the detection process. The photon positions are used to create a grid in which each cell contains one photon — the Voronoi tessellation — where the inverse of the cell area is proportional to the flux at that position. A percolation analysis is used to find all connected cells with areas less than the background limit, producing a source list.

All the methods listed above are being used to produce cluster lists from PSPC pointings: the ROSAT International X-ray and Optical Survey (RIXOS, Castander et al. 1995) uses a sliding-box technique; the ROSAT Distant Cluster Survey (RDCS, Rosati et al. 1995) and Northern Serendipitous High-redshift Archival ROSAT Cluster survey (SHARC, Nichol et al. 1997) use wavelet-transform based techniques; and the Wide-Angle ROSAT Pointed Survey (WARPS, Scharf et al. 1997) use a VTP approach. There is currently no consensus as to the best way of detecting extended sources in X-ray pointings; the publication of the cluster samples from the surveys listed above, combined with this survey, should eventually enable the relative merits of the techniques to be assessed.

The chosen detection method is based upon the sliding box technique, as implemented by the PSS program from the Starlink X-ray reduction package ASTERIX (Allan & Vallance 1995). The reason for using this program was its availability and the fact that it had been successfully used on deep PSPC pointings (e.g. Georgantopoulos et al. 1996). There are two main differences to the sliding box method as described above. The first difference is that the background is estimated from the whole field, rather than from the edges of the detection aperture. This reduces the chance of extended source emission artificially increasing the background estimate, which can lead to extended sources being missed. The second difference is that a maximum-likelihood ratio technique assuming Poisson fluctuations (Cash 1979) is used, rather than assuming Gaussian fluctuations. This is necessary because the PSPC background count rates are so low that the majority of pixels detect no photons during an observation.

PSS places a square aperture on the image and finds the best-fit significance, as described below, of a source centred on the aperture. The aperture is moved across the source image, one pixel at a time, producing a detection significance map; application of a significance threshold to this map produces a source list. These sources are re-analysed, this time stepping the aperture by sub-pixel shifts, to produce a more accurate estimate of the source significance and position.

The following description of the source significance calculation is based upon that

given in Allan & Vallance (1995). The calculation is for a grid of pixels, labelled using the indices i and j, with the source assumed to be at the centre of the grid. Each pixel contains $d_{i,j}$ photons. The model value of pixel (i,j), $m_{i,j}$, is defined as

$$m_{i,j} = As_{i,j} + b_{i,j}\,, \tag{2.2}$$

where A is the source flux, $s_{i,j}$ the source profile amplitude integrated over pixel (i,j), and $b_{i,j}$ is the background signal for this pixel. For a given source profile, the only unknown in equation (2.2) is the source flux, A, since the background is assumed to be known. The probability, P, of observing the source distribution for a given model is

$$P = \prod_{i,j} \frac{e^{-m_{i,j}}\, m_{i,j}{}^{d_{i,j}}}{d_{i,j}\,!}\,. \tag{2.3}$$

The fitting procedure minimises the Cash statistic $C = -2\ln P$ (Cash 1979). Substituting in the value of P into this formula gives

$$\begin{aligned} C &= 2\sum_{i,j}\left[m_{i,j} - d_{i,j}\,\ln m_{i,j} + \ln(d_{i,j}\,!)\right] \\ &= 2\sum_{i,j}\left[As_{i,j} + b_{i,j} - d_{i,j}\,\ln(As_{i,j} + b_{i,j}) + \ln(d_{i,j}\,!)\right]\,. \end{aligned} \tag{2.4}$$

As the $\ln(d_{i,j}\,!)$ term is independent of A, the actual statistic used is $\tilde{C}(A)$, defined as

$$\tilde{C}(A) = 2\sum_{i,j}\left[As_{i,j} + b_{i,j} - d_{i,j}\,\ln(As_{i,j} + b_{i,j})\right]\,. \tag{2.5}$$

This is evaluated to find the maximum-likelihood flux estimate, $\tilde{A}$, when $\partial\tilde{C}/\partial A = 0$, or

$$\sum_{i,j} s_{i,j} - \sum_{i,j} \frac{d_{i,j}\, s_{i,j}}{As_{i,j} + b_{i,j}} = 0\,. \tag{2.6}$$

As $\tilde{C}(A)$ is χ^2_1 distributed about $\tilde{C}(\tilde{A})$ (Cash 1979), the detection significance, S, is given by

$$S^2 = \tilde{C}(0) - \tilde{C}(\tilde{A})\,. \tag{2.7}$$

The approach discussed above is quite general, in that the source profile fitted to the data need not be the instrumental PSF. It also provides a means of testing whether one source profile is a better description of the data than another. This

Clean Data	Exclude time periods using quality constraints.
Produce image	Use the 0.5 – 2.0 keV energy range, with 15″ square pixels, limiting data to within 0.32° of the field centre.
Produce background model	Calculate initial background estimate using a sigma-clipped mean. Detect sources with a significance limit of 4σ and this background estimate. Define the background region by masking out these sources. Calculate the model background from this masked image.
Create 1st pass source list	Detect sources using a 4σ detection threshold and the model background.
Estimate source sizes	Fit a Gaussian to the radial profile of each source.
Create 2nd pass source list	Re-run the detection algorithm on each source, using a 5σ threshold and an aperture optimized for the source size. Calculate the extent significance and hardness ratio of each source.
Extended source list	Accept those sources with an extent significance ≥ 3 and that lie within 18′ of the field centre. Remove any sources which are a target of the observations.

Table 2.1: The various stages in the reduction of one PSPC field.

time, instead of comparing the Cash statistic for the best-fit flux to that for no flux, the comparison is between the best-fit Cash statistic for the two source profiles.

2.2.3 Reduction of a field

Table 2.1 contains a concise description of the various stages in the reduction, which are described in more detail below.

The data for the pointings which are in the public domain are stored at several sites: Leicester University, Goddard Space Flight Center, and MPE. After converting the supplied data to a format usable by the ASTERIX data-reduction package, the first step is to produce a list of bad time-slots — those periods of the observation which do not fulfil certain 'quality' requirements. Since photon detections are tagged

with an arrival time, as well as spatial and energy information, this list can be used to produce an observation containing only photon events which were detected during 'good' observing periods. The first requirement is that the Master Veto Rate, which measures the particle background, is low enough that the model used to calculate the various background components is valid. The second requirement is that the Aspect Error is low, to reduce incorrect telescope pointings causing spurious extended sources. The use of these constraints reduces exposure times by up to twenty percent; observations for which the cleaned observation times are less than 10 ks are removed from the sample. An image, in the energy range $0.5 - 2.0$ keV, of the central $0.32°$ radius of the observation is produced. Figure 2.8 shows an example of the whole $1°$ field of view of one pointing; the region used in the reduction is indicated by the circle.

The source detection routine requires knowledge of the background for each pixel of the field. Such a model background can be estimated from an image of the field in which the sources have been masked out. The method used to create this masked image is to assume the background can be approximated by a single value, the initial background estimate, and then run PSS on the field. The detected sources are then masked from the field, and this image is used to calculate the model background for the field.

As the background count rates are low, both the median and mode of the fields used in the sample are zero, so the initial background estimate is calculated by using a sigma-clipped mean; the use of sigma-clipping reduces the bias in the mean due to the presence of source photons in the field. PSS is then run on the field, detecting sources above a 4σ threshold. The blanking radius to use for each source is defined as the 99.7% radius (3σ) of the best fit Gaussian to the source radial profile. This radius was chosen since it is a compromise between removing a high percentage of the source photons and ensuring enough of the field is left to calculate the model background. The top two images in Figure 2.9 show a field before and after the source masking, whilst the bottom plot shows how the masking changes the photon frequency distribution. The histograms illustrate the low background

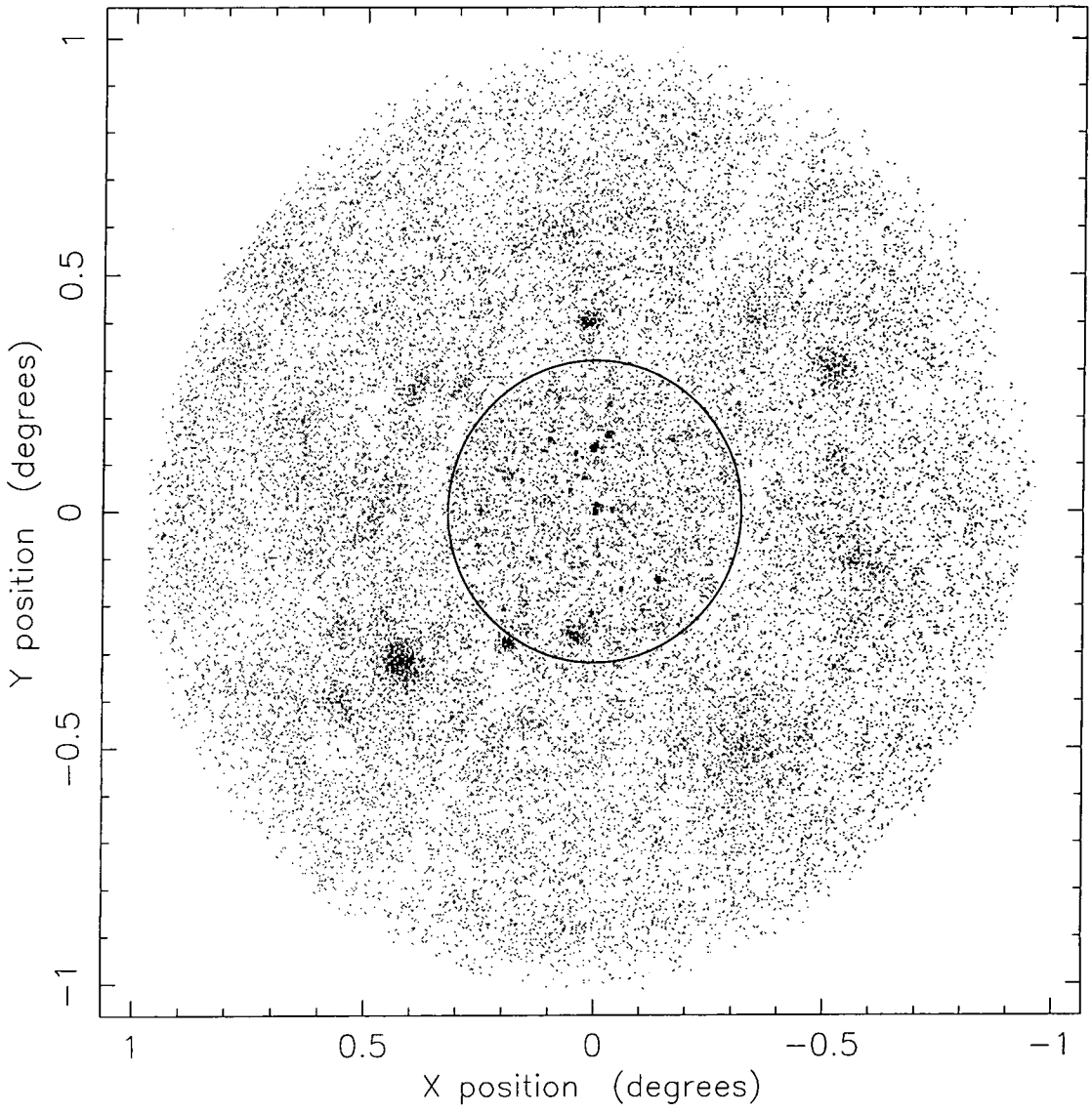

Figure 2.8: The image shows the full 1° field of view of the PSPC for one of the fields in the sample. It is for the 0.5 – 2.0 keV pass-band and has 15″ by 15″ pixels. The circle indicates the region used by the survey — it has a radius of 0.32°. The vignetting caused by the support structure is visible, whilst the apparent increase in source size with radius is due to the off-axis dependence of the PSF.

rates of PSPC observations — approximately 80% of the field contains no photons. Figure 2.10 shows how the background masking changes the radial profile of the field and displays the radial profile of the model background created for this field.

The source detection has been implemented as a two-stage process: the first stage involves running the detection algorithm on the field to produce a source list (the first-pass source list), in the second stage individual sources are examined to see if the photon distribution is extended (the second-pass source list). Since the first-pass detection routine uses an aperture optimised for detecting point sources, a 4σ threshold is used, rather than the 5σ limit used in the second pass. This reduced limit is a compromise between ensuring extended low surface-brightness sources are not missed and not contaminating the sample with background fluctuations.

In the second pass, each source is examined individually. The off-axis PSF at the source position is convolved with Gaussians of full-width-half-maxima ranging from $0'$ to $8'$. Each of these profiles is used by PSS in the fitting procedure, producing a graph of significance versus FWHM. Two examples of these graphs are given in Figure 2.11. The significance of the source being extended is then found by comparing the Cash statistic of the best-fit extended source profile to that of the PSF only. The extent significance depends on the aperture size used by PSS: too small an aperture and not enough of the source signal will be included, too large an aperture and the model used in the fitting procedure — that there is only one source — is no longer valid. As the choice of aperture size depends upon the individual sources, the aperture size for a source is defined as the 99.7% radius (3σ) of the best fit Gaussian to the radial profile of that source.

The spectrum of each source is generated using broad energy bins to improve the signal-to-noise. This spectrum, after background subtraction, is used to calculate the hardness ratio of the source, equation (2.1), where the Hard band is $0.5-2.0$ keV and the Soft band is $0.11-0.5$ keV.

Although the detection procedure uses the field out to a radius of $19.2'$ — to reduce edge effects — only those sources whose centres lie within $18'$ of the detector

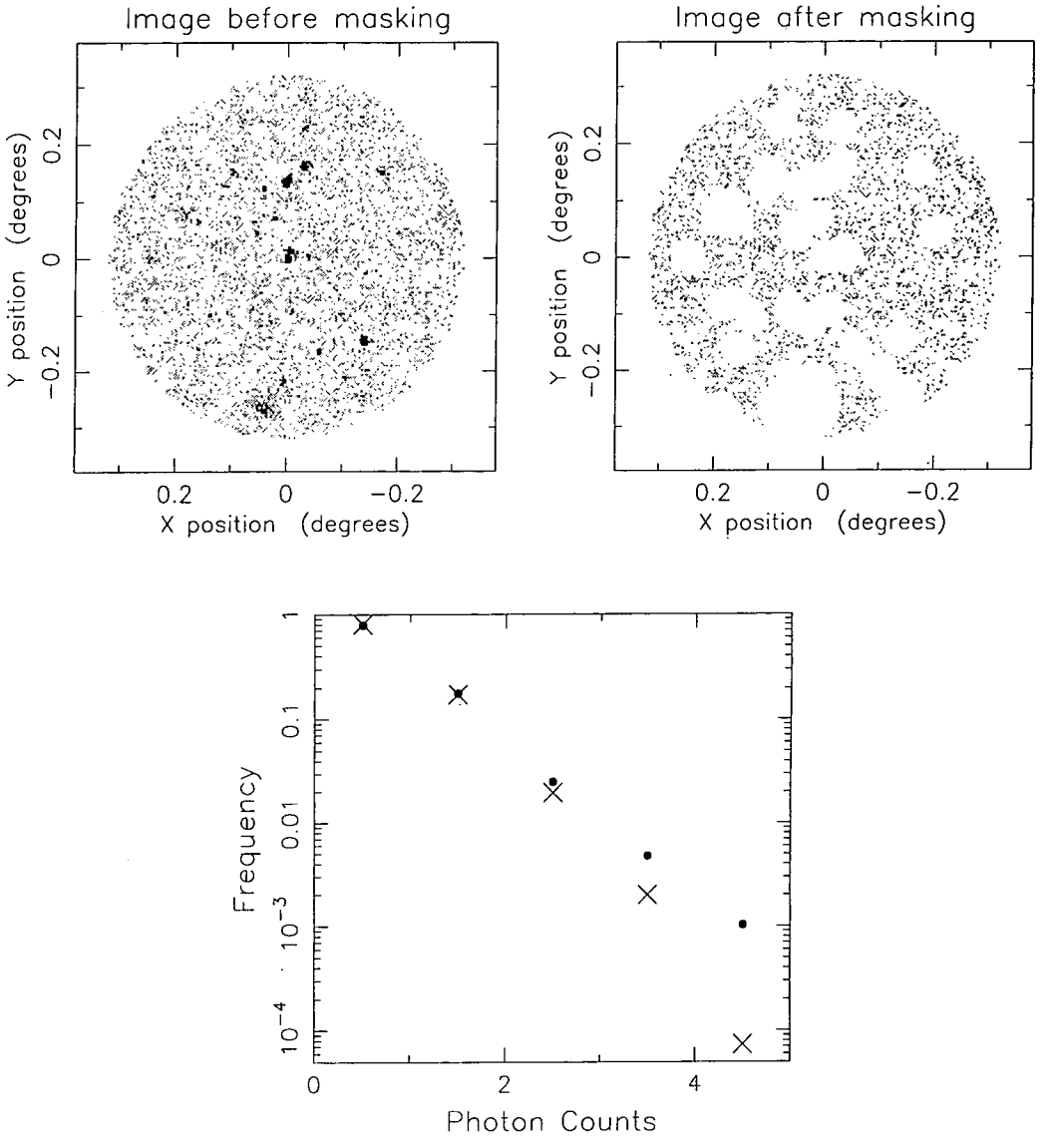

Figure 2.9: The top images show a field before and after masking out the sources used to define the background. The bottom plot shows the frequency distribution of photons in these two images, where the solid points are for the original image and the crosses are for the masked image. Only pixels containing photon counts of 4 or less are shown; this is the full distribution for the masked image, whilst only 0.2% of the pixels in the original image contain more than 4 photons.

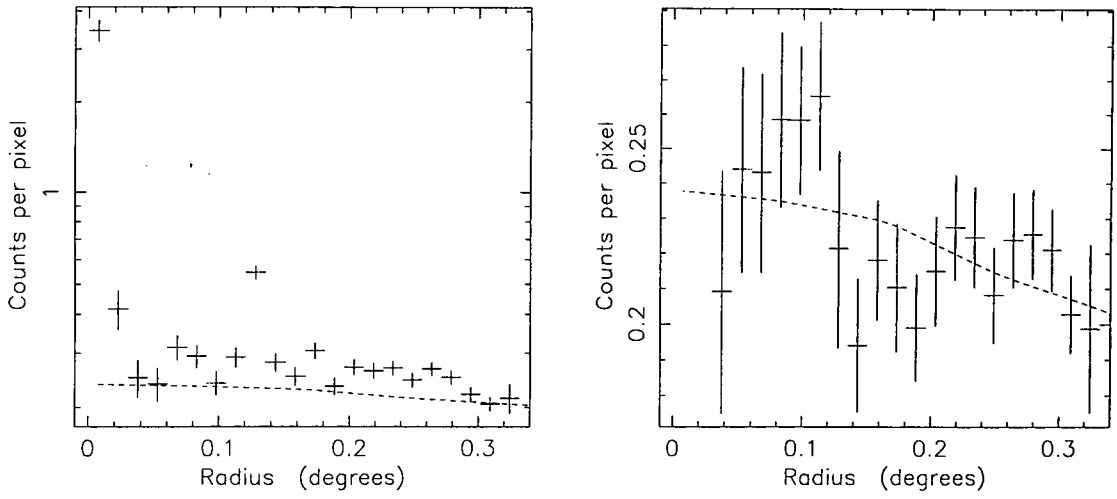

Figure 2.10: The points in the left-hand plot show the radial profile of the field, shown in Figure 2.9, before masking the sources. The points in the right-hand plot show the radial profile after masking out the sources. The dashed line, in both plots, shows the radial profile of the model background created from the masked field.

centre are included in the source list. This is because regions beyond 18′ are affected by vignetting caused by the central support ring of the PSPC. Once all sources have been analysed, those sources with extent significances greater than, or equal to, 3.0 are flagged as extended.

2.2.4 The X-ray catalogue

The survey consists of 66 fields which satisfy the following criteria: cleaned exposure times greater than, or equal to, 10 ks; Galactic latitude greater than 20° away from the Galactic plane; a declination less than +20°; and be suited to detecting distant clusters. The exposure time limit ensures that the observations are deep enough to detect 10^{44} erg s^{-1} clusters at redshifts greater than 0.3, whilst the latitude limit ensures that Galactic absorption is not too high, and that the projected number density of stars, on the sky, is not so large as to make optical cluster identification extremely difficult. The declination limit is a purely operational one, ensuring that there is little overlap with the fields used by the RIXOS survey (e.g. Castander et al. 1995). Fields whose X-ray or optical properties meant that clusters could not be identified over a significant portion of the field were rejected. Cluster observations

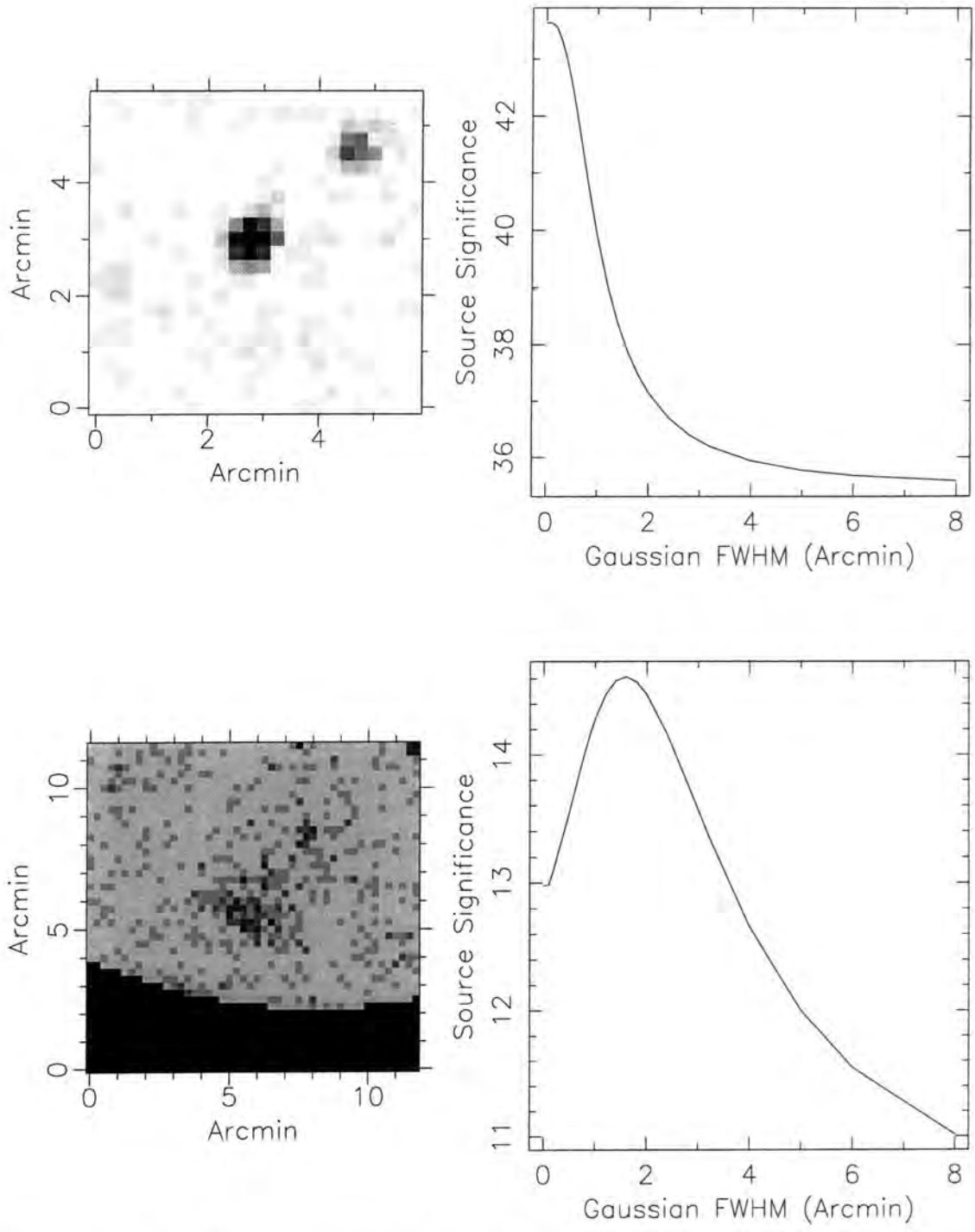

Figure 2.11: The Figures on the left show the photon images of a point source (top) and an extended source (bottom). The graphs on the right show how the detection significance of the source varies with the source profile used by PSS. The abscissa is the FWHM of the Gaussian convolved with the PSF.

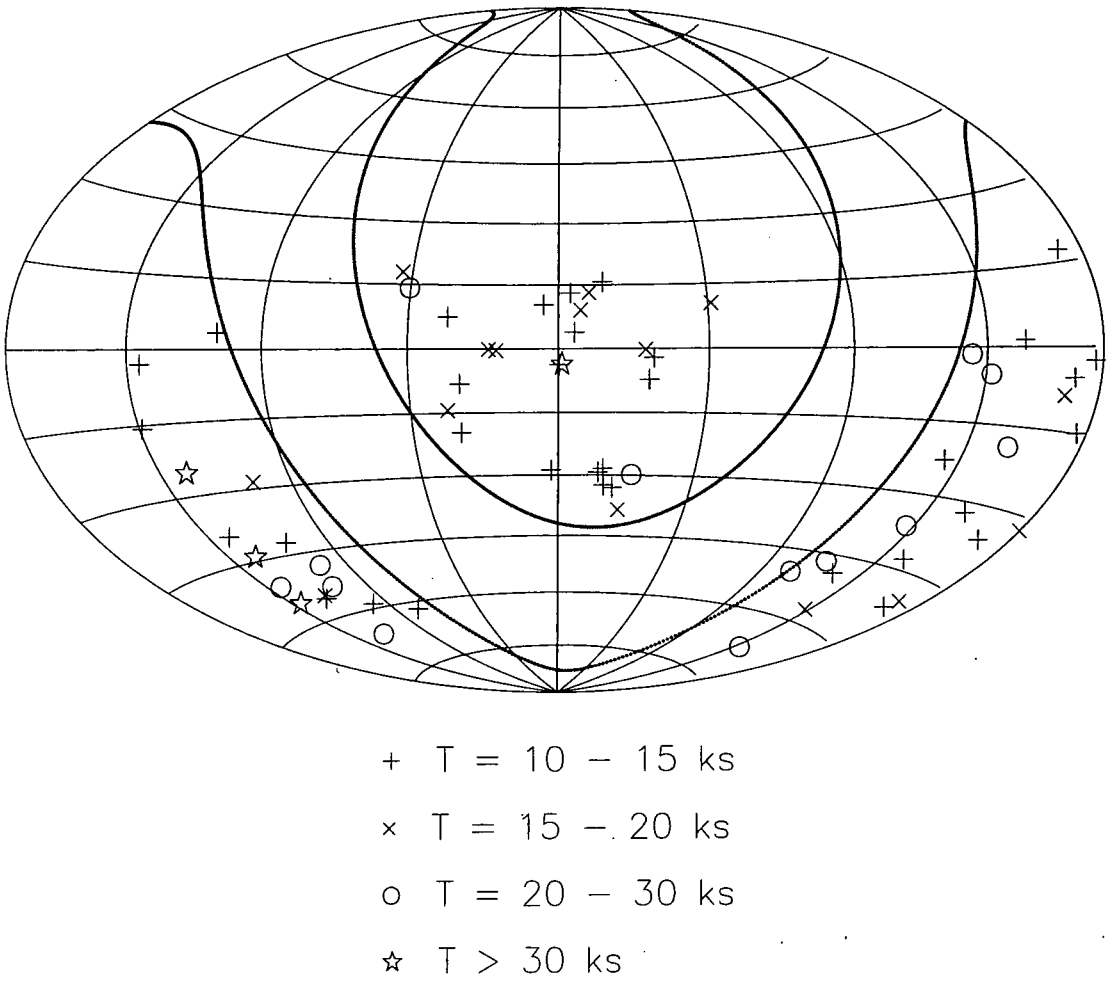

Figure 2.12: Aitoff projection of the fields used in this survey, where the symbol type indicates the exposure time. The lines of longitude and latitude are the same as in Figure 2.2. The solid line indicates the Galactic latitude limit ($|b| > 20°$) of the survey; the lack of Northern fields is due to the Declination limit; and the $0^h - 3^h$ gap in Right Ascension is because this region of sky was unobservable during the observing runs.

were included in the survey, as long as the X-ray emission did not extend beyond a radius of 10′. The fields are listed in Appendix A and plotted on an Aitoff projection of the sky in Figure 2.12.

The ability of the catalogue to fairly sample the universe relies, in part, on there being no relation between the areas of the sky which are searched and the detected clusters. For this reason sources close to the targets of the observations should not be included in the catalogue; as described below, the information provided with the observations allows the majority of such sources to be identified. There is also

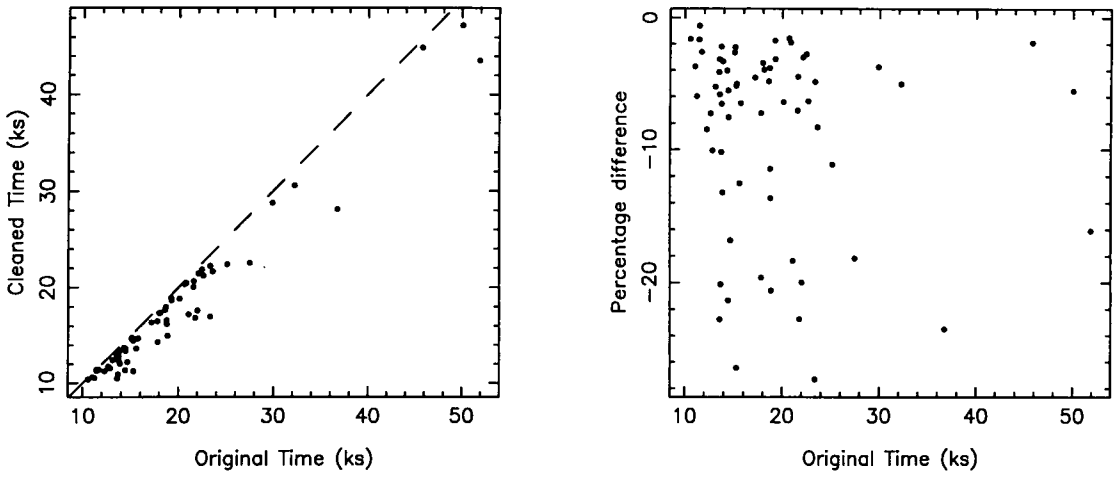

Figure 2.13: The left-hand plot compares exposure times before and after masking out bad-time periods, where the dashed line indicates no change. The right-hand plot shows the percentage difference versus the original exposure time.

the possibility of introducing a bias into the catalogue for observations of targets which were originally serendipitously detected in cluster pointings of previous X-ray missions, since the ROSAT observation may well detect this cluster — a "second-generation serendipity effect". A similar problem arises if observations have been performed so as to include a cluster in the field of view although it is not the main target of the observation — an example being the $z = 0.56$ cluster (0055-279) observed in a ROSAT PSPC pointing near the South Galactic Pole (Roche et al. 1995). Such effects are difficult, if not impossible, to quantify, and have been ignored for the rest of the thesis, except in Section 4.2.1 when discussing the properties of the low-redshift catalogue.

It is important to know, for the simulations described in Section 2.3, the range of various parameters in the survey — the most important being exposure time and background count rate. Figure 2.13 shows that the quality masking reduces exposure times by less than twenty percent. The plots in Figure 2.14 show that the survey is dominated by fields with low exposure times, background count rates and $n_{\rm H}$ values. The $n_{\rm H}$ distribution of the survey is $(1.7 - 7.2) \times 10^{20}$ cm^{-2}, with an average value of 3.6×10^{20} cm^{-2}.

Calculating the flux from an extended object requires the use of a model profile to correct for flux outside the measurement aperture. As the source identifications,

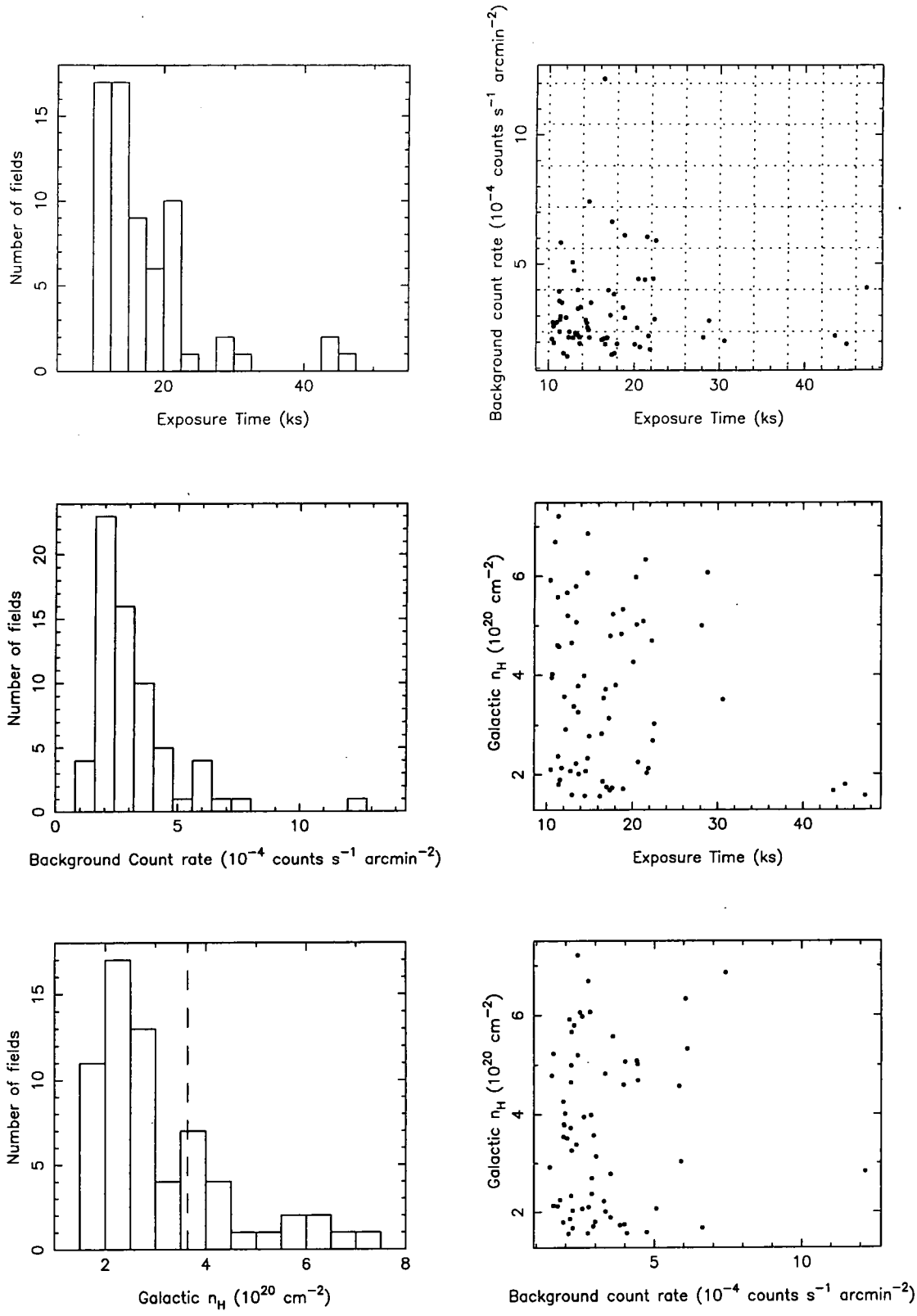

Figure 2.14: The histograms on the left show, from top to bottom, the variation of exposure time, background surface brightness, and Galactic Hydrogen column density for the fields used in the survey. The dashed line in the bottom plot indicates the mean $n_{\rm H}$ value of the survey — 3.6×10^{20} cm^{-2}. The right-hand plots show how these parameters are related. The dotted lines in the top plot show the bins used in the simulations (Section 2.3).

and redshifts, were not known at this stage of the processing, source fluxes were not calculated. Therefore, the output of the survey cannot be directly compared to the $\log N - \log S$ distributions from deep PSPC surveys. However, the average surface density of all sources in this survey, ~ 90 deg^{-2}, corresponds to a flux density of 1×10^{-14} erg cm^{-2} s^{-1} (e.g. Georgantopoulos et al. 1996). As this is roughly the flux limit that the survey is expected to reach, it suggests that the detection procedure produces results similar to those of other deep PSPC surveys.

Figure 2.15 shows how the sources are distributed across the detector, after splitting the sample into point and extended sources. As the majority of fields were centred on sources, both distributions are peaked towards the detector centre. The radial profile of the point-source distribution shows the combined effect of telescope vignetting and PSF degradation on the source counts.

Figure 2.16 shows the hardness ratio plotted against extent significance for each source. As the source selection is only done in the hard band, it is not surprising that the majority of sources have a hardness ratio greater than zero; only one quarter of sources have a hardness ratio less than zero. Therefore the hardness ratio is not a good method for selecting clusters — the fraction of extended sources in the whole survey is 7.9%, which only increases to 9.5% if soft sources (those with hardness ratios less than zero) are removed from the sample.

The results given above are for all sources detected within 18′ of the detector centre, which means that the targets of the observations are also included. Since a serendipitous survey cannot include these sources, it is important that they are removed from the source lists and the survey area reduced to account for this. In the vast majority of cases, the target could be identified from the observation name. The masking radius was determined by examining the X-ray and optical data for these sources, with a minimum value of 3′ and a maximum value of 8.4′— for the majority of sources a radius of 5′ was used. Three fields had two sources which required masking, and there were nine fields for which the whole image could be used, because the target lay outside the central region. For the two fields in which the target could not be identified, a fiducial radius of 5′ was used, placed at the

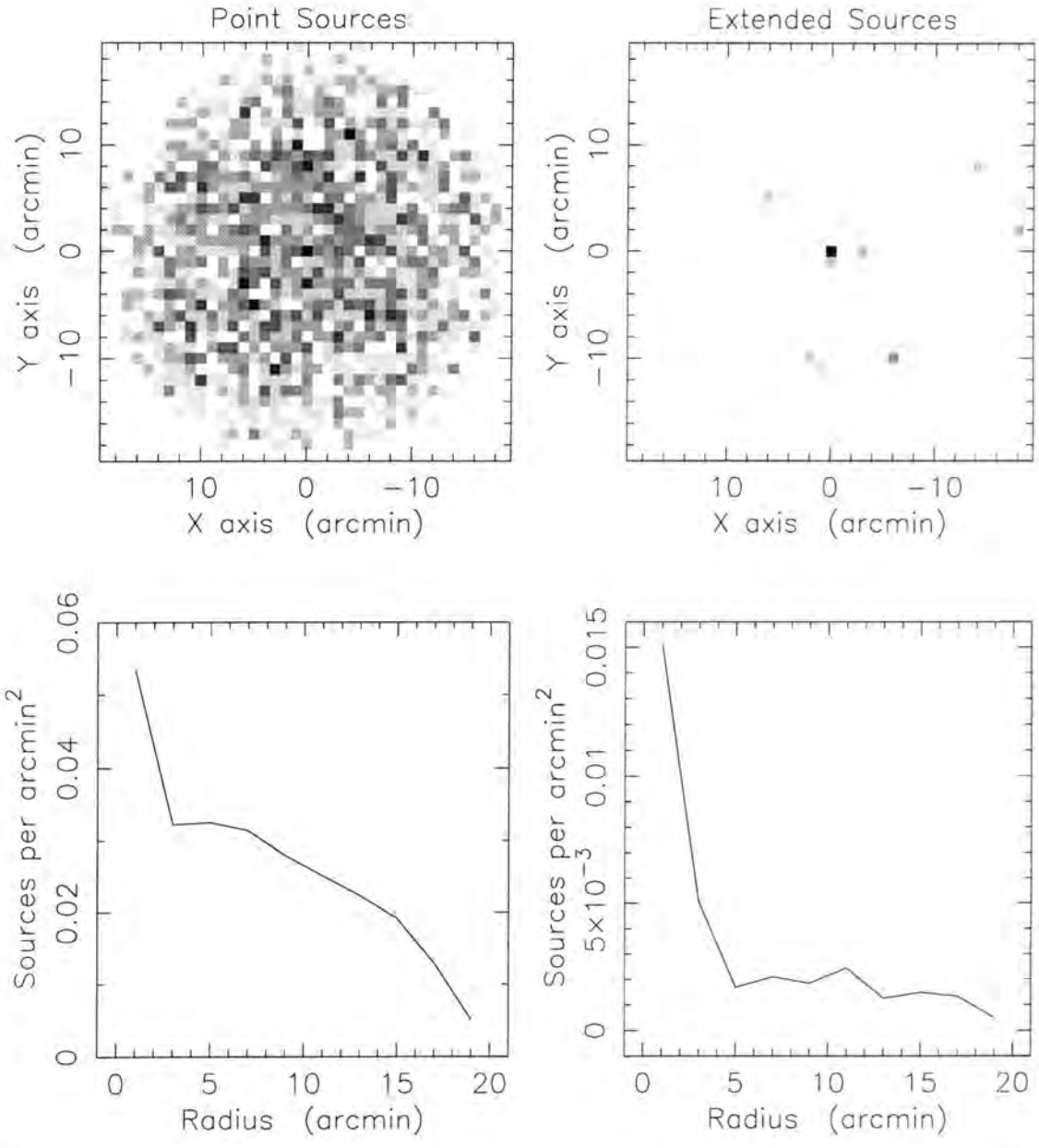

Figure 2.15: Combining the source lists for all the fields, and binning into 1′ square pixels produces the top two images. The left-hand Figure shows the distribution of point sources, whilst the right-hand Figure is for the extended sources. The source lists used here do not have the observation targets masked out, which is why there are peaks in both distributions at the image centres. The bottom two plots show the radial profiles of these distributions, after normalising by the number of fields in the survey.

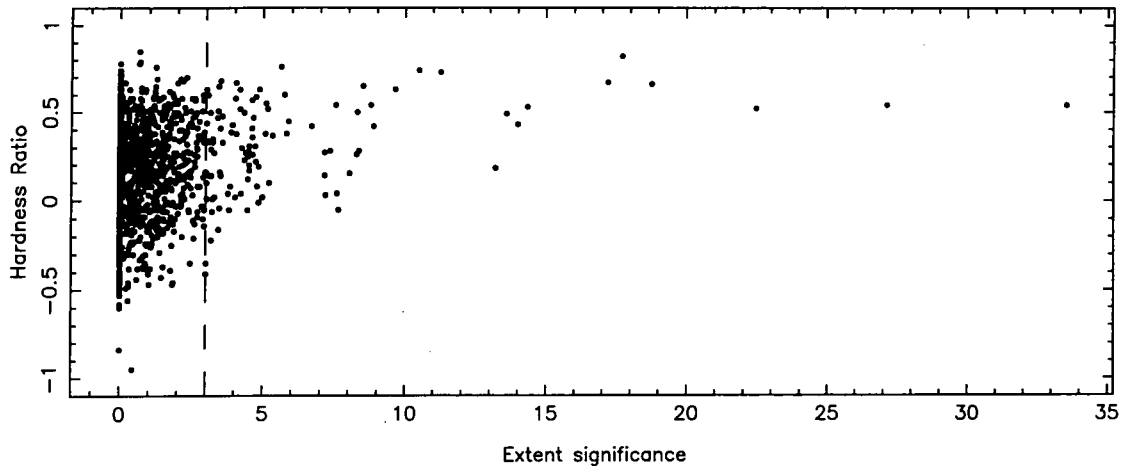

Figure 2.16: This Figure shows how the hardness ratio of a source is related to its extent significance. The vertical dashed line indicates the division between point and extended sources.

centre of the field.

The full survey consists of 1680 sources, 134 (8.0%) of which are extended. Removing the regions around each observation target, as described above, reduces the total number of sources to 1538, and the number of extended sources to 103 (6.7%). Appendix C lists these sources, and Section 3.1 describes the identification process.

2.3 Simulations

The survey selection function is required for the calculations presented in Chapter 4. It is found by calculating the maximum redshift, z_{max}, at which a cluster of a given luminosity would still be included in the cluster catalogue. As clusters are selected using an extent criterion as well as a significance limit, an analytic approach to calculating z_{max}, such as used by Henry et al. (1992), is not possible. The selection function has therefore been calculated using the simulations presented below. Although the survey contains clusters with a range of redshifts, the work presented in Chapter 4 uses the high redshift ($z \geq 0.2$) sample only. Therefore the simulations presented here have concentrated on simulating high-redshift clusters.

The ability to detect a given cluster depends on properties both intrinsic and

extrinsic to it — the relevant cluster characteristics are its luminosity, surface brightness profile and redshift, while those for the survey are exposure time, background count rate and off-axis angle. The simulations assume a universal cluster X-ray surface brightness profile — namely equation (1.9) with a core radius of 250 kpc and $\beta = 2/3$ (Jones & Forman 1984) — that is independent of redshift. Ideally one would use a distribution encompassing the true range of cluster profiles, however the sensitivity and spatial resolution of the current generation of X-ray instruments limit the knowledge of such a distribution to low redshift: the choice of profile is consistent with the average properties of such low redshift cluster samples (e.g. Jones & Forman 1984; Henry et al. 1992).

If there is evolution of, or correlations between, cluster-profile parameters — e.g. core radius changing with redshift or luminosity — then the results from the simulations will be systematically biased, and care must be taken in interpreting calculations that use this data, such as those presented in Chapter 4. An example of the expected amount of change is provided by the cluster-evolution model of Bower (1997) — discussed in detail in Section 4.1 — which predicts a change in core radius of $\lesssim 50\%$ out to $z \simeq 0.5$ for a reasonable range of model parameters. The sensitivity of the selection function to such changes can not be directly tested, since the simulations only use a single core radius. However, examination of the data suggests that the results are not significantly different for angular core sizes in the range $\sim 30'' - 50''$. This is close to the predicted core-size evolution for $z \gtrsim 0.2$ (Figure 2.5). Therefore the simulation results should not be strongly affected, as long as the core size does not drop below ~ 200 kpc.

As the simulations are computationally intensive, analysis was limited to a binned representation of the survey with regard to: exposure time, background surface brightness, and off-axis angle. The bin sizes were chosen so as to be small enough that the selection function did not vary significantly across a bin whilst being large enough that the simulations could be performed in a reasonable amount of time. The exposure time and background surface brightness bins are shown in Figure 2.14; bin widths are 4 ks and 1.6×10^{-4} counts s^{-1} arcmin^{-2} respectively.

The effect of the off-axis degradation of the PSF on the detection procedure was modelled by splitting each field into two: the inner region, out to a radius of 10′, and the outer region, from 10′ to 18′. Since the survey area of each field is known, this binning produces a list of areas as a function of the three variables: exposure time, background surface brightness, and off-axis angle.

2.3.1 Simulation details

The simulations involve creating an observation containing a model cluster and seeing if the reduction procedure detects the cluster as an extended X-ray source. As described above, source photons are distributed using a profile given by equation (1.9), with $r_c = 250$ kpc and $\beta = 2/3$, which is convolved with a model PSPC PSF. One possible way to create the background distribution is to add simulated clusters to the actual observations used to create the cluster sample. This has the advantage of accurately modelling the vignetting and background fluctuations of individual fields — however it is infeasible because the simulations are computationally intensive. As the results of the simulations will be interpolated to produce a selection function at any luminosity, as described in Section 2.3.2, and the uncertainties in the number of cluster photons used in the simulations are of the order of ten percent, there is little point in exactly mimicking the survey. Therefore background photons were distributed using a flat background, which is a good approximation for the spatial extents of distant clusters.

The flux, f, from a cluster of luminosity L, and redshift z, is calculated using

$$f = \frac{L}{4\pi {d_{\rm L}}^2(z)}\, k(z)\,, \tag{2.8}$$

where $d_{\rm L}(z)$ is the luminosity distance of the cluster (e.g. Weinberg 1972), and $k(z)$ converts the cluster rest-frame luminosity into the $0.5 - 2.0$ keV pass-band of ROSAT. The form of $k(z)$ depends on the cluster spectral energy distribution, which is modelled by a thermal bremsstrahlung emission from a plasma at a temperature of 6 keV: a discussion of the choice of this model is given in Section 3.2.2. The flux is converted into a count rate using the PSPC response function, a 6 keV thermal

bremsstrahlung spectrum, and a Galactic absorption model with the average survey value of $n_{\rm H} = 3.6 \times 10^{20}$ cm^{-2}. Although the survey has a range of $n_{\rm H}$ values (Section 2.2.4), the conversion factor varies by less than six percent for this range, so the use of a single value does not significantly bias the results. The expected number of source and background photons equal the exposure time multiplied by the corresponding count rate. The actual number of photons to distribute is found by Poisson distributing the expected number of source and background photons.

The detection process is only sensitive to the emission within a radius of $\sim 1'$, corresponding to an area of $\sim 10^{-3}$ deg^2. The effect of source confusion on the detection process can be estimated by using the typical source density at a flux limit close to that of the deepest fields in the survey, i.e. $\sim 10^{-14}$ erg cm^{-2} s^{-1}. For a source density of 90 deg^{-2} (Georgantopoulos et al. 1996), the expected number of sources falling within the region which the detection process is sensitive to is ~ 0.09. Therefore 10% of the cluster sources in the sample are expected to have a contaminating source within the detection area. No attempt has been made to include source confusion in the simulations presented here.

2.3.2 Results of the simulations

Clusters are simulated for a range of redshifts and luminosities: $z = 0.2 - 1.0$ and $L = (0.1 - 3.0) \times 10^{44}$ erg s^{-1}. Combining the results of these simulations produces the survey area as a function of cluster luminosity and redshift, $\Omega(L, z)$, as shown in Figure 2.17. For clusters beyond a redshift of 0.3 the minimum detectable luminosity is approximately 10^{43} erg s^{-1}, whilst clusters with luminosities of 3×10^{44} erg s^{-1} are observable out to $z \sim 1$.

The work presented in Chapter 4 requires the knowledge of the survey volume at a luminosity, L, in a redshift shell z_1 to z_2, which is defined as

$$V_{\rm max}(L) = \int_{z_1}^{z_2} \Omega(L, z)\, dV(z)\, {\rm d}z\,, \tag{2.9}$$

where $dV(z)$ is the volume per unit area at a redshift z (e.g. Kolb & Turner 1990).

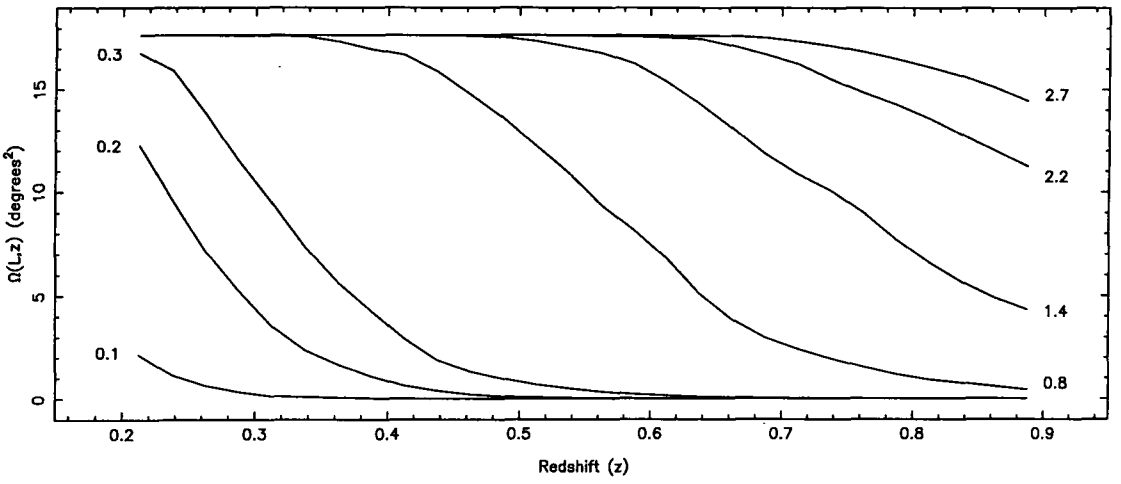

Figure 2.17: Each curve shows $\Omega(L, z)$, the available survey area as a function of cluster luminosity, labelled in units of 10^{44} erg s^{-1}, and redshift.

Luminosity (10^{44} erg s^{-1})	$V_{\max}(L)$ (10^7 Mpc^3)	Luminosity (10^{44} erg s^{-1})	$V_{\max}(L)$ (10^7 Mpc^3)
0.1	0.003	0.9	2.242
0.2	0.087	1.2	2.800
0.3	0.318	1.4	3.047
0.4	0.653	1.9	3.270
0.5	1.025	2.2	3.310
0.6	1.360	2.7	3.337
0.7	1.713	3.0	3.340
0.8	2.031		

Table 2.2: The results of evaluating equation (2.9) for the redshift shell $z = 0.3-0.7$.

Table 2.2 lists the results of equation (2.9) evaluated for the redshift shell $z = 0.3-0.7$. Figure 2.18 shows these points and the line used to interpolate the results.

The dashed line in Figure 2.18 shows the selection function of the simulations if no extent criterion had been used. As expected, the effect of removing the requirement that cluster detections be extended has been to increase the survey volume at low luminosities, whilst at high luminosities, $\gtrsim 2 \times 10^{44}$ erg s^{-1}, there is little effect.

As the maximum search volume is close to 4×10^7 Mpc^3, the survey is unlikely to detect clusters with densities $\lesssim 10^{-8}$ Mpc^{-3}. The range of cluster luminosities which the survey is sensitive to depends on the distant cluster X-ray luminosity function,

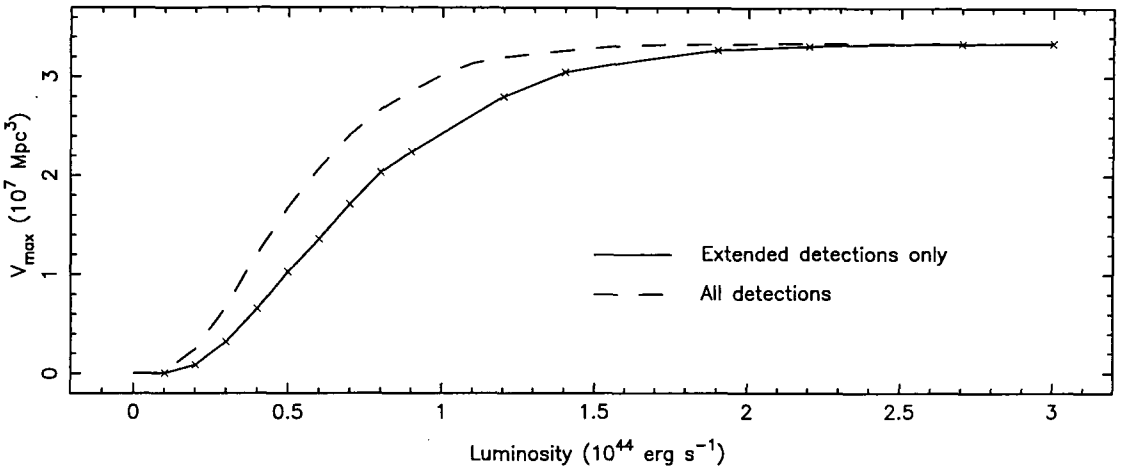

Figure 2.18: The crosses indicate the values of $V_{\max}(L)$, for the redshift shell $z = 0.3 - 0.7$, calculated using equation (2.9) and the curves shown in Figure 2.17. The solid curve is the fit to these points. The dashed line shows the curve obtained if the simulations are analysed without requiring sources to be extended: the volume available is $\sim 25\%$ larger, at 10^{44} erg s^{-1}, compared to the selection function obtained when only extended sources are included.

as discussed in detail in Chapter 4. However, the low redshift cluster sample of Ebeling et al. (1997) suggests that the maximum detected cluster luminosity will be $\lesssim 4 \times 10^{44}$ erg s^{-1}.

Chapter 3

The Cluster Catalogue

Chapter 2 described the steps taken to produce a list of serendipitously-detected cluster candidates from ROSAT PSPC images. Although the use of an extent criterion to select X-ray sources greatly reduces the contamination level of the catalogue, it does not remove all contaminants. The identification of the X-ray sources is described in Section 3.1. Section 3.2 describes the techniques used to measure the X-ray fluxes of the clusters, and presents the X-ray luminosities in both the ROSAT and EMSS pass bands.

3.1 Identification of the X-ray sources

Although the sources are serendipitously selected, some will have identifications in the literature. To find these sources, the NASA Extragalactic Database was queried, using a search radius of five arcminutes about the X-ray centre. This radius, which is much greater than the positional error on the X-ray co-ordinates, was chosen as a compromise between ensuring that extended sources were identified and not including too many unrelated sources. The sources identified in this manner are listed, in Appendix C, with an ID of L. Five sources were identified as contaminants, being a mixture of QSOs, galaxies and an AGN, and eight clusters were identified, all but one with a redshift. Sources that lay within 1 Mpc of an identified cluster

were taken to be part of that cluster: they are labelled by the addition of () to their ID. The radius, which is $\simeq 20\%$ smaller than the value used to estimate the cluster flux (Section 3.2.1), was chosen as a compromise between ensuring that clumps of emission associated with the cluster were not taken to be separate clusters and avoiding combining unrelated sources because of projection effects.

Even though distant clusters are not visible on the Palomar and UK Schmidt Sky Survey plates, it is possible to identify some of the sources using these surveys. Square images, centred on the X-ray co-ordinates and with a width of six arcminutes, were obtained for each source from the Digitized Sky Survey (DSS) service provided by the Space Telescope Science Institute. The X-ray photon image was lightly smoothed, using a Gaussian approximation to the PSPC PSF at the off-axis angle of the source (Hasinger et al. 1994), and the contours added to the DSS image: several examples of these images are shown in Figure 3.1, whilst the full sample is given in Appendix B. Those sources which showed a stellar-like object at the centre of the X-ray emission were removed from the catalogue, and are listed in Appendix C with an ID of P. These objects belong to one of two classes: most are detected as extended because the presence of a nearby point source causes an over-estimate of their extent, whereas a few sources are extremely bright, and the photon statistics are good enough that the differences between the real and model PSF become significant (e.g. RX J2202.5 – 3208, Figure 3.1). Objects whose X-ray contours show contamination by point sources which matched up with point-like objects on the imaging data, were given the ID of M and removed from the catalogue. The source RX J2138.3 – 4253 (Figure 3.1) is an example of a candidate that was rejected with an ID of both P and M. Several sources turned out to be nearby galaxies, these are listed in Appendix C with an ID of G.

This procedure can lead to clusters not being identified — perhaps because the imaging data is not deep enough to detect galaxies fainter than the brightest cluster galaxy — which would cause incompleteness in the catalogue that is not accounted for by the simulations presented in Section 2.3. This is different from the lack of unresolved clusters in the catalogue, which is due to the imposition of an extent

criterion during the X-ray selection, and is modelled in the simulations. The best way to assess the effect of possible selection biases is to compare the catalogue to those of other ROSAT PSPC surveys (e.g. RIXOS, WARPS, RDCS), since these have been created using a variety of X-ray and optical selection techniques, including identification of X-ray point sources. A direct comparison is not yet possible, since the various catalogues are currently not publically available.

This remainder of this Section describes the optical observations: Section 3.1.2 contains detailed descriptions of the instruments used and the observations made; Section 3.1.3 describes the reduction of the optical data; and Section 3.1.4 presents the identifications for the sources.

3.1.1 Optical follow-up of cluster candidates

With telescope time at a premium, the observing strategy for identifying the sources has to be as efficient as possible. Surveys which attempt to identify all the sources detected in X-ray images (e.g. Gioia et al. 1990b; Henry et al. 1995; Georgantopoulos et al. 1996; Boyle, Wilkes & Elvis 1997) require extensive optical follow-up to identify the correct source within the X-ray error-box. Although this is a necessary approach for these surveys, since they do not have any a priori knowledge of the optical properties of the sources, it is not an optimal strategy for searches targeted at clusters. Low redshift, $z \lesssim 0.2$, samples of X-ray clusters show that $70\% - 80\%$ of the clusters have a dominant elliptical galaxy either at, or close to, the centre of the X-ray surface-brightness distribution (Forman & Jones 1994; Romer 1997, private communication). High-redshift, X-ray selected, clusters also show a high fraction of systems with a dominant elliptical galaxy close to the centre of the X-ray emission (Gioia & Luppino 1994). This suggests that the presence of an elliptical galaxy close to the X-ray centroid is indicative of the presence of a cluster. As the majority of the non-cluster sources identified in Section 3.1 have a stellar-like optical counterpart close to their X-ray centre, it seems likely that most of the contaminating sources are characterised by the presence of such an object. The expected contaminants in

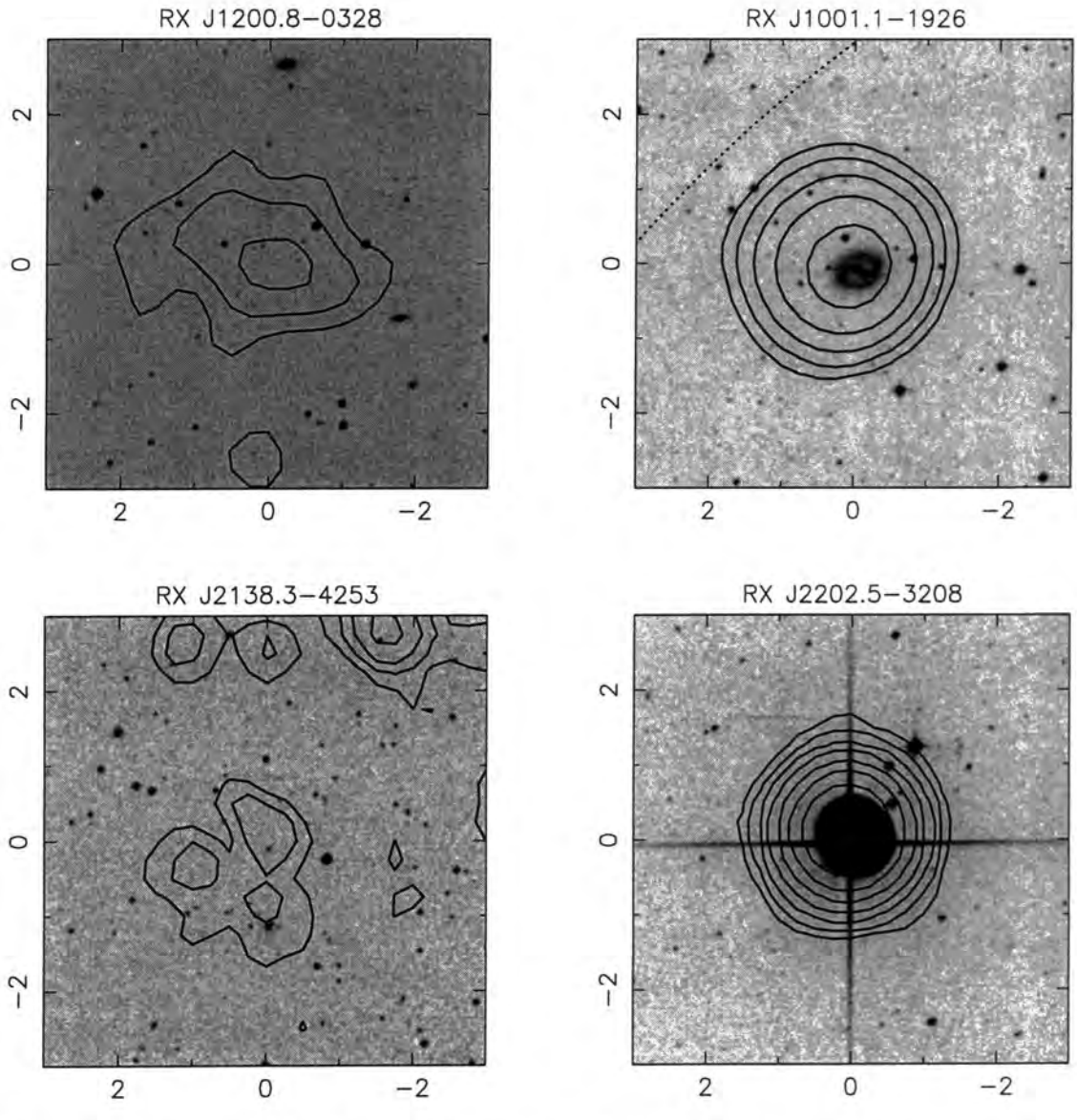

Figure 3.1: Images of four sources in the survey. The images are extracted from the DSS and are six arcminute square, centred on the X-ray co-ordinates, with North to the top and East to the left. The contours show the smoothed X-ray photon image; the levels are $2^{n-1} \times 3\sigma$ above the background value, where n is a positive integer, and the background and σ values were calculated from the smoothed image, after blanking out the detected sources. The dotted line in the top-right plot indicates the edge of the X-ray image, corresponding to the support structure of the PSPC, and is drawn at 19.2′ from the field centre.

the survey are stars, nearby galaxies, AGN, and QSOs. Stellar sources are expected to be either dwarf stars, early-type stars or accreting binaries. The X-ray emission mechanism of galaxies depends on the galaxy type: the collective emission from individual sources, such as accreting binaries and supernovae remnants, are thought to be responsible for the emission from spirals; starburst galaxy emission is due either to supernovae remnants or massive, young stars; ellipticals are encased in a hot, intergalactic medium at temperatures $\lesssim 1.0$ keV, which emits via thermal bremsstrahlung. AGN and QSO emission is thought to be due to a central, compact object.

The first step in identifying the remaining sources is to obtain deep optical images. The central regions of local clusters are known to be dominated by old, red, elliptical galaxies (e.g. Bower et al. 1990), and this has been shown to hold up to redshifts close to one (e.g. Aragón-Salamanca et al. 1993; Stanford, Eisenhardt & Dickinson 1997; Ellis et al. 1997). As the population of field galaxies becomes bluer at fainter apparent magnitudes, since the number-count relation steepens going from red to blue pass bands (e.g. Smail et al. 1995; Hogg et al. 1997), it is usual to use red pass bands to detect distant clusters (e.g. Gunn et al. 1986; Couch et al. 1991; Postman et al. 1996; Zaritsky et al. 1997). The images of the sources were therefore taken using a R-band filter, to increase the contrast between the cluster galaxies and the background galaxy population, and typically reached a magnitude of ≈ 23. The same criteria were applied to the CCD images as to the plate images to remove sources from the catalogue; such objects are listed with an ID of IM or IP in Appendix C.

Once the image of a source has been obtained, the decision is which objects should be spectroscopically identified. As previously described, there is expected to be a source close to the centre of the X-ray emission: an elliptical galaxy for clusters and a point source for contaminating objects. The chosen strategy was to obtain the spectrum of any galaxies close to the X-ray centroid, unless there was a point source close by. For suspected clusters, spectra were also obtained for nearby elliptical-like objects with similar properties to the central galaxy. The aim was to

obtain a minimum of three concordant redshifts for each cluster; the size of the field available for spectroscopy meant that the number of objects observed, per field, was typically between two and ten.

The first two runs used EFOSC-I on the European Southern Observatory (ESO) 3.6m telescope. This instrument, which is described in Section 3.1.2, is ideal for the optical follow up of cluster candidates, since it provides both imaging and spectroscopic capabilities, with a negligible change-over time between the two modes. Spectroscopy can be performed using a single slit (SS) or a mask of slits, which provides a multiple-object capability. The masks are manufactured at the telescope, so it is possible to image a field one night and perform multiple-object spectroscopy (MOS) the next night. To try and ensure that fields were fully identified, the approach taken was to image a source and then decide whether it warranted immediate follow-up with SS spectroscopy. Such sources were those with a point source at the X-ray centre, hence a possible non-cluster identification, and those which appeared to be clusters and the alignment of the galaxies meant that there was little, or no, advantage in using the MOS mode. The SS mode was also used when the weather worsened, since it was found that the MOS mode was not suited to poor weather.

Two runs at the 3.9m Anglo-Australian Telescope (AAT) using LDSS-I, which is also described in Section 3.1.2, completed the bulk of the source identifications. As with EFOSC-I, LDSS-I provides both SS spectroscopy and MOS, although the masks can not be manufactured at the telescope, and so have to be made before the observing run. The sources observed in these runs were those for which spectroscopy either was not possible at ESO, or for which the results were inconclusive. A service application, using LDSS-2 on the William Herschel Telescope (WHT) on La Palma, completed the spectroscopic observations of the X-ray sample. The ID of "–" is given to sources for which the identification is inconclusive: this includes objects which appear to be clusters or groups, but for which spectroscopic identification has not been obtained (e.g. RX J0505.9 – 2826), and those objects with no deep optical data.

	EFOSC-I	LDSS-I	LDSS-2
Detector size (pixels)	512 x 512	1024 x 1024	2048 x 2048
Pixel size (μm/″)	27 / 0.61	24 / 0.62	15 / 0.37
Dark current (e^-/pixel/hour)	< 1	< 1	1.6
Read out noise (e^-)	8.8	4.8	6.0
Read out time (s)	75	75	258

Table 3.1: Physical characteristics of the CCDs used with EFOSC-I, LDSS-I and LDSS-2.

3.1.2 The observing runs

Although the data comes from three different telescope/instrument combinations, the data reduction techniques are the same. This Section concentrates on describing the different instruments used and providing details of the observations made, whilst Section 3.1.3 deals with the techniques used to reduce the data.

Observations at the ESO

Both observing runs at the ESO 3.6m telescope used EFOSC-I — the ESO Faint Object Spectrograph and Camera (Savaglio, Benetti & Pasquini 1997). This is a versatile instrument, providing eight different observing modes: direct imaging; long slit, slitless, echelle and multiple-object spectroscopy; imaging- and spectro-polarimetry; and coronography. The modes used were direct imaging, long (or single) slit spectroscopy and multiple-object spectroscopy. The instrument is placed at the Cassegrain focus of the telescope, using an adaptor which allows it to be rotated about the optical axis of the telescope. Therefore spectroscopy of several objects can be made with the single slit mode, by appropriate choice of the position angle. The CCD used was a 512 by 512 pixel Tektronix chip, ESO #26, details of which are given in table 3.1. It is a cosmetically clean device, with uniform bias, and a quantum efficiency reaching 80% between 6000 Å and 7000 Å.

When used in the imaging mode, the field of view is 5.2′ by 5.2′, although the corners suffer from vignetting, and the 80% encircled-energy diameter is 0.3″ on-axis

and 0.5″ at the field corners. The system is sensitive to light of wavelengths between 3500 Å and 9500 Å; the filter used for imaging was a Bessel R filter, ESO #554, which has a peak transmission of 86% at 6437 Å and a FWHM of 1667 Å.

In the spectroscopic modes, the dispersion direction corresponds to the NS direction for the default position angle of the Cassegrain adaptor (270°), and is aligned with the CCD columns to better than one pixel across the detector. The full-chip area is not available for spectroscopy, being limited to the central 4′ region. The B300 grism was used, which provides a wavelength coverage of 3740 – 6950 Å and a dispersion of 6.3 Å/pixel. With this wavelength range, galaxies can be identified, using the Ca II H and K features, the 4000Å break and Hδ line, out to redshifts of $\simeq 0.7$. For MOS observations, the spectral range depends on the position of the slit along the dispersion direction; to ensure a usable signal was obtained, slits were not placed close to the edges of the field. The design of EFOSC-I is such that the spectral resolution is constant with wavelength, depending only on the slit width. The widths used were 1.5″ and 2.0″ for SS observations and 2.1″ for MOS, corresponding to resolution elements of 16 Å, 21 Å and 22 Å, respectively. The choice of slit width for the SS observations depended upon the seeing.

Creation of the masks for MOS is a two-stage process: the choice of targets and slit positions (the design of the mask), and the physical manufacture of the masks. The mask design allows the positions of the slits to be adjusted to give sufficient sky regions for each source, and to prevent overlap between adjacent slits. Typically ten slits were placed on a mask. The mask design is then sent to the PUMA machine, which creates slits by punching out a series of overlapping circular holes from a metal blank. With this setup, it is possible to observe a field, in MOS mode, the night after obtaining an image of it. The right plot in Figure 3.2 shows an example of a field imaged during the survey, where the circles indicate the objects selected for MOS. The left plot shows the raw spectroscopic image of the field observed through this mask.

Both observing runs were scheduled for 4 nights apiece, although the first run was extended by half a night because engineering work finished earlier than expected.

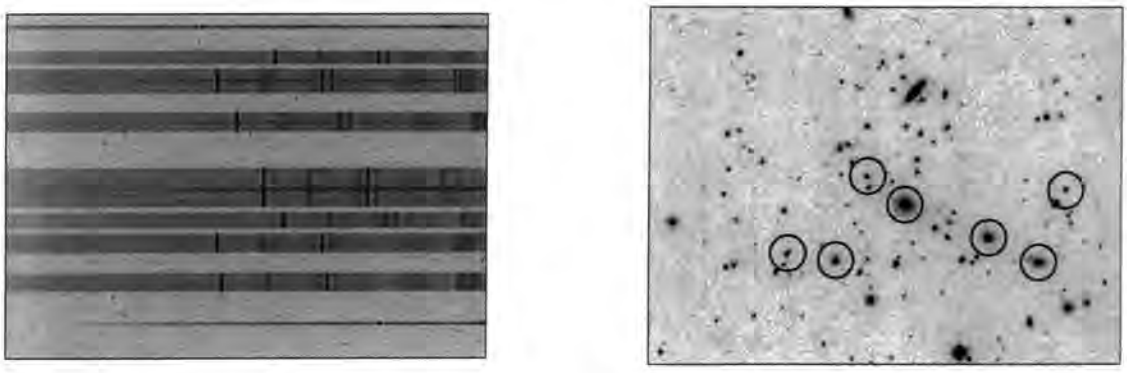

Figure 3.2: The left plot shows the raw data frame from the MOS exposure of the $z = 0.26$ cluster, RX J1204.3 − 0351. The two thin horizontal lines, at the top and bottom of this image, are the spectra of the stars used to ensure correct positioning of the mask. The right plot shows a subset of the R-band image of this cluster, where the circles indicate the objects targeted for MOS.

The first run was during the nights of June 19th to the 23rd, 1995; the second run was February 17th to the 20th, 1996. The weather for the first run was poor, generally being non-photometric and worsening through the run. In contrast, the second run had near-perfect weather, with much better seeing and negligible cloud cover. The difference in the weather is reflected in the number of observations made in each run, presented in table 3.2. Occasionally the filter wheel would stick, causing the requested change of instrument set-up to not take place; these observations produced images with no filter, and are noted in the F column of table 3.2. Exposure times for the observations depended on the optical characteristics of the source and the weather conditions. Images were either five or ten minute exposures, the choice being made on the optical properties of the DSS image and the prevailing weather conditions. The range of exposure times for spectroscopy ranged from several minutes, for very bright stellar sources, to three-quarters of an hour for distant cluster candidates. For the first run, the spectra could be examined by producing profiles along the dispersion direction of the raw frames. Between this run and the second run, a workstation was connected to the CCD controller, which meant that more sophisticated analysis could be made, including collapsing the spectra along the spatial direction, to improve the signal to noise, and sky subtraction. These methods were used to determine if the exposure time had been sufficient, or whether further exposures were required. Although a common technique is to

Telescope	Dates	Imaging		Spectroscopy	
		R	F	S	M
ESO 3.6m	June, 1995	11	4	21	3
ESO 3.6m	February, 1996	38	3	21	7
AAT	May, 1996	–	–	–	10
AAT	July, 1996	–	–	–	5
WHT	September, 1996	–	–	–	1

Table 3.2: The columns refer to the number of observations made, using a particular mode: R means a R band exposure, F means an exposure with no filter, S means a single slit observation, and M means MOS.

take multiple exposures of a source, for purposes of cosmic-ray rejection, many of the sources were observed with single exposures, since the quick reduction of their spectra showed that they were not significantly affected by cosmic-ray events.

Calibration exposures were taken each night. Sets of five bias frames were taken at the start and end of each night. Flat fields, for the imaging mode, were taken of both an illuminated screen inside the telescope dome, and twilight sky-flats. EFOSC-I contains Halogen, Helium and Argon lamps for spectroscopic calibration exposures; the Halogen lamp is used to provide flat-field images of the single slits and MOS masks, the Helium and Argon lamps are used for wavelength-calibration exposures. Before using these lamps, a screen has to be moved over the sky baffle, since the lamps point towards the secondary mirror. The lamps illuminate a white ring, painted on this screen and scaled to simulate the telescope pupil, which reflects the light back to the CCD. The advantage of this arrangement is that the calibration beam is highly uniform and has the same f-ratio as the telescope; the disadvantage is that, since the screen is 4.5m away from the focal plane, the intensity of the light, particularly from the Argon lamp, is low, and so long exposure times are required for the wavelength calibration images. It was found that the pixel-to-wavelength relation was very stable during a night — attributed to there being very little flexure of EFOSC-I with telescope position, or temperature changes (Savaglio et al. 1997). Spectroscopic flat-field images were taken at the start or end of each night, and the wavelength calibration exposures were taken after each spectroscopic observation.

Observations at the AAT

The two observing runs at the 3.9m AAT used the Low Dispersion Survey Spectrograph, LDSS-I (Colless et al. 1990). This is a similar instrument to EFOSC-I, in that it provides modes for imaging, single slit and multiple-object spectroscopy, and is placed at the Cassegrain focus of the telescope. The major difference is in the construction of the MOS masks; there are no manufacturing facilities at the telescope, which means that they have to be prepared well before the observing run. The mask design used the same criteria for selecting objects as was used with EFOSC-I. Once the sources had been selected from the EFOSC-I images, the LEXT software package — which was designed for use with LDSS-I — was used to select slit lengths and to ensure there was no overlap between the slits. It was also possible to optimise the position of the slits, relative to the mask centre, to maximise the wavelength coverage on the CCD. The masks were created by photochemically etching the final design onto steel templates.

The CCD used was a 1024 by 1024 pixel Tektronix chip, the details of which are given in table 3.1. It has no bias structure, and a quantum efficiency approaching 70% at wavelengths between 5500 Å and 7500 Å. Four hot pixels (Tinney 1996) were masked out of all images during the processing. The grism used had a dispersion of 165 Å mm^{-1}, corresponding to a wavelength scale of 4.0 Å/pixel, with a resolution element of 11 Å, since the slits had a width of 1.7″. Although the chip shows fringing at long wavelengths, the peak-to-peak variation is only 1% at a wavelength of 7300 Å, and negligible at shorter wavelengths. For the observed wavelength range, 3700 Å to 7500 Å, the fringing has negligible effect.

There were seven nights of LDSS-I time, split between four nights in May 1996, the 14^{th} to the 17^{th}, and three nights in July 1996, the 16^{th} to the 18^{th}. Both observing runs were affected by poor weather, and only 15 sources were successfully observed, as listed in table 3.2. Calibration exposures were taken using a similar method to that used with EFOSC-I. Bias frames and spectroscopic flat-fields were taken at the start and end of each night, whilst Copper-Argon arc frames were taken

after each observation. Unlike the EFOSC-I runs, at least three science exposures per source were taken.

Service-time observation at the WHT

One source, RX J2038.4 − 0125, which was considered likely to be a distant, $z > 0.5$, cluster, and had not been observed spectroscopically in either the ESO or AAT runs, was observed in service-time at the 4.2m WHT, using LDSS-2. This instrument is essentially the same as LDSS-I, the major difference being that masks can be made at the telescope. The design of the mask followed the same procedures as used for the LDSS-I observations. The observation of this source was split over the nights of September the 6^{th} and 7^{th}, 1996. Three MOS images were obtained as well as flat-field and wavelength-calibration exposures. The choice of the number of observations and their length was a compromise between fitting into the three-hour time limit for service-time observations, ensuring each exposure was sky — rather than read-noise — limited, and having enough exposures for efficient cosmic-ray rejection. The MED/RED grism was used, which has a dispersion of 5.3 Å/pixel and a resolution of 13 Å, for a wavelength coverage of 4000 Å to beyond 8000 Å. Wavelength-calibration images were obtained with a Copper-Argon arc lamp. Although the usual detector for LDSS-2 is the 1024 by 1024 Tek CCD — similar to that used at the AAO — the actual CCD used in the runs was a Lorel device, as listed in table 3.1. This chip has a quantum efficiency greater than 80% for the wavelength range 4000 Å to 8000 Å. Fringing in the chip, visible in the flat-field images, meant that the spectra were limited to wavelengths less than 8000 Å.

3.1.3 Description of the data reduction

A combination of STARLINK reduction packages — CCDPACK (Draper 1996) and FIGARO (Shortridge et al. 1997) — and the LDSS-I reduction package, LEXT (Allington-Smith & Maddox 1994), were used to analyse the data. Since the detectors used were all CCDs, the reduction method is the same for all the data. The

Imaging	Debias
	Flat field
Spectroscopy	Debias
	Orientate images and separate MOS fields
	Flat field
	Identify object and sky regions
	Cosmic-ray rejection
	Collapse object and sky regions
	Subtract sky from object spectra
	Wavelength calibration

Table 3.3: Overview of the various stages in the reduction of the CCD data.

various stages in the reduction are discussed in detail below, and a summary is provided in table 3.3.

The first stage, for both the imaging and spectroscopic data, is to remove the bias signal from the data. For each night, a median bias frame was created, which was then subtracted from each frame, by scaling the median level to the individual bias strips. For the images, the only other step taken was to apply a flat-field image, to remove the effects of pixel-to-pixel variation and vignetting by the telescope. The sky-flats were found to have insufficient signal to noise for this purpose, so the dome flats were used to create a median flat-field image.

Since the spectroscopic images are from more than one instrument, the frames have to be rotated so that they all have the same orientation. The chosen format was to have the spatial direction vertical and the dispersion axis horizontal. Inspection of the images showed that the dispersion axis was tilted by less than one pixel, with respect to the CCD columns, over the whole frame. The MOS frames were then split up into their constituent slits, to allow the same processing procedure to be used on all sources, regardless of whether the observation was with a single slit or a MOS mask. This was done by taking a cross-section through the flat-field image of the mask, and defining the slit edges from this profile. The regions corresponding to each slit were then extracted from the flat-field, arc-lamp and data frames. An example of this procedure is shown in Figure 3.3.

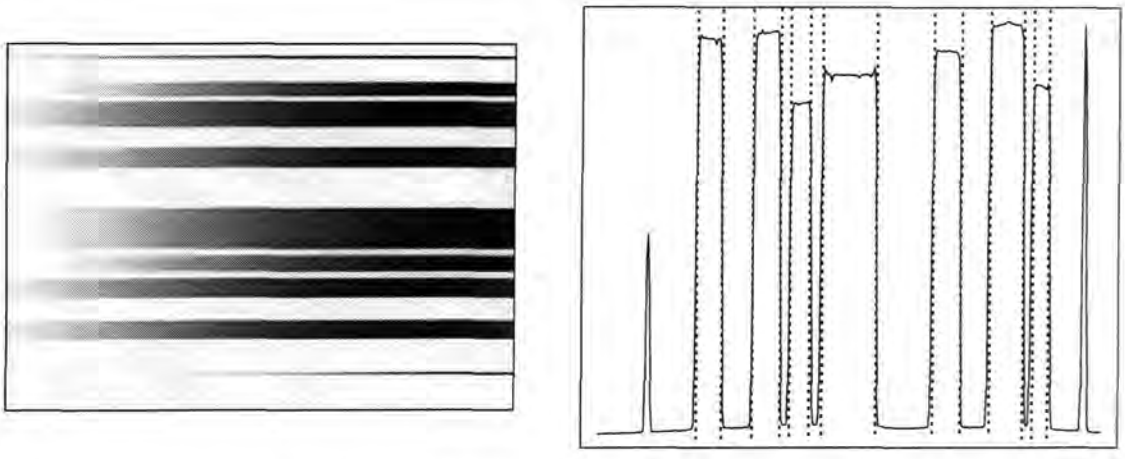

Figure 3.3: The left plot shows the flat-field image of a MOS frame: the dispersion axis is horizontal and the spatial axis vertical. The right plot shows the slit spatial profiles, obtained by collapsing the flat-field frame along the dispersion direction. The dotted, vertical lines indicate the regions selected for each slit. The two narrow peaks, at the edges of this plot, are from the holes for the guide stars.

The data frames were flat fielded in order to remove pixel-to-pixel variations due to the response of the CCD and vignetting caused by imperfectly-machined slit edges. The flat-field images for a particular observation were median combined, and then collapsed along the spatial direction, to produce a spectrum. This spectrum was lightly smoothed, using a Gaussian profile with a FWHM of five pixels, and then divided into each column of the median flat-field image. The resulting image was normalised to have a median value of one and then divided into each data frame, creating a flat-fielded image. Figure 3.4 shows the effect of flat fielding on the spatial profile of a MOS observation — the variations, due to the pixel response of the CCD and the defects in the slit edges, have been removed.

Collapsing the flat-fielded data frames along the dispersion axis produces spatial profiles of the sources — an example of such a profile is shown in Figure 3.4. These profiles are used to identify regions containing sources and regions from which the background sky signal can be estimated. Source regions were selected to include the majority of the source flux without extending into the sky regions, since this leads to an increase in the noise level without significantly increasing the source signal. The background region for a particular source was chosen to be close to the source and to include, if possible, regions on both sides of the source. Since the slits can contain

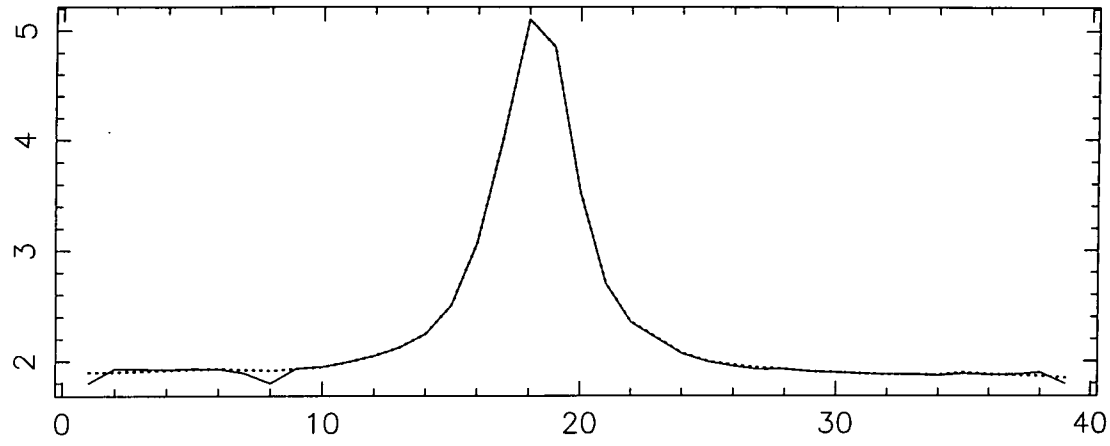

Figure 3.4: The plot shows the spatial profile of a slit from a MOS observation before (solid line) and after (dotted line) flat fielding. The major effect has been to remove the effects of imperfectly-machined slit edges. The abscissa is labelled in units of pixels, whilst the ordinate is in arbitrary units.

more than one source, background regions were chosen for each source, rather than having only one background region per slit. The chosen object and sky regions were then extracted from the data frames.

The next stage was to remove cosmic-ray events from these regions. Since the number of exposures per source was, in most cases, less than three, the common technique of median filtering the exposures could not be used. The approach taken to cosmic-ray rejection is that used by the FIGARO program COSREJ, and is based on the assumption that the spectrum of each spatial element, i.e. column of pixels, in a region is the same, apart from the normalisation and signal to noise. Whilst such an assumption is justified only for the background regions and point sources, the majority of objects observed were only marginally extended, and tests showed that this did not affect the process. The first step was to normalise each column, in a region, by its mean value. Each row of the region, corresponding to a single wavelength value, was then examined for cosmic-ray events. The value of each pixel in the row was compared to the mean value of the other pixels, and rejected if it was more than five standard deviations away from this level. The comparison was repeated until either no more pixels are rejected, or there were only two pixels left in the row. The mean of the remaining pixels was used to replace the values of any rejected pixels. Each row was analysed in this manner, and then the individual

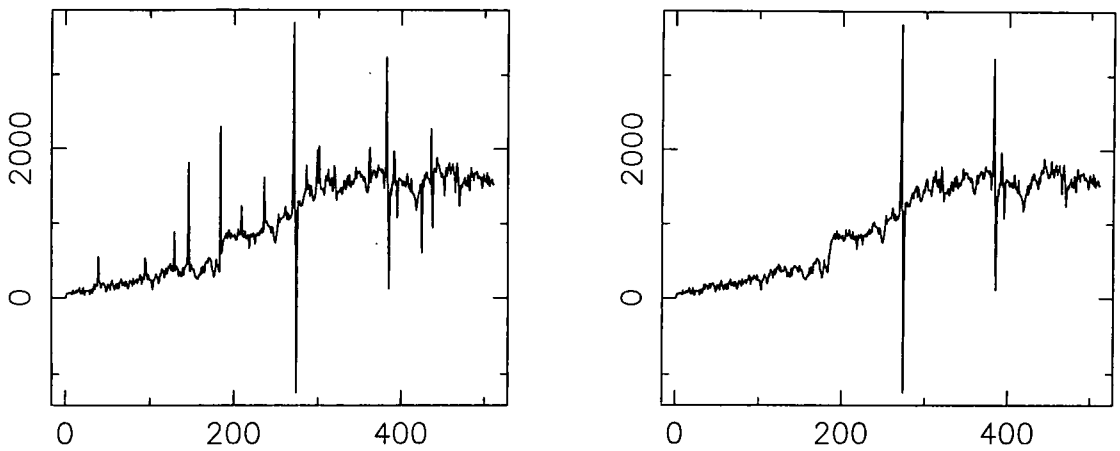

Figure 3.5: Both plots show the background-subtracted spectrum of the same source, before wavelength calibration, where the abscissae are in pixels and the ordinates are in arbitrary units. The difference between the two plots is due to cosmic-ray events; the left-hand plot was calculated without any cosmic-ray rejection, the right-hand plot was calculated after using the cosmic-ray rejection scheme described in the text. The features at ~ 280 and ~ 390 pixels are due to imperfectly-subtracted night-sky emission lines.

columns rescaled to their original levels. The effect of this scheme on the resulting background-subtracted spectra is illustrated in Figure 3.5.

After the cosmic-ray events had been removed, the object and sky regions were collapsed down along the spatial direction. The resulting spectra were then normalised by the number of columns in the collapsed regions, before subtracting the background spectrum from the object spectrum. The final step in the reduction process was to apply a pixel-to-wavelength mapping to the background-subtracted spectra. For each source, a region of the corresponding arc frame was collapsed down to produce an arc-line spectrum. The chosen region encompassed both the regions used to define the object and the background from the science frames. This was to ensure that any changes in the pixel-to-wavelength relation with spatial position along the slit were accounted for. Arc lines were individually identified, using the identification lists provided with the instrument manuals (Savaglio et al. 1997; Allington-Smith & Maddox 1994), and a third or fourth order polynomial fitted to the data, to produce the pixel-to-wavelength calibration for the spectrum. The number of identified lines depended on the position of the slit on the detector, but typically nine lines were used for the EFOSC-I data and ten for the LDSS-I and

LDSS-2 data, producing residuals of $\sim$ 0.2 Å and $\sim$ 0.4 Å respectively. Sky-line residuals, such as those shown in Figure 3.5, were manually removed before the spectra were identified. Examples of background-subtracted, wavelength-calibrated spectra are shown in Figure 3.6 — the typical signal-to-noise value for the spectra is 10.

3.1.4 Identification of the spectra

The classification of a spectrum as belonging to a particular object class is based on the detection of various absorption and emission features. Since the spectra have not been flux-calibrated, the shape of the continuum emission is not a useful diagnostic in this process. Once several features have been identified, the redshift of the object can be found from the shift of the identified features relative to their rest-frame wavelengths (e.g. Costero & Osterbrock 1977; Corwin & Emerson 1982). The most commonly observed features were: in absorption, the Ca II H and K doublet, the 4000 Å break, and the G band; in emission, the $[OII]_{3727}$, Hβ, $[OIII]_{4959}$, and $[OIII]_{5007}$ lines. Identification and redshift determination was performed by fitting the observed spectral features by eye. This process was greatly assisted by the use of Dr. K. Glazebrook's program, REDSHIFT, which allows redshifts to be estimated from guesses to spectral features, and, conversely, identification of features once a redshift has been established.

Another approach to redshift measurement is to cross-correlate the spectra with a library of spectral templates of known redshift (e.g. Heavens 1993). This technique was not adopted for the following reasons: firstly, the large redshift range of objects in the sample did not well match that of the available template spectra, which were limited to redshifts $\lesssim 0.1$ — the small overlap, in the rest-frame pass bands, of the high-redshift galaxies and the template spectra produced redshift estimates with large systematic errors; secondly, Romer (1996) compared both techniques, using a sample of galaxies from low-redshift X-ray selected clusters, and found that the errors of both methods were similar ($\delta z \simeq 0.001$); and finally, even in this

technique, the spectra have to be manually checked to remove objects which are not well matched by the template library — this includes late-type stars with broad metallic absorption lines, and strong emission line objects, such as AGN and QSOs.

Four examples of identified spectra are shown in Figure 3.6. Since the spectra have not been flux-calibrated, the continuum level in these plots is due to the continuum properties of the source, atmospheric absorption, and the wavelength response of the instruments. The spectra have been chosen to illustrate the range of objects contained in the sample. Tables 3.4a and 3.4b list the clusters identified from the sample; the identification of all the sources is given in Appendix C. The listed cluster redshift corresponds to the average value of the galaxy redshifts, the number in the brackets refers to the number of galaxies used to calculate this average.

The catalogue contains 36 clusters, with redshifts between 0.06 and 0.67, sixteen of which have $z \geq 0.3$. Below a redshift of 0.2, 75% of the clusters already have an identification in the literature, whilst above this redshift, all but one cluster is a new detection. Of the 103 extended sources presented in Appendix C, 42 are associated with the clusters, 13 are spectroscopically identified (either from the literature or from the observing runs described above) as not being clusters, 37 are identified as not being clusters from their optical properties (either from the DSS images or deep optical imaging), and 11 remain without any identification. The completeness rate for the survey is therefore 89%. Among the un-identified sources are systems which could be low-redshift clusters, or groups (e.g. RX J0505.9 − 2826 and RX J1313.6 − 3251), and some which could be high-redshift clusters (e.g. RX J0323.8 − 5116 and RX J2138.7 − 4245).

3.2 X-ray fluxes and luminosities

As mentioned in Chapter 2, the poor spectral resolution of the PSPC coupled with the low count rates of the clusters detected in this survey mean that spectral models can not be reliably fit to the X-ray data. Cluster fluxes are therefore estimated by

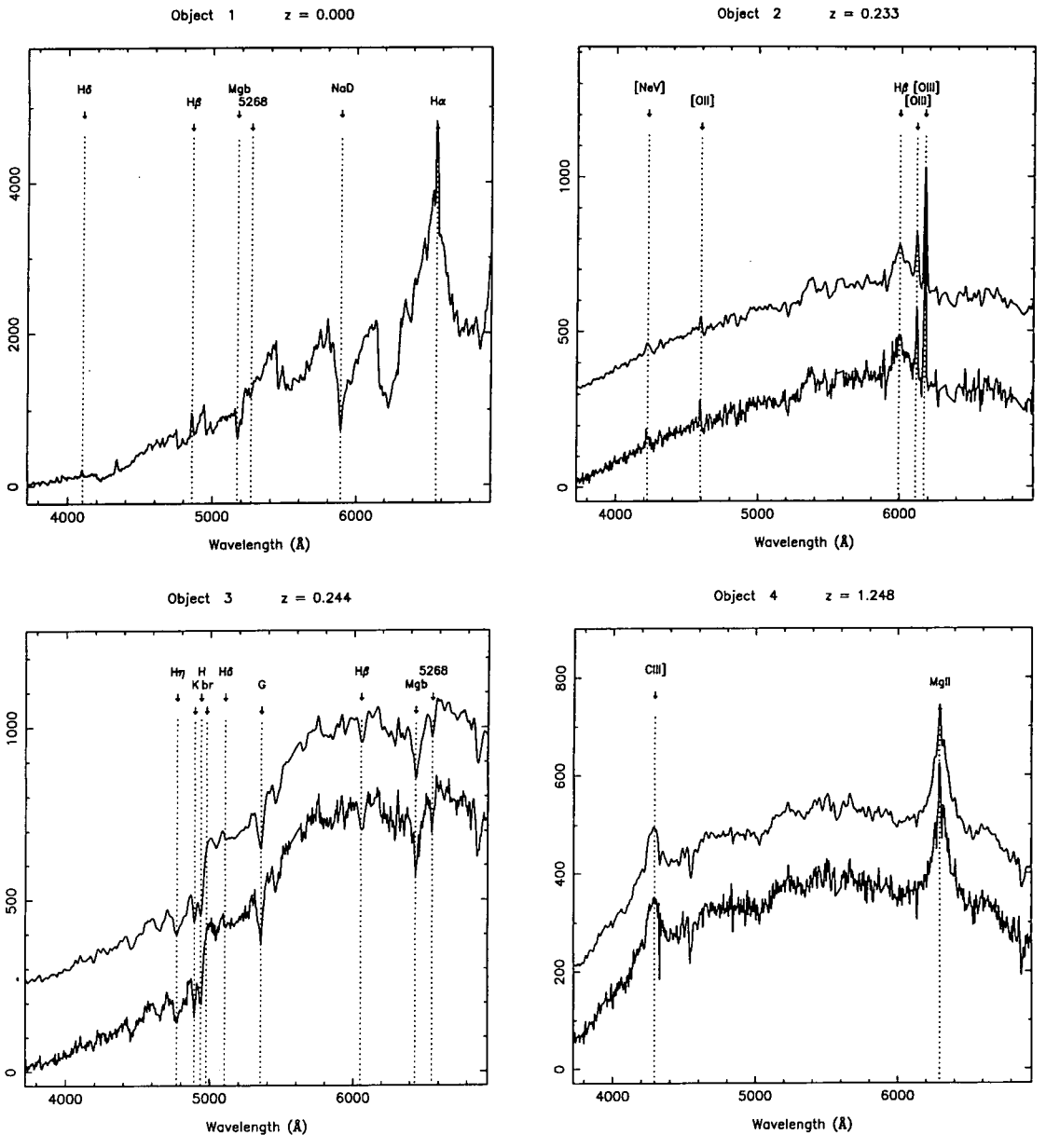

Figure 3.6: The plots show the spectra of a variety of sources detected in the observing runs. The abscissa is the wavelength axis, in units of Å, and the ordinate is the flux axis, which is in arbitrary units. For objects 2, 3, and 4, a smoothed version of the spectrum is also shown, offset vertically for clarity. The redshift of each object is indicated in the top-right of the plot, and identifying spectral features are indicated by the vertical dotted lines.

Name	RA			Declination			ID	z	Notes
	h	m	s	°	′	″			
RX J0318.2 − 0301	3	18	17.4	−3	1	14.7	SC	0.370 (1)	†
RX J0318.5 − 0303	3	18	32.8	−3	2	45.7	SC	0.373 (3)	
RX J0321.9 − 5119	3	21	57.1	−51	19	25.2	LC	0.070	Abell 3120
RX J0333.0 − 3914	3	33	5.5	−39	13	49.4	SC	0.245 (5)	
RX J0333.8 − 3906	3	33	50.1	−39	6	23.5	(LC)	−	(Abell 3135)
RX J0334.0 − 3901	3	34	3.2	−39	0	48.7	LC	0.063	Abell 3135
RX J0334.1 − 3904	3	34	11.0	−39	3	54.1	(LC)	−	(Abell 3135)
RX J0337.7 − 2522	3	37	45.2	−25	22	26.2	SC	0.577 (3)	
RX J0416.7 − 5525	4	16	44.8	−55	25	8.6	SC	0.365 (3)	
RX J0505.3 − 2849	5	5	19.9	−28	49	5.2	SC	0.509 (3)	
RX J0530.5 − 5852	5	30	31.1	−58	51	34.8	SC	0.338 (2)	
RX J0858.4 + 1357	8	58	25.3	+13	57	14.6	SC	0.485 (3)	
RX J0946.5 − 1410	9	46	32.9	−14	9	50.5	SC	0.230 (5)	
RX J0947.9 + 0730	9	47	57.5	+7	30	26.0	SC	0.128 (3)	
RX J1142.0 + 1009	11	42	5.6	+10	8	47.5	LC	0.118	Abell 1354
RX J1142.2 + 1027	11	42	16.8	+10	26	47.1	LC	0.070	Abell 1356
RX J1200.8 − 0328	12	0	48.4	−3	27	50.9	SC	0.395 (4)	
RX J1204.3 − 0351	12	4	22.8	−3	50	59.8	SC	0.262 (5)	

† There is an AGN, identified as being at $z = 0.233$, $\sim 1'$ North of the cluster centre, visible as the point-source component of the smoothed X-ray image in Appendix B. When calculating the cluster flux (Section 3.2), the AGN emission is masked out.

Table 3.4a: The table lists the 36 clusters detected by the survey — a list containing all the sources is given in Appendix C. The co-ordinates refer to the X-ray centre, as given by PSS, and are equinox 2000. The ID column refers to how the cluster was identified: a L indicates the identification comes from the literature (the NASA Extragalactic Database), whilst a S indicates the object was spectroscopically-identified in one of the observing runs. To remain consistent with Appendix C, the C identifier has been left in. Brackets around the ID show that the source is actually part of the cluster whose name is given in the Notes column. For those clusters spectroscopically identified in this thesis (i.e. with an ID of SC), the redshift is the average value of the detected galaxies — where the number in brackets gives the number of redshifts used — whilst for LC clusters the redshift is taken from the literature.

Name	RA			Declination			ID	z	Notes
	h	m	s	°	′	″			
RX J1205.0 − 0333	12	5	2.8	−3	32	31.1	SC	0.368 (5)	
RX J1205.6 − 0338	12	5	38.0	−3	38	20.7	SC	0.207 (3)	
RX J1227.1 + 0856	12	27	7.9	+8	55	57.3	(SC)	−	(RX J1227.2 + 0858)
RX J1227.2 + 0858	12	27	14.5	+8	58	10.1	SC	0.090 (4)	8.0′ from Abell 1541
RX J1227.4 + 0850	12	27	26.6	+8	50	11.0	LC	0.089	Abell 1541
RX J1227.4 + 0855	12	27	29.8	+8	54	37.8	(LC)	−	(Abell 1541)
RX J1235.6 + 1311	12	35	38.2	+13	10	46.5	SC	0.253 (4)	
RX J1253.2 + 1556	12	53	14.7	+15	55	52.7	SC	0.275 (4)	
RX J1259.7 − 3236	12	59	47.6	−32	36	17.9	SC	0.076 (7)	
RX J1325.0 − 3814	13	25	1.6	−38	13	35.3	SC	0.296 (6)	
RX J1325.5 − 3826	13	25	34.8	−38	25	49.5	SC	0.445 (4)	
RX J1338.0 − 2944	13	38	5.8	−29	44	25.3	LC	0.189	MS 1335.2 − 2928
RX J1345.2 − 0009	13	45	14.8	−0	8	31.7	SC	0.087 (2)	
RX J1354.2 − 0222	13	54	17.2	−2	21	45.9	SC	0.551 (5)	
RX J2038.4 − 0125	20	38	29.3	−1	25	16.8	SC	0.673 (2)	
RX J2106.8 − 0510	21	6	49.0	−5	9	54.8	SC	0.449 (7)	
RX J2108.8 − 0517	21	8	49.5	−5	16	39.6	SC	0.320 (2)	
RX J2114.3 − 6801	21	14	20.8	−68	1	4.2	LC	0.130	DS 210958 − 681304‡
RX J2137.8 − 4251	21	37	49.5	−42	50	49.1	SC	0.185 (7)	Abell 3791
RX J2137.8 − 4253	21	37	53.2	−42	52	49.2	(SC)	−	(Abell 3791)
RX J2155.9 + 0110	21	55	54.9	+1	10	3.9	(SC)	−	(RX J2155.9 + 0109)
RX J2155.9 + 0109	21	55	59.1	+1	9	2.1	SC	0.219 (6)	
RX J2202.7 − 1902	22	2	44.6	−19	1	59.8	SC	0.436 (3)	
RX J2359.5 − 3211	23	59	35.9	−32	11	6.5	SC	0.478 (3)	

‡ DS 210958-681304 is also known as the Pavo cluster.

Table 3.4b: Continued.

using a model spectrum, with fixed parameters, to convert the $0.5 - 2.0$ keV count rate into both a flux and a luminosity. Section 3.2.1 describes the techniques used to measure the cluster count rates, whilst Section 3.2.2 describes how these count rates were converted into fluxes and luminosities.

3.2.1 Measuring the cluster X-ray count rate

As the PSPC has a large field of view, the aperture within which to measure the cluster flux can be selected for each cluster, rather than having to use a fixed angular aperture, as in the EMSS (Henry et al. 1992). A circular aperture was used, the radius chosen so that the aperture contained 80% of the flux of a model surface-brightness profile. The profile used for a given cluster was calculated by convolving the King profile (equation (1.9) with $\beta = 2/3$ and $r_c = 250$ kpc, scaled to the cluster redshift) with a model of the PSPC PSF, which includes the off-axis dependence of the PSF. As discussed in Section 2.3, the parameters of the King profile are consistent with those of low redshift cluster samples (e.g. Jones & Forman 1984; Henry et al. 1992). The choice of aperture radius is a compromise between including a high fraction of the cluster flux and keeping down the number of contaminating sources within the region. An advantage to using the 80% radius, r_{80}, is that the correction from the measured to total count rate is insensitive to the actual values of r_c and β of the cluster, as discussed below. Figure 3.7 shows how the convolution with the PSF increases the r_{80} value of the clusters. Since the convolution with the PSF has a small effect on the profile for radii much larger than the core size, the discussion below is for the King profile only, since it is an analytic function, unlike the convolved profile. The flux within a circular aperture, of radius r_m, for the surface-brightness profile in equation (1.9), is

$$\begin{aligned} \mathrm{Flux}(r \leq r_m) &= \int_0^{r_m} 2\pi r S(r)\,\mathrm{d}r \\ &= 2\pi S_0 \int_0^{r_m} r \left(1 + \left(\frac{r}{r_c}\right)^2\right)^{0.5-3\beta} \mathrm{d}r \\ &= \frac{2\pi r_c^2 S_0}{3(2\beta - 1)} \left[1 - \left(1 + \left(\frac{r_m}{r_c}\right)^2\right)^{1.5-3\beta}\right], \end{aligned} \tag{3.1}$$

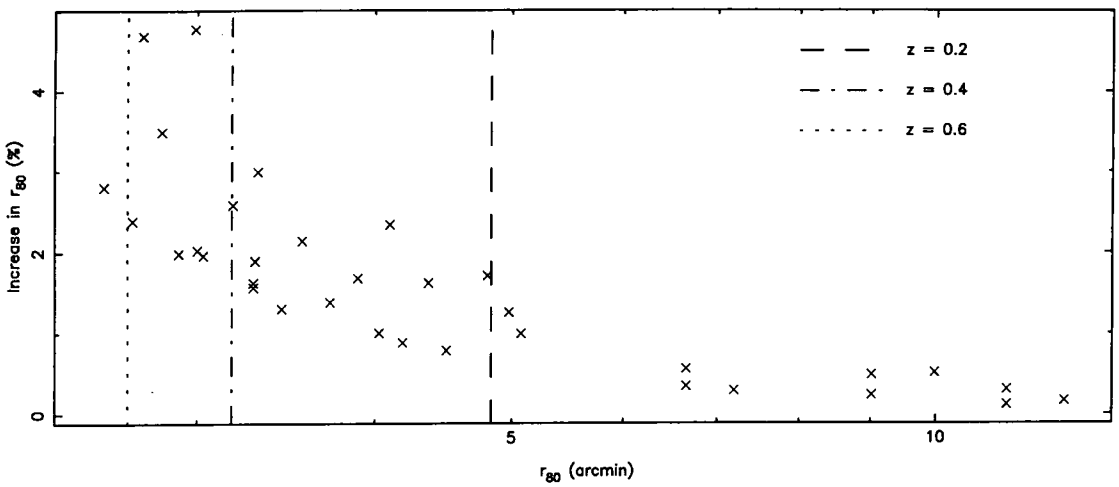

Figure 3.7: The abscissa shows the r_{80} value of the King profile, scaled to the cluster redshift, before convolution by the PSPC PSF. The ordinate shows the percentage increase of r_{80} due to the convolution. The vertical lines indicate the r_{80} values, before convolution, of clusters at redshifts of 0.2, 0.4, and 0.6.

where the final step requires $\beta > 0.5$. As the term in the square brackets tends to zero as r_m tends to infinity, the fraction of the total cluster flux falling within a circular aperture of radius r_m is

$$g(r_m, r_c, \beta) = 1 - \left(1 + \left(\frac{r_m}{r_c}\right)^2\right)^{1.5-3\beta} . \tag{3.2}$$

For $\beta = 2/3$ and $g = 0.8$, this gives $r_{80} = \sqrt{24}\, r_c$. This radius is well outside the region affected by the PSF convolution, for the cluster sizes detected in this survey, which justifies neglecting the convolution in this discussion. Figure 3.8 shows how equation (3.2) varies with r_c and β. For $r_m/r_c \gtrsim 4$, there is an uncertainty of $10 - 20\%$ due to uncertainties in the values of r_c and β.

These graphs show that the measured flux is insensitive to the radius used, as long as it is much larger than the cluster core radius. However, they do not show how accurate the measured flux is if the cluster profile differs from the fiducial values of $r_c = 250$ kpc and $\beta = 2/3$. Since the aperture radius is fixed at $r_m = \sqrt{24} \times 250$ kpc, the fraction of the actual cluster flux within the aperture is found by substituting r_m into equation (3.2), which gives

$$g(r_c, \beta) = 1 - \left(1 + 24\left(\frac{250}{r_c}\right)^2\right)^{1.5-3\beta} . \tag{3.3}$$

Dividing this value by 0.8 gives the fraction of the actual cluster flux that would be

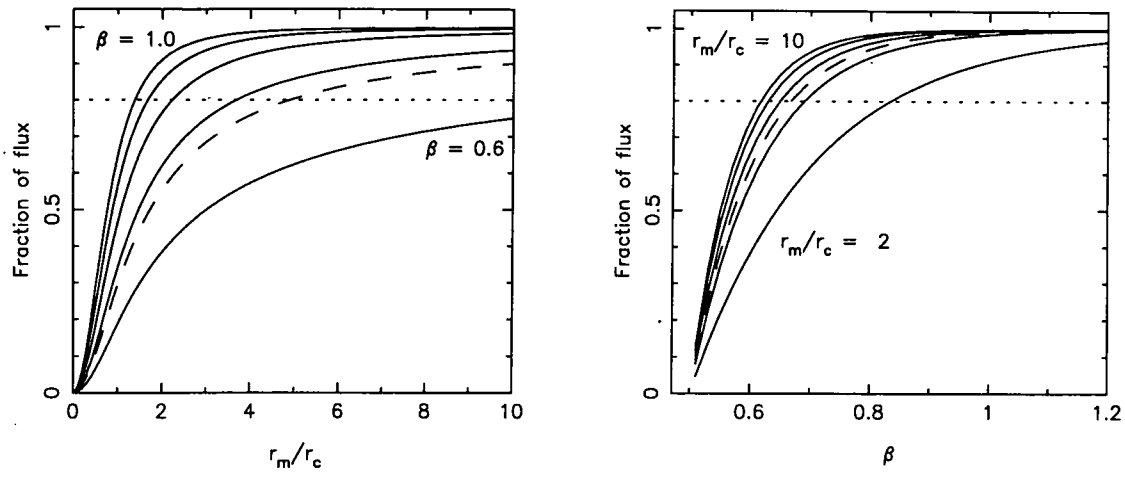

Figure 3.8: The left-hand plot shows how equation (3.2) varies as the aperture radius, r_m, changes. Since there is a degeneracy between r_m and r_c, the abscissa is in units of r_m/r_c. The dashed line indicates the curve for $\beta = 2/3$, the solid lines are for $\beta = 0.6 - 1.0$, in steps of 0.1. The right-hand plot shows the variation with β of the same function. The dashed line is for $r_m/r_c = \sqrt{24}$, the solid lines are for $r_m/r_c = 2 - 10$, in steps of 2.

measured by this process. Figure 3.9 shows this for r_c and β values that encompass the range of local cluster samples (Jones & Forman 1984). For $\beta = 2/3$, the estimated flux is insensitive to the actual cluster core radius — being within 10% of the true value for $100\,\mathrm{kpc} < r_c < 500\,\mathrm{kpc}$. If $\beta \neq 2/3$, the flux estimate is within $\sim 20\%$ of the true value, as long as $\beta \gtrsim 0.6$.

The first step in measuring the cluster count rate was to create a background-subtracted count-rate image. The background subtraction used the model background used in the creation of the X-ray catalogue (Section 2.2.3), and the conversion to a count-rate image corrected for the detector dead time and telescope vignetting before normalising by the exposure time. Two other methods of background subtraction were investigated; both used an annulus to define the background level, with the annulus either centred on, or at the same off-axis angle as, the cluster. All three methods produced source flux estimates which differed by $\lesssim 5\%$: as the fractional Poisson error on the high-redshift cluster fluxes is $\simeq 10\%$ (Figure 3.15), the error due to background uncertainties has been left out of the error budget. When measuring the fluxes, the image out to a radius of 19.2′ was used. In most cases, the region used to calculate the cluster flux contains sources not associated with the

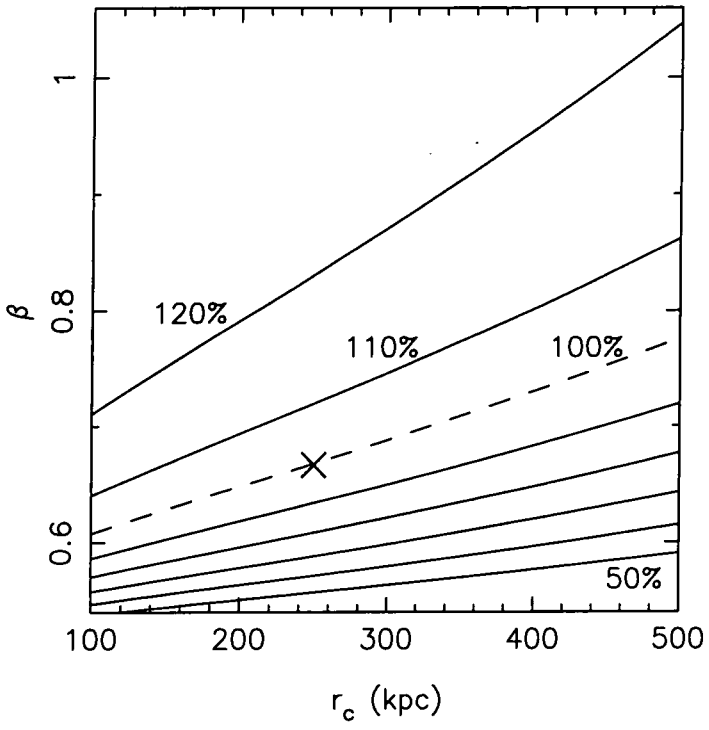

Figure 3.9: The lines indicate the cluster count rate that would be measured, as a percentage of the true value, using the method described in the text. The lines are in steps of 10%, increasing from 50% at the bottom of the plot to 120% at the top of the plot. The line corresponding to 100% has been drawn as a dashed line for clarity. By construction, the count rate from a cluster with $r_c = 250$ kpc and $\beta = 2/3$, indicated by the cross, is correctly measured.

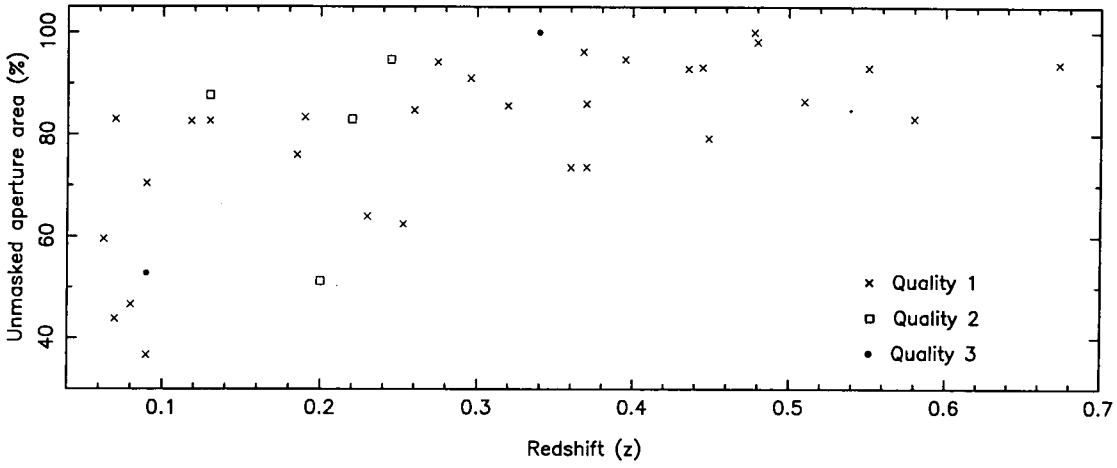

Figure 3.10: The points show the percentage of the aperture, of each cluster, which remained after masking out the contaminating sources.

cluster, which had to be removed before the flux from the cluster could be measured. Therefore, all the sources detected in the second-pass analysis (Section 2.2.3), except for the cluster, were masked from the image. Each source was masked out using a circular aperture, the radius set to the value that defined the aperture used in the second-pass analysis. The fraction of the aperture which remained, after the masking, is plotted in Figure 3.10 and listed in tables 3.6a and 3.6b. A radial profile of the cluster was created from the masked image and each masked pixel was replaced with the corresponding value from this profile. This accounted for the cluster flux within the masked regions. It also allowed the estimation of the count rates of those clusters which extend beyond 19.2′ from the field centre. An example of this process is displayed in Figure 3.11, which shows a count-rate image of a cluster before and after the source masking, the radial profile of the cluster and its growth curve. Tables 3.6a and 3.6b list the aperture radius of each cluster and the total — or corrected — cluster count rates, which are the measured values multiplied by 1.25.

For the majority of clusters, this method produced growth curves which rose quickly and then flattened off by the r_{80} value. The growth curves of these clusters are shown in Figures 3.12a to 3.12e, where the dashed vertical line indicates the aperture used for the flux estimation. These clusters are listed in tables 3.6a and 3.6b as having a quality flag of 1. For the clusters listed in these tables with a quality flag

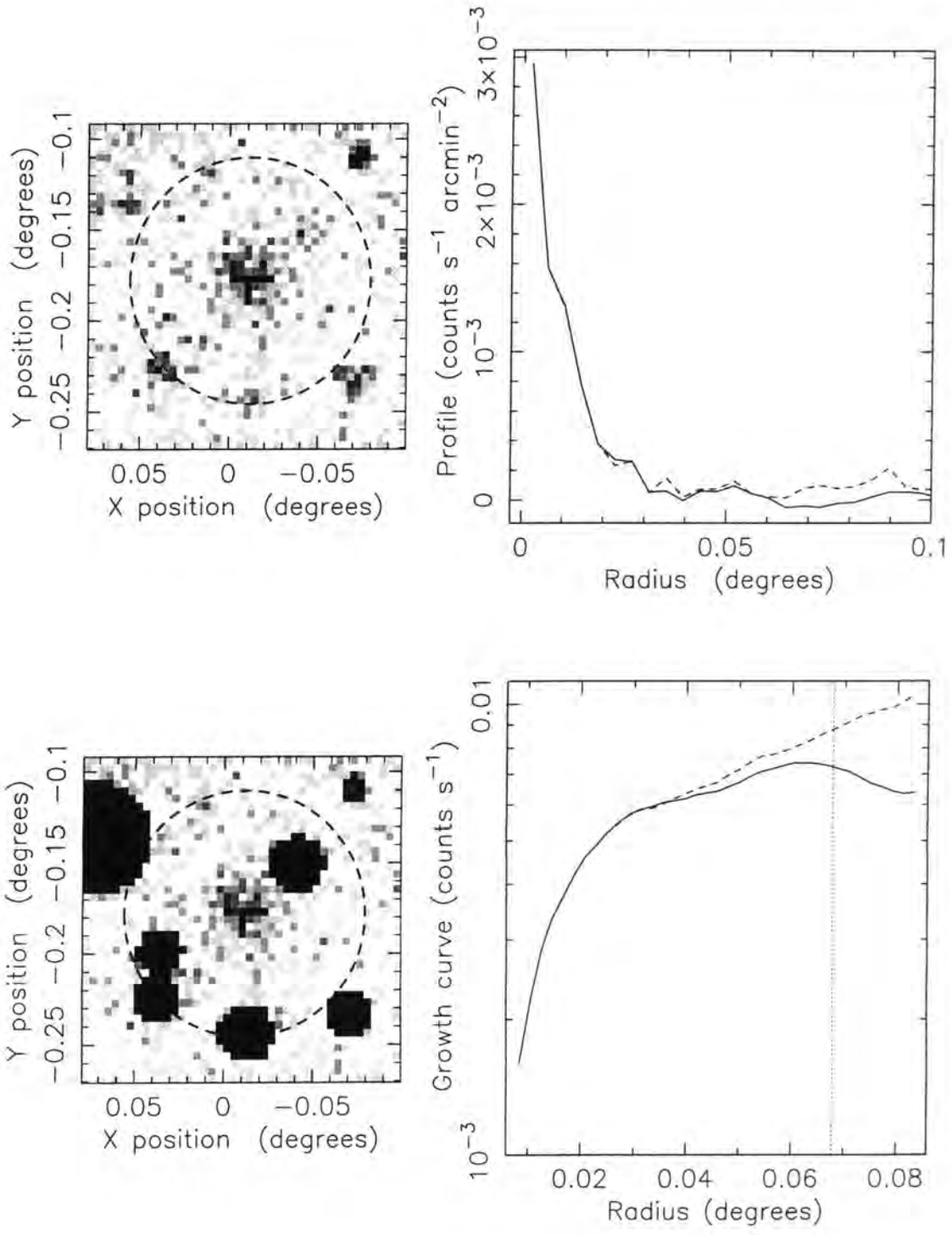

Figure 3.11: The top-left plot shows the count-rate image of the $z = 0.26$ cluster RX J1204.3-0351, where the dashed circle indicates the aperture used for flux measurement and the co-ordinates refer to its position within the PSPC pointing. The bottom-left plot shows this region after masking out the contaminating sources. The top-right plot shows the radial profile of the cluster: the dashed line is the profile from the top-left image, the solid line is the profile obtained from the bottom-left image. The bottom-right image shows the growth curves obtained for the cluster: the solid line for the masked/replaced image, as described in the text, and the dashed line for the original field, with no sources masked out. The dotted line in this plot shows the aperture used to estimate the cluster flux.

Name	z	Radius (degrees)	Count rate (counts s^{-1})	% of flux
RX J0530.5-5852	0.340	0.017	0.00188	38.8
RX J1345.2-0009	0.090	0.058	0.01273	52.3

Table 3.5: The radius and flux values for the highest signal-to-noise points of the growth curves of the two quality 3 clusters shown in Figure 3.14. The final column lists the fraction of the flux, within an aperture of the listed radius, for the model profile.

of 2, the growth curves showed signs of incorrect background subtraction, in that the curve fell significantly after the initial rise. The reduction was therefore repeated for these clusters, estimating the background level from an annulus centred on the cluster. The annulus was chosen interactively, with an inner radius at least 10% larger than r_{80} and an area comparable to the cluster aperture, so that the growth curve resembled those of the quality 1 clusters. Figure 3.13 shows the resulting growth curves: the solid line indicates the interactively chosen background level, the dotted line the original background estimate.

There are two clusters, listed in table 3.5, for which both methods failed to produce believable growth curves — they are listed with a quality flag of 3 in tables 3.6a and 3.6b. For cluster RX J0530.5 − 5852, the aperture contains large regions devoid of photons — which are not typical of the field as a whole — leading to the background being overestimated. For cluster RX J1345.2 − 0009, which is at a redshift of 0.090, 47% of the aperture had to be replaced with values from the cluster radial profile. This high value is because the cluster lies close to the edge of the field of view, and so a large fraction of the aperture is greater than 19.2′ from the field centre. The count rates for these clusters were found by extrapolating the point on the original growth curve with the highest signal-to-noise value. The extrapolation used the convolved profile created to calculate the original aperture radius. Table 3.5 lists the radius and count-rate values used to extrapolate to the total values, and Figure 3.14 shows the growth curves and signal-to-noise profiles of these two clusters.

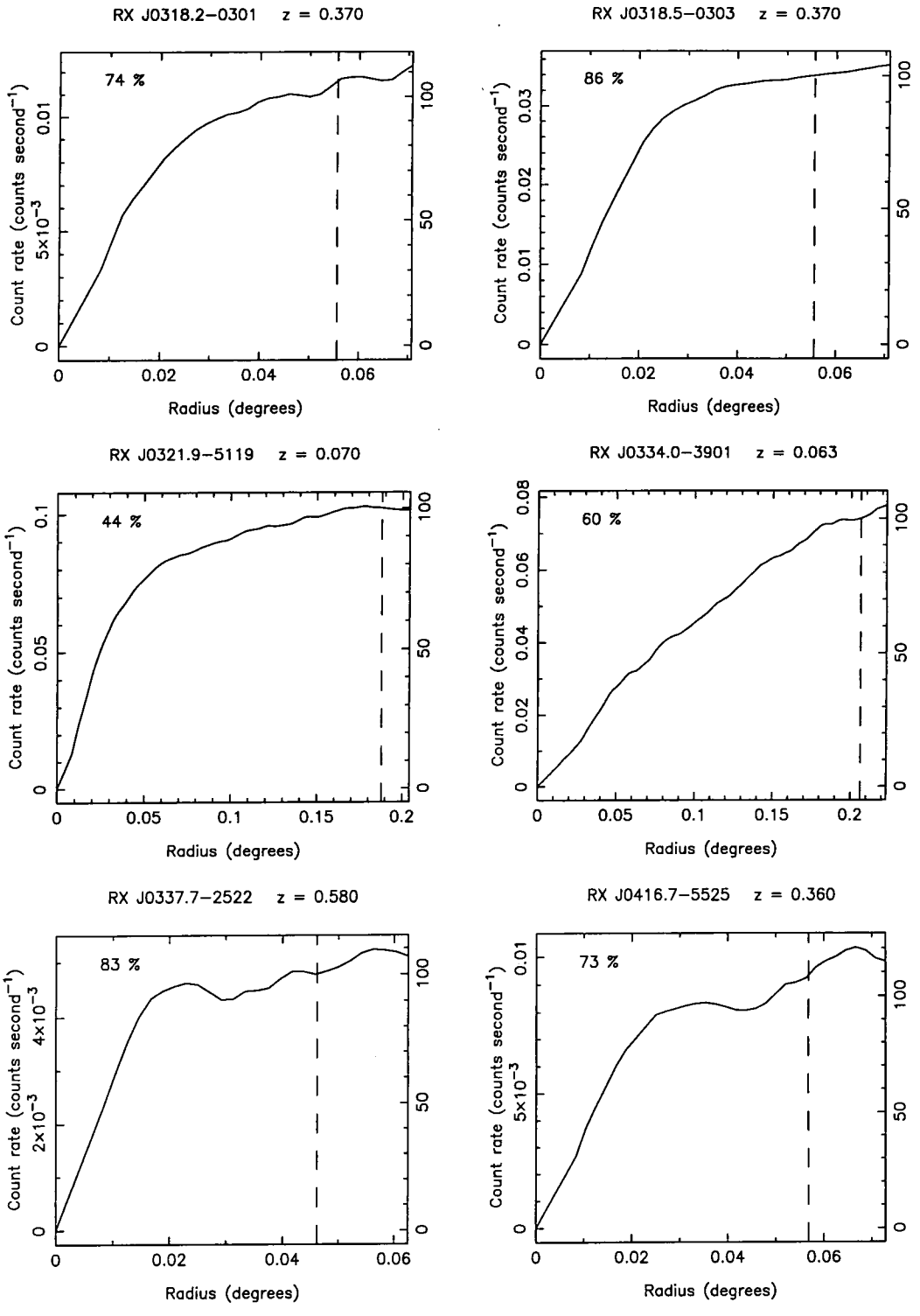

Figure 3.12a: The plots show the growth curves of clusters with a quality flag of 1; the title of each plot gives the cluster name and redshift and the vertical dashed line indicates the r_{80} value for that cluster. The ordinate has been labelled both with count rates and the percentage value relative to the measured value. This value corresponds to 80% of the total count rate, listed in tables 3.6a and 3.6b. The number in the top left corner of each plot refers to the aperture area which remained after the source masking. The clusters are listed in order of ascending RA.

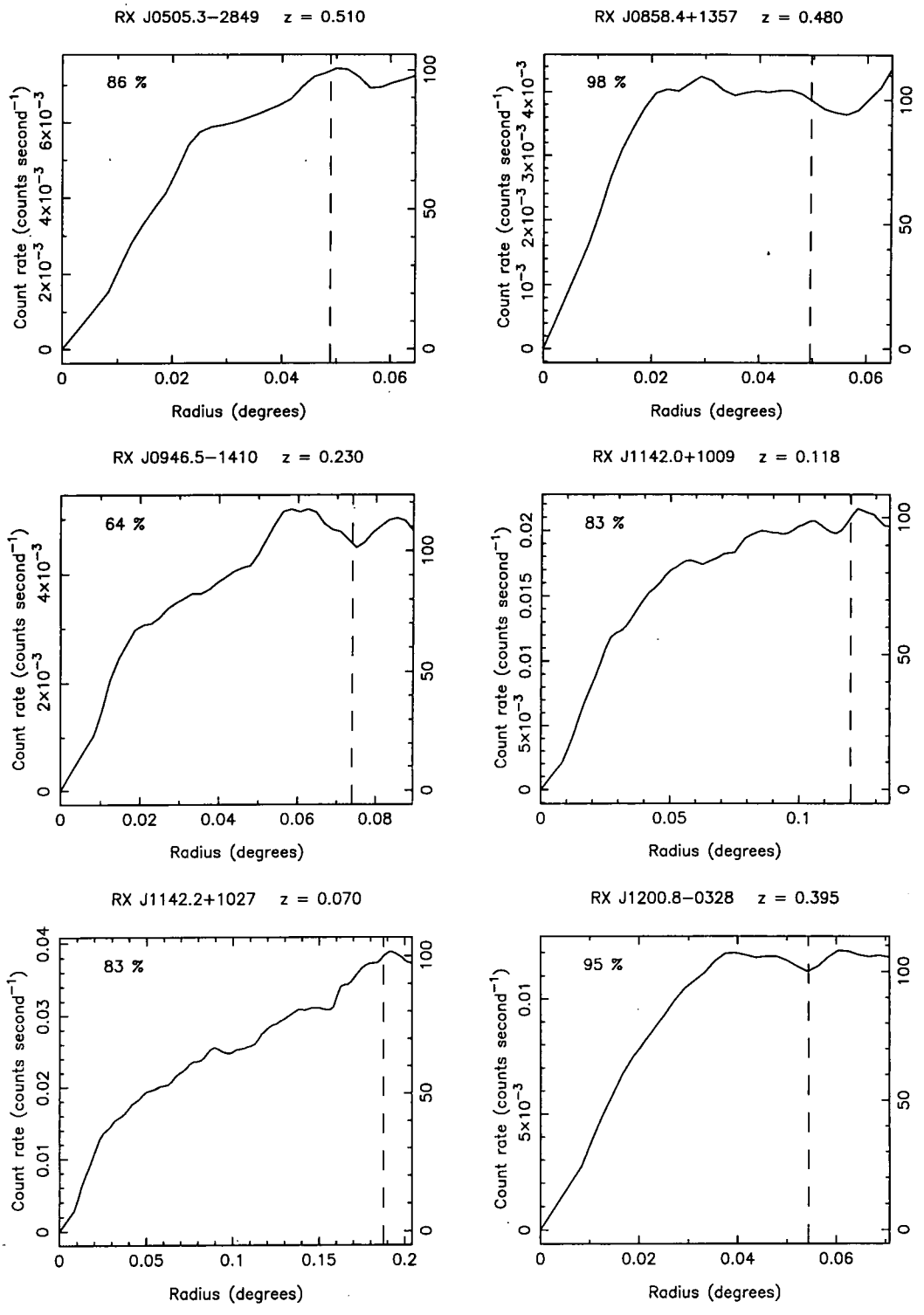

Figure 3.12b: Continued.

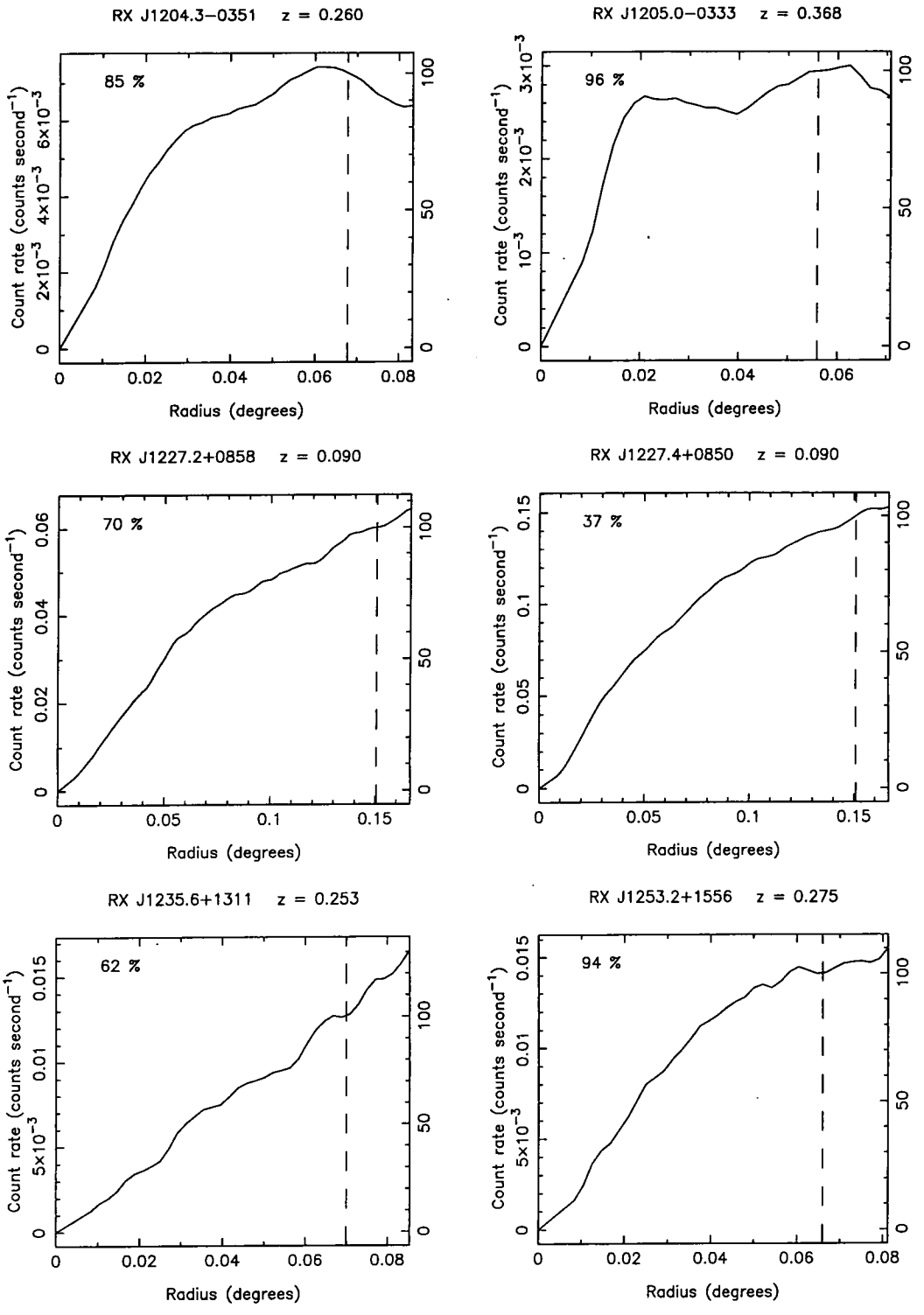

Figure 3.12c: Continued.

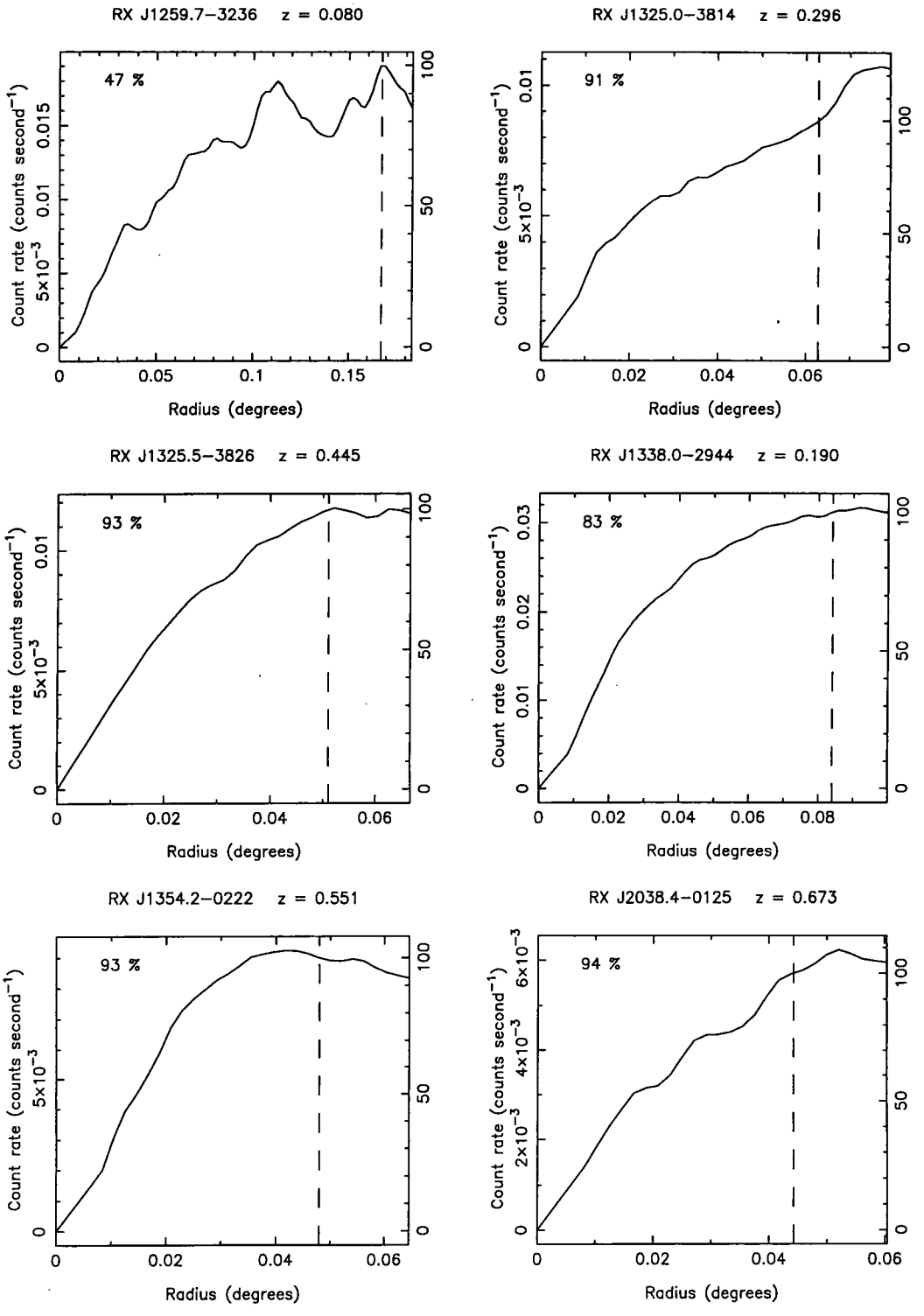

Figure 3.12d: Continued.

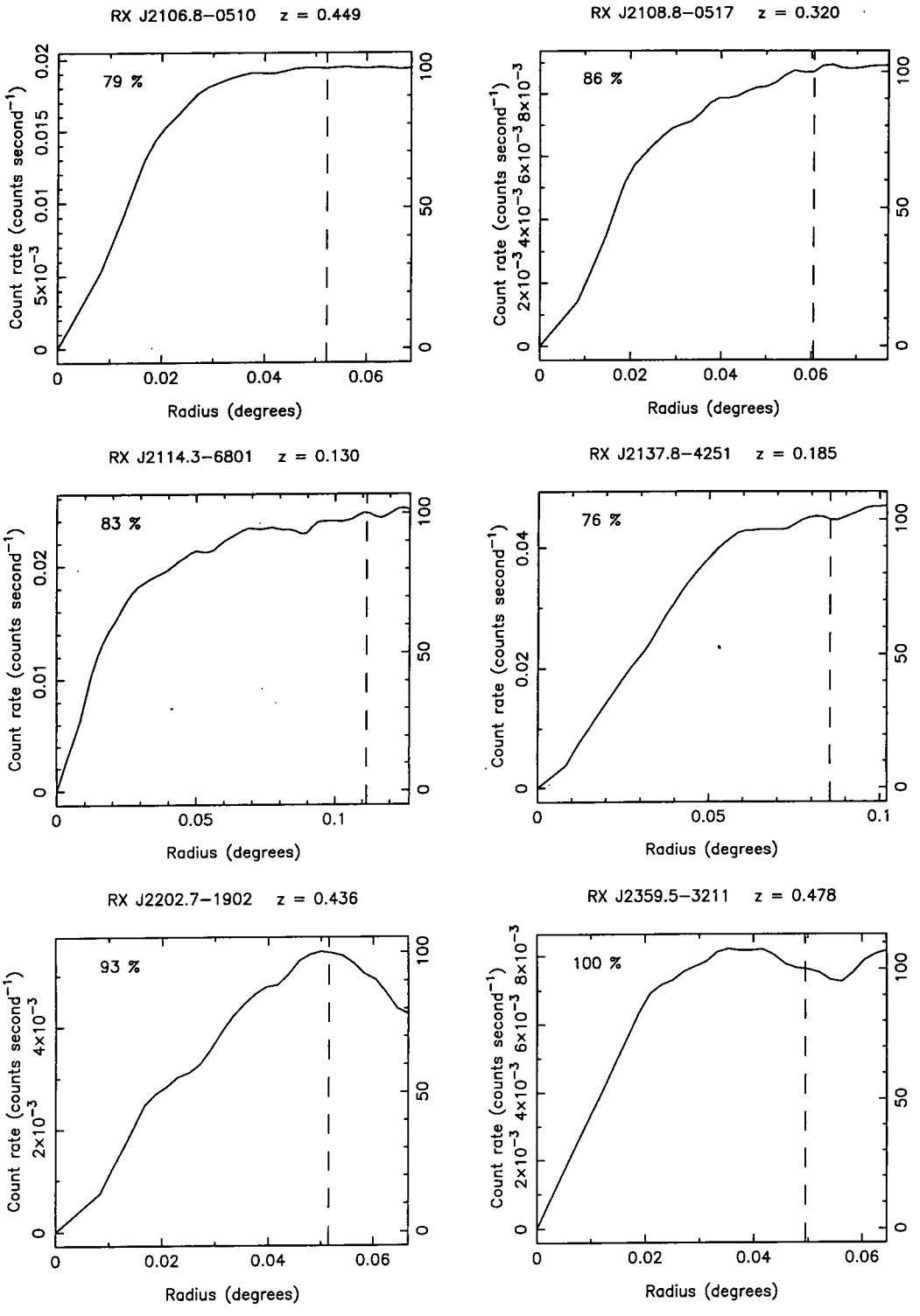

Figure 3.12e: Continued.

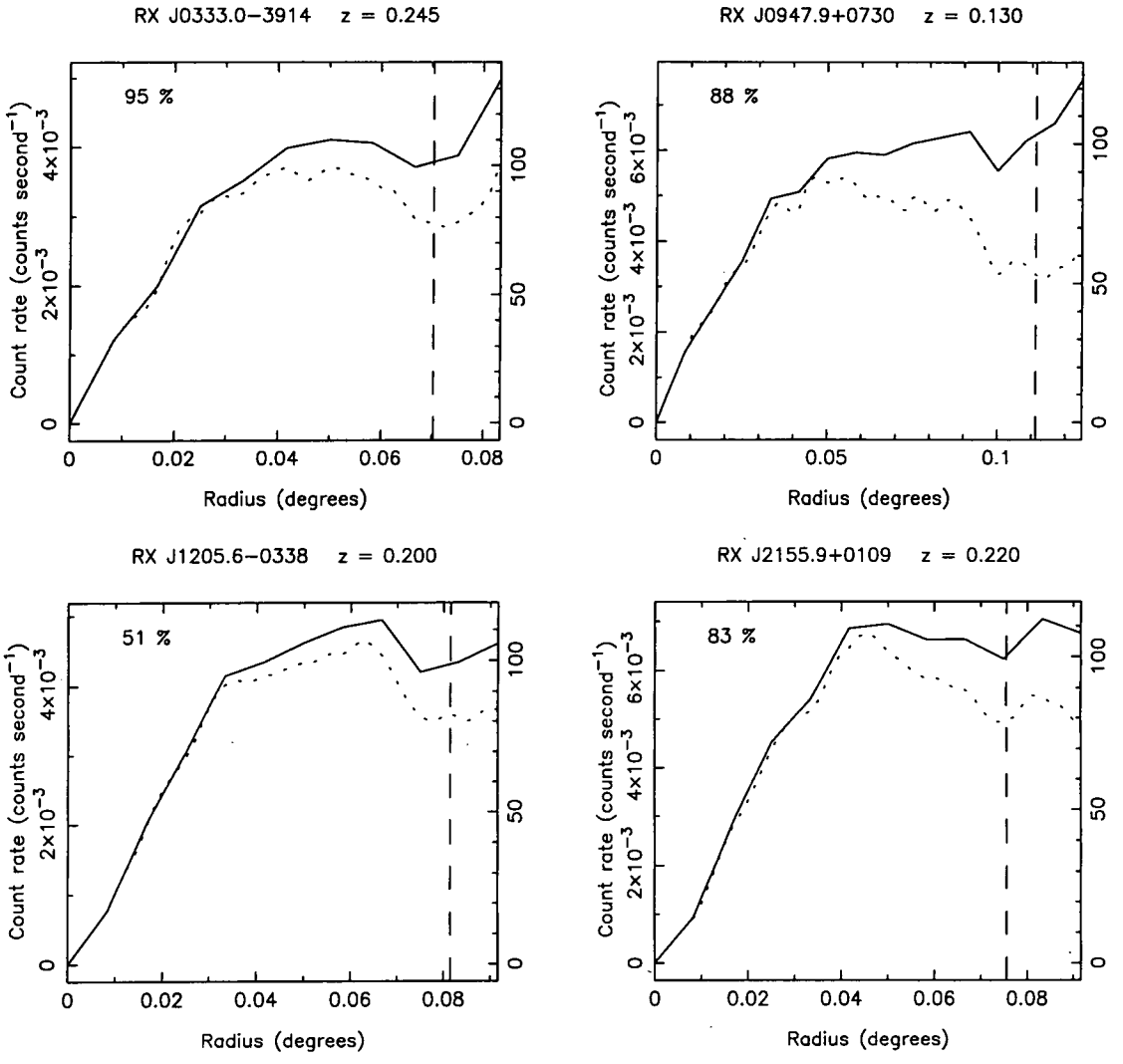

Figure 3.13: These plots show the growth curves of the four clusters with a quality flag of 2. The solid line shows the growth curves created using the interactively-chosen background regions and the dotted lines show the original growth curves. Otherwise the plots are the same as for Figures 3.12a to 3.12e.

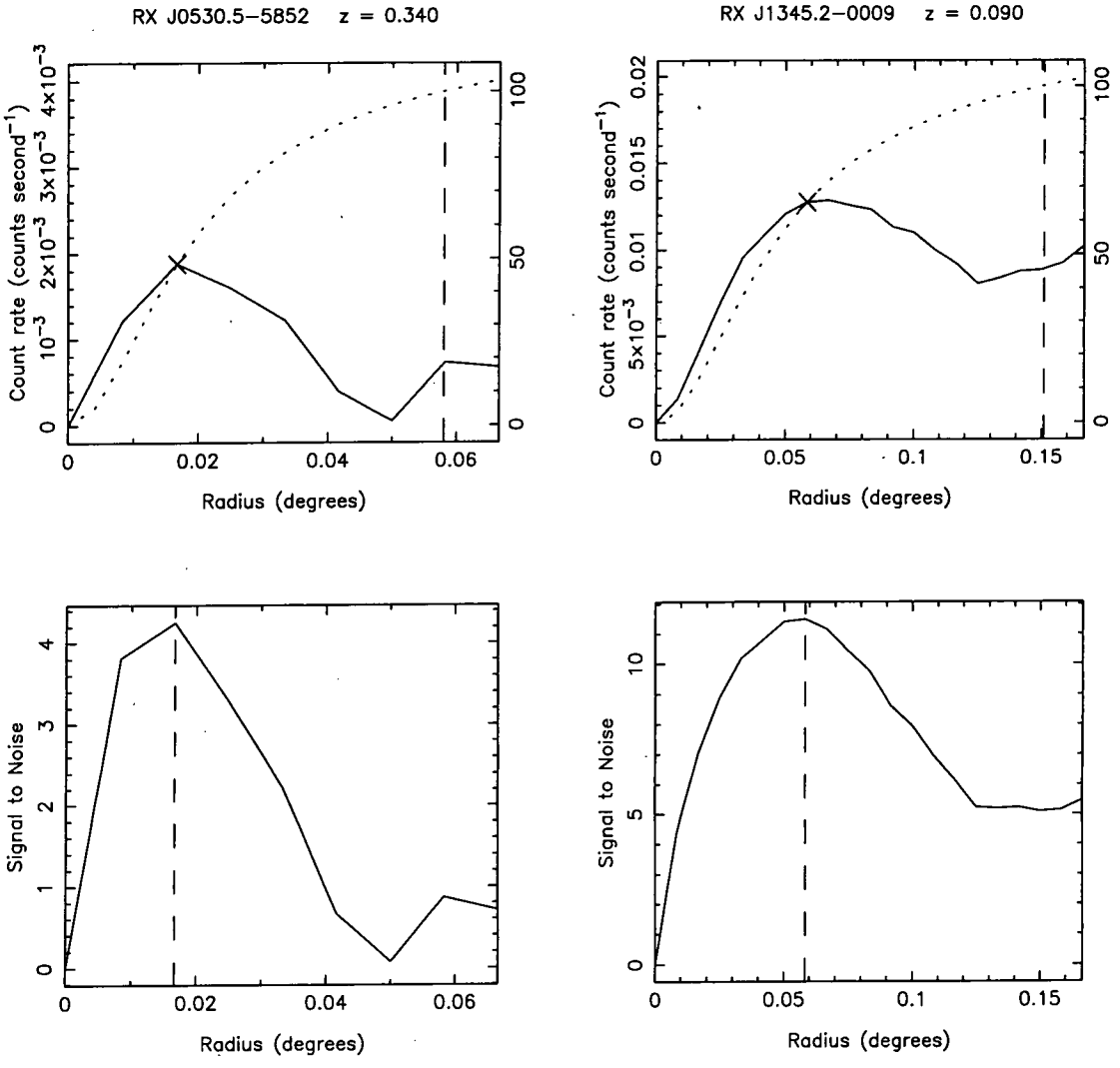

Figure 3.14: The solid lines in the top two plots show the growth curves of the two clusters with a quality flag of 3 (RX J0530.5 – 5852 and RX J1345.2 – 0009) using the model background for the background subtraction. The bottom two plots show the signal-to-noise values of these growth curves, the dashed vertical line indicating the radius with the highest signal-to-noise value. This radius, also listed in table 3.5, is indicated in the top plots by the cross. The dotted lines in the top plots show the model profiles used to extrapolate the flux measured at this radius to the total cluster flux. The r_{80} values for the two clusters are indicated by the vertical dashed lines in the top two plots.

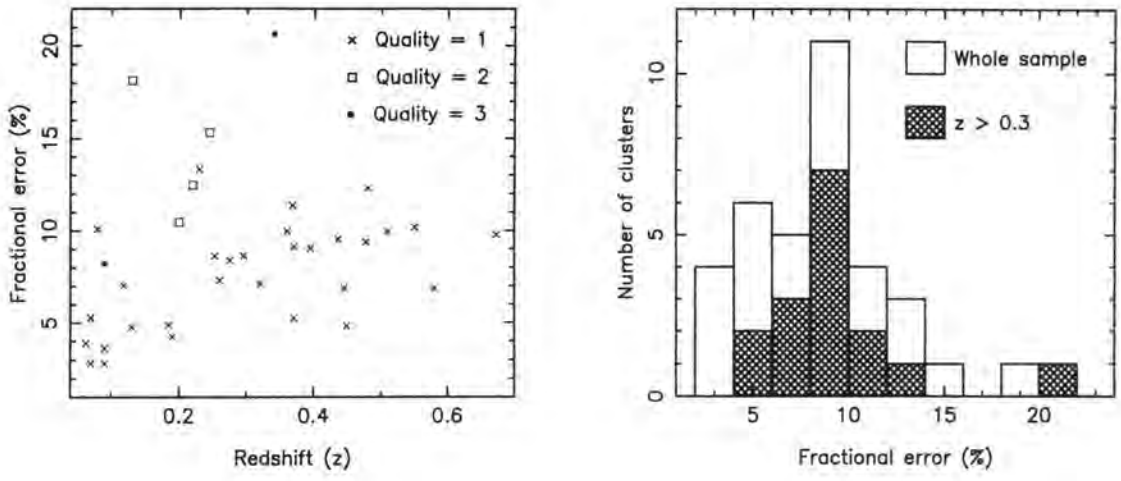

Figure 3.15: The left-hand plot shows the fractional Poisson error on the photons against the cluster redshift. The symbol type indicates the quality flag of each cluster. The right-hand plot shows the histogram of this distribution, for the whole cluster sample (open) and just for the high-redshift clusters (hatched).

The major contribution to the error on the cluster luminosity, as discussed in Section 3.2.2, is the Poisson error on the number of detected photons. Tables 3.6a and 3.6b list the number of source photons detected for each cluster, calculated over the areas used to estimate the cluster count rates. Figure 3.15 shows the fractional Poisson error plotted against redshift, where the symbol types indicate the quality flag of each cluster. The Figure also shows the histogram of this error distribution, for both the whole sample and the high-redshift ($z > 0.3$) sample. The median value for the whole cluster sample is 9%, whilst for the high-redshift cluster sample it is 10%.

3.2.2 Calculating the X-ray luminosity of a cluster

The conversion from a count rate to a flux requires assuming a model source spectrum. For temperatures greater than 2×10^7 K ($\sim$ 2keV), cluster emission is dominated by continuum radiation, rather than line emission (e.g. Section 1.2.2; Sarazin 1988). Therefore a redshifted thermal bremsstrahlung model has been used, rather than models which include line emission — such as the Raymond-Smith (Raymond & Smith 1977) and MEKAL (Mewe et al. 1985) codes. The absorption by Galactic material is accounted for by using the cross-sections of Morrison & McCammon (1983)

and Hydrogen column densities, $n_{\rm H}$, taken from the compilation of Marshall & Clark (1984). The only free parameter is the ICM temperature. Although clusters exhibit a range of temperatures (e.g. David et al. 1993; Mushotzky & Scharf 1997), the temperature was fixed at 6 keV, typical of low-redshift cluster samples. An alternative approach is to use a luminosity-temperature (LT) relation and iterate to obtain an estimate for the cluster temperature (e.g. Henry & Arnaud ; Ebeling et al. 1997). There are three reasons why this approach has not been used: the scatter in the LT relation is large — for a fixed luminosity the scatter in the temperature reaches 50% (David et al. 1993); the errors in the cluster luminosities are dominated by the Poisson errors on the photon counts rather than uncertainties in the temperature; and the flux in the ROSAT pass band is insensitive to the cluster temperature, changing by less than 3% over the temperature range $2 - 10$ keV for a cluster at a redshift of 0.4. This last point is shown in Figure 3.16, which plots the conversion factor for count rates to flux, $C(z,T)$. calculated using a Hydrogen column density typical of the survey. For clusters hotter than 2 keV, the value of $C(z,T)$ is within 3% of the assumed value ($T = 6$ keV) for $z \lesssim 1$. The calculated cluster fluxes, in the $0.5 - 2.0$ keV (ROSAT) rest-frame pass band, are listed in tables 3.6a and 3.6b, and Figure 3.17 plots them against the cluster redshifts. The errors shown in this Figure were calculated by adding, in quadrature, the photon errors and a 3% error, to account for the uncertainties in $C(z,T)$.

The cluster luminosity, L, is calculated from the flux, f, using

$$L = 4\pi d_{\rm L}^2(z)\, f\, k(z,T)\,, \tag{3.4}$$

where $d_{\rm L}(z)$ is the luminosity distance of the cluster (e.g. Weinberg 1972) and $k(z,T)$ is the k-correction, which converts the ROSAT rest-frame luminosity into the cluster rest-frame luminosity. To remain consistent with earlier choices, the k-correction was calculated using a 6 keV thermal bremsstrahlung spectrum. Although the exact value was used when calculating the luminosities, it was found that the k-correction is well approximated by the function $(1+z)^{-0.39}$, being within 0.3% of the true value for redshifts less than one. This functional form corresponds to a power-law spectrum with an energy index of 0.61. Figure 3.18 shows the sensitivity of the

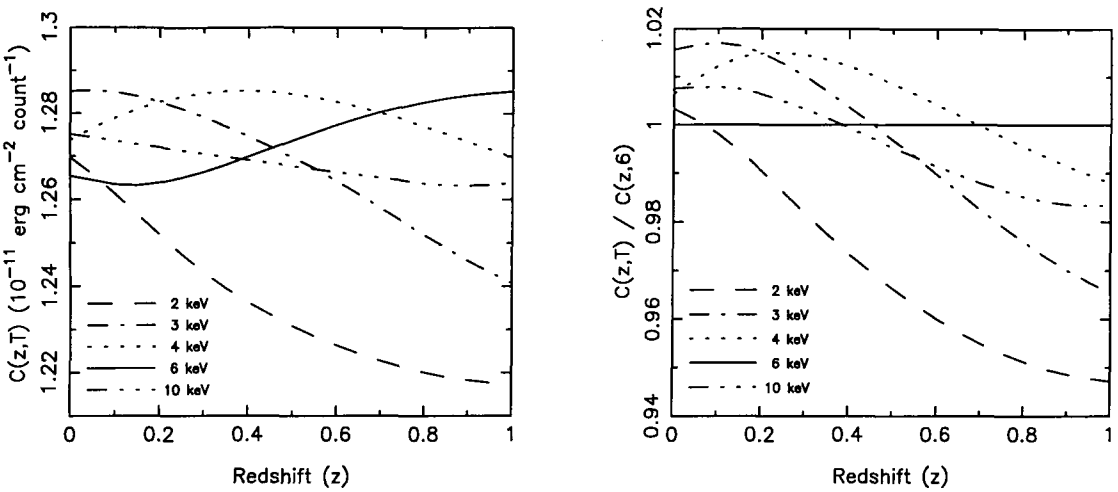

Figure 3.16: The left-hand plot shows the variation of the conversion factor, $C(z,T)$, with redshift, for a range of ICM temperatures, T. $C(z,T)$ converts cluster count rates, in counts s^{-1}, into fluxes, in erg cm^{-2} s^{-1}, and has been calculated using a n_H value of 3.6×10^{20} cm^{-2}, which is a typical value for the survey. The right-hand plot shows the difference in the conversion factor relative to the 6 keV model, for a range of cluster temperatures.

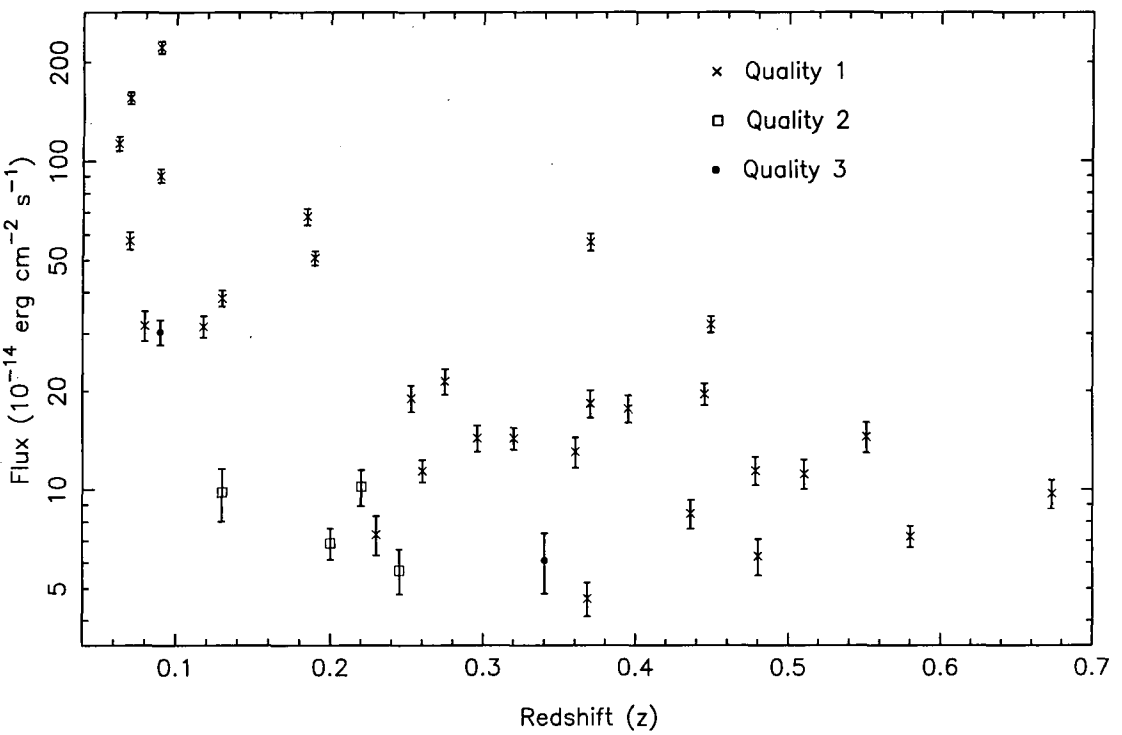

Figure 3.17: The measured cluster flux, in the $0.5 - 2.0$ keV pass band, plotted against cluster redshift. The symbols indicate the quality flag of each cluster. The errors have been calculated by adding, in quadrature, the fractional error due to the number of detected photons and a 3% error to account for the uncertainties in $C(z,T)$.

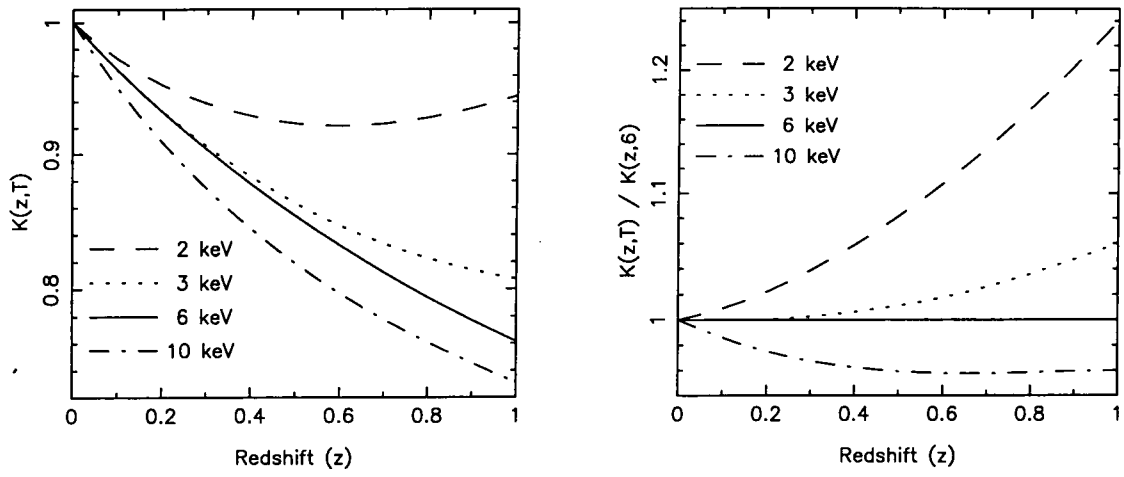

Figure 3.18: The left-hand plot shows the variation of the k-correction, $k(z,T)$, with redshift, for a range of ICM temperatures, T. The right-hand plot shows the difference in the k-correction for a range of cluster temperatures, relative to the 6 keV model.

k-correction to the assumed cluster temperature, where the right-hand plot shows how the k-correction varies relative to the 6 keV model. For a fixed redshift, the variation of the k-correction, with temperature, reaches 20%, at high redshift and low temperatures, although a more realistic value is 5%.

Since the cluster flux, f, is just the count rate multiplied by $C(z,T)$, the overall uncertainty in the luminosity due to assuming a fixed temperature depends on $C(z,T) \times k(z,T)$. This function is shown plotted against redshift, for a range of temperatures, in the top-left plot of Figure 3.19. The top-right plot shows how the function changes relative to the assumed 6 keV value. For temperatures in the range 2 to 10 keV and redshifts less than 0.8, the luminosity varies between 95% and 110% of the calculated value; if the temperature range is restricted to 3 to 6 keV, the difference is only 2%. The bottom-two plots of this Figure use a k-correction which converts the ROSAT count rate into a flux in the 0.3 – 3.5 keV (EMSS) cluster rest-frame pass band ($k_{\rm E}(z,T)$). The error in the luminosity to account for the use of a fixed temperature has been estimated as 5% for both the ROSAT and EMSS pass bands.

Luminosities for both the 0.5 – 2.0 keV and 0.3 – 3.5 keV cluster rest-frame pass bands are plotted in Figure 3.20. The clusters have similar luminosities to the

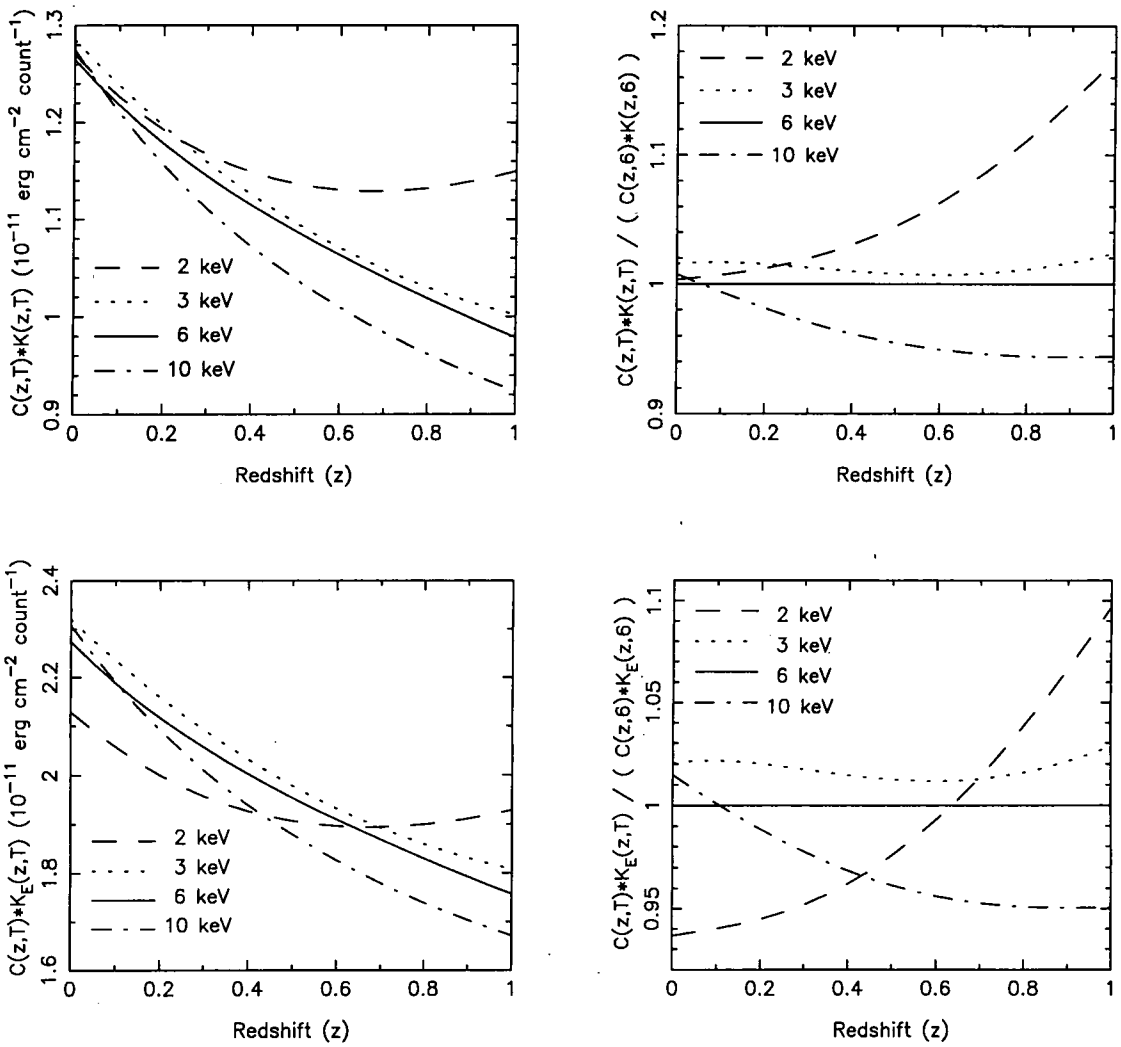

Figure 3.19: The left-hand plots show the variation of $C(z,T)\times k(z,T)$ with redshift, for a range of ICM temperatures, T. The top plot is for the k-correction in the ROSAT pass band ($k(z,T)$), whereas the bottom plot is for the k-correction in the EMSS pass band ($k_{\rm E}(z,T)$). The right-hand plots show the differences in these functions relative to the 6 keV model, for a range of cluster temperatures.

clusters found in the RIXOS survey and are up to three times less luminous than the clusters in the EMSS. Tables 3.6a and 3.6b list the fluxes and luminosities of the clusters, along with the other parameters described in this Section. The errors in the luminosities have been calculated by adding, in quadrature, the fractional error due to the photon counts and a 5% error to account for the use of a single cluster temperature: for most of the clusters, the value is dominated by the Poisson error on the photon counts.

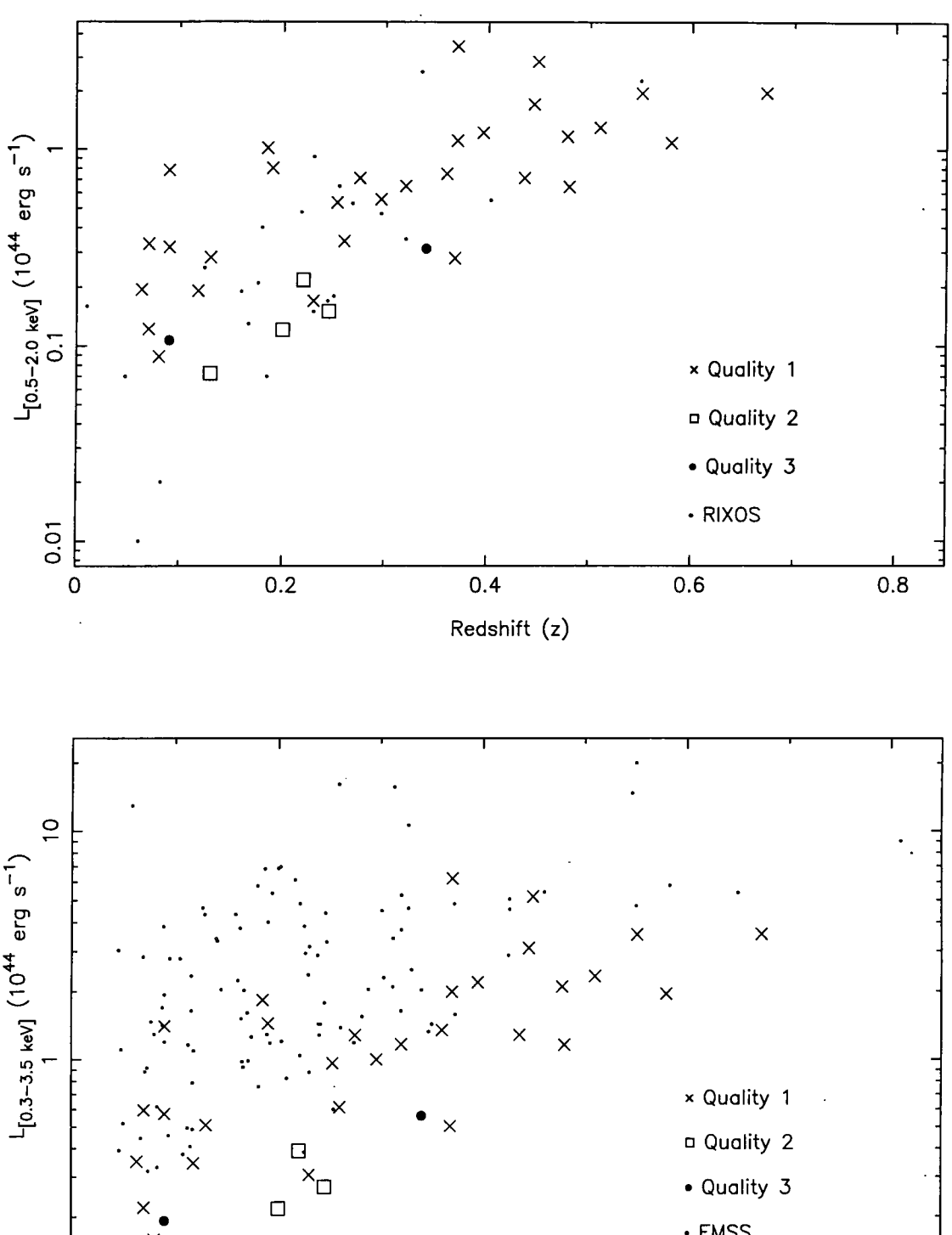

Figure 3.20: The top plot shows the luminosities, in the $0.5 - 2.0$ keV pass band, plotted against cluster redshift. Also plotted are the clusters detected in the RIXOS survey (Castander 1996). The bottom plot is for luminosities in the EMSS pass band, $0.3 - 3.5$ keV, and also shows the EMSS clusters (Gioia & Luppino 1994).

Name	z	r_{80} (arcmin)	Area (%)	$n_{\rm ph}$	Corrected count rate (count s^{-1})	$n_{\rm H}$	f_{14}	$\delta L/L$	L_{44} (ROSAT)	L_{44} (EMSS)	QF
RX J0318.2 – 0301	0.370	3.34	74	120.5	0.01362	5.67	18.28	0.104	1.110	1.995	1
RX J0318.5 – 0303	0.373	3.34	86	364.0	0.04237	5.67	56.85	0.072	3.453	6.204	1
RX J0321.9 – 5119	0.070	11.27	44	1264.2	0.12772	2.25	155.57	0.057	0.331	0.594	1
RX J0333.0 – 3914	0.245	4.22	95	42.5	0.00466	2.33	5.69	0.161	0.150	0.270	2
RX J0334.0 – 3901	0.063	12.38	60	664.3	0.09265	2.33	113.12	0.063	0.195	0.350	1
RX J0337.7 – 2522	0.577	2.77	83	213.0	0.00598	1.57	7.21	0.085	1.085	1.949	1
RX J0416.7 – 5525	0.365	3.41	73	100.7	0.01074	2.07	13.06	0.112	0.751	1.348	1
RX J0505.3 – 2849	0.509	2.93	86	101.0	0.00926	1.73	11.19	0.111	1.298	2.333	1
RX J0530.5 – 5852	0.338	3.48	100	23.5	0.00485	3.26	6.10	0.212	0.312	0.561	3
RX J0858.4 + 1357	0.485	2.98	98	66.1	0.00484	4.26	6.28	0.133	0.645	1.158	1
RX J0946.5 – 1410	0.230	4.44	64	56.6	0.00553	5.23	7.30	0.142	0.170	0.305	1
RX J0947.9 + 0730	0.128	6.68	88	30.3	0.00769	4.02	9.82	0.188	0.072	0.130	2
RX J1142.0 + 1009	0.118	7.21	83	202.0	0.02620	1.80	31.50	0.086	0.191	0.344	1
RX J1142.2 + 1027	0.070	11.25	83	359.1	0.04780	1.80	57.51	0.073	0.122	0.220	1

Table 3.6a: The X-ray fluxes and luminosities of the clusters, listed in order of ascending right ascension: r_{80} gives the radius of the aperture; Area gives the fraction of the aperture which remained after masking out contaminating sources; n_{ph} is the number of source photons within this aperture; the Corrected count rate column gives the cluster count rate, after correcting for the flux falling outside the aperture; $n_{\rm H}$ values are in units of 10^{20} cm^{-2} and are taken from the compilation of Marshall & Clark (1984); f_{14} is the cluster flux in units of 10^{-14} erg cm^{-2} s^{-1}, calculated using the corrected count rate values; and L_{44} is the cluster luminosity in units of 10^{44} erg s^{-1} (ROSAT indicates the $0.5 - 2.0$ keV pass band, EMSS the $0.3 - 3.5$ keV pass band). The error, $\delta L/L$, is the Poisson error on the number of source photons added, in quadrature, to a 5% error to account for uncertainties due to the use of a single temperature. The QF column indicates the quality flag of the cluster: 1 means that the count rate is calculated using the model background from Chapter 2; 2 means that the background came from an interactively-chosen annulus; and 3 means that the count rate was estimated from the point on the growth curve with the highest signal to noise. The co-ordinates of the clusters are given in tables 3.4a and 3.4b.

Name	z	r_{80} (arcmin)	Area (%)	$n_{\rm ph}$	Corrected count rate (count s^{-1})	$n_{\rm H}$	f_{14}	$\delta L/L$	L_{44} (ROSAT)	L_{44} (EMSS)	QF
RX J1200.8 − 0328	0.395	3.26	95	122.1	0.01397	3.38	17.64	0.103	1.222	2.196	1
RX J1204.3 − 0351	0.262	4.07	85	187.9	0.00906	3.51	11.44	0.088	0.341	0.613	1
RX J1205.0 − 0333	0.368	3.36	96	77.3	0.00368	3.51	4.66	0.124	0.280	0.503	1
RX J1205.6 − 0338	0.207	4.89	51	91.0	0.00546	3.51	6.88	0.116	0.121	0.217	2
RX J1227.2 + 0858	0.090	9.03	70	761.2	0.07524	1.75	90.36	0.062	0.318	0.572	1
RX J1227.4 + 0850	0.089	9.05	37	1264.6	0.18513	1.75	222.31	0.057	0.783	1.407	1
RX J1235.6 + 1311	0.253	4.20	62	134.1	0.01582	1.68	18.97	0.100	0.535	0.962	1
RX J1253.2 + 1556	0.275	3.96	94	141.9	0.01761	2.07	21.36	0.098	0.713	1.281	1
RX J1259.7 − 3236	0.076	10.03	47	98.0	0.02384	5.58	31.76	0.113	0.088	0.159	1
RX J1325.0 − 3814	0.296	3.77	91	133.9	0.01082	5.33	14.35	0.100	0.556	0.998	1
RX J1325.5 − 3826	0.445	3.06	93	212.7	0.01465	5.33	19.52	0.085	1.721	3.091	1
RX J1338.0 − 2944	0.189	5.04	83	557.1	0.03898	4.69	50.74	0.066	0.804	1.444	1
RX J1345.2 − 0009	0.087	9.05	53	147.2	0.02432	3.14	30.35	0.096	0.107	0.192	3
RX J1354.2 − 0222	0.551	2.88	93	96.1	0.01125	3.99	14.51	0.114	1.967	3.534	1
RX J2038.4 − 0125	0.673	2.65	94	104.7	0.00713	5.98	9.73	0.110	1.975	3.548	1
RX J2106.8 − 0510	0.449	3.13	79	431.8	0.02423	5.00	32.02	0.069	2.873	5.162	1
RX J2108.8 − 0517	0.320	3.63	86	196.7	0.01089	5.00	14.33	0.087	0.649	1.166	1
RX J2114.3 − 6801	0.130	6.69	83	442.8	0.03084	3.03	38.35	0.069	0.283	0.508	1
RX J2137.8 − 4251	0.185	5.13	76	417.5	0.05585	2.22	67.94	0.070	1.020	1.832	1
RX J2155.9 + 0109	0.219	4.53	83	64.3	0.00785	4.65	10.21	0.134	0.217	0.390	2
RX J2202.7 − 1902	0.436	3.09	93	110.2	0.00681	2.69	8.44	0.108	0.714	1.283	1
RX J2359.5 − 3211	0.478	2.97	100	113.7	0.00953	1.56	11.46	0.106	1.166	2.096	1

Table 3.6b: Continued.

Chapter 4

Constraints on the evolution of X-ray clusters

Chapter 1 introduced the idea that clusters of galaxies can be used as cosmological probes. This Chapter compares various properties of the cluster catalogue, presented in Chapter 3 and referred to as the Southern Serendipitous High-redshift Archival ROSAT Cluster (SHARC) catalogue, with the predictions of various models of structure evolution. Section 4.1 describes the models used; for simplicity an Einstein-de Sitter universe is assumed. Section 4.2 discusses the present evidence for evolution of X-ray clusters before describing, in detail, the constraints that the Southern SHARC catalogue places on such evolution, using several tests: the number counts and $V/V_{\rm max}$ distribution (Section 4.2.1); the redshift distribution (Section 4.2.2); and the high-redshift XLF (Section 4.2.3). Section 4.3 concludes the Chapter, presenting the results drawn from the previous Sections.

4.1 Theoretical models

As described in Section 1.1, the standard picture of structure formation assumes that gravitational instability of small, primordial density fluctuations leads to the

structures observed in the present-day universe. At early epochs the density field is taken to follow a Gaussian distribution, with fluctuations at all scales. In a universe dominated by CDM, structure formation is a bottom-up process: the first objects to form are small, and as the universe evolves, larger, more massive, objects form. The discussion presented here is limited to the X-ray properties of clusters. More general descriptions of structure-formation theories can be found in a wide variety of text books (e.g. Peebles 1980; Peebles 1993; Padmanabhan 1993; Coles & Lucchin 1995).

Clusters of galaxies are the largest, and hence most massive, objects to have decoupled from the Hubble flow. In the above picture, they are the most recent objects to have formed, and so their properties should be closely related to the initial cosmological conditions; processes other than gravity are generally assumed to have had little effect on cluster evolution. Whilst this is valid for the gravitationally-dominant collisionless dark matter, it is not such a useful approximation for the collisional gaseous component, as discussed below. Since the fluctuations from which clusters form are rare, and hence in the tail of the probability distribution, clusters are very sensitive probes of the fluctuation spectrum.

Whilst the initial growth of a perturbation can be solved analytically (e.g. Peebles 1980), once a perturbation has collapsed, the only way to follow the evolution is to use numerical techniques (e.g. Evrard 1990; Cen & Ostriker 1994; Bryan et al. 1994; Navarro, Frenk & White 1995). Current computational techniques can not cope with the huge range in scales — of time, length, and mass — necessary to accurately simulate the general cluster population. Therefore, a common approach is to use analytic approximations to the growth of mass condensations, and use physically-motivated relations to predict the form of the observable cluster population from the mass distribution. The discussion below focuses on some of the more popular approaches in the literature.

Kaiser (1986) discussed cluster evolution in an Einstein-de Sitter universe, in which the density fluctuations can be described by a scale-free power spectrum, with spectral index n. It was assumed that non-gravitational forces could be neglected, so that there is no physical scale in the growth process, other than the mass, or

length, of the fluctuations collapsing at any given epoch — the self-similar model. With such assumptions it is possible to predict, in a statistical sense, the evolution of the density field by suitably scaling the present-day density field. Whilst this field is not known, the scaling procedure can be applied to an observable distribution function, such as clusters of galaxies, so long as no physical scale is used to define the parameters of the function. If the following characteristic values of the density field are measured within a surface of given density contrast, then the mass M_*, density ρ_*, virial temperature T_*, and number density N_*, scale with redshift as:

$$M_* \propto (1+z)^{-6/(n+3)}, \tag{4.1}$$

$$\rho_* \propto (1+z)^3, \tag{4.2}$$

$$T_* \propto (1+z)^{(n-1)/(n+3)}, \tag{4.3}$$

$$N_* \propto (1+z)^{6/(n+3)}. \tag{4.4}$$

As the X-ray emission from clusters is mainly due to thermal bremsstrahlung radiation, the characteristic luminosity is given by (e.g. equation 1.5)

$$L_* \propto \rho_* M_* {T_*}^{\alpha} \propto (1+z)^{(\alpha(n-1)+3(n+1))/(n+3)}, \tag{4.5}$$

where the value of α depends on whether the luminosity is measured in a low-energy pass band ($\alpha \approx 0$), such as that of ROSAT, or a bolometric pass band ($\alpha = 0.5$). Combining the results of equations (4.4) and (4.5), the cumulative cluster XLF at a redshift z can be found by scaling the zero-redshift relation by:

$$\Delta \log L = \left(\frac{\alpha(n-1)+3(n+1)}{n+3}\right) \log(1+z), \tag{4.6}$$

$$\Delta \log N = \left(\frac{6}{n+3}\right) \log(1+z), \tag{4.7}$$

as given by Kaiser (1986, 1991) for $\alpha = 0.5$.

For realistic power spectra, these scaling relations predict that the luminosity varies slowly with redshift, whilst the number density increases strongly. Therefore the self-similar models predict strong positive evolution, in that the amplitude of the XLF increases with look-back time. Although, as discussed in Section 4.2, there is no consensus on the degree of XLF evolution, the current discussion concentrates

on whether there is negative (e.g. Edge et al. 1990; Henry et al. 1992; Castander et al. 1995), or no (e.g. Ebeling et al. 1997; Collins et al. 1997; Nichol et al. 1997) evolution. The self-similar model is not in agreement with the data.

There is therefore interest in models which break the self-similar evolution of the gaseous component. Both Kaiser (1991) and Evrard & Henry (1991) present models in which the ICM is imprinted with an initial entropy at early epochs. If cooling of the gas is neglected, the entropy can not decrease, and the gas evolves adiabatically — its density being set by the virial temperature of the dark-matter potential. As the luminosity depends upon the density (e.g. equation 4.5), the change in behaviour of the gas density, compared to the self-similar case, means that the luminosity evolution is different from that given by equation (4.6). Kaiser (1991) and Evrard & Henry (1991) showed that these constant-entropy models produce negative evolution of the XLF, more in line with the data than the self-similar model. An attractive interpretation of these models is that the constant entropy is caused by an early injection of heat into the ICM from an early generation of supernovae. Evidence for a lack of evolution in both the luminosity-temperature relation and ICM metallicity (e.g. Mushotzky & Scharf 1997; Henry 1997) suggests that the thermal history of the gas is more complicated than assumed in the the self-similar model.

Bower (1997) has extended the analysis of Kaiser (1986) and Evrard & Henry (1991) to allow a range of models to be tested. For a monatomic gas, with a spatial distribution following the King profile, equation (1.9) with $\beta = 2/3$, the luminosity evolution is given by

$$\Delta \log L = \left(\alpha \left(\frac{n-1}{n+3} \right) + \frac{3(3-\epsilon)}{4} - \frac{9}{n+3} \right) \log(1+z)\,, \tag{4.8}$$

where ϵ determines the evolution of the entropy of the gas in the cluster core. Since the dark-matter haloes are assumed to grow self-similarly, the scaling of the number density of objects is given by equation (4.7). The advantage of this approach is that the value of ϵ is related to physical processes: values greater than zero mean that cooling of the gas dominates the gas evolution; a value equal to zero corresponds to a constant-entropy model; and values less than zero occur when the gas is heated during each generation of cluster collapse. Bower (1997) shows that this approach

includes the self-similar model of Kaiser (1986) for

$$\epsilon_{ss} = -\left(\frac{n+7}{n+3}\right) . \tag{4.9}$$

The relation presented in equation (4.8) is based on the assumption that the gas is confined within the virialised dark-matter halo. As shown in Figure 4.6, the region of parameter space for which this condition is not true does not affect the models used in Section 4.2.

An alternative approach is to use an analytic function to predict the distribution of dark-matter haloes with mass at a given epoch, and then use a relation between mass and an observable quantity, such as luminosity, to predict the observed distribution function. Two popular approaches are the Press-Schechter method (Press & Schechter 1974; Bond et al. 1991; Bower 1991; Lacey & Cole 1993) and the peaks formalism (Bardeen et al. 1986; Manrique & Salvador-Solé 1995; Bond & Myers 1996). The basic premise of these theories is that the distribution of dark-matter haloes can be associated with peaks in the smoothed density field, where the object mass is related to the smoothing length. The Press-Schechter approach is commonly used because of its simplicity, and because its predictions agree remarkably well with those of numerical simulations (e.g. Efstathiou et al. 1985; Lacey & Cole 1994; Eke et al. 1996). Henry et al. (1992), extending the Press-Schechter based formalism of Henry & Arnaud (1991), derive an analytic form for the cluster XLF at a given redshift, assuming that the gas density depends on the cluster mass, so that

$$\rho_* \propto M^{1/4}(1+z)^3 , \tag{4.10}$$

rather than as given by the self-similar model (equation 4.2). The motivation for this additional dependence is that it predicts a luminosity-temperature relation with a slope in agreement with the observed, local, value (Henry & Arnaud 1991). Using a conversion factor between the bolometric and $0.5-2.0$ keV pass bands (Henry 1997, private communication), equation (6) of Henry et al. (1992), which gives the differential cluster XLF at a luminosity L, and redshift z, becomes

$$\begin{aligned} n(L,z) &= 1.74\times10^{-6}(1+z)(1+z_f)^{(3-n)/3}\mathcal{K}^{(3+n)/2}\mathcal{L}^{(9n-111)/84}(3+n)\sqrt{\mathcal{G}(n)} \\ &\quad \times \exp\left\{-3.1(1+z)^2(1+z_f)^{-2(3+n)/3}\mathcal{K}^{(3+n)}\mathcal{L}^{9(n+3)/42}\mathcal{G}(n)\right\} , \end{aligned} \tag{4.11}$$

where

$$\begin{aligned} \mathcal{G}(n) &= \frac{2^n n(1-n)(3-n)(2+n)}{\Gamma(3+n)\sin(n\pi/2)}, \\ \mathcal{K} &= 9.5k_0/h, \\ \mathcal{L} &= L/4.13, \end{aligned}$$

L is measured in units of 10^{44} erg s^{-1} in the $0.5-2.0$ keV pass band, and the late-collapse approximation ($z_f = z$) is assumed. Henry et al. (1992) found that the EMSS data could be fit by $n = -(2.10^{+0.27}_{-0.15})$ and $k_0 = 0.029^{+0.008}_{-0.013}$ hMpc^{-1}. This approach is one of several which break the self-similar scaling relations by assuming that the gas density is related to the mass of the dark-matter halo (e.g. Evrard & Henry 1991; Cavaliere, Colafrancesco & Menci 1993; David et al. 1993). One interpretation of such models is that there is a decrease in the efficiency of galaxy formation with increasing richness (Arnaud et al. 1992; David & Blumenthal 1992).

For a scale-free XLF, the scaling models presented above allow the possibility of a non-evolving XLF, where the change in space density of clusters due to the expansion of the universe is exactly balanced by the change in luminosity due to the gravitational growth of structures. Although more realistic XLFs include a break at high luminosities, such as those discussed in Section 4.2, this approximation is valid for luminosities less than the break, where the distribution can be fit reasonably well by a power law. Such a model is motivated by the current uncertainty in the amount of XLF evolution present in the cluster population, mentioned previously and discussed in depth below.

4.2 Comparing the models to the data

This Section begins with a review of the current evidence for evolution in the X-ray properties of clusters. There is currently no clear picture of what the data mean; the discussion below begins with the conclusions drawn from pre-ROSAT datasets, and then compares them to the results from cluster samples observed with ROSAT. Sections 4.2.1, 4.2.2, and 4.2.3 discuss the properties of the Southern

SHARC catalogue — the number counts, together with the $V/V_{\rm max}$ distribution, the redshift distribution, and high-redshift XLF respectively — with the aim of testing these results.

Currently the largest sample of X-ray selected, high-redshift clusters is that of the *Einstein* EMSS (Henry et al. 1992; Gioia & Luppino 1994; Nichol et al. 1997). Initial evidence for evolution in the X-ray properties of the EMSS clusters was presented in Gioia et al. (1990a), although this has now been superseded by the analysis of Henry et al. (1992), which showed that the high redshift XLF had a steeper slope than at low redshifts. The difference is significant at the 3σ level, and suggests that there has been significant evolution between redshifts of 0.17 and 0.33, the median redshifts of the two shells. The re-analysis of the sample by Nichol et al. (1997) is discussed later in this Section. The form of this evolution — the number density of luminous clusters decreasing with redshift — is in agreement with that seen by Edge et al. (1990). The details are, however, different: the evolution is seen at much lower redshifts ($z \sim 0.1$) and at higher luminosities ($\gtrsim 5 \times 10^{44}$ erg s^{-1}) in the Edge et al. (1990) sample.

ROSAT-selected cluster samples allow the testing of these results by two complementary approaches: local cluster samples selected from the RASS, and distant cluster samples detected in the PSPC pointed-phase observations. The first approach allows the mapping of the local cluster X-ray population, with the aim of providing a well constrained XLF over a wide range of luminosities, whereas the faint-flux limits obtainable in the second approach mean that distant cluster samples can be constructed at luminosities several times fainter than possible in the EMSS, as illustrated in the bottom plot of Figure 3.20.

There are currently two available XLFs from X-ray-selected RASS cluster samples: the Brightest Cluster Sample (BCS) of Ebeling et al. (1997) and the ESO Key Project sample (ESO-KP; De Grandi 1996; De Grandi et al. 1997). The differential XLFs of both samples are well described by a Schechter function (Schechter 1976) of the form

$$\phi(L) = A_s \exp(-L/L_*)\, L^{-\alpha_s} . \qquad (4.12)$$

Survey	pass band (kev)	α_s	L_* (10^{44} erg s^{-1})	A_s (Mpc^{-3} (10^{44} erg s^{-1})$^{\alpha-1}$)
BCS	$0.5-2.0$	1.85	5.70	3.32
BCS	$0.3-3.5$	1.82	10.7	4.95
ESO-KP	$0.5-2.0$	1.35	2.78	4.49

Table 4.1: This table lists the values of the best-fit Schechter function, equation (4.12), for the BCS of Ebeling et al. (1997), and the ESO-KP cluster sample (De Grandi 1996; De Grandi 1997, private communication). The fits are made to $\simeq 180$ and $\simeq 110$ clusters, for the BCS and ESO-KP results respectively.

The parameters of the fits are given in table 4.1. For cluster luminosities close to 10^{44} erg s^{-1} the two samples agree; the flatter faint-end slope of the ESO-KP sample is likely to be due to differences in the selection techniques of the surveys (Ebeling et al. 1997; De Grandi 1997, private communication). As well as providing a well-determined low-redshift XLF which can be compared to the high-redshift cluster samples, these samples can be used to test for evolution in the local population. Ebeling et al. (1997) show that the BCS is consistent with no evolution of the XLF out to $z \simeq 0.2$. The evolution seen by Edge et al. (1990) is claimed to be due to a combination of their high flux limit and a lack of X-ray luminous clusters around $z \sim 0.15$ (Ebeling et al. 1995; Ebeling et al. 1997).

The first ROSAT-selected cluster sample to be able to examine the $z > 0.3$ population was the RIXOS cluster catalogue (Castander et al. 1995; Castander 1996). Castander et al. (1995) presented the results from 59 fully identified PSPC fields from the full survey of 81 fields. Over a survey area of 14.9 deg^2 they detected 278 X-ray sources to a flux limit of 3.0×10^{-14} erg cm^{-2} s^{-1} in the $0.5-2.0$ keV pass band. The catalogue contains 22 spectroscopically-confirmed clusters, ranging from a redshift of 0.01 to 0.55, and from the unidentified sources there is only one other source which could be a cluster, which has been tentatively identified as being at $z \sim 1.0$. Figure 3.20 shows that the RIXOS clusters have similar luminosities to those in the Southern SHARC catalogue.

Castander et al. (1995) compared the redshift distribution of the $z \geq 0.2$ RIXOS

clusters to theoretical predictions, using models similar to those discussed in Section 4.1. Using the Edge et al. (1990) estimate of the local XLF, they showed that the catalogue was not consistent with a no-evolution model, being well fit by a constant-entropy model. Castander et al. (1995) claim that the negative evolution seen in the RIXOS cluster catalogue extends to lower luminosities that seen in the EMSS (Henry et al. 1992). Bower (1997) reports that the degree of evolution seen in the RIXOS catalogue is consistent with a 40% fall in the XLF amplitude at a luminosity of 10^{44} erg s^{-1}. Although the results are somewhat dependent upon the form of the local XLF, Castander (1996) reports that the predictions are not significantly affected by changes to the local XLF.

However, a recent re-analysis of the EMSS sample by Nichol et al. (1997), using both the updated catalogue presented by Gioia & Luppino (1994) and new flux determinations from ROSAT PSPC observations, reduces the significance of the differences in the slope of the high and low redshift EMSS XLFs. The result is that a no-evolution model is consistent with the EMSS data. Another piece of evidence for mild, or no, evolution in the cluster population is the lack of evolution in the luminosity-temperature relation out to $z \sim 0.4$ (Henry, Jiao & Gioia 1994; Donahue 1996; Mushotzky & Scharf 1997; Henry 1997). There has also been a claim that the lack of high-redshift clusters in the RIXOS catalogue is due to biases in the detection method, rather than because of cluster evolution (Scharf et al. 1997). The log N-log S distribution of two other ROSAT-selected, distant cluster catalogues (RDCS; WARPS) have recently been used to constrain cosmological models (Kitayama & Suto 1997; Mathiesen & Evrard 1998; Kitayama, Sasaki & Suto 1998). The results are consistent with little evolution in the cluster population at recent epochs.

In the Sections below, the Southern SHARC catalogue is used to test the evolution seen in the RIXOS cluster sample, and to put constraints on the evolutionary models described in Section 4.1. The calculations assume that the survey selection function is well approximated by the results of the simulations presented in Section 2.3: possible biases due to changes of cluster X-ray surface-brightness profiles

with either luminosity or redshift (Section 2.3), or incompleteness introduced by the optical identification process (Section 3.1.1) have been ignored.

4.2.1 The cluster number counts and $V/V_{\rm max}$ distribution

The calculation of the integrated number counts — the number of clusters above a given flux limit per unit area, commonly referred to as $N(>S)$ — requires knowledge of the survey area over which each cluster is visible. The results of the simulations presented in Section 2.3 include $\Omega(L,z)$, the area over which a cluster with luminosity L and redshift z is visible (e.g. Figure 2.17). Using equation 2.8, Ω can be parameterised by flux rather than luminosity, and will be labelled, in this section, as $A(S,z)$ — where S indicates the total cluster flux (i.e. the measured value corrected for flux falling outside the aperture).

If the clusters are placed in order of descending flux, the integrated cluster number counts, $N(>S)$, can be calculated using

$$N(>S) = \sum_{S_i>S} \frac{1}{A(S_i,z_i)}, \tag{4.13}$$

where S_i and z_i are the total flux and redshift of cluster number i. Applying this equation to the Southern SHARC catalogue produces the distribution shown as solid squares in Figure 4.1. The error bar on the faintest point has been calculated assuming poisson statistics (Gehrels 1986), giving $N(>S) = 3.17^{+0.62}_{-0.53}$ deg^{-2} at a flux of 4.7×10^{-14} erg cm^{-2} s^{-1}. No correction has been applied to account for the high-flux clusters that are missing from the catalogue because of the small survey area.

The crosses in Figure 4.1 show the corresponding $N(>S)$ distribution for the WARPS catalogue (Jones, private communication). Whilst the surveys are similar at the faint end — at a flux of 6×10^{-14} erg cm^{-2} s^{-1} the WARPS survey has a cluster number density of 1.9 ± 0.4 deg^{-2} compared to 2.7 ± 0.5 deg^{-2} for the Southern SHARC catalogue — the distributions are different, since the WARPS points lie below the Southern SHARC points at all fluxes.

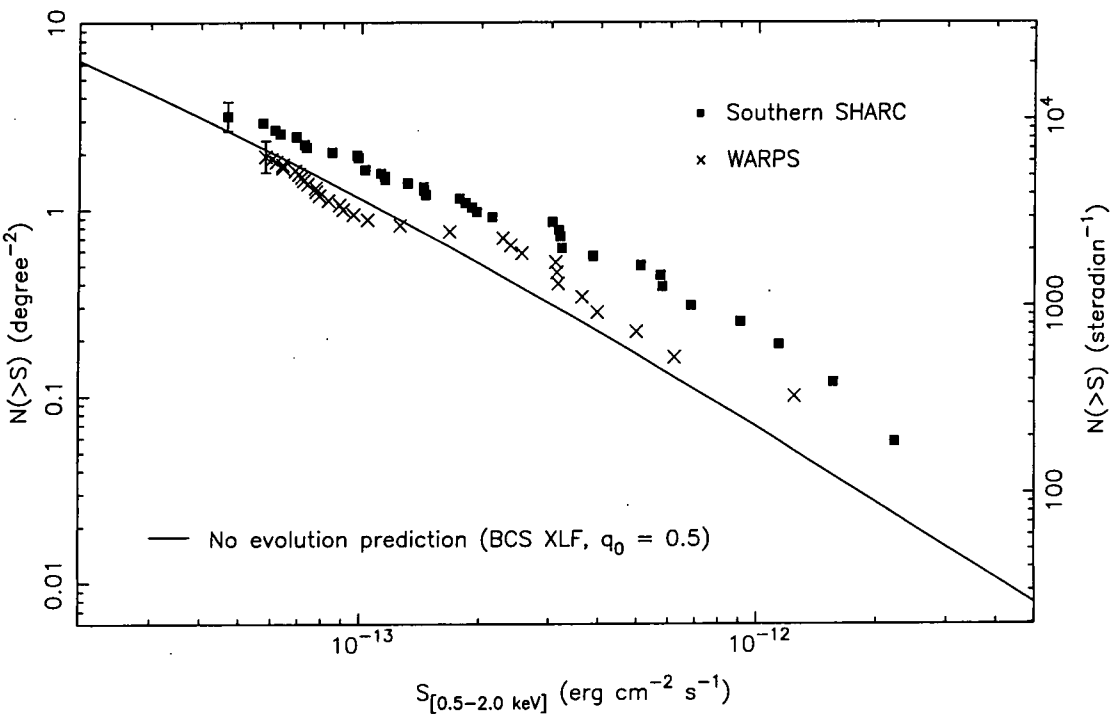

Figure 4.1: The solid squares show the log N–log S distribution for the Southern SHARC catalogue, the crosses give the WARPS distribution (Jones, private communication), and the error bars on the faintest points indicate poisson errors. A non-evolving cluster population would produce a distribution indicated by the solid line, assuming the BCS XLF and $q_0 = 0.5$.

The expected number-counts relation can be computed given a model for the evolution of the cluster XLF with redshift, $\phi(L,z)$, by

$$N_{\rm pred}(>S) = \int_{z=0}^{\infty} \int_{L(S,z)}^{\infty} \phi(L,z)\,{\rm d}V(z)\,{\rm d}L\,{\rm d}z\,, \tag{4.14}$$

where ${\rm d}V(z)$ is the volume per unit area at a given redshift, z, and $L(S,z)$ is the luminosity of a cluster with flux S when placed at that redshift. The solid line in Figure 4.1 shows the prediction for a non-evolving cluster population, where $\phi(L,z) \equiv \phi(L,0)$. The local XLF was chosen to be that of the BCS (Ebeling et al. 1997), q_0 was set to 0.5, and the luminosity and redshift ranges of the calculation were limited to those used by Jones et al. (1998): $L = 10^{42} - 10^{47}$ erg s^{-1} and $z = 0 - 2$. Changing these limits only affects the prediction at fluxes fainter than those probed by either survey. Figure 4.1 shows that the Southern SHARC survey lies above the non-evolving prediction, whereas the WARPS distribution is consistent with the prediction, as discussed by Jones et al. (1998). The reason for the small discrepancy between the predictions shown in Figure 4.1 and Figure 2 of Jones et al. (1998) is due to their use of XLF parameters slightly different to that given in Ebeling et al. (1997).

Since the difference in the two distributions is most noticeable at high fluxes — i.e. mainly low-redshift clusters — the above analysis has been repeated for subsets of the Southern SHARC catalogue generated by excluding clusters below a given redshift, z_{min}. The non-evolving predictions where re-evaluated by starting the redshift integration at z_{min} rather than at zero. The results are shown in Figure 4.2 for $z_{min} = 0.1$, 0.15, and 0.2. It can be seen that removing the low-redshift clusters from the sample greatly improves the agreement with the model prediction: a comparison of the three graphs suggests that the excess in the $N(>S)$ distribution is removed by setting $z_{min} \simeq 0.15$. Possible reasons for the discrepancy at high fluxes will be discussed after deriving the $V/V_{\rm max}$ distribution of the catalogue.

The $V/V_{\rm max}$ distribution (Schmidt 1986; Avni & Bahcall 1980) provides a means of estimating the uniformity of the space distribution of a catalogue. For each object, the ratio of the survey volume enclosed by that object (V) to the maximum survey volume over which that object would be detectable ($V_{\rm max}$) is calculated. If

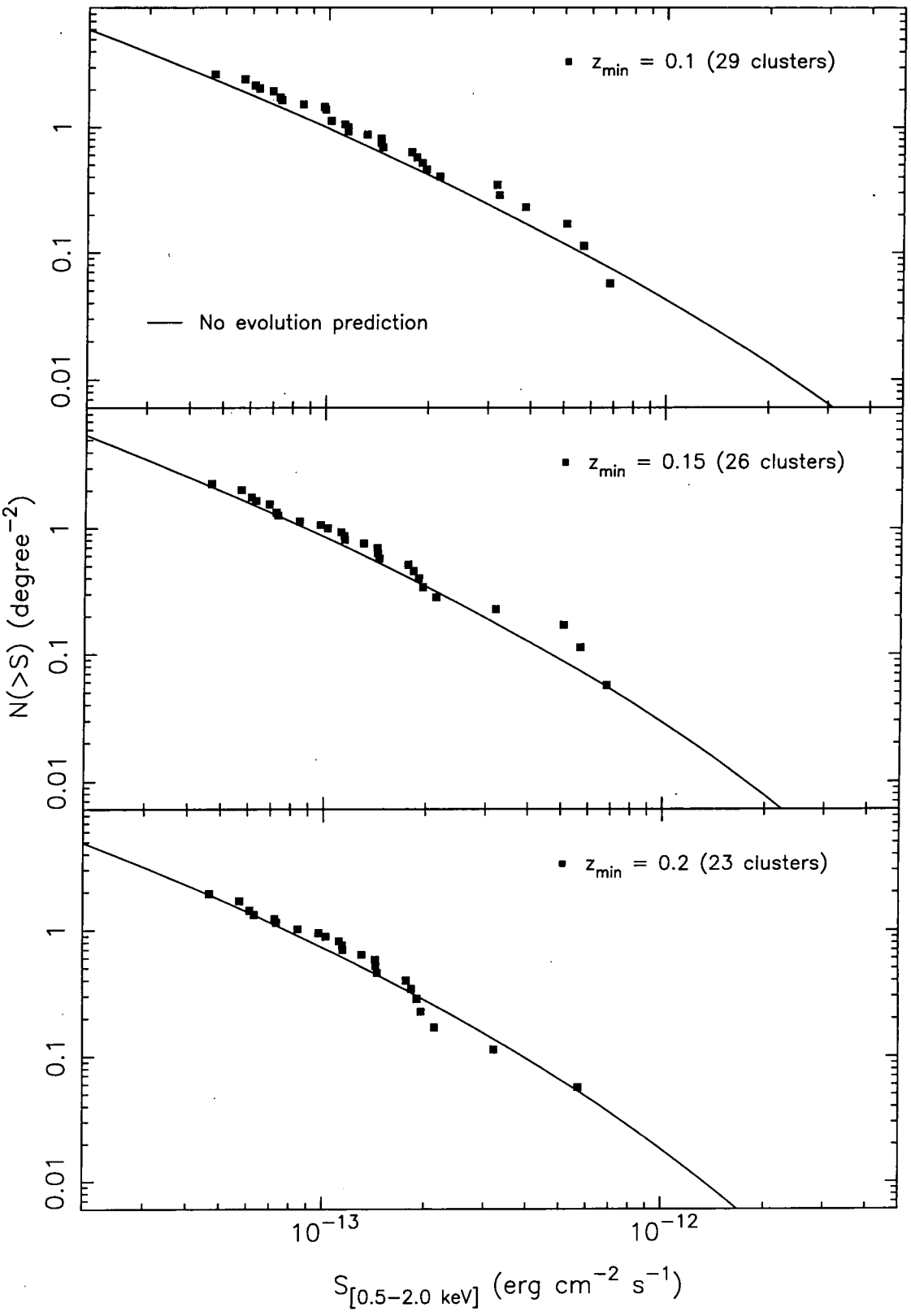

Figure 4.2: Each graph shows the log N–log S distribution for a subset of the Southern SHARC catalogue, generated by excluding all clusters with redshifts less than $z_{\rm min}$, together with the corresponding no-evolution prediction. The label in each graph indicates the value of $z_{\rm min}$ and the number of clusters in the sample.

the catalogue is uniformly distributed in space, the $V/V_{\rm max}$ values will be uniformly distributed in the range $0 < V/V_{\rm max} \leq 1$ with a mean of 0.5 and a variance of $(12N)^{-1}$, for a sample of N objects (Avni & Bahcall 1980).

Figure 4.3 shows the $V/V_{\rm max}$ distribution for the Southern SHARC.catalogue, which was calculated using equation 2.9, with $z_1 = 0$, to calculate both V (z_2 set to the cluster redshift) and $V_{\rm max}$ ($z_2 = \infty$) for each cluster. The top plot shows that the distribution of the whole catalogue is not uniform, and that removing low-redshift clusters produces a more uniform distribution. The bottom plot illustrates this point by showing $V/V_{\rm max}$ values as a function of redshift: there is an apparent excess of points with low values of both $V/V_{\rm max}$ and redshift when compared to the rest of the plot.

Two statistical tests have been used to see whether the differences between the high and low redshift samples are significant. Firstly, the mean $V/V_{\rm max}$ value, denoted $\langle V/V_{\rm max} \rangle$, has been compared to the expected value of 0.5 (Avni & Bahcall 1980). Secondly, the Kolmogorov-Smirnov test (e.g. Press et al. 1992) has been applied in order to check that the sample values are consistent with being uniformly distributed between 0 and 1 (e.g. Qin & Xie 1997; Dalcanton 1998). The results for both tests, when applied to several redshift-limited samples, are given in table 4.2: only when the low-redshift clusters ($z \lesssim 0.1$) are excluded is the catalogue consistent with a uniform distribution, at the greater than 95% confidence level.

Therefore both the number counts and the $V/V_{\rm max}$ distribution of the Southern SHARC catalogue are consistent with a non-evolving cluster population when the sample is restricted to $z \gtrsim 0.1$; the constraints on cluster evolution that can be derived from the $z \geq 0.2$ catalogue are discussed below (Sections 4.2.2 and 4.2.3). The low-redshift points are, however, not consistent with this picture — which disagrees with the results from the much larger low-redshift cluster samples selected from the RASS (Ebeling et al. 1997; De Grandi et al. 1997).

Two possible reasons for this low-redshift discrepancy are an enhancement in the number of clusters over the expected value, or over-estimation of the fluxes. An ex-

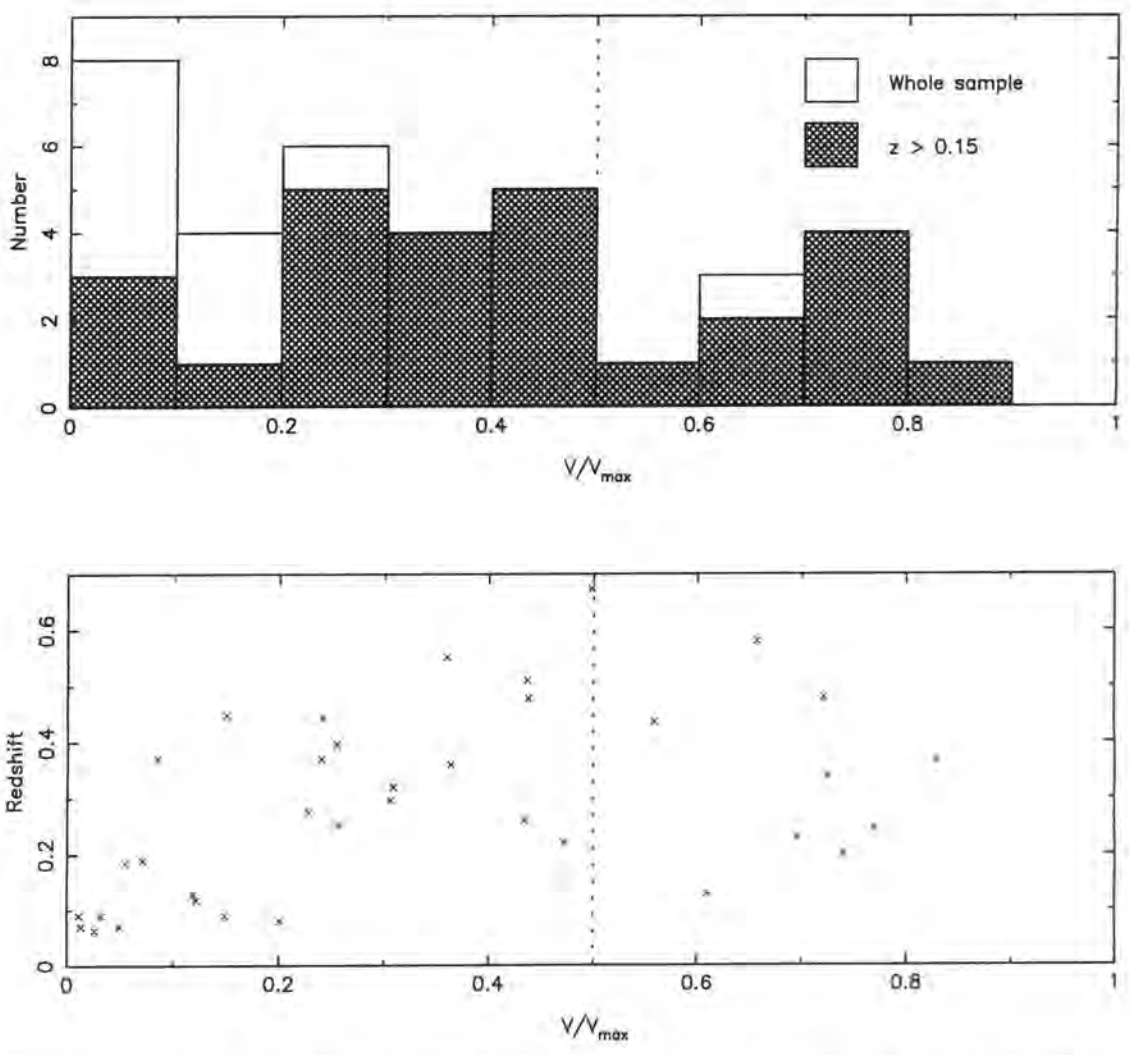

Figure 4.3: The top plot shows histograms of the $V/V_{\rm max}$ values obtained when using the whole Southern SHARC sample (open histogram) and a sample restricted to $z > 0.15$ (hatched histogram). The bottom plot shows the individual $V/V_{\rm max}$ points plotted against the cluster redshift. The dotted line indicates the expected mean value for a catalogue of objects which are uniformly distributed in space.

Sample	$N_{\rm clus}$	$\langle V/V_{\rm max}\rangle$	σ	D	$P_{\rm KS}$
Full	36	0.340	3.3	0.256	0.014
$z \geq 0.1$	29	0.405	1.8	0.197	0.187
$z \geq 0.15$	26	0.419	1.4	0.194	0.253
$z \geq 0.2$	24	0.449	0.9	0.189	0.324
$z \geq 0.3$	16	0.429	1.0	0.213	0.416

Table 4.2: Results of the two statistical tests applied to the $V/V_{\rm max}$ distribution for various redshift-limited samples of the Southern SHARC catalogue. The column labelled σ gives the number of standard deviations that the mean value ($\langle V/V_{\rm max}\rangle$) is away from the expected value of 0.5, when the variance is set to $(12N_{\rm clus})^{-1}$ (Avni & Bahcall 1980). The absolute value of the maximum difference between the cumulative distribution and that of a uniformly distributed sample is given in the column labelled D. This is used in the Kolmogorov-Smirnov test to calculate P_{KS}, the probability that the points are drawn from a uniform distribution.

cess of sources could be due to serious contamination of the catalogue by non-cluster objects — although this is unlikely since the majority of the low-redshift detections are clearly extended (Appendix B) — or because of the "second-generation serendipity effect" discussed in Section 2.2.4. Inspection of Figure 4.1 suggests that the fluxes would have to be over-estimated by $\sim 100\%$ to explain the difference. At $z \sim 0.1$, a flux of 4×10^{-14} erg cm^{-2} s^{-1} corresponds to a luminosity of $\sim 10^{42}$ erg s^{-1}, typical of groups, rather than clusters, of galaxies (e.g. Henry et al. 1995). As groups have core radii roughly five-times smaller than, and a similar distribution of β values to, clusters (Pildis, Bregman & Evrard 1995), the assumption of a surface-brightness profile typical of clusters could lead to systematic errors in the calculated fluxes. However, the maximum over-estimate is only 25% (equation 3.3 and Figure 3.9), unless the use of an over-sized aperture leads to the inclusion of emission from contaminating sources which have not been masked out. As the sources are too faint to have been detected in RASS cluster samples, it is currently not possible to compare the fluxes presented here with those from an independent survey. As the Southern SHARC catalogue is designed to study the high-redshift cluster population, the low-redshift population will not be investigated further.

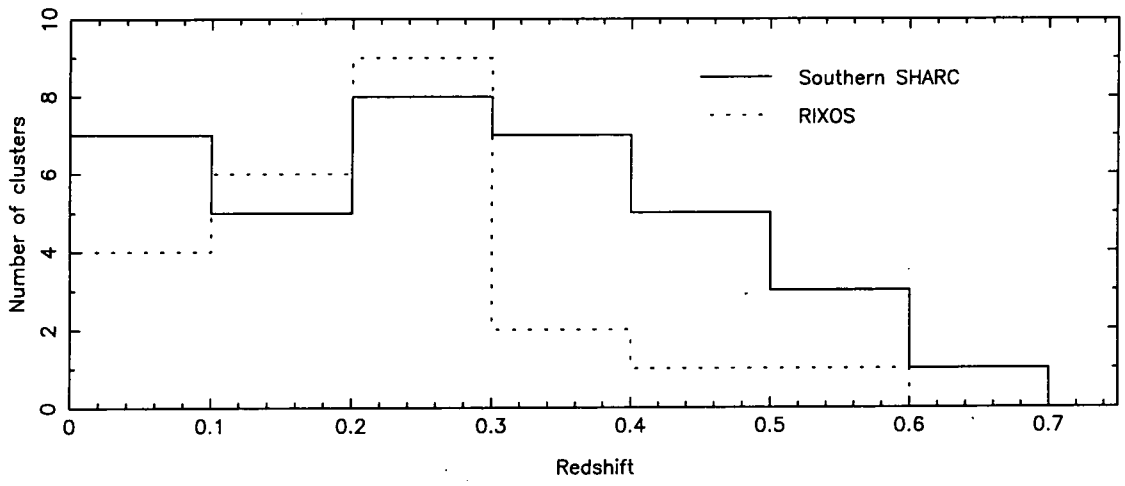

Figure 4.4: The solid line shows the redshift distribution of the Southern SHARC sample, using redshift bins of width 0.1. The dotted line shows the corresponding distribution for the RIXOS cluster sample, taken from Castander et al. (1995) and Castander (1996).

4.2.2 The redshift distribution of the Southern SHARC catalogue

The redshift distribution of the Southern SHARC cluster sample is shown in Figure 4.4, together with that of the RIXOS cluster catalogue (Castander et al. 1995; Castander 1996). Whilst the RIXOS cluster catalogue has a different selection function to the Southern SHARC catalogue, and covers a slightly smaller area — 14.9 deg^2 compared to 17.7 deg^2— it does reach a similar depth, and it is qualitatively obvious that the Southern SHARC catalogue contains more high-redshift clusters than the RIXOS cluster catalogue. Since it is the absence of such clusters that Castander et al. (1995) claim is evidence for negative evolution of the cluster population, it is important to quantify the significance of this difference.

The discussion presented below extends that presented in Collins et al. (1997); the main difference is that the selection function is calculated from the simulations presented in Section 2.3, rather than an analytic model. As in Castander et al. (1995), the analysis is restricted to clusters with redshifts greater than 0.2, both to ensure that uncertainties in the faint-end slope of the low redshift XLF (e.g. table 4.1) do not affect the results and because the low-redshift sample is not suited

to such analysis (Section 4.2.1).

For a given differential XLF, $\phi(L)$, the expected number of clusters in the Southern SHARC catalogue, in the redshift shell z_1 to z_2, is given by

$$\int_0^\infty V_{\max}(L)\,\phi(L)\,\mathrm{d}L\,, \tag{4.15}$$

where $V_{\max}(L)$ is the search volume available for a cluster of luminosity L in the redshift range z_1 to z_2, and is calculated using equation 2.9. For each model XLF, the expected number of clusters was calculated for the $z \geq 0.2$ redshift bins shown in Figure 4.4; the results are listed in table 4.3. For the comparisons discussed below, the errors on the model predictions have been neglected, since it is assumed that the Poisson errors on the observed number of clusters will dominate. Figure 4.5 compares several of these predictions to the observed redshift distribution.

The models used to create $\phi(L)$, for use in equation (4.15), have been chosen to illustrate the evolutionary behaviour of the models discussed in Section 4.1, and include:

No evolution model

If there is no evolution in the cluster XLF, then a local determination of the XLF can be used to calculate the expected number of clusters. Both the BCS and ESO-KP determinations of the XLF have been used; there is no significant difference between the two predictions. Whilst the models predict a flatter distribution than that observed, the overall number of clusters in the redshift range $z = 0.3 - 0.7$ agrees well with the observed value. This is in direct contrast to the result of Castander et al. (1995), who find that a no-evolution model, based on the local XLF of Edge et al. (1990), does not fit the RIXOS cluster redshift distribution.

Self-similar scaling

Assuming that the gas and dark matter evolve self-similarly, the scaling relations given in equations (4.6) and (4.7) have been applied to the BCS XLF. Two models were used: ssn1, which has $n = -1$, as in the standard CDM

model on cluster scales, and ssn2, which has a flatter power spectrum, with $n = -2$. Both models agree with the low-redshift bin, but show strong positive evolution at higher redshifts, which does not fit the observed distribution.

Constant entropy model

The BCS XLF has been scaled using equations (4.8) and (4.7), which assumes that the dark matter evolves self similarly, but the entropy of the gas in the cluster core remains constant with time, so $\epsilon = 0$. As with the self-similar model, two values of the spectral index have been used: e0n1 has $n = -1$ and e0n2 has $n = -2$. The $n = -1$ model shows good agreement with the observed distribution, unlike the $n = -2$ model, for which the flatter power spectrum leads to too much evolution at low redshifts.

Press-Schechter

The model presented in Henry et al. (1992), corrected to work in the $0.5 - 2.0$ keV pass band (equation 4.11), has been used to predict the cluster redshift distribution. For this calculation, the best-fit values of $n = -2.10$ and $k_0 = 0.029h$ Mpc^{-1} from Henry et al. (1992) have been adopted, and the results are labelled as EMSS in table 4.3. Whilst this model produces the best fit to the low redshift bin of all the models presented here, the evolution at higher redshifts is stronger than observed. However, over the redshift range $z = 0.3 - 0.7$, the predicted number of clusters is 8.7, only $\sim 2\sigma$ below the observed value.

Equations (4.7) and (4.8) were used to scale the BCS XLF, for a range of n and ϵ values, and a maximum-likelihood technique (Cash 1979) used to find the values which produced the best fit to the redshift distribution of the Southern SHARC catalogue. The best-fit values are $n = -2.2$ and $\epsilon = -4.6$, corresponding to reasonably strong heating of the ICM, but not as strong as that of the self-similar model, which has $\epsilon = -5.7$ for this value of the spectral index. Figure 4.6 shows the 68% and 90% confidence contours from this fitting procedure; for a CDM-like power spectrum, a constant entropy model lies within the one-sigma limits. Similar results were obtained using the ESO-KP XLF ($n = -2.0$ and $\epsilon = -3.1$); for the

Model	Number of clusters					
	$0.2-0.3$	$0.3-0.4$	$0.4-0.5$	$0.5-0.6$	$0.6-0.7$	$0.3-0.7$
S SHARC	$8^{+4.0}_{-2.8}$	$7^{+3.8}_{-2.6}$	$5^{+3.4}_{-2.2}$	$3^{+2.9}_{-1.6}$	$1^{+2.3}_{-0.8}$	$16^{+5.1}_{-4.0}$
BCS	4.9	4.7	4.0	3.3	2.6	14.6
ESO-KP	4.0	4.4	4.2	3.7	3.1	15.4
ssn1	9.6	11.7	12.2	12.2	11.7	47.8
ssn2	9.5	10.8	9.8	7.9	5.6	34.1
e0n1	5.8	5.7	4.6	3.5	2.4	16.2
e0n2	3.7	2.4	1.0	0.2	0.0	3.6
EMSS	7.3	4.7	2.4	1.1	0.5	8.7
best fit	6.2	5.9	4.4	2.9	1.6	14.8

Table 4.3: The table shows the predicted number of clusters, as a function of redshift, in the Southern SHARC survey, for a range of evolutionary models. For ease of comparison, the first line shows the number of clusters detected in the Southern SHARC survey, together with the one-sigma Poisson errors from Gehrels (1986). Both the BCS and ESO-KP refer to a non-evolving XLF model, where the XLF is taken to be that listed in table 4.1. The ssn1 and ssn2 lines refer to self-similar models, with $n = -1$ and $n = -2$ respectively. Similarly, e0n1 and e0n2 label the constant-entropy models, with $n = -1$ and $n = -2$. The model listed as EMSS refers to equation (4.11), with $n = -2.10$ and $k_0 = 0.029h$ Mpc^{-1} (Henry et al. 1992). The last line, labelled best fit, refers to the best-fit Bower (1997) model to both the Southern SHARC and EMSS catalogues ($n = -1.8$ and $\epsilon = -1.7$) described in the text.

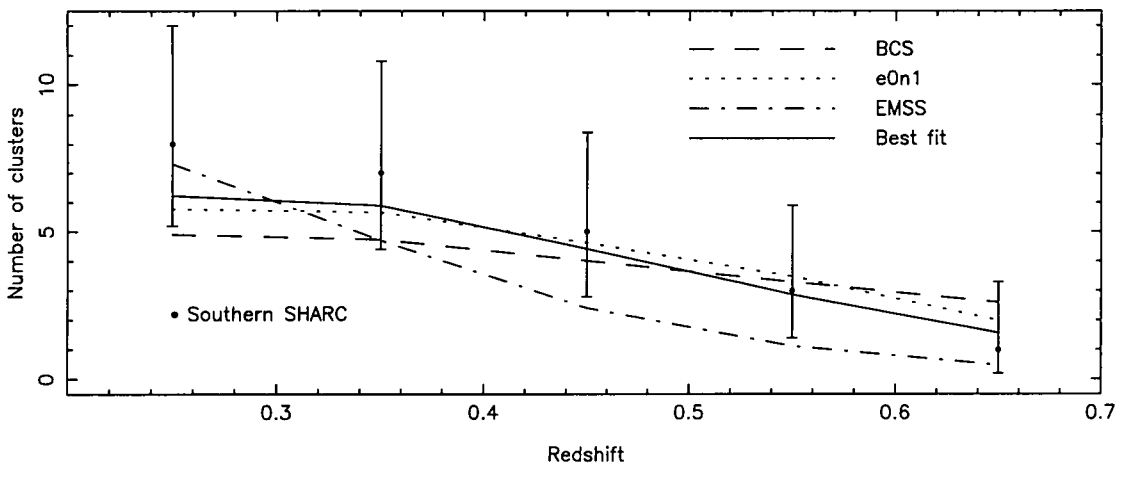

Figure 4.5: The solid points show the redshift distribution of the Southern SHARC sample, for $z > 0.2$, where the error bars are the one-sigma limits from table 4.3. The lines show the predicted number of clusters for selected models from table 4.3.

remainder of this Chapter the BCS XLF will be used to represent the low-redshift cluster population. The dot-dashed line plotted in this Figure shows the self-similar prediction of Kaiser (1986), which indicates that this model only agrees with the observations if $n < -2$. As discussed in Section 4.1, the change in the amplitude of the XLF is a function of n and ϵ for the luminosity range well described by a power-law XLF, corresponding to luminosities $\lesssim 10^{44}$ erg s^{-1} for the BCS XLF. The dotted lines indicate the evolutionary constraints at $z = 0.35$ from the literature, assuming the differential XLF has a slope of -2.2 (e.g. Section 4.2.3; Bower 1997). The lower line corresponds to no evolution of the XLF (Nichol et al. 1997), whilst the upper line is for a 40% fall in the normalisation (Castander et al. 1995; Bower 1997). This shows that, as discussed above, the Southern SHARC catalogue is consistent with little, or no, evolution in the cluster XLF, whilst it is inconsistent with the degree of evolution seen in the RIXOS cluster sample.

Also plotted in Figure 4.6, as the solid dot, is the best-fit value for the EMSS sample (Gioia & Luppino 1994; Nichol et al. 1997). For this calculation, the selection function described in Henry et al. (1992) was used, together with the 0.3 – 3.5 keV BCS XLF from table 4.1. Although the EMSS data favours a steeper power spectrum ($n = -1.4$) with no entropy evolution ($\epsilon = 0.0$), it just lies outside the one-sigma region of the fit to the Southern SHARC catalogue. A simultaneous fit to both data sets was performed, and Figure 4.7 shows the confidence contours; the best-fit value is $n = -1.8^{+0.8}_{-0.3}$ and $\epsilon = -1.7^{+2.5}_{-2.2}$, where the errors are one-sigma limits. Including the EMSS data in the fit has lead to the rejection of power spectra with $n \lesssim -2.0$. The predictions of the best-fit model are included in table 4.3, and plotted in Figure 4.8, with the label 'best fit'.

Since it is not obvious what effect a particular model has on the cluster XLF, Figure 4.8 shows the predictions of several of the models presented above. The XLFs have been scaled to a redshift of $z = 0.44$, the median redshift of the $z > 0.3$ Southern SHARC sample. The models which fit the cluster redshift distribution are those which produce little evolution for cluster luminosities around 10^{44} erg s^{-1}. The constraints possible on the amount of evolution at the bright end of the XLF

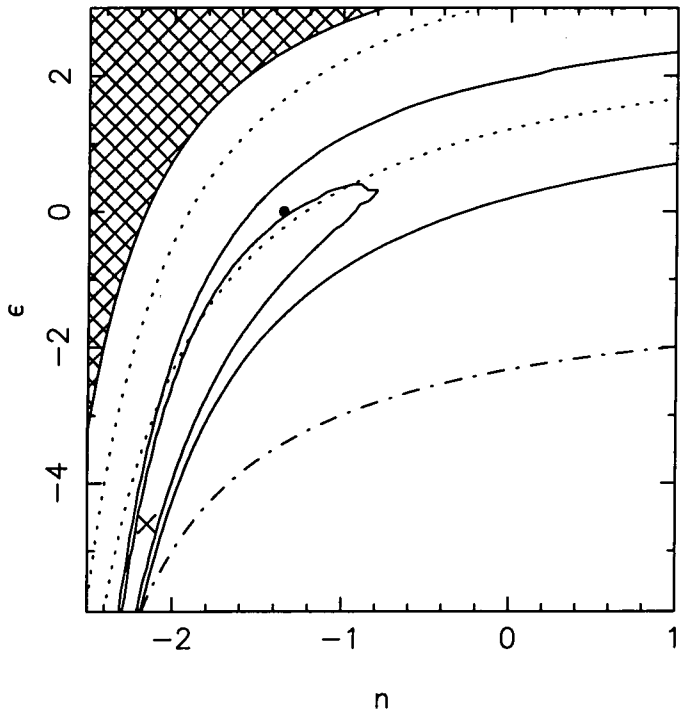

Figure 4.6: The solid contours show the 68% and 90% confidence contours from fitting the BCS XLF, using the Bower (1997) scaling relations, to the $z \geq 0.2$ redshift distribution of the Southern SHARC catalogue. The cross marks the best-fit value of $n = -2.2$ and $\epsilon = -4.6$, whilst the filled circle indicates the value obtained from fitting to the EMSS data only ($n = -1.4$ and $\epsilon = 0.0$). For clusters evolving self-similarly, n and ϵ are restricted to the locus indicated by the dot-dashed line, as given by equation (4.9). The lower dotted line indicates the models which produce no evolution of a power-law XLF (Nichol et al. 1997), whilst the upper line shows those models consistent with the evolution seen in the RIXOS data (Bower 1997). The hatched region shows the region of parameter space for which the Bower (1997) model is no longer valid at a redshift of 0.7.

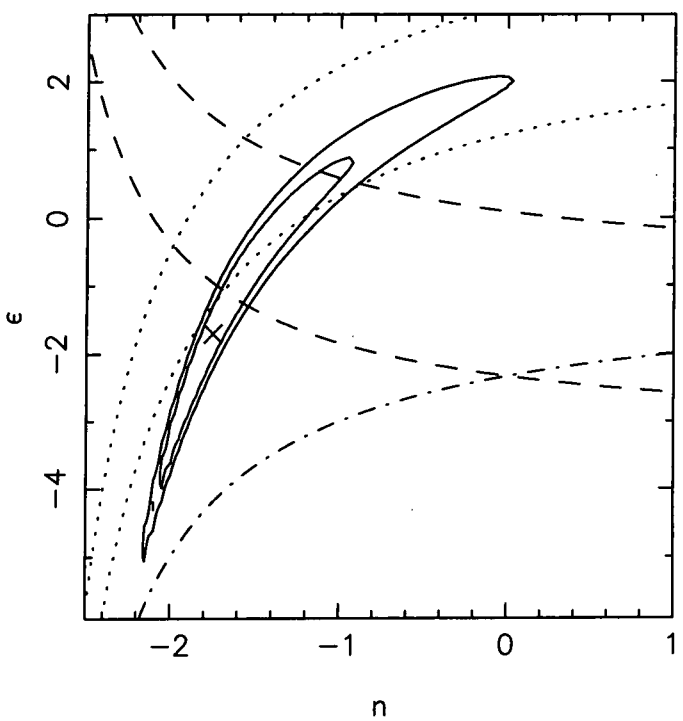

Figure 4.7: The solid contours indicate the 68% and 90% confidence limits for the simultaneous fit to the Southern SHARC and the EMSS redshift distributions. The cross indicates the best-fit model of $n = -1.8^{+0.8}_{-0.3}$ and $\epsilon = -1.7^{+2.5}_{-2.2}$. The dashed lines indicate the one-sigma limits on the evolution of the LT relation presented by Henry (1997). The dotted and dot-dashed lines have the same meaning as in Figure 4.6.

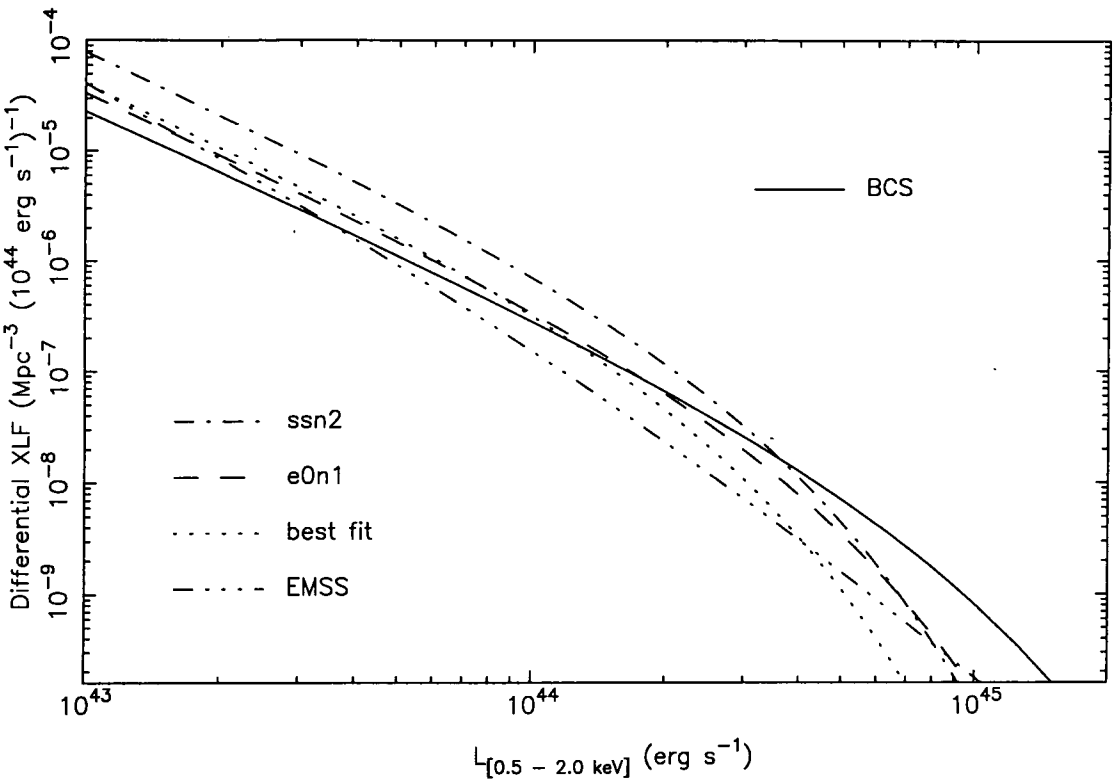

Figure 4.8: The solid line shows the BCS XLF, as listed in table 4.1. The other lines indicate the cluster differential XLF, at a redshift of 0.44, for the models discussed in the text. The ssn2, e0n1 and best fit curves were calculated by scaling the BCS XLF using the relations discussed in Section 4.1, whilst the EMSS curve was calculated using equation (4.11).

are discussed in Section 4.2.3.

Tighter constraints on models of structure formation can be achieved by studying the evolution of cluster X-ray temperatures as well as luminosities. With the advent of the ASCA satellite, it has become possible to obtain temperatures for clusters at redshifts $z \gtrsim 0.3$; since cluster samples are generally flux-limited, rather than temperature-limited, most work has concentrated on measuring the luminosity-temperature (LT) relation. There have been several pieces of work suggesting little evolution in the LT relation at redshifts up to $z \sim 0.4$ (Henry, Jiao & Gioia 1994; Donahue 1996; Mushotzky & Scharf 1997; Henry 1997), and the result used here is that of Henry (1997), which shows that the amplitude of the LT relation at a redshift of $z = 0.32$ is 0.92 ± 0.07 times that of the present day relation (David et al. 1993). The dashed lines in Figure 4.7 indicate the one-sigma limits that this evolutionary constraint corresponds to; since the cluster luminosities are in the $2-10$ keV energy

range, these curves were derived assuming a temperature dependence of $\alpha = 0.5$ in equation (4.5). The constraints from the evolution of the LT relation are approximately perpendicular to those obtained from the redshift distribution. Combining these limits suggests that the spectral index lies in the range $-1.7 \lesssim n \lesssim -1.0$, and that the entropy evolution parameter lies in the range $-1.2 \lesssim \epsilon \lesssim 0.7$, where the ranges correspond to the one-sigma limits, although, as can be seen from the Figure, the errors are correlated.

4.2.3 The Southern SHARC high-redshift X-ray luminosity function

The previous Section showed that the redshift distribution of the Southern SHARC catalogue is compatible with little, or no, evolution of the cluster XLF. A more direct test is to measure the XLF of the high-redshift sample and compare it to a low-redshift XLF. Rather than estimate the low-redshift XLF using the Southern SHARC catalogue, the BCS XLF (table 4.1) was used; the BCS XLF is better defined since it is compiled from a much larger cluster catalogue. This approach is similar to that of Henry et al. (1992), who looked for evolution in the cluster population by comparing the slopes of their high and low redshift XLFs.

The XLF has been calculated using the methods described in Henry et al. (1992) and Nichol et al. (1997): a non-parametric method based on the $1/V_a$ method of Avni & Bahcall (1980), which requires binning of the data; and a parametric method, which uses a maximum-likelihood fitting procedure on the unbinned data. The results presented below are for the redshift shell $z = 0.3 - 0.7$, which has a median redshift of 0.44, and are presented for both the $0.5 - 2.0$ keV and $0.3 - 3.5$ keV pass bands; the conversion between the two bands was performed using a 6 keV thermal bremsstrahlung spectrum.

For the non-parametric estimation of the XLF, the clusters were grouped into log luminosity bins, which have a width of $\Delta \log L = 0.3$, in both the $0.5 - 2.0$ keV and $0.3 - 3.5$ keV pass bands. The bins were chosen so that there were at least two

clusters in each bin. For a bin centred at a luminosity L, the differential XLF, $n(L)$, is given by

$$n(L) = \sum_i \frac{1}{V_{\rm max}(L_{\rm i})\,\Delta L}\,, \tag{4.16}$$

where the sum is over all the clusters that lie in the bin. Various other ways of binning the data were tried — including variable widths so that each bin contained four clusters — and no significant difference was found in the resulting XLF.

For the parametric analysis, the best-fit parameters of a model differential XLF, $\phi(L)$, were found by maximising the likelihood, $\mathcal{L}$, given by

$$\mathcal{L} = \prod_i \frac{\int_0^\infty V_{\rm max}(L)\,\phi(L)\,E_i(L)\,{\rm d}L}{\int_0^\infty V_{\rm max}(L)\,\phi(L)\,{\rm d}L}\,. \tag{4.17}$$

The product is over all the cluster detections in the redshift shell, and $E_i(L)$ is a normal distribution, with mean L_i and standard deviation equal to the error on L_i. The presence of $E_i(L)$ allows the effect of luminosity errors on the fitting procedure to be estimated (Nichol et al. 1997). Two model XLFs were used: a power law, of the form

$$\phi(L) = A_p\,L^{-\alpha_p}\,, \tag{4.18}$$

as used by Henry et al. (1992) and Nichol et al. (1997); and a Schechter function (equation 4.12). For the latter case, L_* was set to 5.70 (0.5 – 2.0 keV) and 10.7 (0.3 – 3.5 keV) — as given by Ebeling et al. (1997) — since the survey is not sensitive to clusters with luminosities $\gtrsim L_*$. The form of equation (4.17) means that $\mathcal{L}$ is independent of the XLF normalisation (i.e. A_p or A_s), so it is a function of the power-law slope (α_p or α_s) only. Therefore, for each model, $\mathcal{L}$ was evaluated for a range of power-law slopes, and the normalised probability distribution calculated. The best-fit value corresponds to the peak of this distribution, and the error was found by integrating the curve out until the enclosed area equalled 68.3%. The normalised distributions are plotted in Figure 4.9 for both the 0.5 – 2.0 keV and 0.3 – 3.5 keV pass bands. Apart from the tails of the distribution, both are well approximated by Gaussian probability distributions, hence the listed errors are the symmetric one-sigma values. The normalisation of the XLF was calculated by setting the predicted number of clusters to the observed number, and the errors were found by allowing the slope to take its one-sigma limits. As discussed in Henry et al. (1992), the fitting

Pass band (keV)	$\log L^{\dagger}$	$N_{\rm cl}$	$\log n(L)^{\ddagger}$
$0.5-2.0$	43.50	2	-5.52 $(+0.37,-0.45)$
$0.5-2.0$	43.80	4	-6.26 $(+0.25,-0.28)$
$0.5-2.0$	44.10	6	-6.61 $(+0.20,-0.22)$
$0.5-2.0$	44.40	4	-7.17 $(+0.25,-0.28)$
$0.3-3.5$	43.75	2	-5.78 $(+0.37,-0.45)$
$0.3-3.5$	44.05	4	-6.51 $(+0.25,-0.28)$
$0.3-3.5$	44.35	6	-6.86 $(+0.20,-0.22)$
$0.3-3.5$	44.65	4	-7.42 $(+0.25,-0.28)$

$\dagger$ L has units of erg s^{-1}

$\ddagger$ $n(L)$ has units of Mpc^{-3} $(10^{44}$ erg s$^{-1})^{-1}$

Table 4.4: The table lists the non-parametric XLF for the Southern SHARC survey. As discussed in the text, the log luminosity bins have a constant width and were chosen so that each bin contained at least two clusters. $N_{\rm cl}$ lists the number of clusters in each bin, and the errors on $n(L)$ are the 68% Poisson limits from Gehrels (1986).

procedure gives some weight to luminosities at which no clusters were detected, which produces a steeper slope than the non-parametric data would suggest.

Tables 4.4 and 4.5, and Figures 4.10 and 4.11, give the results of these calculations. Comparing the $0.5-2.0$ keV XLF to that of the BCS shows that, at luminosities $\sim 10^{44}$ erg s^{-1}, the two data sets are in agreement: the faint-end slope of the Schechter function, $\alpha_s = 1.77 \pm 0.30$, is the same, within the errors, as the BCS value ($\alpha_s = 1.85 \pm 0.09$). The power-law slope, in the $0.3-3.5$ keV pass band, $\alpha_p = 2.22 \pm 0.25$, is also consistent with the slope of the low-redshift shell of Henry et al. (1992) and of the re-worked EMSS sample of Nichol et al. (1997), for which $\alpha_p = 2.19 \pm 0.21$ and $\alpha_p = 2.60 \pm 0.37$ respectively. This lack of evolution in the XLF agrees with the conclusions from Section 4.2.2.

The only other published XLF for X-ray selected clusters at redshifts above 0.3 is that of Henry et al. (1992), from 21 clusters in the range $z = 0.3-0.6$, with a median redshift of 0.33. They find a steep power-law slope, $\alpha_p = 3.27 \pm 0.29$, which they claim is the result of negative evolution, whilst the Nichol et al. (1997) re-analysis of the EMSS data finds a shallower high-redshift slope, with $\alpha_p = 3.08 \pm 0.32$.

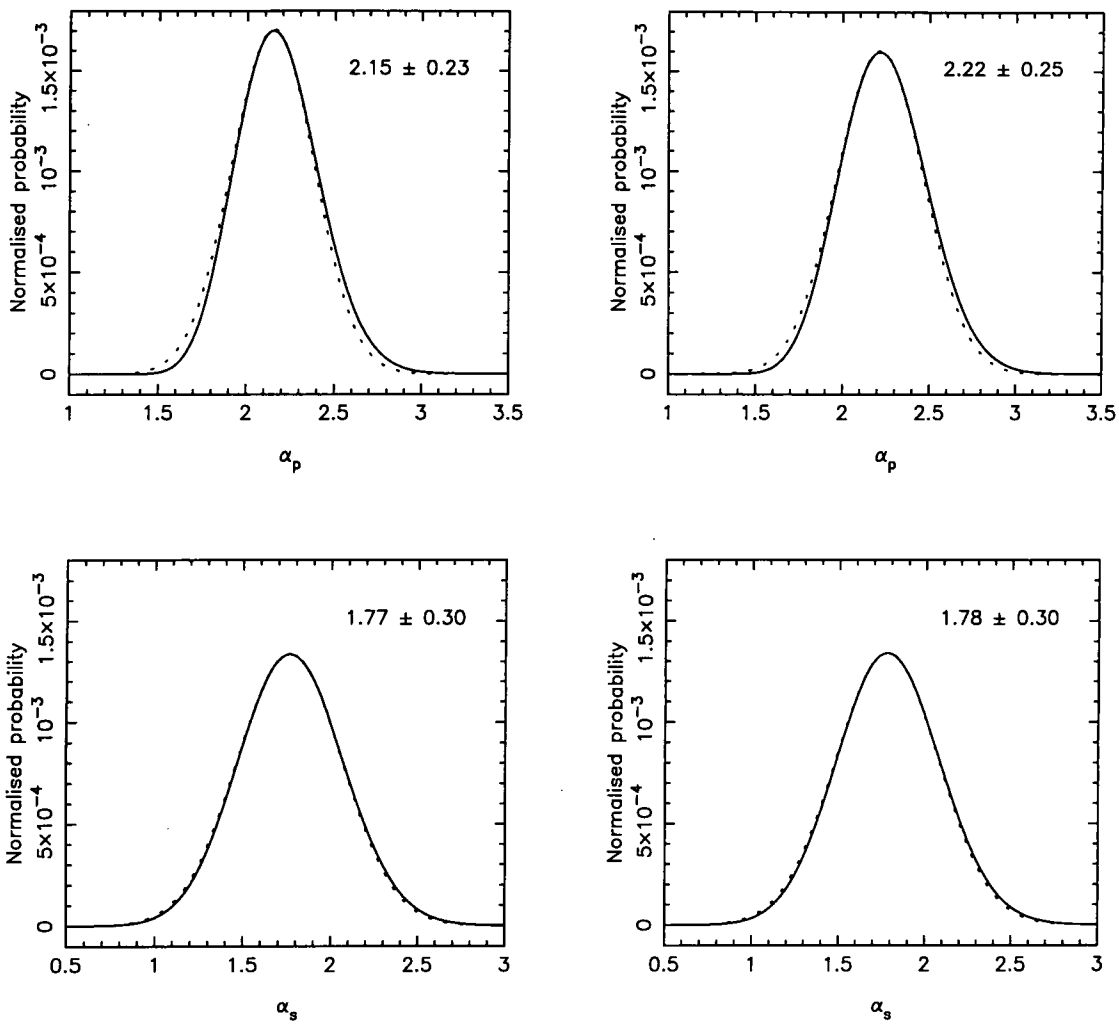

Figure 4.9: The top plots show the normalised probability distributions obtained for the power-law fit to the high-redshift cluster data. The left-hand plot is for the $0.5 - 2.0$ keV pass band, whilst the right hand plot is for the $0.3 - 3.5$ keV pass band. The bottom plots are for the Schechter-function fit. The dashed lines in the plots indicate a Gaussian probability distribution, with a mean and width equal to the best-fit values which are listed in the top-right of each plot.

pass band	power law		Schechter function	
(keV)	α_p	$A_p^\dagger$	α_s	$A_s^\dagger$
0.5 - 2.0	2.15 ± 0.23	2.72 ± 0.12	1.77 ± 0.30	3.64 ± 0.16
0.3 - 3.5	2.22 ± 0.25	4.99 ± 0.77	1.78 ± 0.30	5.68 ± 1.04

† Units of 10^{-7} Mpc^{-3} $(10^{44}\,\mathrm{erg\,s^{-1}})^{\alpha-1}$

Table 4.5: The table lists the best-fit parameters for the power-law and Schechter-function forms of the differential XLF. For comparison, the high-redshift XLF of the EMSS is described by a power law, with $\alpha_p = 3.27 \pm 0.29$ and $A_p = (12.33 \pm 3.87) \times 10^{-7}$ Mpc^{-3} $(10^{44}\,\mathrm{erg\,s^{-1}})^{\alpha-1}$ in the $0.3 - 3.5$ keV pass band (Henry et al. 1992).

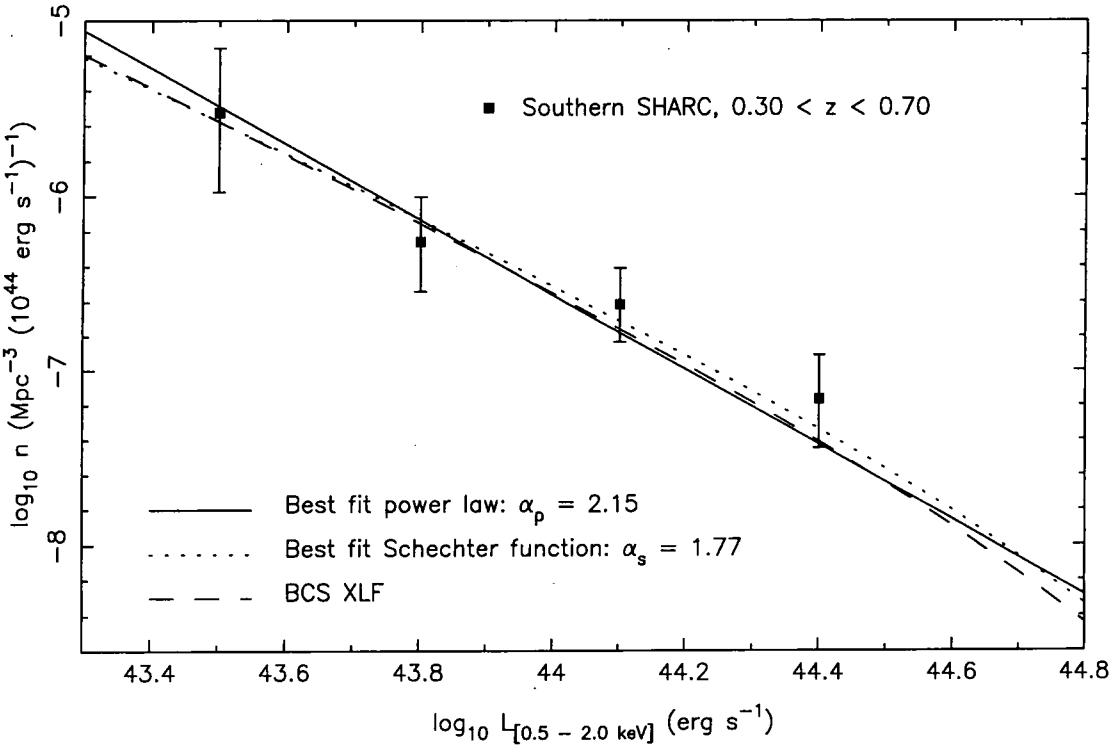

Figure 4.10: The solid points show the non-parametric XLF of the Southern SHARC catalogue in the 0.5 – 2.0 keV pass band, whilst the solid and dotted lines indicate the best power-law and Schechter-function parametric fits respectively. The solid line shows the low-redshift XLF of the BCS (Ebeling et al. 1997), which is virtually indistinguishable, over this luminosity range, from the fitted models.

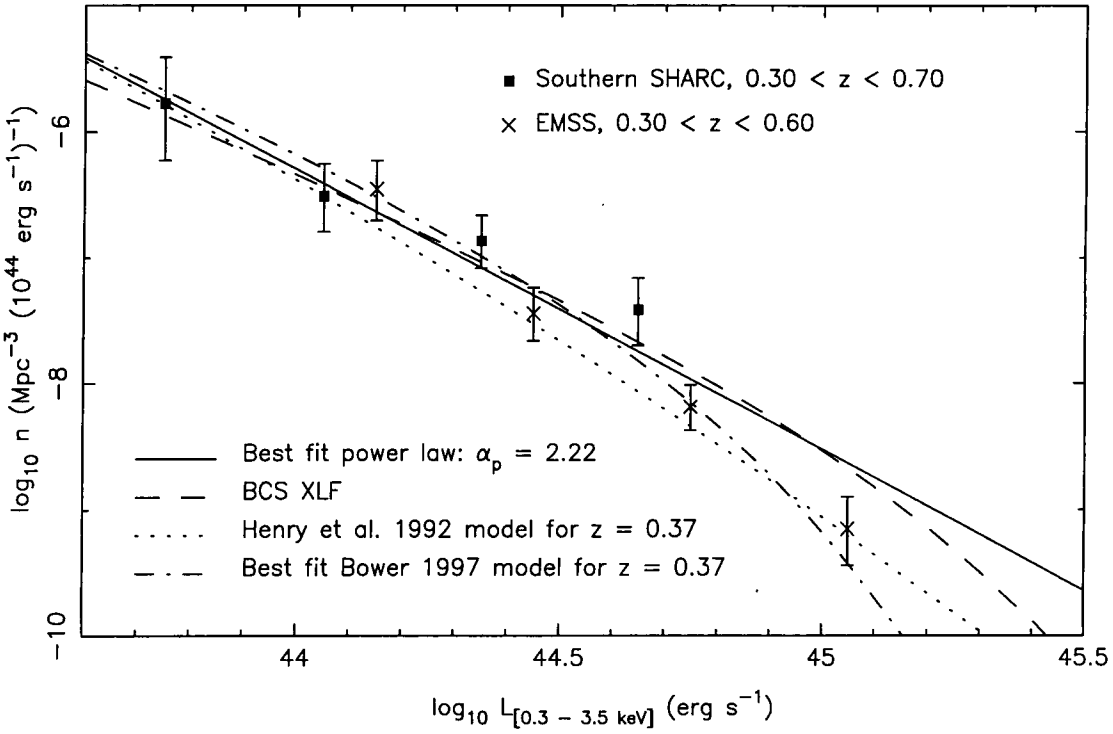

Figure 4.11: The solid points show the non-parametric XLF of the Southern SHARC catalogue in the $0.3 - 3.5$ keV pass band, and the solid line is the best power-law fit. The crosses indicate the high-redshift XLF from Henry et al. (1992), with the dotted line showing their best-fit model ($n = -2.10$, $k_0 = 0.029h$ Mpc^{-1}) evaluated at a redshift of 0.37, the median value of the combined cluster sample. The dashed line is the XLF of the BCS (Ebeling et al. 1997), whilst the dot-dashed line shows this XLF scaled to $z = 0.37$, using the best-fit model from Section 4.2.2.

Neither slope is significantly different from that found in the Southern SHARC catalogue, the differences being at the 2.7σ and 2.1σ levels respectively. As shown in Figure 4.11, the non-parametric XLFs of the two surveys are in agreement for luminosities $\lesssim 5 \times 10^{44}$ erg s^{-1} $(0.3 - 3.5$ keV), hence any evolution of the cluster population is restricted to luminosities $\gtrsim 3 \times 10^{44}$ erg s^{-1} $(0.5 - 2.0$ keV). For the redshift shell $z = 0.3 - 0.7$, the surface density of clusters with luminosities greater than 3×10^{44} erg s^{-1} $(0.5 - 2.0$ keV) is 0.083 deg^{-2}, assuming a 100% detection efficiency and a non-evolving BCS XLF. Therefore the expected number of such clusters in the Southern SHARC catalogue is only ~ 1.5, and so the lack of high luminosity clusters in the survey is not unexpected. This means that the Southern SHARC catalogue can not be used to test the evolution of the brightest clusters $(L \gtrsim L_*)$, or to examine the differences between the conclusions of Henry et al. (1992) and Nichol et al. (1997).

4.3 Discussion and Conclusions

The main result of this Chapter is that both the redshift distribution and the XLF of the high-redshift Southern SHARC catalogue are consistent with little, or no, evolution in the space density of clusters with luminosities around 10^{44} erg s^{-1}. This is in direct contrast to earlier claims of strong negative evolution at such luminosities (Castander et al. 1995). Preliminary results from the other ROSAT-selected cluster catalogues agree with the lack of evolution seen in the Southern SHARC catalogue (Rosati et al. 1995; Scharf et al. 1997; Rosati 1997, private communication). Assuming that the Southern SHARC catalogue is representative of the high-redshift cluster population, this suggests that the lack of high-redshift clusters in the RIXOS is either because their detection method is biased against detecting clusters (Scharf et al. 1997), or because of misclassification in the optical follow-up survey. At $z \lesssim 0.1$, the clusters in the catalogue are not representative of the low-redshift cluster population, as shown by their anomalous number counts and $V/V_{\rm max}$ distribution.

Whilst the Southern SHARC catalogue is able to constrain the evolution at luminosities $\sim 10^{44}$ erg s^{-1}, it does not cover a large enough area to be sensitive to evolution at luminosities $\gtrsim L_*$. Therefore, no comment can be made on the different conclusions drawn by Henry et al. (1992) and Nichol et al. (1997) from the EMSS cluster catalogue.

For a critical density universe, in which the scaling relations of Bower (1997) (Section 4.1) are valid, the redshift distributions of the combined Southern SHARC and EMSS catalogues are best fit by a spectral index of $n = -1.8^{+0.8}_{-0.3}$ and entropy evolution parameter of $\epsilon = -1.7^{+2.5}_{-2.2}$, for one-sigma errors. The inclusion of constraints on the evolution of the cluster luminosity-temperature relation (Henry 1997) produces one-sigma limits of $-1.7 \lesssim n \lesssim -1.0$ and $-1.2 \lesssim \epsilon \lesssim 0.7$. Constant-entropy models (e.g. Kaiser 1991; Evrard & Henry 1991) are consistent with both the redshift distributions, and the LT constraints, if $-1.4 \lesssim n \lesssim -1.2$.

Whilst the evolution of the XLF can be used to measure cosmological parameters, it is preferable to use the X-ray temperature function (XTF) for this purpose, since the gas temperature is a better tracer of the cluster mass than the luminosity. Recently, Henry (1997) used a sample of ASCA-observed EMSS clusters to measure the $z = 0.32$ XTF. Using a Press-Schechter based analysis to compare the result to the local distribution, derived by Henry & Arnaud (1991), Henry (1997) reported that $\Omega_0 \simeq 0.5$ for both open and flat cosmologies. In such a low-density universe, the growth rate of structures is less than in a critical universe. The lack of evolution of the XLF seen in the Southern SHARC catalogue is therefore also qualitatively consistent with a low-density universe. Various X-ray selected cluster samples have been used to show that their properties are consistent with a low value of the density parameter. The mass-to-light ratio (Carlberg et al. 1996) and number density (Carlberg et al. 1997) of the clusters in the CNOC redshift survey of selected EMSS clusters (Yee, Ellingson & Carlberg 1996) suggest $\Omega_0 \simeq 0.2 - 0.6$. A number of authors (Kitayama & Suto 1997; Mathiesen & Evrard 1998; Kitayama, Sasaki & Suto 1997) have used the log N - log S distribution of ROSAT-selected clusters (RDCS; WARPS; BCS), together with a Press-Schechter based analysis, to show

that $\Omega_0 \simeq 0.3 - 0.5$ models are a good fit to the data.

Chapter 5

Conclusions and Future Work

This thesis has presented an X-ray selected catalogue of galaxy clusters — the Southern SHARC catalogue — and used it to study the properties of the high-redshift cluster population. Section 5.1 presents the conclusions of this thesis, whilst Section 5.2 highlights several future avenues of research.

5.1 Conclusions

After reviewing the X-ray properties of galaxy clusters and the capabilities of ROSAT, Chapter 2 discussed various possible strategies for the creation of an X-ray selected cluster sample. The chosen method was to use the angular extent of the X-ray sources as a primary discriminant: the intrinsic sizes of clusters, coupled with the angular resolution of the ROSAT PSPC, means that clusters of modest luminosity, 10^{44} erg s^{-1}, should be visible out to $z \simeq 0.6$ in a 10 ks exposure, whilst the contamination in the catalogue due to AGN and QSOs — the main component of the X-ray sky at these flux limits — will be greatly reduced, because these sources are point-like. A range of source-detection techniques were then discussed, the chosen method uses a maximum-likelihood technique (Cash 1979) together with a model of the surface-brightness profile to define the detection significance. The method also provides a means of calculating the extent significance of a source, by comparing

the observed photon distribution to a range of extended profiles. A full description of the X-ray reduction method is followed by details of the resulting catalogue of extended X-ray sources. The Chapter finishes with the simulations performed to calculate the selection function of the survey, which is used in the calculations presented in Chapter 4. For clusters at redshifts beyond 0.3, the minimum luminosity detectable is $\simeq 10^{43}$ erg s^{-1}, approximately three times lower than that possible with the EMSS (Henry et al. 1992).

Not all the sources in the X-ray catalogue presented in Chapter 2 are clusters; nearby galaxies, which are genuinely extended sources, as well as objects which appear extended due to source confusion, or a mis-match between the real and model PSF, have to be removed from the list. The first half of Chapter 3 discusses the steps taken to remove these contaminating sources. The optical follow-up of the cluster candidates was described: both the strategy used to identify the X-ray sources and the reduction techniques used on the optical data. Out of the 103 extended sources, 36 clusters are identified. The survey is 90% complete, with 11 sources requiring identification: the optical properties of these sources suggest that some may be low-redshift groups, whilst others could be high-redshift clusters.

The second half of Chapter 3 is devoted to the calculation of the X-ray luminosities of the clusters. The large detector area of the PSPC means that the aperture used to measure the flux can be adjusted for each cluster, rather than using a fixed angular aperture as with the EMSS (Henry et al. 1992). The aperture was chosen to contain 80% of the flux from a King profile, with a core radius of 250 kpc and $\beta = 2/3$ — typical of local cluster samples — when scaled to the cluster redshift. The conversion from measured to total count rate was therefore just a multiplication by 1.25. This is in contrast to the EMSS (Henry et al. 1992), which used a fixed angular aperture. Although cluster X-ray emission is due to both thermal bremsstrahlung radiation and line emission from metals in the ICM, the continuum emission dominates. The conversion from a count rate into both a flux and a luminosity was therefore made assuming a thermal bremsstrahlung spectrum, with the temperature set to 6 keV. Although clusters exhibit a range of temperatures, it

was shown that the errors on the cluster luminosities was dominated by the Poisson errors on the detected photons, rather than the assumption of a fixed temperature. The Chapter finishes by presenting the redshifts, fluxes and luminosities of the Southern SHARC catalogue, which contains 36 clusters, over the redshift range $0.05 < z < 0.7$, and with luminosities of 7×10^{42} erg s^{-1} to 4×10^{44} erg s^{-1}. The high-redshift sample consists of the 16 clusters with $z \geq 0.3$ and with luminosities greater than 2×10^{43} erg s^{-1}.

Chapter 4 presents the $z > 0.2$ redshift distribution of the Southern SHARC catalogue, and shows that it is consistent with the predictions of a no-evolution model, based on the local XLF of the BCS (Ebeling et al. 1997). This is in direct contrast with the findings of Castander et al. (1995), who use a similar technique to demonstrate that the RIXOS cluster catalogue shows strong negative evolution for clusters of luminosities $\sim 10^{44}$ erg s^{-1}. Whilst it is not yet clear what the difference is due to, preliminary evidence from the other ROSAT-selected distant-cluster surveys (RDCS, Rosati 1997, private communication; WARPS, Scharf et al. 1997) suggest that they are consistent with little evolution at this luminosity. The analysis is restricted to high redshifts since the number counts and $V/V_{\rm max}$ distribution of the low-redshift clusters ($z \lesssim 0.1$) are not consistent with the properties of much larger cluster samples over the same redshift range (BCS, Ebeling et al. 1997; ESO-KP, De Grandi et al. 1997).

The scaling relations presented in Bower (1997), which include the possibility of physical processes other than gravity affecting the ICM, were fit to the redshift distributions of both the Southern SHARC and EMSS (Gioia & Luppino 1994; Nichol et al. 1997) catalogues. For an Einstein-de Sitter universe, in which the scaling relations are valid, the best-fit values of the spectral index and entropy evolution parameter are $n = -1.8^{+0.8}_{-0.3}$ and $\epsilon = -1.7^{+2.5}_{-2.2}$ respectively. Although the BCS XLF was used for this calculation, the results are similar if another local XLF is used, such as that of the ESO-KP sample (De Grandi 1997; De Grandi 1997, private communication). The best-fit value suggests that the ICM evolution is dominated by heating, rather than cooling, processes, although the amount required is not

consistent with the shock-heating in a self-similar model (Kaiser 1986), which has $\epsilon = -4.3$ for this value of the spectral index. Recent constraints on the evolution of the LT relation (Henry 1997) restrict the 68% confidence region of the model values to $-1.7 \lesssim n \lesssim -1.0$ and $-1.2 \lesssim \epsilon \lesssim 0.7$. For the constant-entropy models introduced by Kaiser (1991) and Evrard & Henry (1991), the data suggest that the spectral index lies in the range $-1.4 \lesssim n \lesssim -1.2$.

The high-redshift ($0.3 \leq z < 0.7$) XLF of the Southern SHARC catalogue was calculated using both non-parametric and parametric techniques. This is the first measurement of the cluster XLF for luminosities $\lesssim 10^{44}$ erg s^{-1} at these redshifts. Fitting a power-law to the data produced: $\alpha_p = 2.15 \pm 0.23$ and $A_p = (2.72 \pm 0.12) \times 10^{-7}$ Mpc^{-3} $(10^{44}\,\mathrm{erg\,s^{-1}})^{\alpha-1}$ for the $0.5 - 2.0$ keV pass band; $\alpha_p = 2.22 \pm 0.25$ and $A_p = (4.99 \pm 0.77) \times 10^{-7}$ Mpc^{-3} $(10^{44}\,\mathrm{erg\,s^{-1}})^{\alpha-1}$ for the $0.3 - 3.5$ keV pass band. These results are in good agreement with the local XLF of the BCS and the low-redshift shell of the EMSS, for both the original (Henry et al. 1992) and re-analysed (Nichol et al. 1997) samples. The power-law fit is shallower than the EMSS high-redshift shell, the difference being significant at the 2.7σ and 2.1σ levels, for the original and re-analysed fits respectively. Comparing the non-parametric version to that from Henry et al. (1992) shows that the surveys are similar for luminosities $\lesssim 3 \times 10^{44}$ erg s^{-1} ($0.5 - 2.0$ keV); at larger luminosities the XLFs disagree, although there is not enough overlap in luminosity to see if the difference is significant. The conclusion drawn from these results is that, as with the redshift distribution, the Southern SHARC catalogue is consistent with no evolution of the cluster XLF at luminosities $\sim 10^{44}$ erg s^{-1}. Any evolution of the cluster population can therefore only occur for luminosities brighter than $\sim 3 \times 10^{44}$ erg s^{-1}.

The above analysis was performed assuming an Einstein-de Sitter universe. However, the lack of evolution in the XLF is also qualitatively consistent with a low value of the density parameter Ω_0. Recent results from X-ray selected cluster samples have also provided evidence for $\Omega_0 < 1$: Henry (1997) uses the evolution of the XTF to show $\Omega_0 \simeq 0.5$; the mass-to-light ratios (Carlberg et al. 1996) and number density (Carlberg et al. 1997) of clusters in the CNOC survey are consistent with

$\Omega_0 \simeq 0.2 - 0.6$; and the log N - log S distributions of ROSAT-selected cluster samples are fit by models with $\Omega_0 \simeq 0.3 - 0.5$ (Kitayama & Suto 1997; Mathiesen & Evrard 1998; Kitayama, Sasaki & Suto 1998).

5.2 Future work

In the near future, the results from the other ROSAT-selected distant cluster catalogues — RDCS and WARPS — will become available. The results of these surveys should shed light on whether the X-ray cluster population evolves strongly at luminosities around 10^{44} erg s^{-1}, as suggested by the RIXOS data, or is consistent with no evolution, as argued in this thesis. A comparison of the selection techniques of the various catalogues would be useful in determining the sensitivity of the measured evolution to possible selection biases (Castander 1997, private communication). As with the Southern SHARC survey, the sizes of both the RDCS and the WARPS (Rosati 1997, private communication; Jones 1997, private communication) are not large enough to test the evolution of the cluster population at luminosities $\gtrsim L_*$. For this, large area surveys such as the RASS NEP project (e.g. Bower et al. 1996) and the Bright SHARC survey (Nichol 1997, private communication) are required.

The interest in these luminous clusters stems from the fact that they are the most massive virialised systems in the universe, and so the redshift evolution of their abundance is an extremely sensitive test of cosmological models. Since the X-ray luminosity is not a good measure of the cluster mass, an alternative is required. The most common technique is to use the cluster temperature, since it is expected to be similar to the virial temperature of the cluster and hydrodynamic simulations can be used to normalise the predictions (e.g. Evrard, Metzler & Navarro 1996). However, most cluster samples are selected on the basis of their flux, rather than temperature, so there is interest in combining the two approaches by measuring the evolution of the luminosity-temperature relation using an X-ray selected catalogue (e.g. Eke et al. 1996; Oukbir, Bartlett & Blanchard 1997; Bower 1997). Section 4.2.2 provides an example of such an approach, where the constraints on the Bower (1997)

model, fitted to the redshift distributions of the Southern SHARC and EMSS catalogues, were improved by including the Henry (1997) results on the evolution of the LT relation. Although ASCA can measure ICM temperatures for clusters beyond redshifts of 0.3, it can only do this for the brightest systems. The launch of the Advanced X-ray Astronomy Facility (AXAF) satellite, in August 1998, and the X-ray Multi-Mirror (XMM) satellite, in late 1999, will enable such measurements to be performed for clusters with luminosities typical of those detected in the Southern SHARC survey.

Little is known about the evolution of the surface-brightness profile of clusters. Both XMM and AXAF have the necessary spatial resolution and sensitivity to provide images of clusters at high redshift. As well as testing the assumption used throughout this thesis, that the surface-brightness profile can be modelled by an non-evolving isothermal sphere, such a study can be compared to the predictions of the models presented in Section 4.1, and so determine what physical processes affect the evolution of the ICM. Temperature and gas density profiles can be used to measure the distribution of mass within the cluster.

An alternative method of measuring the mass of a cluster is to use the lensing signature caused by the cluster potential well (e.g. Fort & Mellier 1994). Massive clusters can produce giant arcs — such as seen in the spectacular HST image of Abell 2218 — which can be used to constrain the mass within the region encompassed by the arcs. Such an approach is only suited to the most massive of clusters, since the formation of the arcs requires a high mass concentration, and only provides an estimate of the mass within the cluster core, since this is where the arcs are seen. A more suitable approach for the general cluster population is to deduce the mass from the small distortions (weak lensing) produced in the background galaxy population as the light-rays pass through the cluster (e.g. Kaiser & Squires 1993; Wilson, Cole & Frenk 1996). The advent of large-area CCD cameras means that it is now possible to measure the mass profile well beyond the cluster core. Two examples of the work possible with mass estimates of ROSAT-selected clusters are a study of the luminosity-mass relation as a function of cluster luminosity, and the

comparison of the mass and gas spatial profiles. The results of both studies would provide tests of the theories of structure formation.

Another means of selecting clusters is to use the Sunyaev-Zel'dovich (SZ) effect, where the inverse Compton scattering of CMB photons by the high-energy electrons in the ICM distorts the blackbody spectrum of the CMB (Sunyaev & Zel'dovich 1972). The SZ effect has now been reliably measured (e.g. Birkinshaw & Hughes 1994; Carlstrom, Marshall & Grego 1996) and future instruments, such as the European PLANCK satellite and the Japanese Large Millimeter and Submillimeter Array, have the capability of detecting large numbers of clusters. Initial interest in the SZ effect has been the measurement of Hubble's constant (e.g. Birkinshaw & Hughes 1994), whilst current work has shown that the evolution of the SZ decrement can be used to measure Ω_0, in an analogous manner to the X-ray temperature function (e.g. Barbosa et al. 1996; Eke et al. 1996; Colafrancesco et al. 1997)

Throughout this thesis the approach has been to consider a cluster as containing a gaseous component trapped in the virialised region of the potential well of the dark matter halo — the galaxy population has effectively been ignored. However, the galaxy population is important in its own right, and can also provide important information on the formation history of the cluster, particularly of the ICM (e.g. Trentham 1994; Nath & Chiba 1995; López-Cruz et al. 1997). Currently, the studies of galaxy populations in distant clusters are limited to either optically-selected clusters, hence subject to the uncertainties inherent to these catalogues, or to the most luminous X-ray clusters, and so are not representative of the general cluster population. The inclusion of ROSAT-selected clusters in these samples means that the dependence of the galaxy populations on the system mass, as well as redshift, can be studied.

An example of such a project is the study of the Brightest Cluster Galaxies (BCGs) in X-ray selected clusters. Collins & Mann (1998) show that the K-band absolute magnitude of BCGs is a good standard candle, with a dispersion of ~ 0.2 mag out to $z \sim 0.8$, for the most X-ray luminous clusters. The evidence is that lower luminosity clusters have a larger scatter, although as the cluster sample is

selected from the EMSS, it has only been possible to measure this at low redshift. The inclusion of ROSAT-selected clusters in this sample will test how the scatter evolves with redshift, providing constraints on the evolutionary history of the BCGs.

This Section has presented a somewhat potted look at the projects possible with X-ray selected clusters of galaxies. The common theme of these projects has been to use the increased luminosity base-line now available at high redshift to study evolutionary effects as a function of cluster mass, as well as redshift.

References

Abell, G. O. 1958, ApJS, 3, 211

Abell, G. O., Corwin, H. G., & Olowin, R. P. 1989, ApJS, 70, 1

Allan, D. J., & Vallance, R. J. 1995, Starlink User Note, 98.6

Allington-Smith, J. R. A., & Maddox, S. J. 1994, LDSS User's Manual

Almaini, O., Shanks, T., Boyle, B. J., Griffiths, R. E., Roche, N., Stewart, G. C., & Georgantopoulos, I. 1996, MNRAS, 282, 295

Aragón-Salamanca, A., Ellis, R. S., Couch, W. J., & Carter, D. 1993, MNRAS, 262, 764

Aranud, M., Rothenflug, R., Boulade, O., Vigroux, L., & Vagioni-Flam, E. 1992, A&A, 254, 49

Avni, Y. 1976, ApJ, 210, 642

Avni, Y., & Bahcall, J. N. 1980, ApJ, 235, 694

Bahcall, N. A., & Soneira, R. M. 1983, ApJ, 270, 20

Bahcall, N. A., Soneira, R. M., & Burgett, W. S. 1986, ApJ, 311, 15

Barbosa, D., Bartlett, J. G., Blanchard, A., & Oukbir, J. 1996, A&A, 314, 13

Bardeen, J. M., Bond, J. R., Kaiser, N., & Szalay, A. S. 1986, ApJ, 304, 15

Bennett, C. L., Banday, A. J., Gorski, K. M., Hinshaw, G., Jackson, P., Keegstra, P., Kogut, A., Smoot, G. F., Wilkinson, D. T., & Wright, E. L. 1996, ApJ, 464, L1

Birkinshaw, M., & Hughes, J. P. 1994, ApJ, 420, 33

Bond, J. R., Cole, S., Efstathiou, G., & Kaiser, N. 1991, ApJ, 379, 440

Bond, J. R., Efstathiou, G., & Silk, J. 1980, Phys. Rev. Lett., 45, 1980

Bond, J. R., & Myers, S. T. 1996, ApJS, 103, 1

Bond, J. R., & Szaly, A. S. 1983, ApJ, 274, 443

Bower, R. G. 1991, MNRAS, 248, 332

Bower, R. G. 1997, MNRAS, 288, 355

Bower, R. G., Castander, F. J., Couch, W. J., Ellis, R. S., & Böhringer, H. 1997, MNRAS, 291, 353

Bower, R. G., Ellis, R. S., Rose, J. A., & Sharples, R. M. 1990, AJ, 99, 530

Bower, R. G., Hasinger, G., Castander, F. J., Aragón-Salamanca, A., Ellis, R. S., Gioia, I. M., Henry, J. P., Burg, R., Huchra, J. P., Bohringer, H., Briel, U. G., & Mclean, B. 1996, MNRAS, 281, 59

Boyle, B. J., Wilkes, B. J., & Elvis, M. 1997, MNRAS, 285, 511

Briel, U. G., Aschenbach, B., Hasinger, G., Hippmann, H., Pfeffermann, E., Predehl, P., Schmitt, J. H. M. M., Voges, W., Zimmermann, U., George, I. M., Snowden, S. L., Turner, T. J., David, L., Harnden, F. R., Kearns, K. E., Zombeck, M. V., Barstow, M. A., Osborne, J. P., Pye, J. P., Watson, M., West, R. G., & Willingale, R. 1994, ROSAT Users' Handbook (Garching: MPE)

Brown, R. L., & Gould, R. J. 1970, Phys. Rev. D, 1, 2252

Bryam, G. L., Cen, R. Y., Norman, M. L., Ostriker, J. P., & Stone, J. M. 1994, ApJ, 428, 405

Byram, E. T., Chubb, T. A., & Friedman, H. 1966, Science, 152, 66

Carlberg, R. G., Morris, S., Yee, H. K. C., & Ellingson, E. 1997, ApJ, 479, L19

Carlberg, R. G., Yee, H. K. C., Ellingson, E., Abraham, R., Gravel, P., Morris, S., & Pritchet, C. J. 1996, ApJ, 462, 32

Carlstrom, J. E., Marhshall, J., & Grego, L. 1996, ApJ, 456, L75

Cash, W., ApJ, 1979, 228, 939

Castander, F. J. 1996, Ph.D. thesis, IOA, Cambridge

Castander, F. J., Bower, R. G., Ellis, R. S., Aragón-Salamanca, A., Mason, K. O.,

Hasinger, G., Mcmahon, R. G., Carrera, F. J., Mittaz, J. P. D., Perez-Fournon, I., & Lehto, H. J. 1995, Nature, 377, 39

Castander, F. J., Ellis, R. S., Frenk, C. S., Dressler, A., & Gunn, J. E. ApJ, 1994, 424, 79

Cavaliere, A., Colafrancesco, S., & Menci, N. 1993, ApJ, 415, 50

Cavaliere, A., & Fusco-Femiano, R. 1976, A&A, 49, 137

Cavaliere, A., Gursky, H., & Tucker, W. H. 1971, Nature, 231, 437

Cen, R., Gnedin, N. Y., Kofman, L. A., & Ostriker, J. P. 1992, ApJ, 399, L11

Cen, R. Y., & Ostriker, J. P. 1994, ApJ, 429, 4

Colafrancesco, S., Mazzotta, P., Rephaeli, Y., & Vittorio, N. 1997, ApJ, 479, 1

Coles, P., & Lucchin, F. 1995, Cosmology : The Origin and Evolution of Cosmic Structure (Chichester: John Wiley & Sons)

Colless, M., Ellis, R. S., Taylor, K., & Hook, R. N. 1990, MNRAS, 244, 408

Collins, C. A., Burke, D. J., Romer, A. K., Sharples, R. M., & Nichol, R. C. 1997, ApJ, 479, L117

Collins, C. A., Guzzo, L., Nichol, R. C., & Lumsden, S. L. 1995, MNRAS, 274, 1071

Collins, C. A., & Mann, R. G. 1998, MNRAS, 297, 128

Corwin, H. G., & Emerson, D. 1982, MNRAS, 200, 621

Costero, R. & Osterbrock, D. E. 1977, ApJ, 211, 675

Couch, W. J., Ellis, R. S., Malin, D. F., & Maclaren, I. 1991, MNRAS, 249, 606

Croft, R. A. C., Dalton, G. B., Efstathiou, G., Sutherland, W. J., & Maddox, S. J. 1997, MNRAS, 291, 305

Cruddace, R. G., Hasinger, G., Trümper, J., Schmidt, J. H. M. M., Hartner, G. D., Rosso, C., & Snowden, S. L. 1991, Exp. Astr., 1, 365

Dalcanton, J. J. 1996, ApJ, 466, 92

Dalcanton, J. J. 1998, ApJ, 495, 251

Dalton, G. B., Efstathiou, G., Maddox, S. J., & Sutherland, W. J. 1992, ApJ, 390, L1

Dalton, G. B., Efstathiou, G., Maddox, S. J., & Sutherland, W. J. 1994, MNRAS, 269, 151

David, L. P., & Blumenthal, G. 1992, ApJ, 389, 510

David, L. P., Jones, C., & Forman, W. 1995, ApJ, 445, 578

David, L. P., Slyz, A., Jones, C., Forman, W., Vrtilek, S., & Arnaud, K. 1993, ApJ, 412, 479

Davidsen, A., Bowyer, S., Lampton, M., & Cruddace, R. G. 1975, ApJ, 198, 1

Davis, M., Summers, F. J., & Schlegel, D. 1992, Nature, 359, 393

De Grandi, S. 1996, in MPE Report 263, Proceedings of Röntgenstrahlung from the Universe, ed. Zimmermann H. U., Trümper J., Yorke H. (Munich:MPE), 577

De Grandi, S., Molendi, S., Böhringer, H., Chincarini, G., & Voges, W. 1997, ApJ, 486, 738

Donahue, M. 1996, ApJ, 468, 79

Draper, P. W. 1996, Starlink User Note, 139.6

Ebeling, H. 1993, Ph.D. thesis, MPE Report 250, MPE, Garching

Ebeling, H., Böhringer, H., Briel, U. G., Voges, W., Edge, A. C., Fabian, A. C., & Allen, S. W. 1995, in Wide Field Spectroscopy and the Distant Universe, ed. Maddox, S. J., & Aragón-Salamanca, A., (Singapore: World Scientific), 221

Ebeling, H., Edge, A. C., Fabian, A. C., Allen, S. W., Crawford, C. S., & Böhringer, H. 1997, ApJ, 479, L101

Ebeling, H., Voges, W., Böhringer, H., Edge, A. C., Huchra, J. P., & Briel, U. G. 1996, MNRAS, 281, 799

Ebeling, H., & Wiedenmann, G. 1993, Phys. Rev. E, 47, 704

Edge, A. C., & Stewart, G. C. 1991, MNRAS, 252, 414

Edge, A. C., Stewart, G. C., Fabian, A. C., & Arnaud, K. A. 1990, MNRAS, 245, 559

Efstathiou, G. 1996, in Cosmology and Large Scale Structure, Les Houches Summer

School Proceedings, ed. Schaeffer, R., Silk, J., Spiro, M., & Zinn-Justin, J. (Amsterdam: Elsevier Science)

Efstathiou, G., Davis, M., Frenk, C. S., & White, S. D. M. 1985, ApJS, 57, 241

Efstathiou, G., Sutherland, W. J. & Maddox, S. J. 1990, Nature, 348, 705

Eke, V. R., Cole, S., & Frenk, C. S. 1996, MNRAS, 282, 263

Ellis, R. S., Smail, I,, Dressler, A., Couch, W. J., Oemler, A., Butcher, H., & Sharples, R. M. 1997, ApJ, 483, 582

Evrard, A. E. 1989, ApJ, 341, L71

Evrard, A. E. 1990, ApJ, 363, 349

Evrard, A. E., & Henry, J. P. 1991, ApJ, 383, 95

Evrard, A. E., Metzler, C. A., & Navarro, J. F. 1996, ApJ, 469, 494

Fabian, A. C. 1994, ARA&A, 32, 277

Forman, W., & Jones, C. 1994, in Proceedings of 'Cosmological Aspects of X-Ray Clusters of Galaxies', ed. Seitter, W. C., (Dordrecht: Kluwer Academic Publishers), 39

Fort, B., & Mellier Y. 1994, Astron. Astrophys Rev., 5, 239

Frenk, C. S. 1986, Phil. Trans. R. Soc. Lond. A, 330, 517

Frenk, C. S. 1991, Physica Scripta, T36, 70

Frenk, C. S., White, S. D. M., Efstathiou, G., & Davis, M. 1990, ApJ, 351, 10

Fritz, G., Davidsen, A., Meekins, J. F., & Friedman, H. 1971, ApJ, 164, L81

Gehrels, A. 1986, ApJ, 303, 336

Georgantopoulos, I., Stewart, G. C., Shanks, T., Boyle, B. J., & Griffiths, R. E. 1996, MNRAS, 280, 276

Gioia, I. M., & Luppino, G. A. 1994, ApJS, 94, 583

Gioia, I. M., Henry, J. P., Maccacaro, T., Morris, S. L., Stocke, J. T., & Wolter, A. 1990a, ApJ, 356, L35

Gioia, I. M., Maccacaro, T., Schild, R. E., Wolter, A., Stocke, J. T., Morris, S. L.,

& Henry, J. P. 1990b, ApJS, 72, 567

Gunn, J. E., Hoessel, J. G., & Oke, J. B. 1986, ApJ, 306, 30

Gursky, H., Solinger, A., Kellogg, E., Murray, S., Tananbaum, H., Giacconi, R., & Cavaliere, A. 1972, ApJ, 173, L99

Gush, H. P., Halpern, M., & Wishnow, E. 1990, Phys. Rev. Lett., 65, 537

Guyot, M., & Zel'dovich, Ya. B. 1970, A&A, 9, 227

Harrison, E. R. 1970, Phys. Rev. D 1, 2726

Hasinger, G., Boese, G., Predehl, P., Turner, J. T., Yusaf, R., Georgem I. M., & Rohrbach, G. 1994, MPE/OGIP Calibration Memo, CAL/ROS/93-015

Heavens, A. F. 1993, MNRAS, 263, 735

Henry, J. P. 1997, ApJ, 489, L1

Henry, J. P., & Arnaud, K. A. 1991, ApJ, 372, 410

Henry, J. P., Gioia, I. M., Huchra, J. P., Burg, R., Mclean, B., Böhringer, H., Bower, R. G., Briel, U. G., Voges, W., Macgillivray, H., & Cruddace, R. G. 1995, ApJ, 449, 422

Henry, J. P., Gioia, I. M., Maccacaro, T., Morris, S. L., Stocke, J. T., Wolter, A. 1992, ApJ, 386, 408

Henry, J. P., Jiao, L., & Gioia, I. M. 1994, ApJ, 432, 49

Henry, J. P., & Lavery, R. J. 1984, ApJ, 280, 1

Heydon-Dumbleton, N. H., Collins, C. A., & McGillivray, H. T. 1989, MNRAS, 238, 379

Hogg, D. W., Pahre, M. A., McCarthy, J. K., Cohen, J. G., Blandford, R., Smail, I., & Soifer, B. T. 1997, MNRAS, 288, 404

Hubble, E. 1926, ApJ, 64, 231

Hubble, E. 1927, Proc. Nat. Acad. Sci., 15, 168

Hubble, E., & Humason, M. 1931, ApJ, 74, 43

Huchra, J. P., Henry, J. P., Postman, M., & Geller, M. J. 1990, ApJ, 365, 66

Jones, C., & Forman, W. 1984, ApJ, 276, 38

Jones, L. R., Scharf, C., Ebeling, H., Perlman, E., Wegner, G., Malkan, M., & Horner, D. 1998, ApJ, 495, 100

Kaiser, N. 1986, MNRAS. 222, 323

Kaiser, N. 1991, ApJ. 383, 104

Kaiser, K., & Squires, G. 1993, ApJ, 404, 441

Karzas, W., & Latter, R. 1961, ApJS, 6, 167

Katgert, P., Mazure, A., Perea, J., den Hartog, R., Moles, M., Le Fèvre, O., Dubath, P., Focardi, P., Rhee, G., Jones, B., Escalera, E., Biviano, A., Gerbal, D., & Giuricin, G. 1996, A&A, 310, 8

Kellogg, E. M., Baldwin, J. R., & Koch, D. 1975, ApJ, 199, 299

Kellogg, E. M., Gursky, H., Leong, C., Schreier, E., Tananbaum, H., & Giacconi, R. 1971, ApJ, 165, L49

Kellogg, E. M., Murray, S., Giacconi, R., Tananbaum, H., & Gursky, H. 1973, ApJ, 185, L13

King, I. R. 1962, AJ, 67, 471

Kitayama, T., Sasaki, S., & Suto, Y. 1998, PASJ, 50, 1

Kitayama, T., & Suto, Y. 1997, ApJ, 490, 557

Kofman, L. A., Gnedin, N. Y., & Bahcall, N. A. 1993, ApJ, 413, 1

Kolb, E. W. & Turner, M. S. 1990, The Early Universe (Redwood City: Addison Wesley)

Kowalski, M. P., Ulmer, M., & Cruddace, R. G. 1983, ApJ, 268, 540

Lacey, C., & Cole, S. 1993, MNRAS, 262, 627

Lacey, C., & Cole, S. 1994, MNRAS, 271, 676

Lahav, O., Edge, A. C., Fabian, A. C., & Putney, A. 1989, MNRAS, 238, 881

Longair, M. S. 1992, High Energy Astrophysics, Volume 1 (Cambridge: Cambridge University Press)

López-Cruz, O., Yee, H. K. C., Brown, J. P., Jones, C., & Forman, W. 1997, ApJ, 475, L97

Lucey, J. R. 1983, MNRAS, 204, 33

Lumsden, S. L., Nichol, R. C., Collins, C. A., & Guzzo, L. 1992, MNRAS, 258, 1

Maddox, S. J., Efstathiou, G., Sutherland, W. J., & Loveday, J. 1990, MNRAS, 242, 43p

Manrique, A., & Salvador-Solé, E. 1995, ApJ, 453, 6

Markevitch, M. 1996, ApJ, 465, L1

Markevitch, M. Mushotzky, R. F., Inque, H., Yamashita, K., Furuzawa, A., & Tawara, Y. 1996, ApJ, 456, 437

Marshall, F. J., & Clark, G. W. 1984, ApJ, 287, 633

Mathiesen, B., & Evrard, A. E. 1998, MNRAS, 295, 769

Meekins, J. F., Gilbert, F., Chubb, T. A., Friedman, H., & Henry, R. C. 1971, Nature, 231, 107

Mewe, R., Gronenschild, E. H. B. M., & van den Oord, G. H. J. 1985, A&AS, 62, 197

Mészáros, P. 1974, A&A, 37, 225

Mitchell, R. J., Culhane, J. L., Davison, P. J., & Ives, J. C., 1976, MNRAS, 176, 29p

Morrison, R., & McCammon, D. 1983, ApJ, 270, 119

Mushotzky, R. F., & Scharf, C. A. 1997, ApJ, 482, L13

Navarro, J. F., Frenk, C. S., & White, S. D. M. 1995, MNRAS, 275, 720

Nath, B. B. & Chiba, M. S. 1995, ApJ, 454, 604

Nichol, R. C., Collins, C. A., Guzzo, L., & Lumsden, S. L. 1992, MNRAS, 255, 21p

Nichol, R. C., Holden, B. P., Romer, A. K., Ulmer, M. P., Burke, D. J., & Collins, C. A. 1997, ApJ, 481, 644

Oukbir, J., Bartlett, J. G., & Blanchard, A. 1997, A&A, 320, 365

Padmanabhan, T. 1993, Structure formation in the universe (Cambridge: Cambridge University Press)

Peebles, P. J. E. 1980, The Large-Scale Structure of the Universe (Princeton: Princeton University Press)

Peebles, P. J. E. 1982, ApJ, 258, 415

Peebles, P. J. E. 1993, Principles of Physical Cosmology (Princeton: Princeton University Press)

Penzias, A. A., & Wilson, R. W. 1965, ApJ, 142, 419

Piccinotti, G., Mushotzky, R. F., Boldt, E. A., Holdt, S. S., Marshall, F. E., Selemitsos, P. J., & Shafer, R. A. 1982, ApJ, 253, 485 1982

Pildis, R. A., Bregman, J. N., & Evrard, A. E. 1995, ApJ, 443, 514

Press, W. H., & Schechter, P. 1974, ApJ, 187, 425

Press, W. H., Teukolsky, S. A., Vetterling, W. T., & Flannery, B. P. 1992, Numerical Recipes in C: the art of scientific computing (Cambridge: Cambridge University Press)

Postman, M., Geller, M. J., & Huchra, J. P. 1986, AJ, 91, 1267

Postman, M., Huchra, J. P., & Geller, M. J. 1992, ApJ, 384, 404

Postman, M., Lubin, L. M., Gunn, J. E., Oke, J. B., Hoessel, J. G., Schneider, D. P., & Christensen, J. A. 1996, AJ, 111, 615

Qin, Y. P., & Xie, G. Z. 1997, ApJ, 486, 100

Raymond, J. C., & Smith, B. W. 1977, ApJS, 35, 419

Roche, N., Shanks, T., Almaini, O., Boyle, B. J., Georgantopoulos, I., Stewart, G. C., & Griffiths, R. E. 1995, MNRAS, 276, 706

Romer, A. K. 1996, Ph.D. thesis, ROE, Edinburgh

Romer, A. K., Collins, C. A. Böhringer, H., Ebeling, H., Cruddace, R. C., & MacGillivray, H. T. 1994, Nature, 372, 75

Rosti, P., Della Ceca, R., Burg, R., Norman, C., & Giacconi, R. 1995, ApJ, 445, L11

Sachs, R. K., & Wolfe, A. M. 1967, ApJ, 147, 73

Sarazin, C. L. 1988, X-ray emission from clusters of galaxies (Cambridge: Cambridge University Press)

Savaglio, S., Benetti S., & Pasquini, L. 1997, EFOSC-I Operating Manual

Scaramella, R., Zamorani, G., Vettolani, G., & Chincarini, G. 1991, AJ, 101, 342

Scharf, C. A., Jones, L. R., Ebeling, H., Perlman, E., Malkan, M., & Wegner, G. 1997, ApJ, 477, 79

Schechter, P. 1976, ApJ, 203, 297

Schmidt, M. 1968, ApJ, 151, 393

Serlemitsos, P. J., Smith, B. W., Boldt, E. A., Holt, S. S., & Swank, J. H., 1977, ApJ, 211, L63

Shortridge, K., Meyerdierks, H., Currie, M., & Clayton M. 1997, Starlink User Note, 86.13

Slezak, E., de Lapparent, V., & Bijaoui, A. 1993, ApJ, 409, 517

Smail, I., Hogg, D. W., Yan, L., & Cohen, J. G. 1995, ApJ, 449, L105

Smith, S. 1936, ApJ, 83, 23

Smoot, G. F., Bennett, C. L., Kogut, A., Wright, E. L., Aymon, J., Boggess, N. W., Cheng, E. S., De Amici, G., Gulkis, S., Hauser, M. G., Hinshaw, G., Jackson, P. D., Janssen, M., Kaita, E., Kelsall, T., Keegstra, P., Lineweaver, C., Loewenstein, K., Lubin, P., Mather, J., Meyer, S. S., Moseley, S. H., Murdock, T., Rokke, L., Silverberg, R. F., Tenorio, L., Weiss, R., & Wilkinson, D. T. 1992, ApJ, 396, L1

Snowden, S. L., McCammon, D., Burrows, D. N., & Mendehall, J. A. 1994, ApJ, 424, 714

Stanford, S. A., Eisenhardt, P. R., & Dickinson, M. 1997, ApJ, in press

Strubble, M. F., & Rood, H. J. 1991, ApJ, 374, 395

Sunyaev R. A., & Zel'dovich Ya. B. 1972, Comm. Astrophys. Space Phys. 4, 173

Sutherland, W. J. 1988, MNRAS, 234, 159

Taylor, A. N., & Rowan-Robinson, M. 1992, Nature, 359, 396

Tinney, C. G. 1996, The AAO CCD Imaging Manual, AAO User Manual 35

Trentham, N. 1994, Nature, 372, 157

Tyson, T. A. 1988, AJ, 96, 1

Vikhlinin, A., Forman, W., Jones, C., & Murray, S. 1995a, ApJ, 451, 542

Vikhlinin, A., Forman, W., Jones, C., & Murray, S. 1995b, ApJ, 451, 564

Walker, T. P., Steigman, G., Schramm, D. N., Olive, K. A., & Kang, H. 1991, ApJ, 378, 186

Weinberg, S. 1972, Gravitation and cosmology: Principles and applications of the general theory of relativity, (New York: Wiley)

White, D. A., & Fabian, A. C. 1995, MNRAS, 273 72

White, M., Scott, D., Silk, J., & Davis, M. 1995, MNRAS, 276, 69p

White, S. D. M., Frenk, C. S., & Davis, M. 1983, ApJ, 274, L1

White, S. D. M., Frenk, C. S., Davis, M., & Efstathiou, G. 1987, ApJ, 313, 505

White, S. D. M., Navarro, J. F., Evrard, A. E., & Frenk, C. S. 1993, Nature, 366, 429

Wilson, G., Cole, S., & Frenl, C. S. 1996, MNRAS, 280, 199

Yee, H. K. C., Ellingson, E., & Carlberg, R. G. 1996, ApJS, 102, 269

Zaritsky, D., Nelson, A. E., Dalcanton, J. J., & Gonzalez, A. H. 1997, ApJ, 480, L91

Zel'dovich, Ya. B. 1972, MNRAS, 160, 1p

Zwicky, F. 1933, Helvetica Physica Acta, 6, 110

Zwicky, F., Herzog, E., & Wild, P. 1968, Catalog of Galaxies and of Clusters of Galaxies (Pasadena: California Institute of Technology)

Appendix A

ROSAT PSPC fields

The following table lists the fields used in the cluster survey presented in this thesis. The column labelled ROR refers to the identification number of the ROSAT observation. The co-ordinates refer to the centre of the X-ray pointing and are equinox 2000. The column labelled $n_{\rm H}$ lists the Galactic Hydrogen column density of the field centre, taken from the compilation of Marshall & Clark (1984), and is in units of 10^{20} cm^{-2}. The columns labelled Time give the original, and cleaned (Section 2.2.3), exposure times of the observation, and are in units of seconds. The column labelled background lists the average background surface-brightness level of each field, and is in units of 10^{-4} counts s^{-1} arcmin^{-2}.

ROR	RA			Declination			$n_{\rm H}$	Time		Background
	h	m	s	°	′	″		Original	Cleaned	
800566	03	03	31.2	−15	40	48	2.92	14681	12209	1.45
701036	03	15	09.6	−55	13	48	1.79	45788	44925	1.92
800555	03	17	57.6	−02	57	00	5.67	13757	12353	2.19
800371	03	23	12.0	−51	05	24	2.25	21624	20651	1.81
800367	03	32	57.6	−39	06	36	2.33	15138	14794	2.18
300079	03	37	55.2	−25	21	00	1.57	50058	47278	4.06
900632	03	42	12.0	−44	07	48	1.67	51918	43552	2.23
800171	04	12	55.2	−65	51	00	5.02	20861	20467	4.41
600623	04	15	28.8	−55	37	12	2.07	15320	14547	2.56
600456	04	20	00.0	−54	56	24	1.86	17808	16520	2.14
300221	04	53	26.3	−42	13	48	2.13	12676	11754	1.57
600436	04	54	14.4	−53	21	36	2.12	22487	21861	1.72

ROR	RA			Declination			n_H	Time		Background
	h	m	s	°	′	″		Original	Cleaned	
701557	05	02	07.2	+03	31	48	7.21	11477	11284	2.40
700233	05	05	50.4	−28	35	24	1.73	22018	17618	3.83
800368	05	13	33.6	−48	18	36	2.03	23622	21661	2.24
300130	05	29	28.7	−58	54	36	3.26	14451	13649	2.19
200638	06	48	12.0	−61	55	48	5.92	10562	10390	2.12
800370	08	47	40.7	+17	54	00	3.72	21792	16835	2.17
700436	08	58	40.8	+14	09	00	4.26	21580	20060	1.91
701458	09	45	43.2	−14	19	48	5.23	18602	17700	1.57
701587	09	47	45.6	+07	25	12	4.02	11045	10633	1.97
800359	10	00	21.6	−19	39	00	5.20	13129	12437	2.40
600178	10	02	00.0	−08	09	36	5.80	14468	13374	2.28
201243	10	37	04.8	−00	08	24	4.79	18111	17393	1.52
800366	10	46	04.8	−00	24	00	3.80	18711	17990	1.93
600420	11	42	09.6	+10	16	48	1.80	11719	11412	2.99
600113	11	51	02.4	−28	48	36	6.06	15097	14693	2.47
701202	12	01	14.3	−03	40	48	3.38	13563	13134	2.35
201367	12	04	25.7	−03	40	19	3.51	32219	30589	2.04
800421	12	14	21.6	+13	05	24	2.01	14310	13732	3.34
600166	12	19	09.6	+03	51	36	1.89	12865	11567	3.51
600587	12	26	28.8	+09	01	12	1.75	23368	16986	3.98
600437	12	36	48.0	+13	10	12	1.68	17988	17368	6.63
300093	12	52	24.0	−29	15	00	6.86	15751	14726	7.42
800393	12	53	33.5	+15	42	36	2.07	13575	12781	5.06
800374	12	58	26.3	−28	26	24	6.69	13689	10932	2.76
800384	13	01	02.4	−32	26	24	5.58	15302	11255	3.58
300219	13	13	16.7	−32	59	24	5.07	13752	13447	3.99
600419	13	25	19.2	−38	24	36	5.33	20136	18845	6.11
600188	13	37	00.0	−29	52	12	4.69	23364	22221	4.43
800369	13	44	04.8	−00	10	48	3.14	21108	17228	3.02
800637	13	49	02.4	−07	12	36	2.78	18864	14979	3.51
701500	13	54	07.2	−02	05	59	3.99	17835	14334	2.85
700257	15	04	02.4	+10	26	24	2.83	17185	16399	12.17
201597	18	53	04.7	−50	10	48	6.33	22136	21464	6.05
300272	19	35	48.0	−46	40	48	5.09	22670	21234	4.39
700488	20	09	26.3	−48	49	48	4.57	11487	11415	5.83
700547	20	37	31.2	−22	42	36	4.60	12291	11250	3.94
300218	20	38	14.3	−01	21	00	5.98	20668	20344	2.55
201374	20	47	45.6	−36	35	24	6.07	29899	28778	2.82
700538	20	52	02.4	−57	04	12	4.83	19283	18671	3.32
300389	21	07	55.2	−05	16	12	5.00	36737	28104	2.18
900133	21	14	24.0	−67	47	24	3.03	27530	22522	5.90
800336	21	39	07.1	−42	51	36	2.22	13894	13431	3.29
800344	21	56	04.8	+01	19	48	4.65	13770	12866	2.17
800419	22	02	04.8	−31	58	12	1.59	13525	12964	4.74
700516	22	03	04.8	−18	55	12	2.69	25168	22370	2.88
600177	23	04	36.0	−51	28	12	1.57	15275	14480	2.74
701250	23	04	43.2	−08	41	24	3.54	18767	16616	1.92
201339	23	05	24.0	−35	52	12	2.10	13588	10496	2.77
400144	23	14	00.0	−49	39	36	1.71	19246	18910	2.93
300220	23	16	02.4	−05	27	00	3.78	15605	13648	1.95
600439	23	20	31.2	+17	13	48	3.95	11241	10569	2.61
701205	23	43	31.2	−14	55	12	2.37	14434	11356	2.87
800357	23	47	26.3	−02	18	36	3.57	13886	12050	2.94
800372	23	59	16.7	−32	17	24	1.56	18789	16222	2.09

Appendix B

Source images

The following pages in this Appendix show the DSS images of the 103 extended sources, detected in Chapter 2, in order of increasing Right Ascension. The images are extracted from the DSS and are six arcminute square, centred on the X-ray co-ordinates, with North to the top and East to the left. The title of each image gives both the name and ID of the source — details of what the ID values mean are given in Appendix C. The contours show the smoothed X-ray photon image: the levels are $2^{n-1} \times 3\sigma$ above the background value, where n is a positive integer and the background and σ values were calculated from the smoothed image, after blanking out the sources. The dotted line visible in some of the plots (e.g. RX J0321.9−5119) indicates the edge of the X-ray image, corresponding to the support structure of the PSPC, and is drawn at 19.2′ from the field centre.

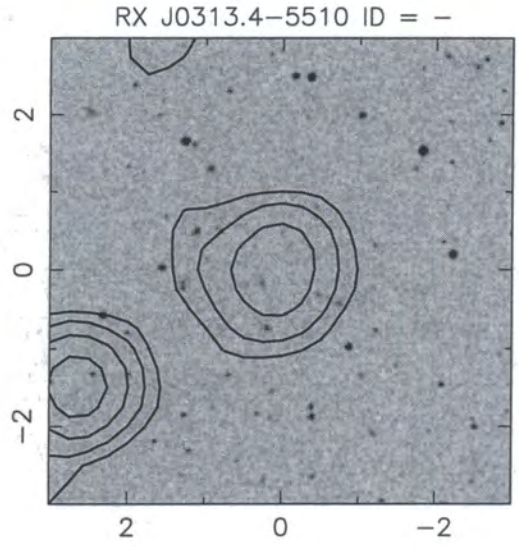
RX J0313.4−5510 ID = −
2
0
−2
2
0
−2

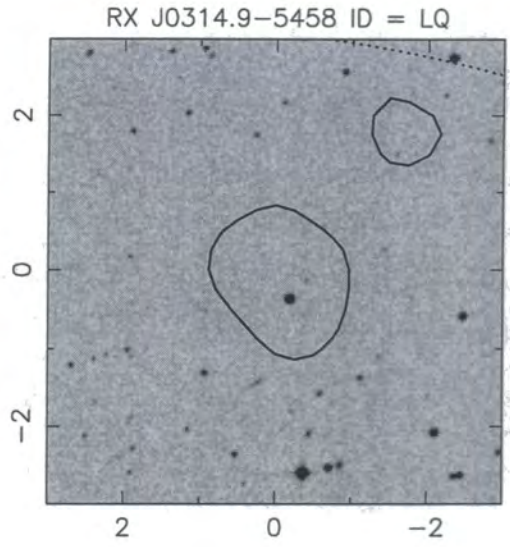
RX J0314.9−5458 ID = LQ
2
0
−2
2
0
−2

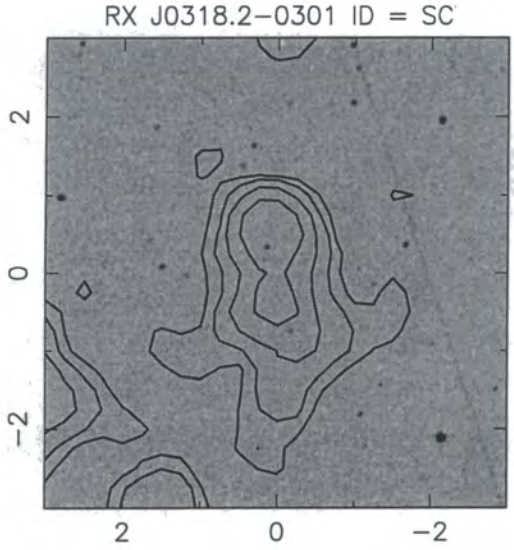
RX J0318.2−0301 ID = SC
2
0
−2
2
0
−2

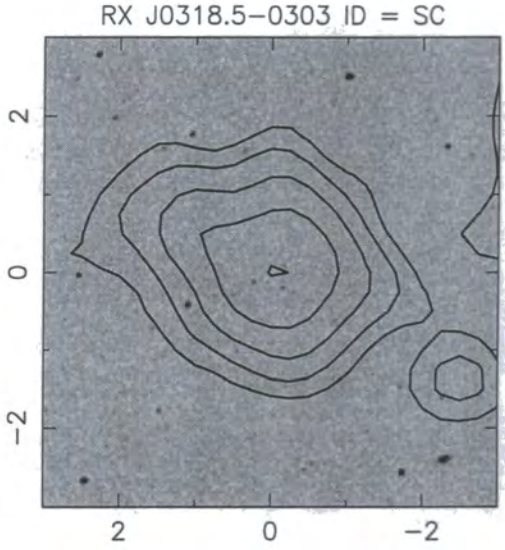
RX J0318.5−0303 ID = SC
2
0
−2
2
0
−2

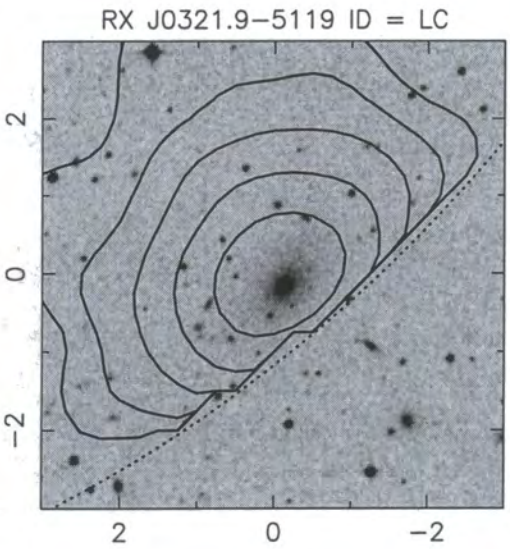
RX J0321.9−5119 ID = LC
2
0
−2
2
0
−2

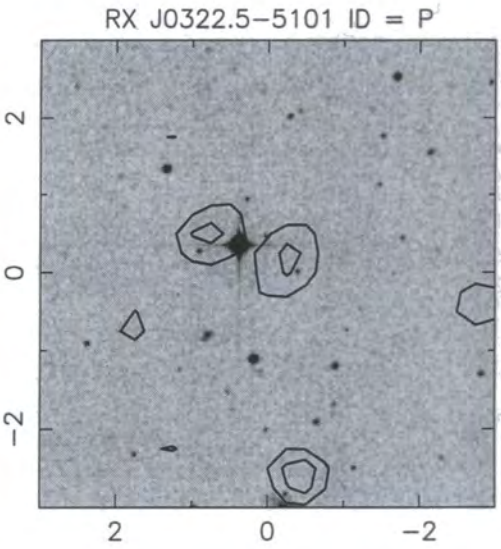
RX J0322.5−5101 ID = P
2
0
−2
2
0
−2

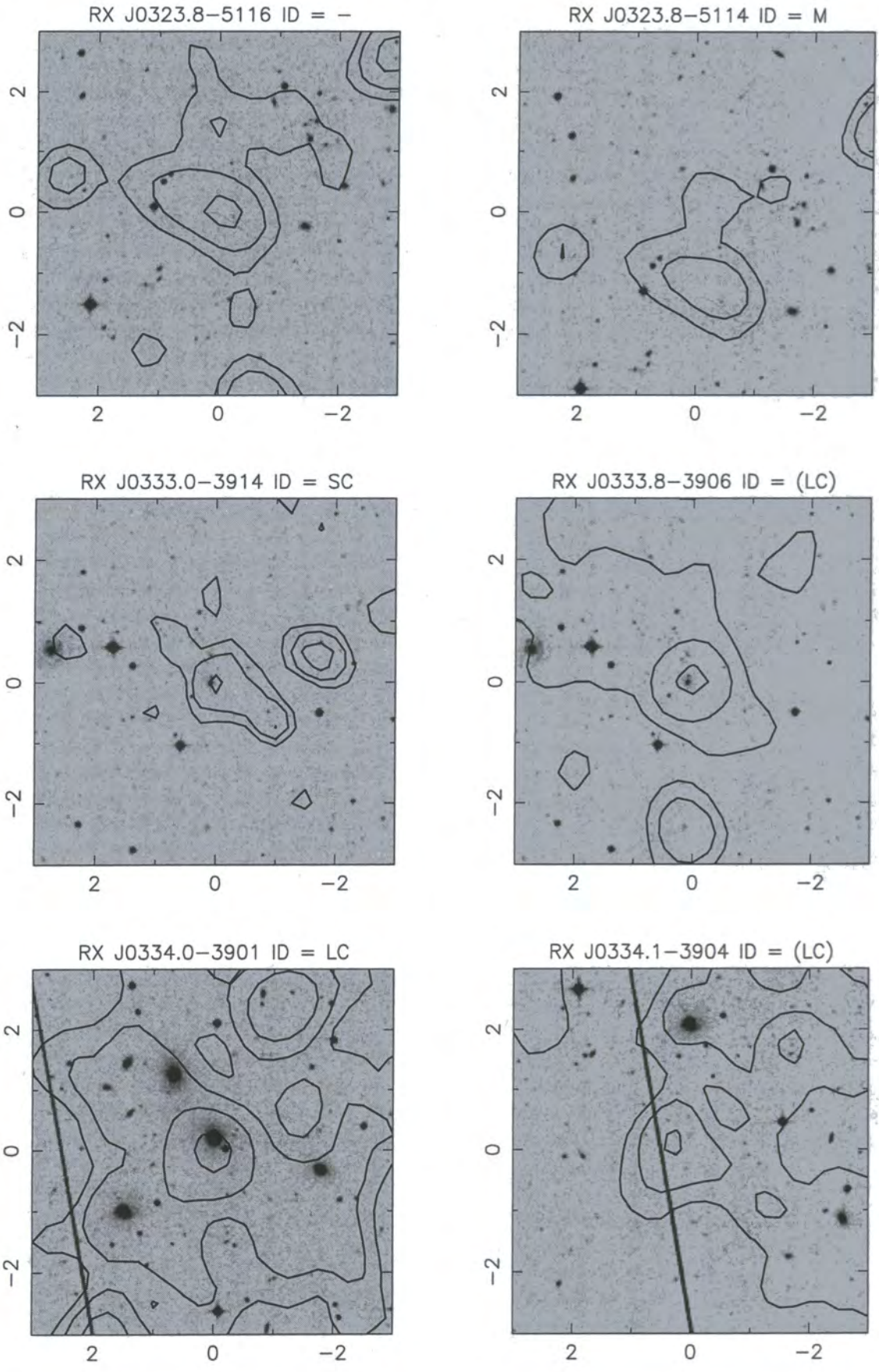
RX J0323.8−5116 ID = −
RX J0323.8−5114 ID = M
RX J0333.0−3914 ID = SC
RX J0333.8−3906 ID = (LC)
RX J0334.0−3901 ID = LC
RX J0334.1−3904 ID = (LC)
2
0
−2

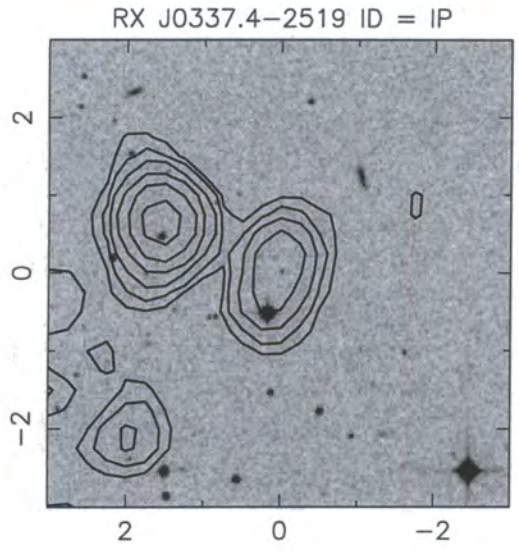
RX J0337.4−2519 ID = IP
2
0
−2
2
0
−2

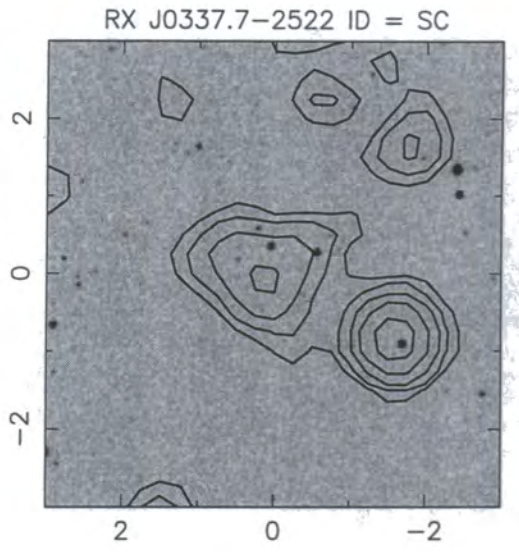
RX J0337.7−2522 ID = SC
2
0
−2
2
0
−2

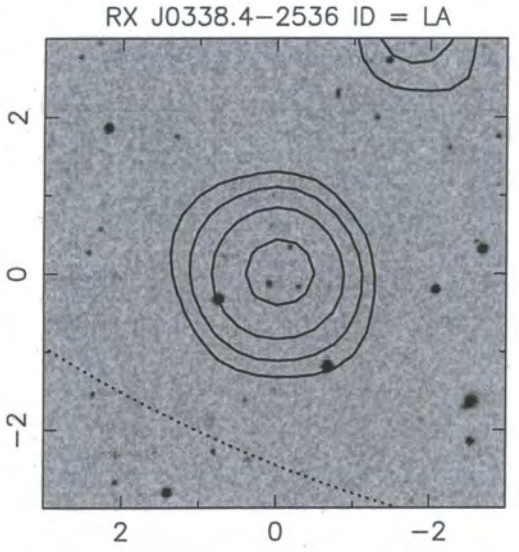
RX J0338.4−2536 ID = LA
2
0
−2
2
0
−2

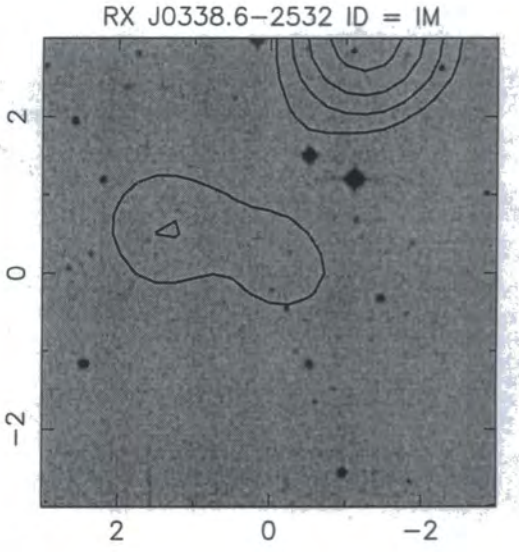
RX J0338.6−2532 ID = IM
2
0
−2
2
0
−2

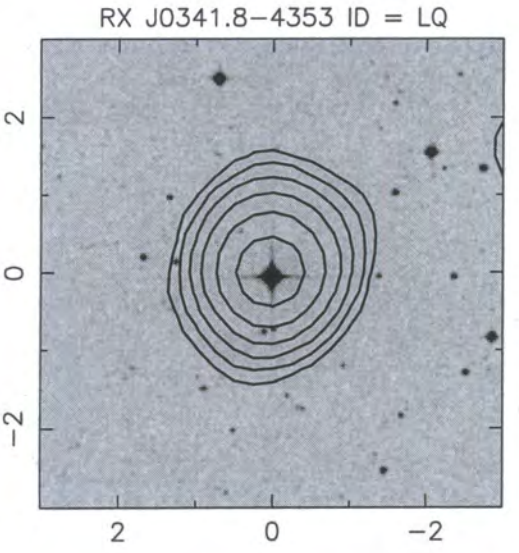
RX J0341.8−4353 ID = LQ
2
0
−2
2
0
−2

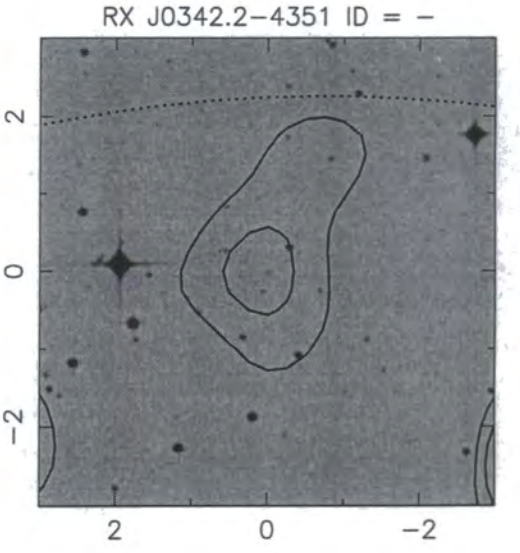
RX J0342.2−4351 ID = −
2
0
−2
2
0
−2

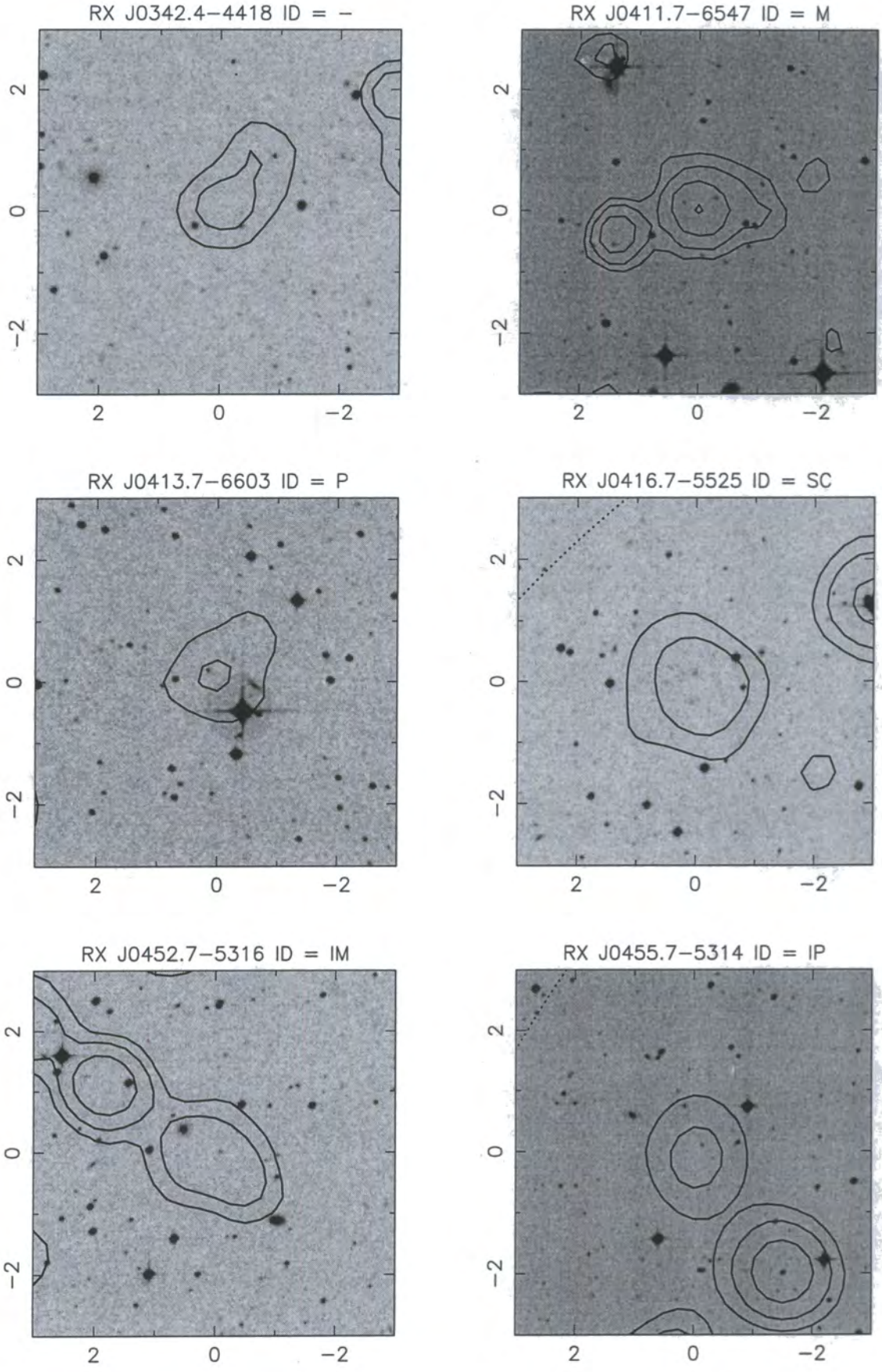
RX J0342.4−4418 ID = −
RX J0411.7−6547 ID = M
RX J0413.7−6603 ID = P
RX J0416.7−5525 ID = SC
RX J0452.7−5316 ID = IM
RX J0455.7−5314 ID = IP
2
0
−2

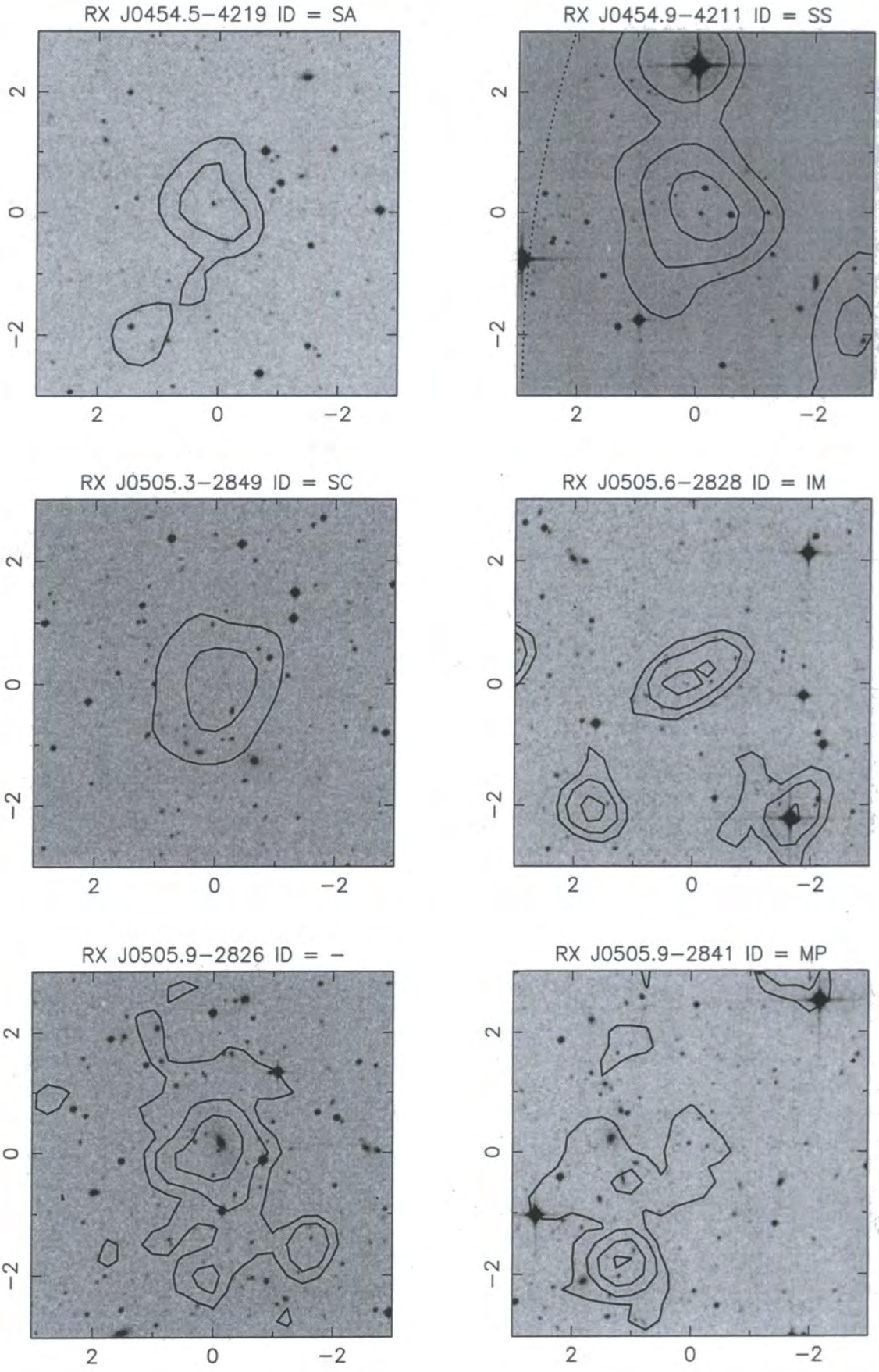
RX J0454.5−4219 ID = SA
RX J0454.9−4211 ID = SS
RX J0505.3−2849 ID = SC
RX J0505.6−2828 ID = IM
RX J0505.9−2826 ID = −
RX J0505.9−2841 ID = MP
2
0
−2

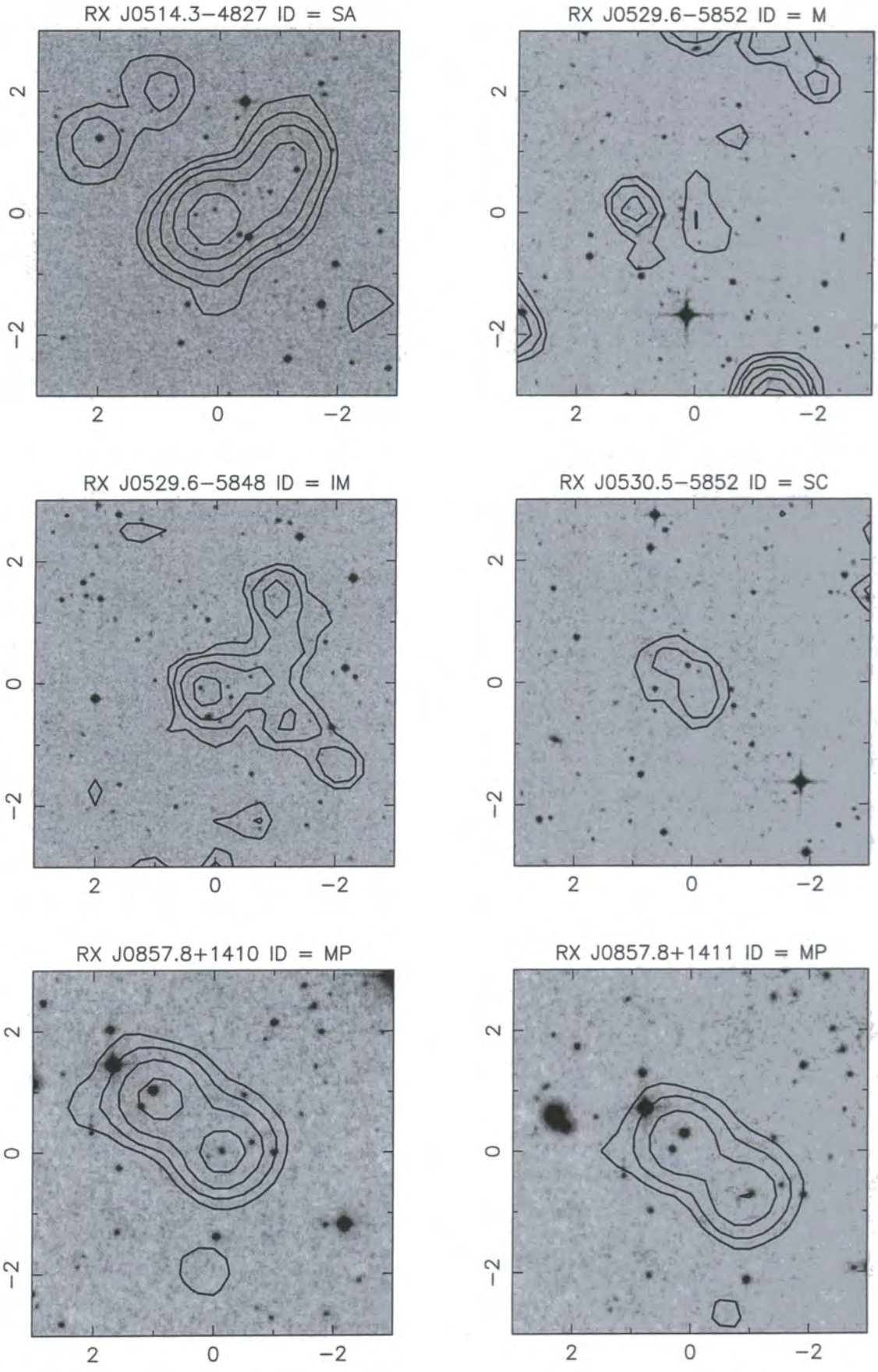
RX J0514.3−4827 ID = SA
RX J0529.6−5852 ID = M
RX J0529.6−5848 ID = IM
RX J0530.5−5852 ID = SC
RX J0857.8+1410 ID = MP
RX J0857.8+1411 ID = MP
2
0
−2

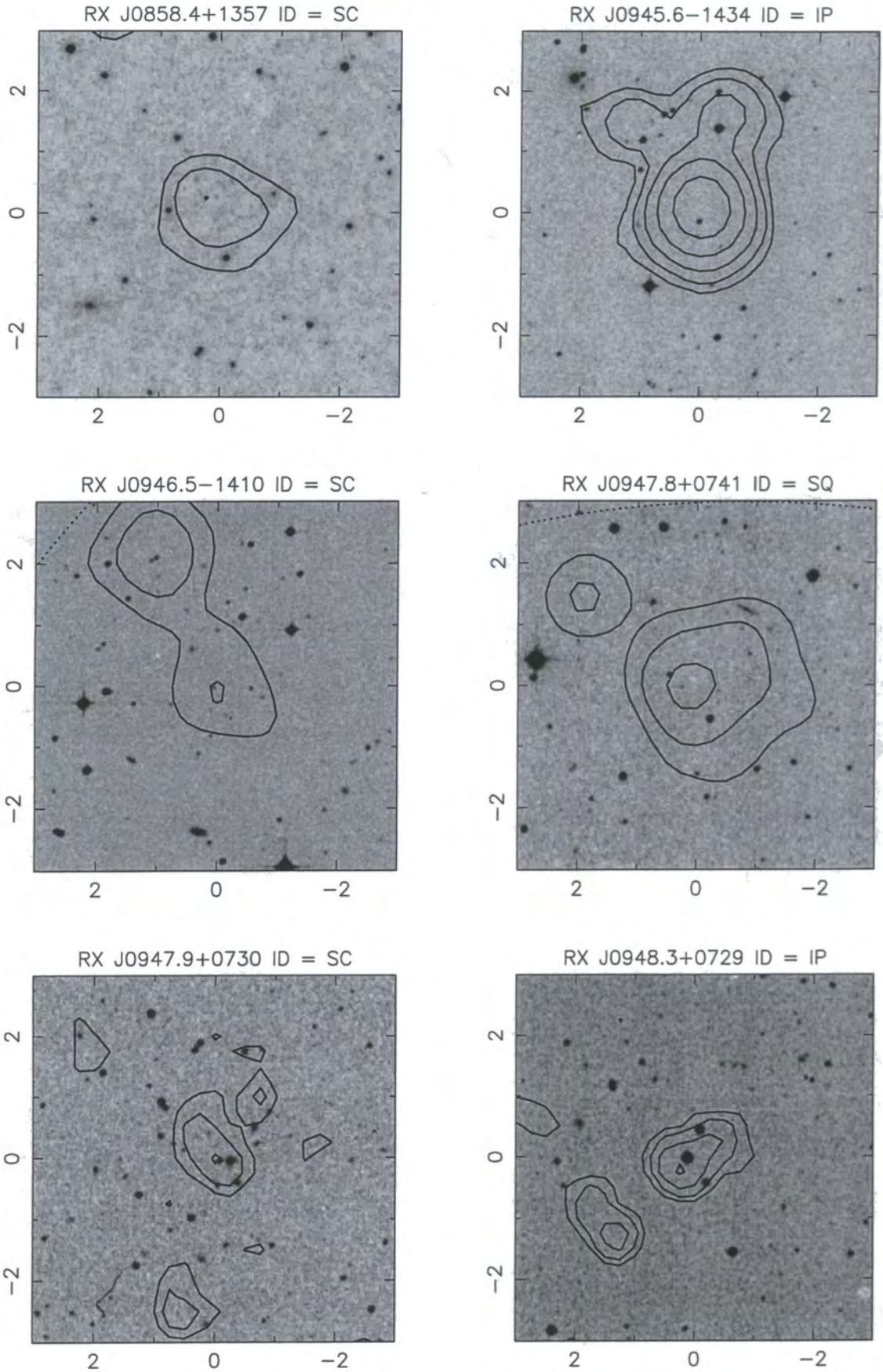
RX J0858.4+1357 ID = SC
RX J0945.6−1434 ID = IP
RX J0946.5−1410 ID = SC
RX J0947.8+0741 ID = SQ
RX J0947.9+0730 ID = SC
RX J0948.3+0729 ID = IP
2
0
−2

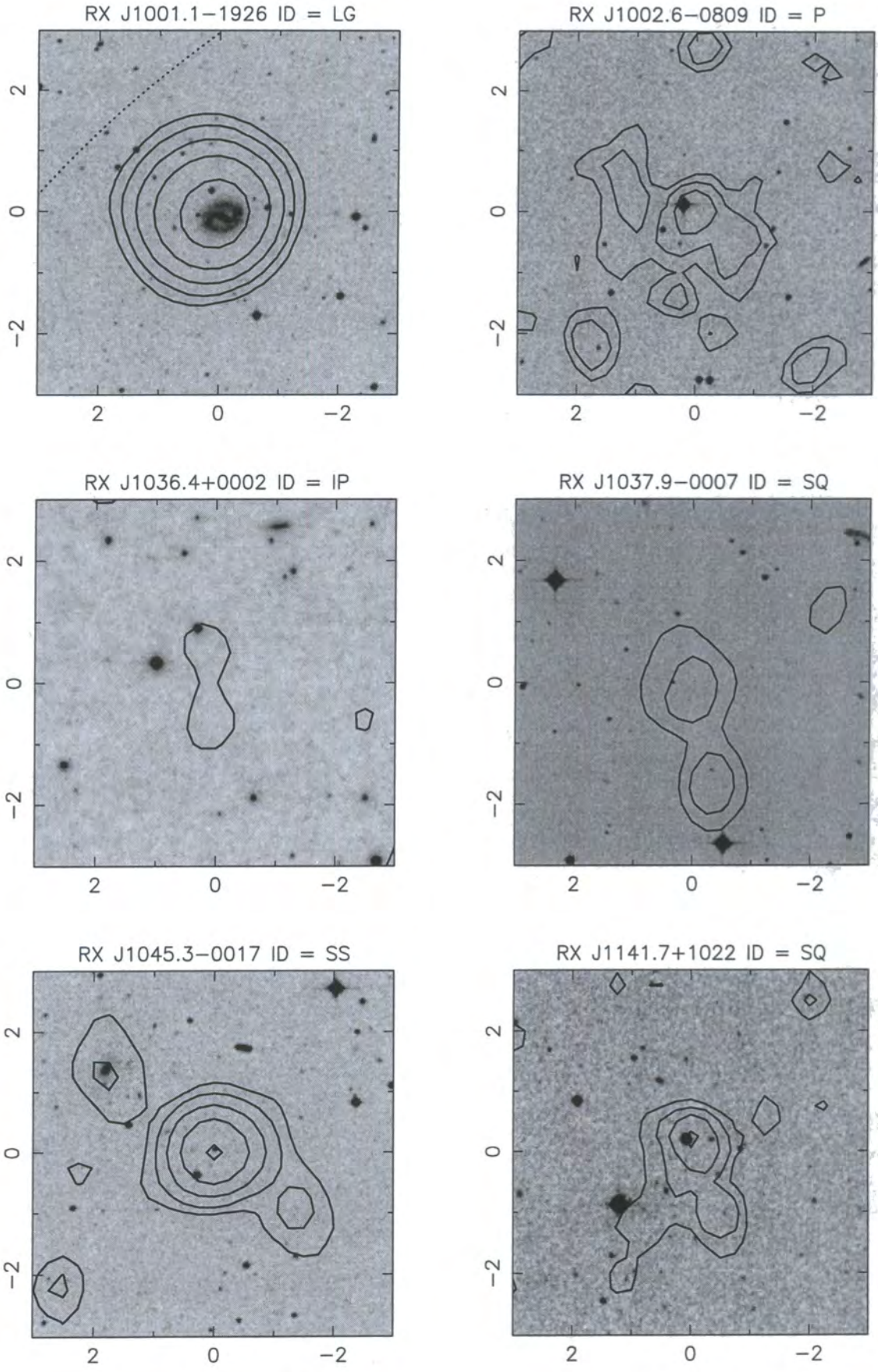
RX J1001.1−1926 ID = LG
RX J1002.6−0809 ID = P
RX J1036.4+0002 ID = IP
RX J1037.9−0007 ID = SQ
RX J1045.3−0017 ID = SS
RX J1141.7+1022 ID = SQ
2
0
−2

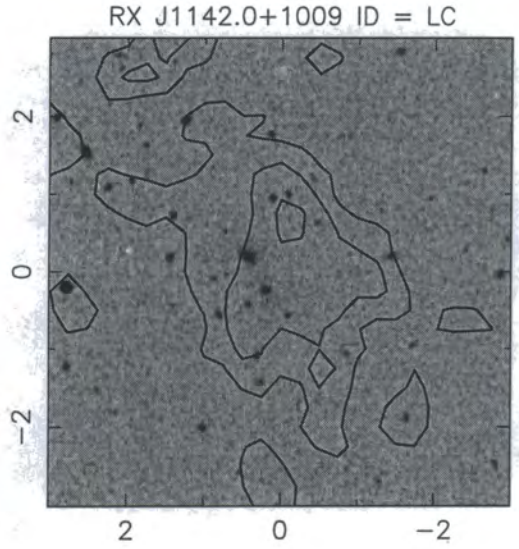
RX J1142.0+1009 ID = LC
2
0
−2
2
0
−2

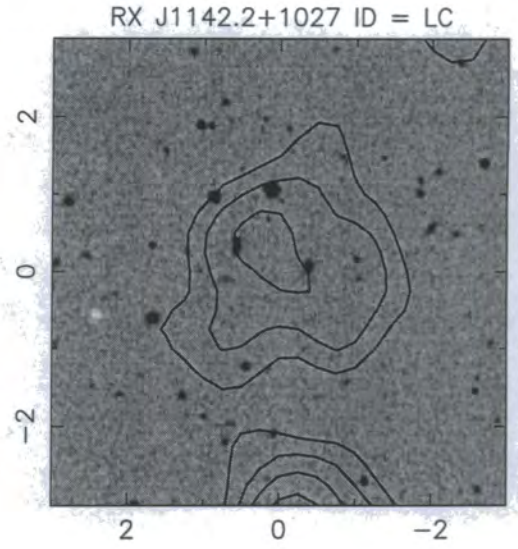
RX J1142.2+1027 ID = LC
2
0
−2
2
0
−2

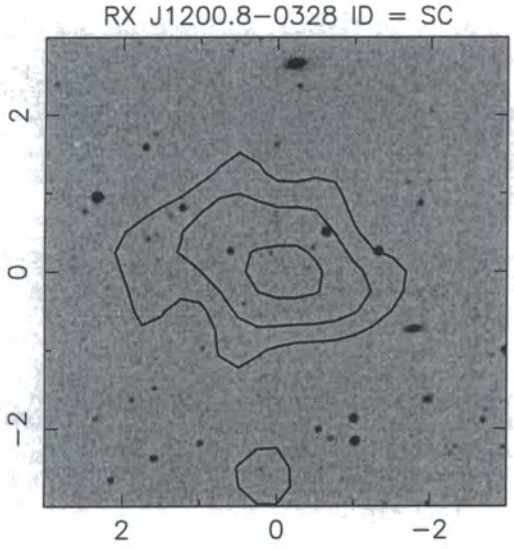
RX J1200.8−0328 ID = SC
2
0
−2
2
0
−2

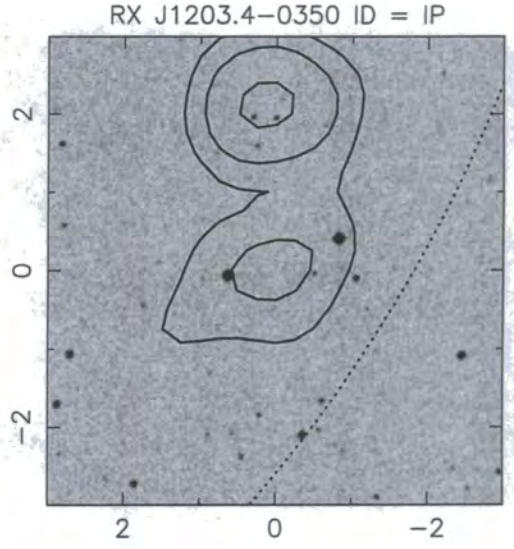
RX J1203.4−0350 ID = IP
2
0
−2
2
0
−2

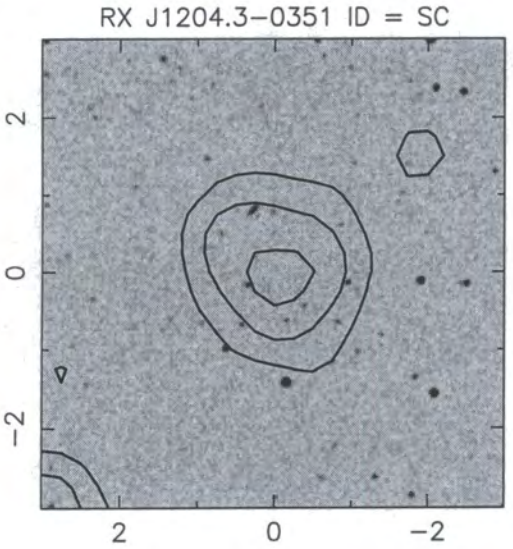
RX J1204.3−0351 ID = SC
2
0
−2
2
0
−2

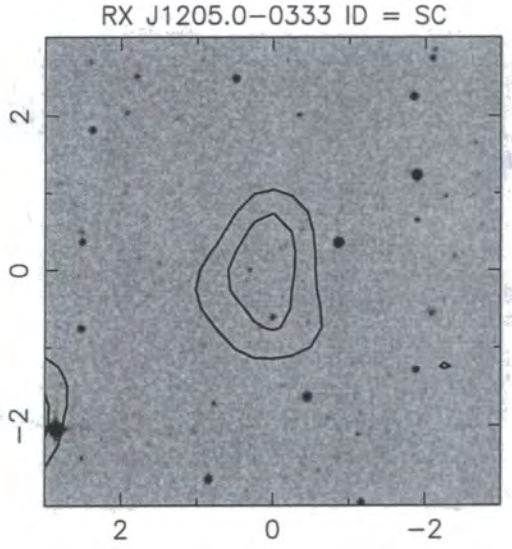
RX J1205.0−0333 ID = SC
2
0
−2
2
0
−2

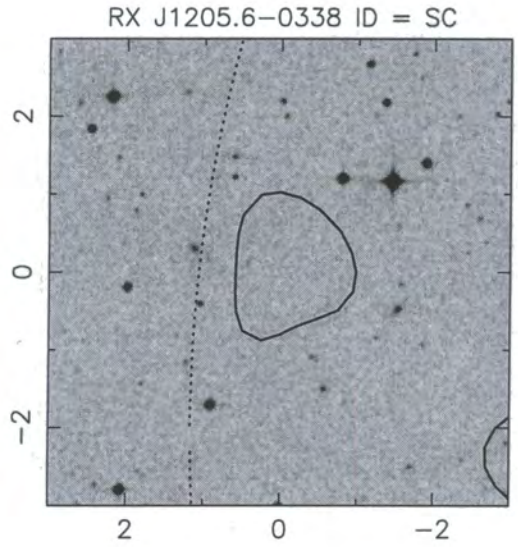
RX J1205.6−0338 ID = SC
2
0
−2
2
0
−2

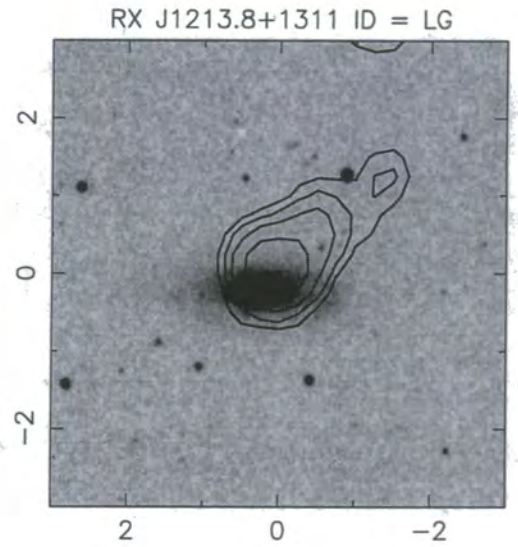
RX J1213.8+1311 ID = LG
2
0
−2
2
0
−2

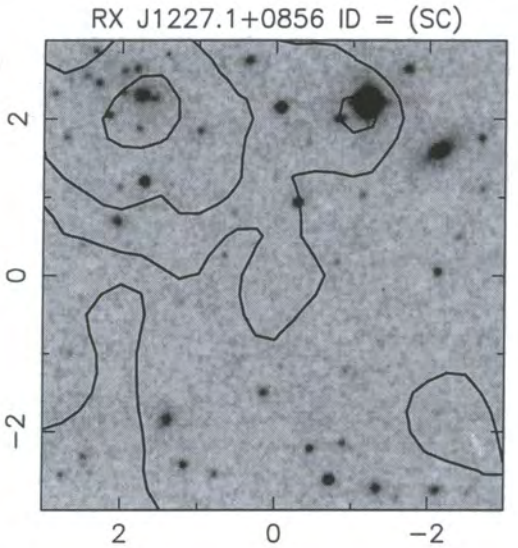
RX J1227.1+0856 ID = (SC)
2
0
−2
2
0
−2

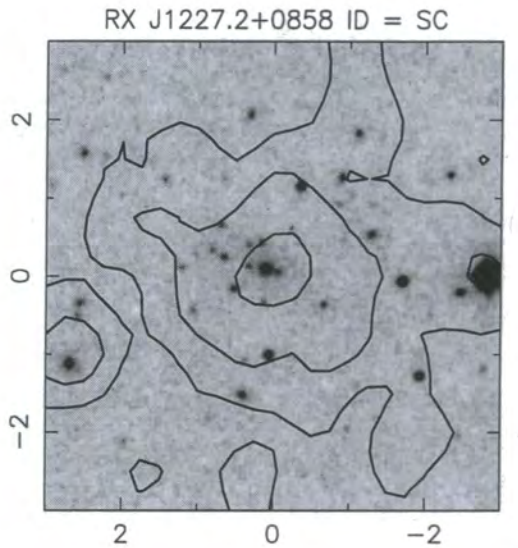
RX J1227.2+0858 ID = SC
2
0
−2
2
0
−2

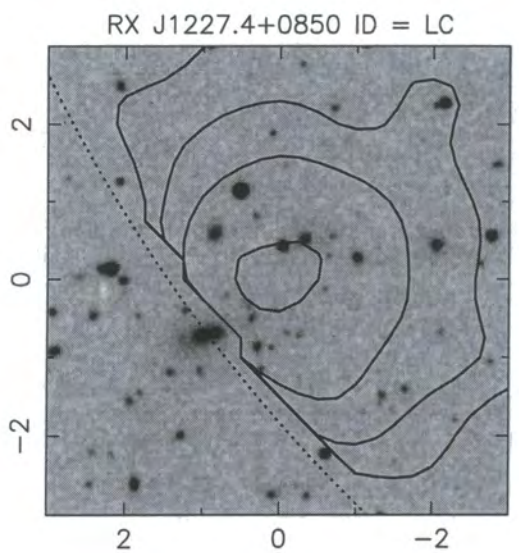
RX J1227.4+0850 ID = LC
2
0
−2
2
0
−2

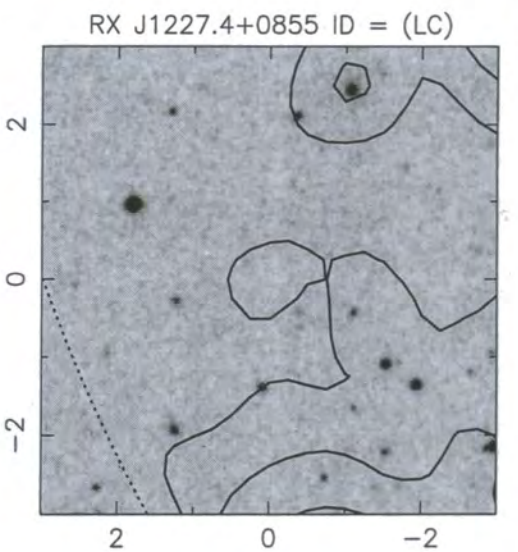
RX J1227.4+0855 ID = (LC)
2
0
−2
2
0
−2

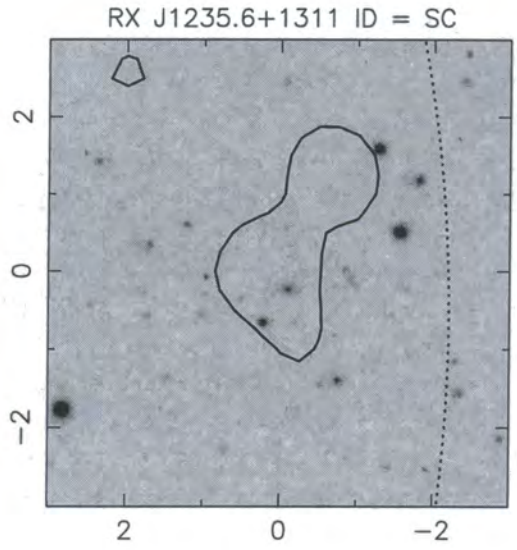
RX J1235.6+1311 ID = SC
2
0
−2
2
0
−2

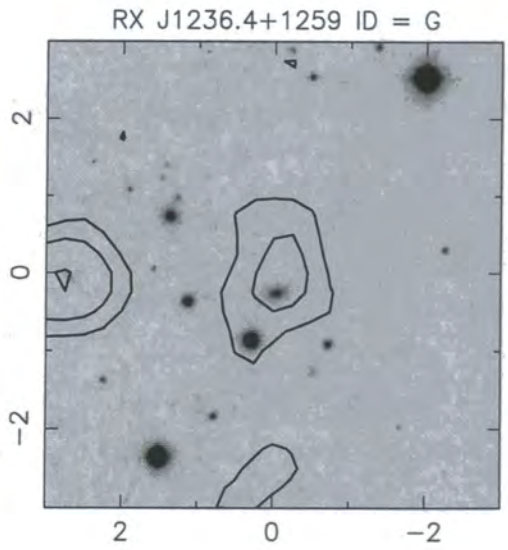
RX J1236.4+1259 ID = G
2
0
−2
2
0
−2

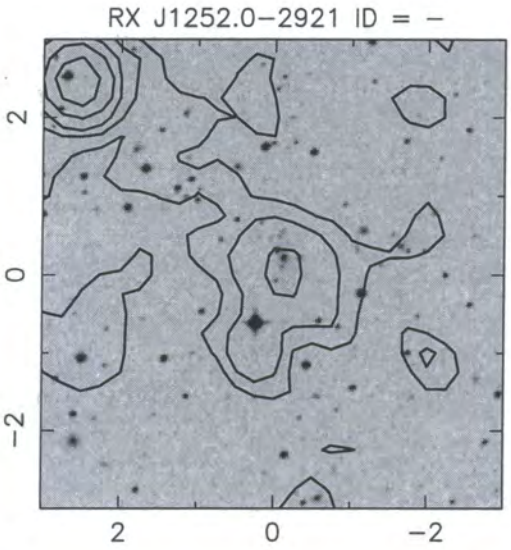
RX J1252.0−2921 ID = −
2
0
−2
2
0
−2

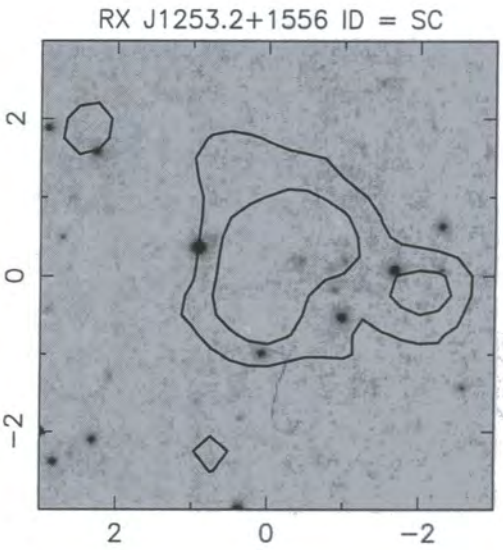
RX J1253.2+1556 ID = SC
2
0
−2
2
0
−2

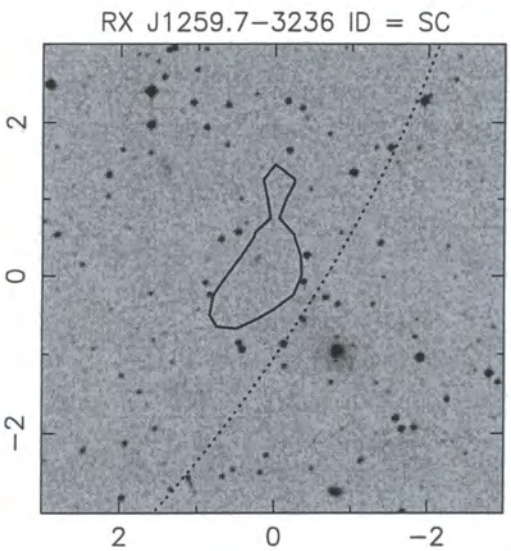
RX J1259.7−3236 ID = SC
2
0
−2
2
0
−2

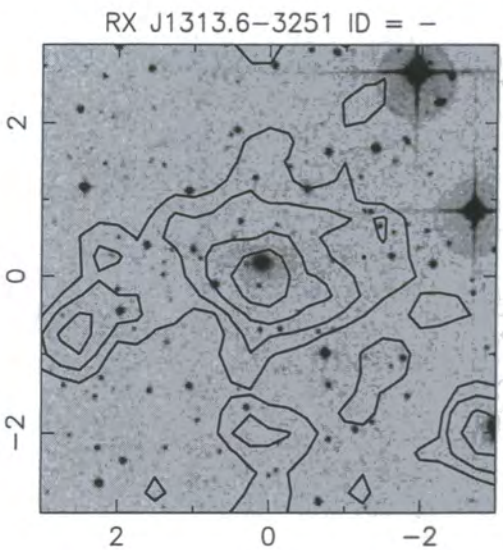
RX J1313.6−3251 ID = −
2
0
−2
2
0
−2

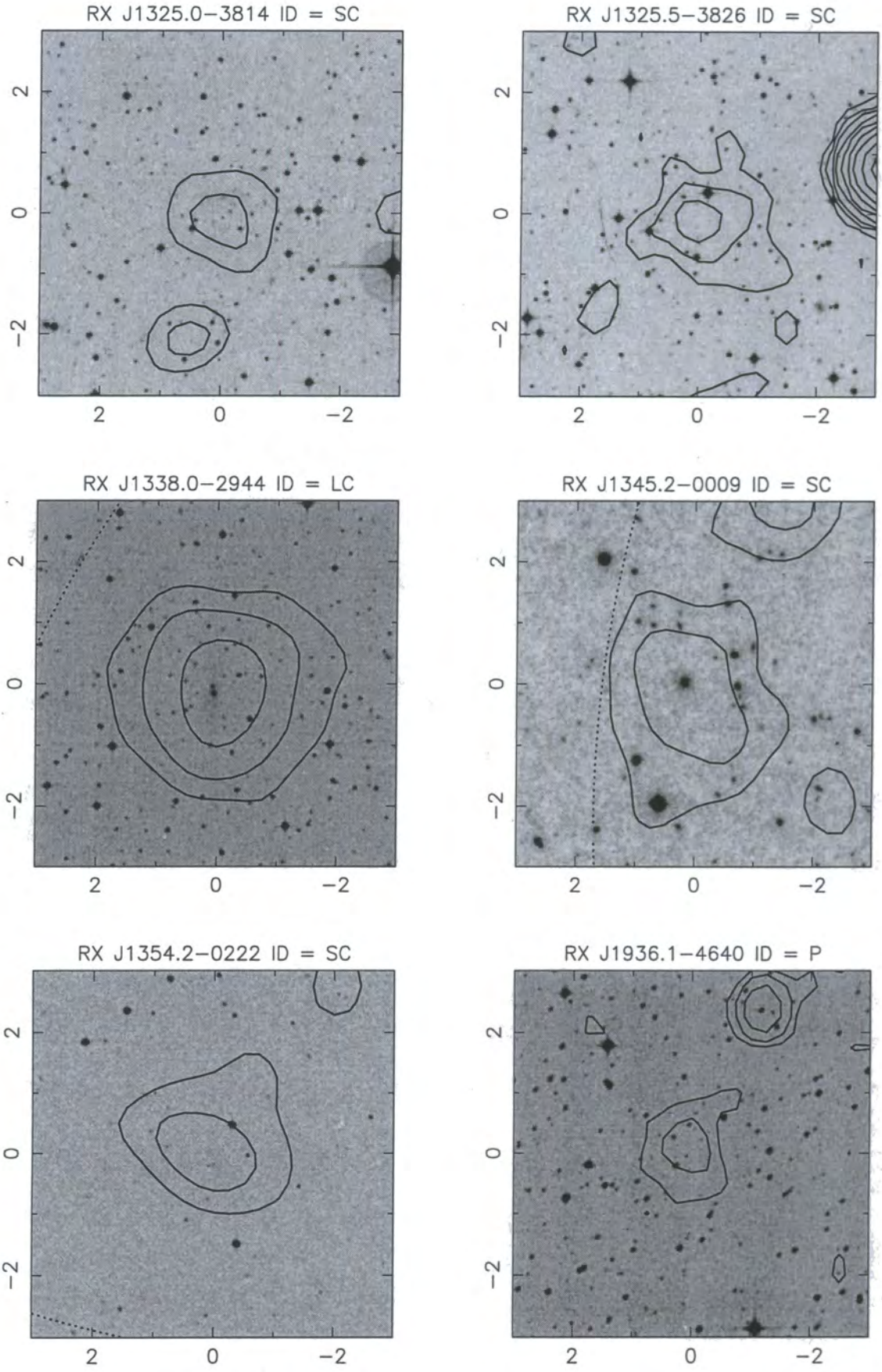
RX J1325.0−3814 ID = SC
RX J1325.5−3826 ID = SC
RX J1338.0−2944 ID = LC
RX J1345.2−0009 ID = SC
RX J1354.2−0222 ID = SC
RX J1936.1−4640 ID = P
2
0
−2

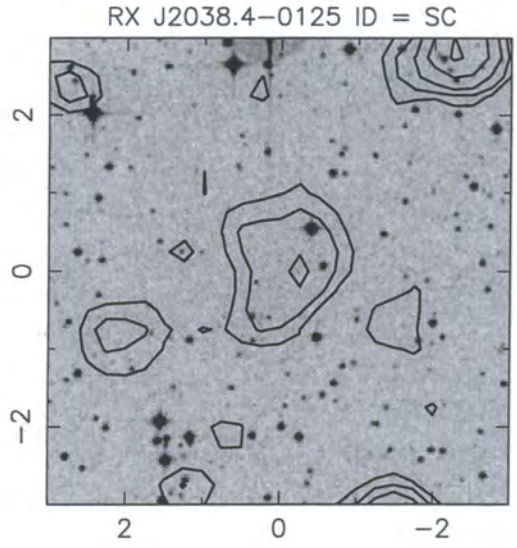
RX J2038.4−0125 ID = SC
2
0
−2
2
0
−2

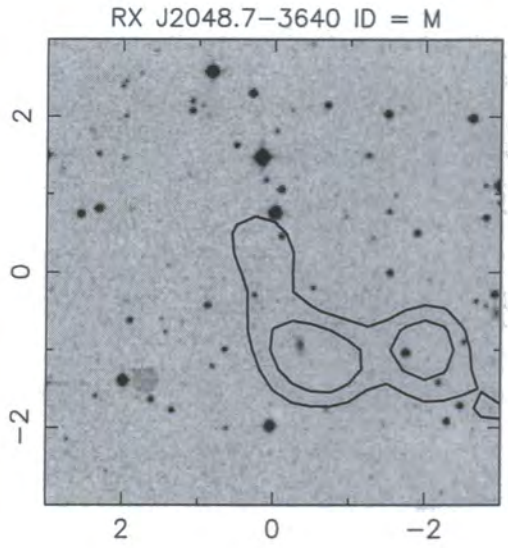
RX J2048.7−3640 ID = M
2
0
−2
2
0
−2

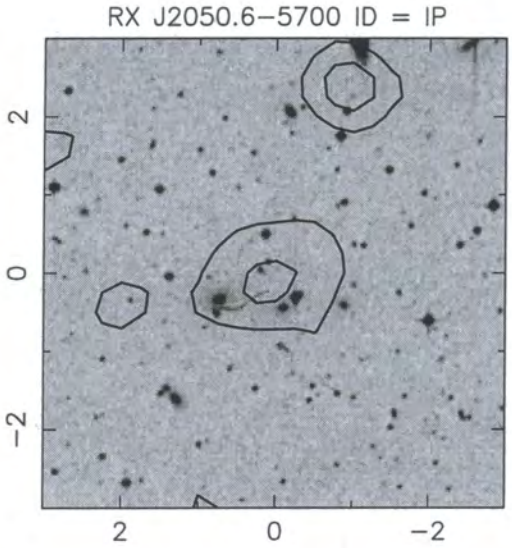
RX J2050.6−5700 ID = IP
2
0
−2
2
0
−2

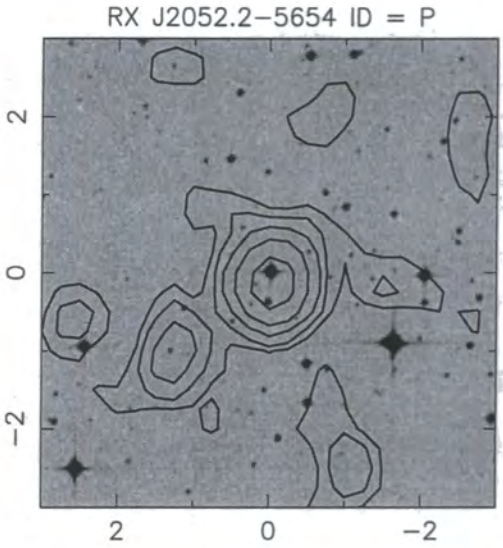
RX J2052.2−5654 ID = P
2
0
−2
2
0
−2

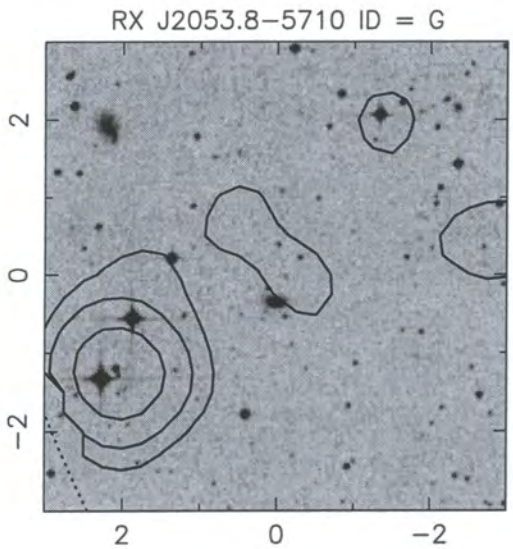
RX J2053.8−5710 ID = G
2
0
−2
2
0
−2

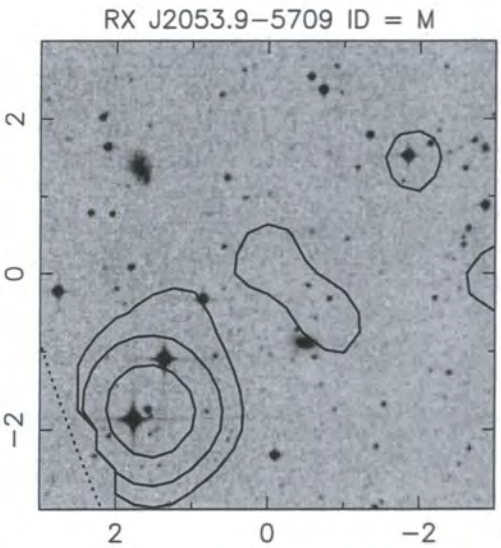
RX J2053.9−5709 ID = M
2
0
−2
2
0
−2

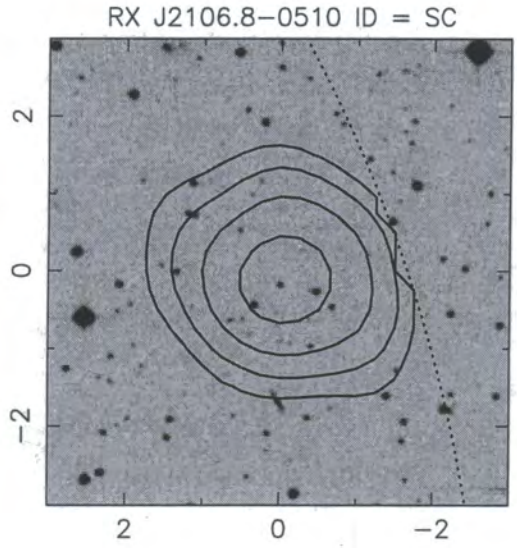
RX J2106.8−0510 ID = SC
2
0
−2
2
0
−2

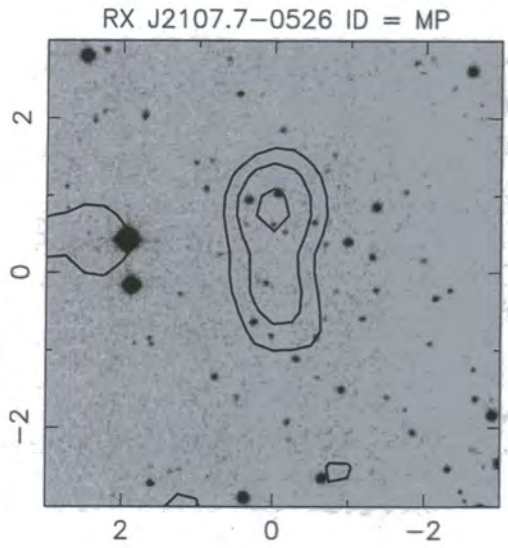
RX J2107.7−0526 ID = MP
2
0
−2
2
0
−2

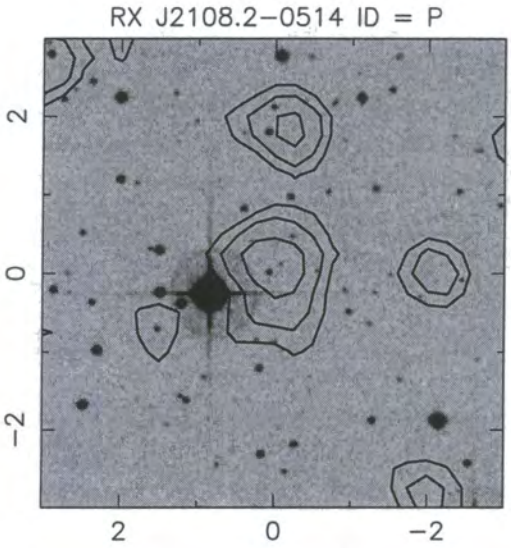
RX J2108.2−0514 ID = P
2
0
−2
2
0
−2

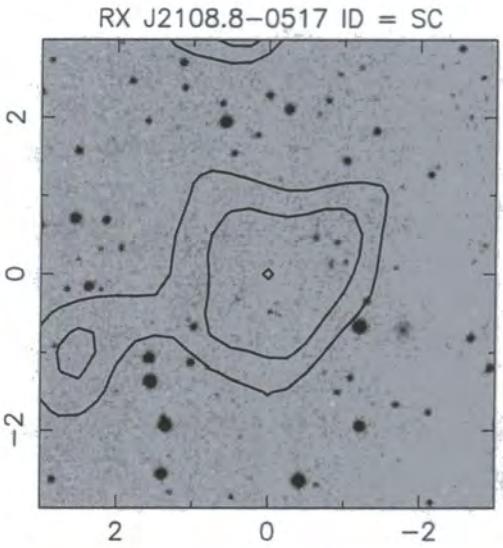
RX J2108.8−0517 ID = SC
2
0
−2
2
0
−2

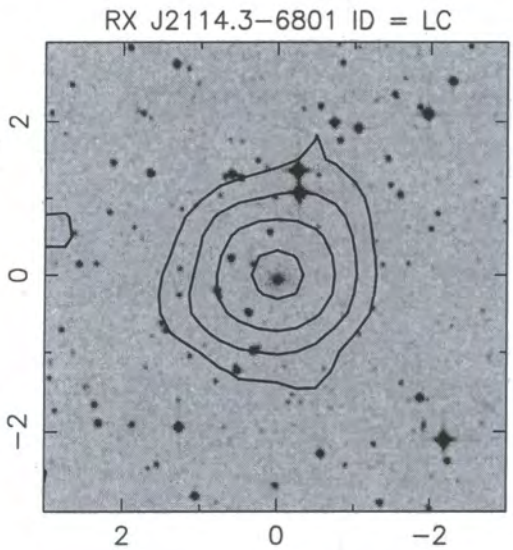
RX J2114.3−6801 ID = LC
2
0
−2
2
0
−2

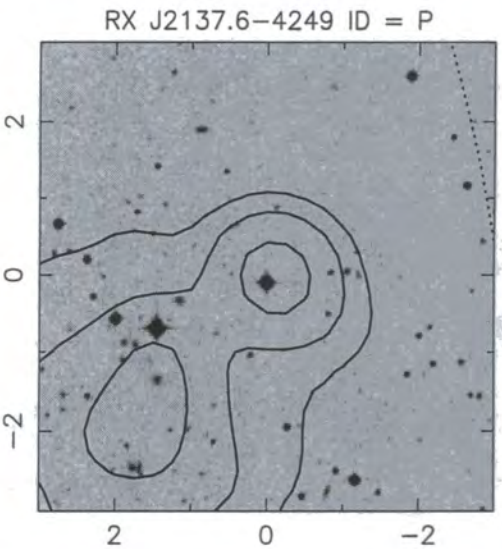
RX J2137.6−4249 ID = P
2
0
−2
2
0
−2

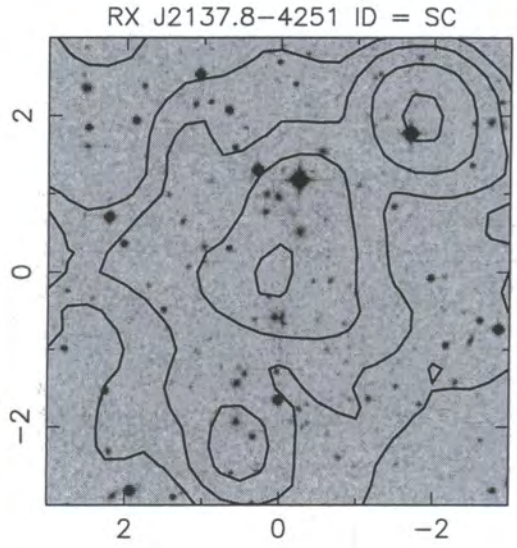
RX J2137.8−4251 ID = SC
2
0
−2
2
0
−2

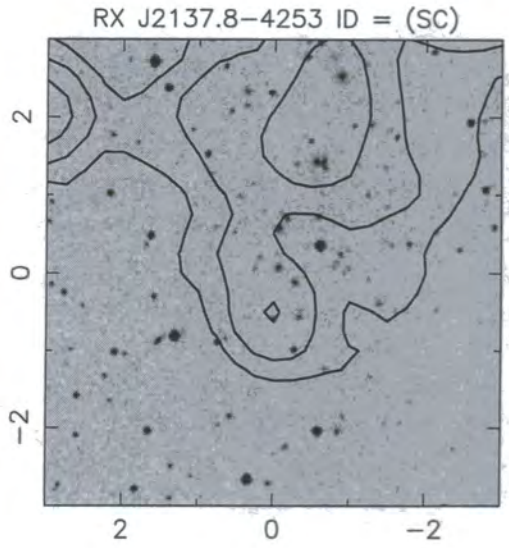
RX J2137.8−4253 ID = (SC)
2
0
−2
2
0
−2

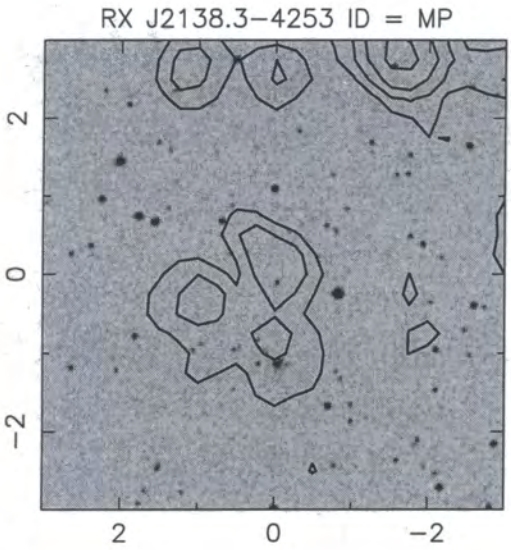
RX J2138.3−4253 ID = MP
2
0
−2
2
0
−2

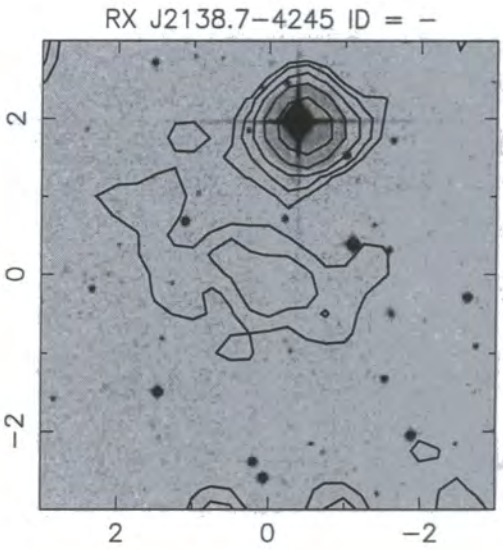
RX J2138.7−4245 ID = −
2
0
−2
2
0
−2

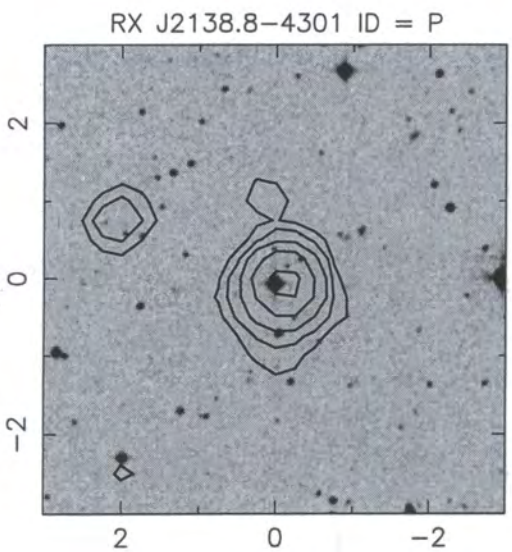
RX J2138.8−4301 ID = P
2
0
−2
2
0
−2

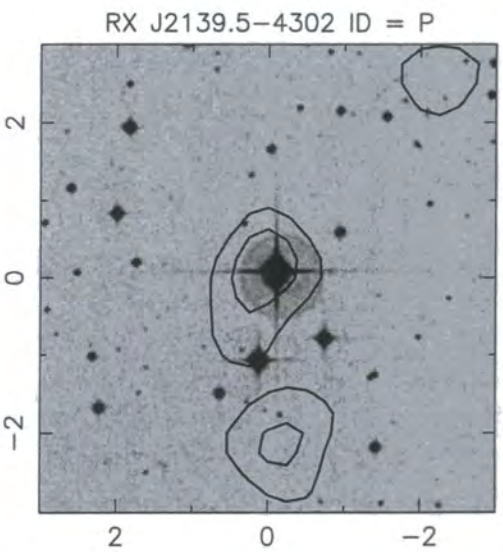
RX J2139.5−4302 ID = P
2
0
−2
2
0
−2

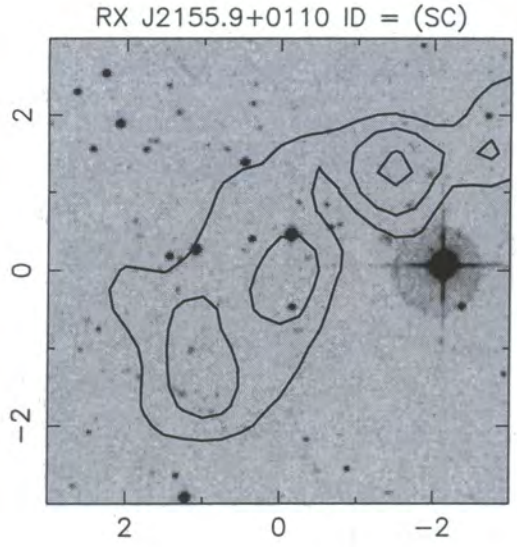
RX J2155.9+0110 ID = (SC)
2
0
−2
2
0
−2

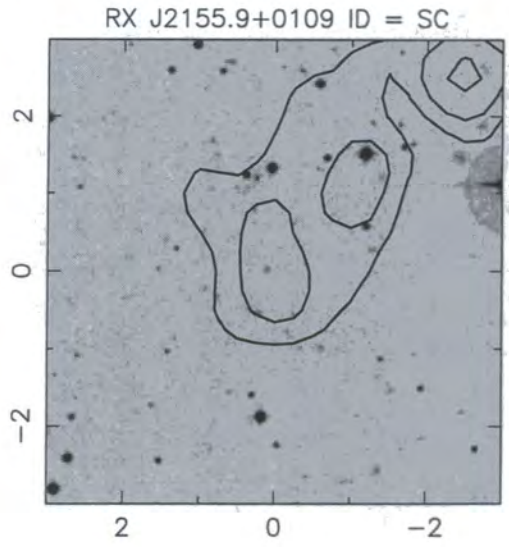
RX J2155.9+0109 ID = SC
2
0
−2
2
0
−2

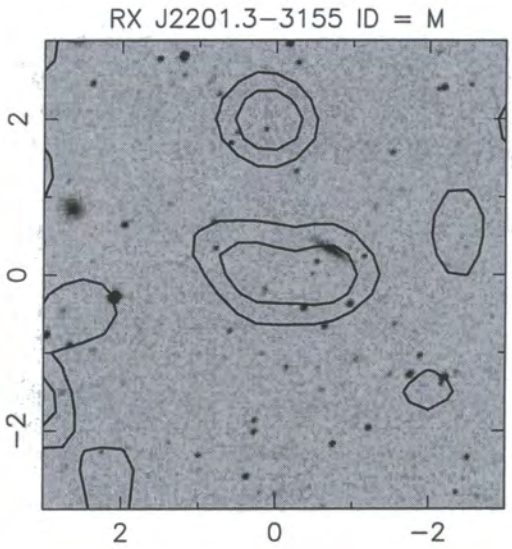
RX J2201.3−3155 ID = M
2
0
−2
2
0
−2

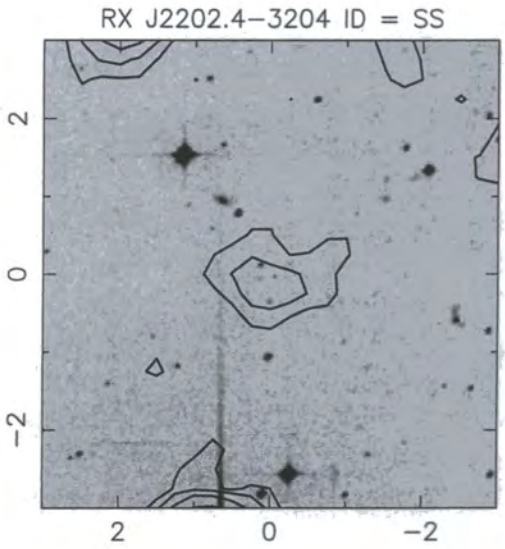
RX J2202.4−3204 ID = SS
2
0
−2
2
0
−2

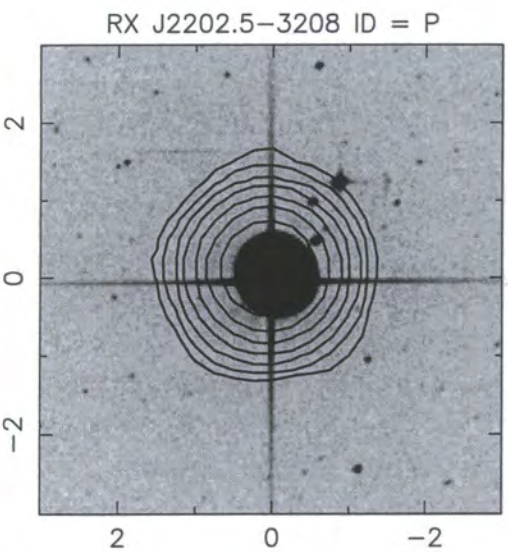
RX J2202.5−3208 ID = P
2
0
−2
2
0
−2

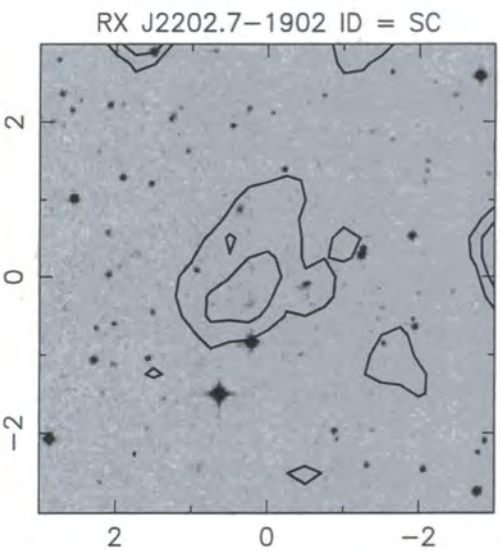
RX J2202.7−1902 ID = SC
2
0
−2
2
0
−2

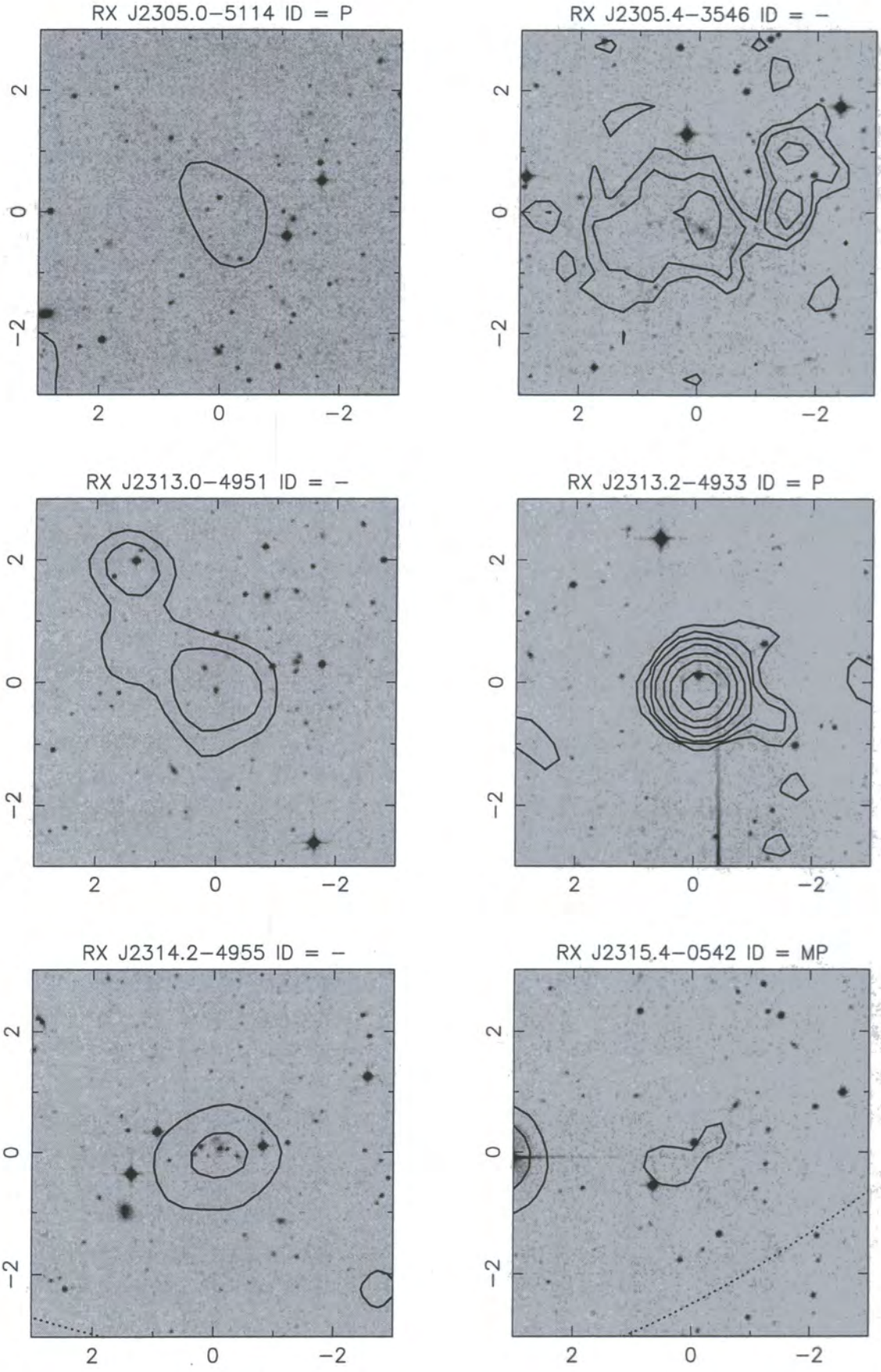
RX J2305.0−5114 ID = P
RX J2305.4−3546 ID = −
RX J2313.0−4951 ID = −
RX J2313.2−4933 ID = P
RX J2314.2−4955 ID = −
RX J2315.4−0542 ID = MP
2
0
−2

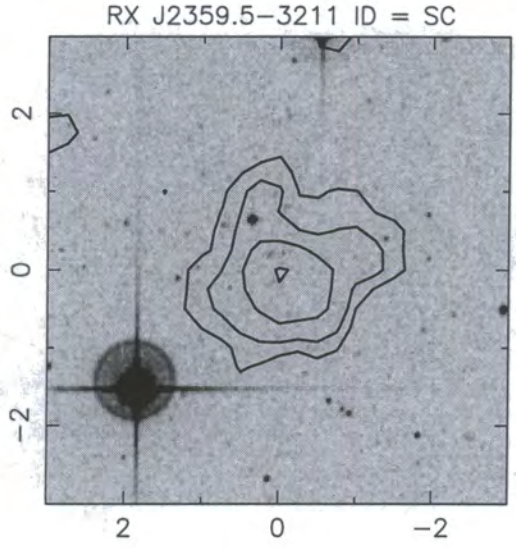
RX J2359.5−3211 ID = SC
2
0
−2
2
0
−2

Appendix C

Extended sources

The table below lists the 103 extended sources detected by the survey described in Chapter 2. The co-ordinates refer to the X-ray centre, as given by PSS, and are equinox 2000. The ID column lists the identification of the source. The first letter — if it is one of L, S, or I — refers to how the source was identified: a L indicates the identification comes from the literature (the NASA Extragalactic Database); a S indicates the object was spectroscopically-identified in one of the observing runs described in Chapter 3; and an I indicates that the identification was based on a deep, R-band, image of the source obtained with the ESO 3.6m telescope. If the first letter is none of these, then the identification is based on the DSS image shown in Appendix B. The second letter lists which class of object the source belongs to: a C means a cluster; a G means a galaxy; a Q means a QSO; an A means an AGN; and a S means a star. The letter P shows that there is an optical point source close to, or at, the centre of the X-ray emission. The letter M refers to the case when the X-ray emission is actually from multiple point sources, rather than one extended source. An ID of – means that the source has no identification, and brackets around an ID show that it is actually part of the source whose name is given in the Notes column. The redshift column, z, lists the redshift of the source, obtained either from the data obtained during the observing runs, or from the literature. For those clusters spectroscopically identified in this thesis (i.e. with an ID of SC), the redshift

is the average value of the detected galaxies, where the number in brackets gives the number of redshifts used. The Notes column gives the name of the object from the literature.

Name	RA			Declination			ID	z	Notes
	h	m	s	°	′	″			
RX J0313.4 – 5510	3	13	29.7	−55	10	25.7	–	–	
RX J0314.9 – 5458	3	14	55.8	−54	57	47.3	LQ	1.829	[MZZ88] 01558
RX J0318.2 – 0301	3	18	17.4	−3	1	14.7	SC	0.370(1)	†
RX J0318.5 – 0303	3	18	32.8	−3	2	45.7	SC	0.373(3)	
RX J0321.9 – 5119	3	21	57.1	−51	19	25.2	LC	0.070	Abell 3120
RX J0322.5 – 5101	3	22	33.9	−51	0	53.4	P	–	
RX J0323.8 – 5116	3	23	49.0	−51	15	45.3	–	–	
RX J0323.8 – 5114	3	23	50.4	−51	14	23.3	M	–	
RX J0333.0 – 3914	3	33	5.5	−39	13	49.4	SC	0.245(5)	
RX J0333.8 – 3906	3	33	50.1	−39	6	23.5	(LC)	–	(Abell 3135)
RX J0334.0 – 3901	3	34	3.2	−39	0	48.7	LC	0.063	Abell 3135
RX J0334.1 – 3904	3	34	11.0	−39	3	54.1	(LC)	–	(Abell 3135)
RX J0337.4 – 2519	3	37	28.1	−25	18	30.6	IP	–	
RX J0337.7 – 2522	3	37	45.2	−25	22	26.2	SC	0.577(3)	
RX J0338.4 – 2536	3	38	26.6	−25	36	23.6	LA	0.334	MS 0336.3 – 2546
RX J0338.6 – 2532	3	38	40.7	−25	32	0.1	IM	–	
RX J0341.8 – 4353	3	41	52.0	−43	53	21.6	LQ	1.751	QS F3:12
RX J0342.2 – 4351	3	42	16.0	−43	50	51.2	–	–	
RX J0342.4 – 4418	3	42	27.6	−44	18	19.6	–	–	
RX J0411.7 – 6547	4	11	42.8	−65	46	48.4	M	–	
RX J0413.7 – 6603	4	13	44.0	−66	2	30.4	P	–	
RX J0416.7 – 5525	4	16	44.8	−55	25	8.6	SC	0.365(3)	
RX J0452.7 – 5316	4	52	44.2	−53	15	31.7	IM	–	
RX J0455.7 – 5314	4	55	45.0	−53	13	31.5	IP	–	
RX J0454.5 – 4219	4	54	35.2	−42	19	17.2	SA	0.231	
RX J0454.9 – 4211	4	54	54.2	−42	11	3.9	SS	star	
RX J0505.3 – 2849	5	5	19.9	−28	49	5.2	SC	0.509(3)	
RX J0505.6 – 2828	5	5	36.7	−28	27	56.1	IM	–	
RX J0505.9 – 2826	5	5	57.6	−28	25	56.0	–	–	
RX J0505.9 – 2841	5	5	59.4	−28	40	38.0	MP	–	
RX J0514.3 – 4827	5	14	18.4	−48	27	2.5	SA	0.230	
RX J0529.6 – 5852	5	29	39.4	−58	51	37.1	M	–	
RX J0529.6 – 5848	5	29	39.9	−58	48	20.7	IM	–	
RX J0530.5 – 5852	5	30	31.1	−58	51	34.8	SC	0.338(2)	

† There is an AGN, identified as being at $z = 0.233$, $\sim 1'$ North of the cluster centre, visible as the point-source component of the smoothed X-ray image in Appendix B. When calculating the cluster flux (Section 3.2), the AGN emission is masked out.

Name	RA			Declination			ID	z	Notes
	h	m	s	°	′	″			
RX J0857.8 + 1410	8	57	48.4	+14	9	57.1	MP	–	
RX J0857.8 + 1411	8	57	52.2	+14	10	41.5	MP	–	
RX J0858.4 + 1357	8	58	25.3	+13	57	14.6	SC	0.485(3)	
RX J0945.6 − 1434	9	45	40.5	−14	34	6.2	IP	–	
RX J0946.5 − 1410	9	46	32.9	−14	9	50.5	SC	0.230(5)	
RX J0947.8 + 0741	9	47	48.8	+7	41	24.7	SQ	0.631	
RX J0947.9 + 0730	9	47	57.5	+7	30	26.0	SC	0.128(3)	
RX J0948.3 + 0729	9	48	20.9	+7	28	58.7	IP	–	
RX J1001.1 − 1926	10	1	9.3	−19	26	23.7	LG	–	ESO 567- G 003
RX J1002.6 − 0809	10	2	40.2	−8	8	48.1	P	–	
RX J1036.4 + 0002	10	36	26.5	+0	2	6.2	IP	–	
RX J1037.9 − 0007	10	37	57.6	−0	6	53.3	SQ	0.746	
RX J1045.3 − 0017	10	45	23.2	−0	16	50.6	SS	star	
RX J1141.7 + 1022	11	41	45.5	+10	21	47.8	SQ	1.250	
RX J1142.0 + 1009	11	42	5.6	+10	8	47.5	LC	0.118	Abell 1354
RX J1142.2 + 1027	11	42	16.8	+10	26	47.1	LC	0.070	Abell 1356
RX J1200.8 − 0328	12	0	48.4	−3	27	50.9	SC	0.395(4)	
RX J1203.4 − 0350	12	3	26.4	−3	49	58.1	IP	–	
RX J1204.3 − 0351	12	4	22.8	−3	50	59.8	SC	0.262(5)	
RX J1205.0 − 0333	12	5	2.8	−3	32	31.1	SC	0.368(5)	
RX J1205.6 − 0338	12	5	38.0	−3	38	20.7	SC	0.207(3)	
RX J1213.8 + 1311	12	13	52.6	+13	10	36.2	LG	0.008	NGC 4193
RX J1227.1 + 0856	12	27	7.9	+8	55	57.3	(SC)	–	(RX J1227.2 + 0858)
RX J1227.2 + 0858	12	27	14.5	+8	58	10.1	SC	0.090(4)	8.0′ from Abell 1541
RX J1227.4 + 0850	12	27	26.6	+8	50	11.0	LC	0.089	Abell 1541
RX J1227.4 + 0855	12	27	29.8	+8	54	37.8	(LC)	–	(Abell 1541)
RX J1235.6 + 1311	12	35	38.2	+13	10	46.5	SC	0.253(4)	
RX J1236.4 + 1259	12	36	25.5	+12	58	59.1	G	–	
RX J1252.0 − 2921	12	52	4.6	−29	20	42.6	–	–	
RX J1253.2 + 1556	12	53	14.7	+15	55	52.7	SC	0.275(4)	
RX J1259.7 − 3236	12	59	47.6	−32	36	17.9	SC	0.076(7)	
RX J1313.6 − 3251	13	13	39.1	−32	50	44.3	–	–	
RX J1325.0 − 3814	13	25	1.6	−38	13	35.3	SC	0.296(6)	
RX J1325.5 − 3826	13	25	34.8	−38	25	49.5	SC	0.445(4)	
RX J1338.0 − 2944	13	38	5.8	−29	44	25.3	LC	0.189	MS 1335.2 − 2928
RX J1345.2 − 0009	13	45	14.8	−0	8	31.7	SC	0.087(2)	
RX J1354.2 − 0222	13	54	17.2	−2	21	45.9	SC	0.551(5)	

Name	RA			Declination			ID	z	Notes
	h	m	s	°	′	″			
RX J1936.1 − 4640	19	36	6.9	−46	40	4.1	P	–	
RX J2038.4 − 0125	20	38	29.3	−1	25	16.8	SC	0.673(2)	
RX J2048.7 − 3640	20	48	45.4	−36	39	52.8	M	–	
RX J2050.6 − 5700	20	50	41.6	−56	59	39.6	IP	–	
RX J2052.2 − 5654	20	52	12.2	−56	54	26.6	P	–	
RX J2053.8 − 5710	20	53	51.2	−57	9	41.1	G	–	
RX J2053.9 − 5709	20	53	55.0	−57	9	9.2	M	–	
RX J2106.8 − 0510	21	6	49.0	−5	9	54.8	SC	0.449(7)	
RX J2107.7 − 0526	21	7	47.7	−5	26	11.6	MP	–	
RX J2108.2 − 0514	21	8	15.6	−5	13	44.1	P	–	
RX J2108.8 − 0517	21	8	49.5	−5	16	39.6	SC	0.320(2)	
RX J2114.3 − 6801	21	14	20.8	−68	1	4.2	LC	0.130	DS 210958 − 681304‡
RX J2137.6 − 4249	21	37	40.0	−42	49	0.4	P	–	
RX J2137.8 − 4251	21	37	49.5	−42	50	49.1	SC	0.185(7)	Abell 3791
RX J2137.8 − 4253	21	37	53.2	−42	52	49.2	(SC)	–	(Abell 3791)
RX J2138.3 − 4253	21	38	18.9	−42	53	20.5	MP	–	
RX J2138.7 − 4245	21	38	42.8	−42	44	35.6	–	–	
RX J2138.8 − 4301	21	38	52.2	−43	1	5.6	P	–	
RX J2139.5 − 4302	21	39	31.5	−43	1	50.5	P	–	
RX J2155.9 + 0110	21	55	54.9	+1	10	3.9	(SC)	–	(RX J2155.9 + 0109)
RX J2155.9 + 0109	21	55	59.1	+1	9	2.1	SC	0.219(6)	
RX J2201.3 − 3155	22	1	19.0	−31	54	33.8	M	–	
RX J2202.4 − 3204	22	2	29.4	−32	4	10.9	SS	star	
RX J2202.5 − 3208	22	2	32.8	−32	7	56.9	P	–	
RX J2202.7 − 1902	22	2	44.6	−19	1	59.8	SC	0.436(3)	
RX J2305.0 − 5114	23	5	3.2	−51	13	38.7	P	–	
RX J2305.4 − 3546	23	5	25.1	−35	45	40.3	–	–	
RX J2313.0 − 4951	23	13	4.0	−49	51	18.8	–	–	
RX J2313.2 − 4933	23	13	17.1	−49	33	20.3	P	–	
RX J2314.2 − 4955	23	14	15.8	−49	55	17.8	–	–	
RX J2315.4 − 0542	23	15	28.2	−5	41	43.7	MP	–	
RX J2359.5 − 3211	23	59	35.9	−32	11	6.5	SC	0.478(3)	

‡ DS 210958-681304 is also known as the Pavo cluster.